Visible and Near Infrared imaging spectroscopy and the exploration of small scale hydrothermally altered and hydrated environments on Earth and Mars

By

Jennifer Kate Harris

A thesis submitted to Birkbeck College, University of London for the degree of Doctor of Philosophy (PhD)

I, Jennifer K Harris, confirm that the work submitted in this thesis is my own. Where information has been derived from other sources, this is clearly indicated in the text.

Abstract

The use of Visible and Near Infrared (VNIR) imaging spectroscopy is a cornerstone of planetary exploration. This work shall present an investigation into the limitations of scale, both spectral and spatial, in the utility of VNIR images for identifying small scale hydrothermal and potential hydrated environments on Mars, and regions of the Earth that can serve as martian analogues. Such settings represent possible habitable environments; important locations for astrobiological research.

The ESA/Roscosmos ExoMars rover PanCam captures spectrally coarse but spatially high resolution VNIR images. This instrument is still in development and the first field trial of an emulator fitted with the final set of geological filters is presented here. Efficient image analysis techniques are explored and the ability to accurately characterise a hydrothermally altered region using PanCam data products is established.

The CRISM orbital instrument has been returning hyperspectral VNIR images with an 18 m^2 pixel resolution since 2006. The extraction of sub-pixel information from CRISM pixels using Spectral Mixture Analysis (SMA) algorithms is explored. Using synthetic datasets a full SMA pipeline consisting of publically available Matlab algorithms and optimised for investigation of mineralogically complex hydrothermal suites is developed for the first time. This is validated using data from Námafjall in Iceland, the region used to field trial the PanCam prototype. The pipeline is applied to CRISM images covering four regions on Mars identified as having potentially undergone hydrothermal alteration in their past. A second novel use of SMA to extract a unique spectral signature for the potentially hydrated Recurring Slope Lineae features on Mars is presented. The specific methodology presented shows promise and future improvements are suggested.

The importance of combining different scales of data and recognising their limitations is discussed based on the results presented and ways in which to take the results presented in this thesis forward are given.

Acknowledgements

The work presented here is the result of almost 4 years of work (although arguably the preceding 29 contributed significantly too) and would not have been possible without the help and encouragement of numerous people.

Firstly I need to thank my supervisors Prof Ian Crawford and Dr Claire Cousins who allowed me to follow my own research instincts and made sure I managed to reach this final stage, ending up with a piece of work that I'm proud of.

Secondly my huge appreciation to all of the other people I have worked with here in the UK and in various cold and windy sites in the Atlantic; Dr Pete Grindrod and Dr Matt Gunn for providing gin and wine opening capabilities and emergency computer triage during field work, and Prof Dave Barnes, Mr Steve Hirons, Dr Alasdair McArthur, Prof Andrew Coates and Dr Steve Pugh for letting me use their instruments and helping make it possible to spend my summers messing around on windy hill tops and cliffs in the name of science.

Thirdly thanks to my fellow junior academics from the CPS, Birkbeck and UCL who have helped to keep me sane, largely through judicious application of alcohol and loud music. In no particular order thank you Louise, Lucy, Ceri, Josh, Tom N, Tom W, Debbie, Lexi, Mark, Nikki, Mike, Rick, Elliot, Roberto, Joel, Pete, SJ and everyone else I've no doubt missed out, my lunchtimes and Thursday and Friday evenings won't be the same without you all.

And last but not least to all the others who've helped see me through this process, in particular Vanessa for being such a great flatmate when I first moved to London and Sarah for providing a constant ear (and eye) for my frequent rants despite living on a different continent. And of course much love to my family for all the support (and in certain cases frequent sarcastic comments) they've provided for as long as I've been around. I wouldn't have been able to remain a student for as long as I have without them.

Table of Contents

Abstract 3
Acknowledgements 4
Table of Contents 5
List of Acronyms and Variables 10
List of Figures 13
List of Tables 16
Chapter 1: Introduction 17
1.1: Thesis motivation 17
1.2: Thesis outline 19
Chapter 2: Spectral imaging, Mars and habitability 21
2.1: Introduction 21
2.2: Visible and Near Infrared (VNIR) geological reflectance spectroscopy 21
2.2.1: Physics of VNIR reflectance spectra 21
2.2.2: Reflectance spectroscopy of minerals associated with hydrothermal alteration 22
2.2.2.1: Carbonates 24
2.2.2.2: Iron-oxides and hydroxides 24
2.2.2.3: Phyllosilicates 24
2.2.2.4: Silicates 25
2.2.2.5: Sulfates 25
2.2.3: Imaging Spectroscopy 25
2.3: Martian mineralogy 27
2.4: Environmental habitability 29
2.4.1: Habitability and the exploration of Mars 29
2.4.2: Hydrothermal activity on Mars 30
2.5: Comparative planetology and analogue sites for Mars 33
2.5.1: Earth analogues for hydrothermal systems on Mars 34
2.5.2: Field trials of Mars rover instruments in analogue sites 36
2.6: Summary 37
Chapter 3: ExoMars PanCam and hydrothermal alteration in Iceland 38
3.1: Introduction 38
3.2: Background 38
3.2.1: PanCam and ground-based spectral imagers on Mars 38

3.2.2: Námafjall and Iceland as a Mars analogue site 43
3.3: Data collection and processing 46
3.3.1: AUPE-2 46
3.3.2: Ocean Optics Jaz Spectrometer 47
3.3.3: X-Ray Diffraction and laboratory VNIR spectroscopy of rock and soil samples . 47
3.3.4: Spectral Parameters 48
3.3.5: Principal Components Analysis (PCA) 49
3.4: Results 51
3.4.1: A04_Tuff 54
3.4.2: A06_Soils 57
3.4.3: A07_Pillow 59
3.4.4: A08_Veins 62
3.4.5: Principal Components Analysis results 64
3.5: Discussion of results 65
3.5.1: Data quality and issues 65
3.5.1.1: NIR/RWAC spectral discrepancies 65
3.5.1.2: NIR/RWAC image artefacts 68
3.5.1.3: Stereo field-of-view (FoV) limitations 69
3.5.1.4: AUPE-2 vs ExoMars PanCam 69
3.5.2: Deduction of hydrothermal alteration and environmental type 70
3.6: Future work 71
3.7: Summary 71
Chapter 4: Spatial scale, sub-pixel information and Spectral Mixture Analysis 73
4.1: Introduction 73
4.2: Issues of spatial scale in spectral analysis on Earth and Mars 73
4.3: Spectral Mixture Analysis 74
4.3.1: How many endmembers are present? 77
4.3.2: What are the endmember spectra? 79
4.3.2.1: Endmember extraction from linear mixtures 80
4.3.2.2: Endmember extraction from non-linear mixtures 83
4.3.3: How much of each endmember is present? 83
4.4: Spectral Mixture Analysis applied to Mars 87
4.5: Applicability, availability and accessibility of SMA 90
4.6: Summary 91

Chapter 5: Development of a best practice, publically available Spectral Mixture Analysis pipeline for the detection of small scale hydrothermal surface alteration 92
5.1: Introduction 92
5.2 Synthetic images 93
5.3: SMA related algorithms used in this work 96
5.3.1: Endmember Dimensionality Algorithms (EDA) 97
5.3.2: Endmember Extraction Algorithms (EEA) 99
5.3.3: Abundance Estimation Algorithms (AEA) 100
5.4: Results of testing the SMA algorithms on synthetic images 101
5.4.1: Endmember Dimensionality Algorithm (EDA) Results 101
5.4.1.1: Number of endmembers (high p value) 101
5.4.1.2: Number of pixels (low N value) 102
5.4.1.3: Inter-endmember spectral variation 102
5.4.1.4: Non-linear mixing 103
5.4.1.5: Optimum EDA 104
5.4.2: Endmember Extraction Algorithm (EEA) Results 106
5.4.2.1: Number of endmembers (high p value) 107
5.4.2.2: Number of pixels (low N value) 107
5.4.2.3: Inter-endmember spectral variation 107
5.4.2.4: Non-linear mixing 107
5.4.2.5: Optimal EEA 110
5.4.2.6: Wrong p value 111
5.4.3: Abundance Estimation Algorithm (AEA) Results 112
5.4.3.1: Number of endmembers (high p value) 112
5.4.3.2: Number of pixels (low N value) 113
5.4.3.3: Inter-endmember spectral variation 113
5.4.3.4: Non-linear mixing 113
5.4.3.5: SSA conversion 113
5.4.3.6: Overall Scene Abundances 115
5.4.3.7: Errors and timing 116
5.5: Optimum pipeline based on results of synthetic image tests 116
5.6: Test on real data from Námafjall, Iceland 118
5.6.1: Aerial dataset 119
5.6.2: Field dataset 119

5.6.3: Groundtruth dataset 120
5.7: Iceland data results 123
5.7.1: Aerial data 123
5.7.2: Field data 127
5.8: Discussion of differences between synthetic sensitivity and Iceland results 131
5.9: Future work 132
5.10: Summary 132
Chapter 6: Application of Spectral Mixture Analysis on hydrothermally altered regions on Mars 133
6.1: Introduction 133
6.2: Data collection 133
6.2.1: The Compact Reconnaissance Imaging Spectrometer for Mars (CRISM) 133
6.2.2: Selection of hydrothermal targets 135
6.2.3: CRISM data processing 136
6.3: SMA results 138
6.3.1: Nili Patera 138
6.3.2: Hecates Tholus 149
6.3.3: Aromatum Chaos 158
6.3.4: Unnamed (Kirkcaldy) Crater (17.367 N, 291.213 E) 165
6.4: Hydrothermal region unmixing discussion 174
6.5: Future Work 176
6.6: Summary 176
Chapter 7: Spectral Mixture Analysis applied to Recurring Slope Lineae 178
7.1: Introduction 178
7.2: Recurring Slope Lineae (RSL) 178
7.3: RSL and Spectral Unmixing 179
7.4: Image preparation 180
7.5: SMA results 183
7.6: Discussion of SMA results – a suitable technique for RSL? 186
7.6: Future work 187
7.7: Summary 188
Chapter 8: Conclusions 189
8.1: PanCam – high spatial, low spectral resolution 189
8.2: CRISM and SMA – high spectral and low spatial resolution 190

8.3: Importance of image pre-processing 193
8.4: Scale, why it matters and how it can be enhanced 194
8.5: Future work 195
References 197
Appendix I: AUPE-2 processing pipeline and associated IDL code **Error! Bookmark not defined.**
Final Full Processing Pipeline in ENVI 230
IDL codes 232
Appendix II: Synthetic image endmember plots from Chapter 5 236
Appendix III: Matlab codes for EDA's from Chapter 5 243
ODM 243
ELM 245
Appendix IV: Tables listing results of all SMA synthetic image tests 247
EDA 247
EEA 259
AEA 267

List of Acronyms and Variables

Variables

L = number of spectral bands

p = number of endmembers in a scene/dataset

N = number of pixels in an image

$\boldsymbol{x}$ = L x 1 pixel spectrum vector

$\boldsymbol{\alpha}$ = p x 1 vector containing the endmember abundances

$\boldsymbol{R}$ = L x p matrix whose columns are the L x 1 endmember spectra

$\boldsymbol{\varepsilon}$ = L x 1 noise vector

i = incidence angle

e = emissions angle

w = single scattering albedo

R = reflectance

$H(\mu)$ = Hapke's approximation to Chandrasekhar's multiple scattering equation

Acronyms

AEA	Abundance Estimation Algorithm
ANC	Abundance Non-Negative Constraint
ARSF	Airborne Research and Survey Facility
ART	Adaptive Resonance Theory
ASC	Abundance Sum-to-one Constraint
ASD	Analytical Spectral Devices
AUPE-2	Aberystwyth University PanCam Emulator 2
BPSS	Bayesian Point Source Separation
CRISM	Compact Reconnaissance Imaging Spectrometer for Mars
DISORT	Discrete Ordinates Radiative Transfer Program for a Multi-Layered Plane-Parallel Medium
EDA	Endmember Dimensionality Algorithm
EEA	Endmember Extraction Algorithm
ELM	Eigenvalue Likelihood Maximisation
ESA	European Space Agency
FATT	Factor Analysis and Target Transformation
FCLLS	Fully Constrained Linear Least Squares
FoV	Field of View

FRT	Full Resolution Targeted
FSF	Field Spectroscopy Facility
FWHM	Full Width Half Maximum
HFC	Harsanyi-Farrand-Chang
HiRISE	High Resolution Imaging Science Experiment
HRC	High Resolution Camera
HRT	Half Resolution Targeted
HySIME	Hyperspectral Signal Subspace Identification by Minimum Error
I/F	"I/F is defined as the spectral radiance divided by the solar spectral irradiance of the Sun at Mars distance divided by [*the illumination angle*]. Another way to put it is that it is the ratio of the radiance observed from a surface to that of a perfect white Lambertian surface illuminated by the same light but at normal incidence." (Bennett et al., 2011)
ICE	Iterated Constrained Endmembers
IQR	Interquartile Range
ISEM	Infrared Spectrometer for ExoMars
KFCLS	Kernalised Fully Constrained Least Squared
MAP	Maximum Probability Estimator
MELSUM	Multiple Endmember Linear Spectral Unmixing Model
MER	Mars Exploration Rovers
MESMA	Multiple Endmember Spectral Mixture Analysis
MGM	Modified Gaussian Model
MLP	Multilayer Perceptron
MNF	Minimum Noise Fraction transformation
MRO	Mars Reconnaissance Orbiter
MSL	Mars Science Laboratory
MVC-NMF	Minimum Volume Constrained Negative Matrix Factorization
MVES	Minimum Volume Enclosing Simplex
MVSA	Minimum Simplex Volume Analysis
NASA	National Aeronautics and Space Administration
NLPCA	Non-Linear Principal Components Analysis
ODM	Outlier Detection Method
OMEGA	Observatoire pour la Minéralogie, l'Eau, les Glaces et l'Activité
OSP	Orthogonal Subspace Projection

PCA	Principal Components Analysis
PPI	Pixel Purity Index
PPNM	Polynomial Post-Nonlinear Model
RBF	Radial Basis Function
RGB	Red, Green, Blue
RMVES	Robust Minimum Volume Enclosing Simplex
ROI	Region of Interest
RR	Relative Reflectance
RSL	Recurring Slope Lineae
SISAL	Simplex Identification via Split Augmented Lagrangian
SMA	Spectral Mixture Analysis
SMACC	Sequential Maximum Angle Convex Cone
SNR	Signal to Noise Ratio
SPICE	Sparsity Promoting Iterated Constrained Endmembers
SSA	Single Scattering Albedo
SU	Spectral Unmixing
SVDD	Support Vector Data Description
SVM	Support Vector Machine
SWIR	Short Wave Infrared
TES	Thermal Emission Spectrometer
THEMIS	Thermal Emission Imaging Spectrometer
VCA	Vector Component Analysis
VD	Virtual Dimensionality
VNIR	Visible and Near Infrared
WAC	Wide Ange Camera
XRD	X-Ray Diffraction

List of Figures

2.1 USGS spectral library spectra of minerals common to hydrothermal environments 23
2.2 Hyperspectral imaging spectroscopy 26
2.3 Regions of Mars identified as being previously hydrothermally active 32
2.4 Map showing locations of Mars analogue locations on Earth 33

3.1 PanCam-type instrument narrowband geology filter wavelengths and widths from recent Mars landers and rovers 39
3.2 Localities used for field-testing the ExoMars PanCam emulator "AUPE-2" in Námafjall, Iceland 44
3.3 Field photographs showing spatial context of AUPE-2 target sites 45
3.4 Laboratory ASD VNIR reflectance spectra of AUPE-2 ROI target samples 54
3.5 AUPE-2 datasets for site A04_Tuff 56
3.6 AUPE-2 datasets for site A06_Soils 59
3.7 AUPE-2 datasets for site A07_Pillow 60
3.8 AUPE-2 datasets for site A08_Vein 63
3.9 AUPE-2 datasets for site A08_Vein 64
3.10 Principal Components Analysis plots showing the groupings for spectral classes as observed with AUPE-2 R* data 65
3.11 Comparison of AUPE-2 R* spectra with in-situ field spectrometer ROI measurements and the ASD laboratory spectra both resampled to AUPE-2 spectral bands 67
3.12 BD950 spectral parameter image from site A07_Pillow calculated using the 950 and 1000nm filter images showing prominent concentric circle artefacts caused by internal scattering within the WAC optics 68

4.1 Linear spectral mixture model 75
4.2 Intimate and layered non-linear spectral mixture scenarios 76
4.3 Endmember Extraction simplex examples 82
4.4 Hapke model geometry 85

5.1 Example ODM output plots 98

5.2 Example HySIME output plots 99
5.3 EDA results from synthetic images 2a, 2b, 3a and 3b 103
5.4 EDA results from synthetic image 5 104
5.5 EDA results from synthetic image 10a 105
5.6 SISAL and RMVES extracted endmembers from synthetic image 10b, SNR 35 dB and 55 dB 109
5.7 Flowchart detailing the optimum SMA pipeline for analysis of hydrothermally altered terrain 118
5.8 Field photo showing outline of 18m^2 grid on flat altered plain at Námafjall, Iceland 120
5.9 Eagle RGB (bands 638.7, 548.4, 461.4 nm) 2 m pixel image highlighting ROI extracted for SMA processing 124
5.10 Mean SISAL extracted endmembers from the 2 m pixel ARSF ROI 126
5.11 Mean SISAL extracted endmembers from ASD field spectrometer dataset 129
5.12 RMSE values from final reconstructed ASD field spectrometer pipeline results ... 130

6.1 Map of Mars indicating locations of hydrothermal SMA targets and images highlighting CRISM and HiRISE coverage over each target 137
6.2 Nili Patera CRISM image FRT000106258_07_IFS_TRR3 RGB with HiRISE image ESP_013582_185_COLOR overlain 139
6.3 SISAL extracted endmember spectra for Nili Patera 142
6.4 Abundance maps for SISAL extracted endmember spectra from Nili Patera 144
6.5 RMSE map for pipeline results from Nili Patera 148
6.6 Hecates Tholus CRISM image HRL00007331_07_IF183S_TRR3 RGB composite overlain with HiRISE image ESP_017055_1975_COLOR and SMA ROI regions 150
6.7 Hecates Tholus SISAL extracted endmembers from ROI1_south and ROI2_north 151
6.8 Abundance maps for SISAL extracted endmember spectra from Hecates Tholus ROI1_south and ROI2_north 154
6.9 RMSE maps for pipeline results for Hecates Tholus ROI1_south and ROI2_north 157
6.10 Aromatum Chaos CRISM image FRT00024F8_07_IF165S_TRR3 RGB composite and overlain HiRISE image ESP_026891_1790_RED 160
6.11 SISAL extracted endmembers from Aromatum Chaos 161
6.12 Abundance maps for SISAL extracted endmember spectra from

Aromatum Chaos 162
6.13 RMSE map for pipeline results for Aromatum Chaos 164
6.14 Kirkcaldy Crater CRISM image FRT00017463_07_IF165S_TRR3 RGB composite overlain with HiRISE image ESP_017055_1975_COLOR 166
6.15 SISAL extracted endmember from Kirkcaldy Crater 168
6.16 Abundance maps for SISAL extracted endmember spectra from Kirkcaldy Crater 170
6.17 RMSE map for pipeline results for Kirkcaldy Crater 173

7.1 HiRISE image ESP_032381_1380 showing prominent RSL with CRISM pixel outlines in Palikir Crater 181
7.2 SMA extracted endmember spectra from Palikir Crater 183

List of Tables

2.1 Minerals detected on Mars from both orbital and ground-based observations (taken from Ehlmann and Edwards (2014)) 27

3.1 PanCam-type instrument geology narrowband filter wavelengths and widths from recent Mars landers and rovers 40
3.2 Technical specifications of the current configuration of the ExoMars PanCam and the Aberystwyth University PanCam Emulator (AUPE-2) 41
3.3 Spectral parameters designed for AUPE-2 WAC multispectral data 48
3.4 Summary of data collected in-situ in Námafjall, Iceland 50
3.5 Summary of AUPE-2 Námafjall ROI target sites, their mineralogy, and VNIR spectral features 51

4.1 SMA algorithms used to analyse Mars spectral imagery 83

5.1 Details of synthetic images used to evaluate sensitivity of SMA algorithms to spectral image complexities inherent in small scale hydrothermally altered environments 89
5.2 XRD and laboratory VNIR mineral identifications from Námafjall altered plain samples 112
5.3 EDA values for aerial ARSF Iceland dataset 114
5.4 SISAL endmember identifications and overall scene abundance percentages for the Námafjall field spectra dataset 118

6.1 Nili Patera SISAL extracted endmember mineral identifications, matching to entries in the USGS and CRISM spectral libraries 129
6.2 Hecates Tholus ROI details and resulting ODM p values 137
6.3 Hecates Tholus ROI SISAL extracted endmember ROI total scene abundances 143
6.4 Aromatum Chaos SISAL extracted endmember ROI total scene abundances 150
6.5 Kirkcaldy Crater SISAL extracted endmember ROI total scene abundances 154

Chapter 1: Introduction

1.1: Thesis motivation

The search for life on Mars is a major driving goal of the ongoing and upcoming missions to the planet. One of the first steps in this endeavour is to identify regions of the planet that may have once been habitable to early microbial life. Current exploration of the surface of Mars is restricted to remotely operated instruments giving large scale aerial views (satellites) and smaller scale ground based vehicles (rovers and landers). This difference in scale is an important factor in the search for specific environments known to be hospitable to life, and the accurate identification and characterisation of their mineralogy.

One technique used by both types of exploratory vehicle is reflectance Visible and Near Infrared (VNIR) spectroscopy. VNIR (defined in this thesis as the wavelength range from 0.35 to 2.5 µm) spectral signatures can be used to identify the rocks and minerals within an instrument's field of view (FoV). VNIR imaging spectrometers currently in use and in development for martian exploration can be divided into two clear camps, distinct in their spatial and spectral resolution. Orbital instruments such as the Compact Reconnaissance Imaging Spectrometer (CRISM) can produce images covering many kilometres with a 544 point spectrum over 0.36 – 3.9 µm with spectral resolution as fine as 6.55 nm and a spatial pixel resolution of 18 m^2 (Murchie et al., 2007). Rover and lander VNIR capabilities are provided by multispectral cameras such as the 2018 ExoMars rover PanCam. The ExoMars PanCam will be the newest in a series of similar instruments used on numerous ground-based vehicles starting with the NASA *Pathfinder* to the most recent MSL *Curiosity* rover. It will return 12 point multispectral images in the wavelength range 400 – 1000 nm with pixel resolutions that can be as small as millimetres (Griffiths et al., 2006).

Spectral resolution can have a significant impact on the level of information extractable from a VNIR image. CRISM is a hyperspectral imager, the spectrum of each of its pixels contains hundreds of data points over a wavelength range of 0.362 – 3.94 µm (Murchie et al., 2007). The ExoMars PanCam on the other hand is a multispectral imager, returning only 12 point spectra over a much smaller wavelength range. The majority of the mineralogically diagnostic spectral features occur in the near and mid infrared portion of the electromagnetic spectrum (Clark et al., 1990; Hunt, 1977). Whilst CRISM covers these regions PanCam only sees a fraction of the NIR and is therefore not sufficient for uniquely identifying many of the minerals seen on the martian surface, in particular those that occur in hydrated

environments. These diagnostic spectral features are also often much less than 100 nm wide (Gaffey, 1985; Hunt & Ashley, 1979; Hunt et al., 1971; Hunt & Salisbury, 1970; Hunt & Salisbury, 1971) and so even when they occur within the wavelength range of PanCam they are not fully resolvable due to the instrument's coarse spectral resolution. CRISM however has a narrow enough spectral resolution to distinguish the bulk of these diagnostic spectral features.

Spatial scale can also greatly affect the level of detail extractable from an image. Whilst an orbital spectrometer such as CRISM is, given enough years, theoretically capable of covering the entire planet at its optimal resolution, a rover is never going to be able to do the same in a reasonable time frame. However the surface that is covered by the rover is done so at a much finer spatial resolution than the orbital instruments are capable of, with many significant structural surface features being on a spatial scale below that of the highest resolution orbital spectral imager. Planetary exploration using both the orbital and ground-based images is therefore a compromise between the amount of surface that can be covered and the spatial and spectral detail of that coverage.

Numerous types of environment that are of interest in the search for life are characterised by mineral deposits and formations that are on a metre scale or less. Regions of hydrothermal and hydrous alteration and hydrovolcanism are such environments (Cousins & Crawford, 2011), as are the recently discovered Recurring Slope Lineae (McEwen et al., 2014, 2011). The fine structural and mineralogical details of these environmental types are within the spatial resolution of rover instruments such as PanCam but are too small to be picked out within a CRISM image, being obscured within individual pixels. The ability to identify these environmental types from orbit is an important goal both as a guide with respect to choosing future rover landing sites and the more general expansion of our knowledge of the past habitability of Mars to cover more than the handful of locations ground-based missions have visited and will visit in the foreseeable future. Analysis techniques are required that can expand the level of detail extractable from the orbital data, thereby increasing the small-spatial-scale coverage our current suite of instruments are capable of.

Spectral Mixture Analysis (SMA) is a family of techniques developed to extract sub-pixel spectral information from imaging spectrometers (Keshava & Mustard, 2002). This is a multi-step technique that has the potential to greatly expand the amount of information we can gather from the set of VNIR spectrometers that are currently or will shortly be exploring

Mars. However, whilst the vast majority of the VNIR images returned from Mars are freely available to the entire planetary science community, the majority of the SMA algorithms that have been discussed in the literature are not, either as open source or commercial programs. Without the time and necessary skills to write large, often complex computer programs based on a single description paper these SMA algorithms therefore remain unusable to planetary scientists. Investigating which SMA algorithms have been made available and how accurate they are when applied to mineralogically complex environments and CRISM data in particular will help the Mars science community to continue mining the vast wealth of imagery that has been collected and still remains to be studied in detail.

1.2: Thesis outline

This thesis will (i) assess the capabilities of both ground and aerial or orbital based VNIR spectrometers to identify small scale hydrothermal environments, (ii) detail the development of a full, publically available Spectral Mixture Analysis (SMA) pipeline designed to increase the amount of spatial and spectral detail extractable from existing orbital spectrometers, and (iii) field trail an emulator of the PanCam included in the science instrument payload on the European Space Agency (ESA)/Roscosmos 2018 ExoMars, testing both the fidelity of the spectral data captured and the utility of the instrument datasets in correctly identifying a hydrothermally altered Mars analogue environment. This shall be broken down across the following seven chapters…

Chapter 2 shall introduce the concept of Visible and Near Infrared (VNIR) reflectance spectroscopy, discussing the spectra of important and common hydrated mineral species, and detailing how this has been integrated into the creation of VNIR imaging spectrometers. The global mineralogy of Mars will be covered and evidence introduced for the presence of hydrothermal systems in various locations over the planets history. The use of regions of the Earth to test instruments and techniques relating to the exploration and evolution of Mars are also discussed.

Chapter 3 will detail the first deployment of the most recent incarnation of the Aberystwyth University PanCam Emulator (AUPE-2), an emulator of the ExoMars PanCam instrument, to a hydrothermally active region in Iceland. The ability of the data returned to accurately characterise this environment is investigated, efficient and versatile data products are developed and the fidelity of the spectral data established.

Chapter 4 introduces the concept of Spectral Mixture Analysis (SMA) and gives an overview of the current suite of algorithms that have been developed for general purposes and those that have previously been applied to martian datasets.

Chapter 5 details the development of a best practice full SMA pipeline using publically available algorithms written in the Matlab programming language. This pipeline is optimised for application to hydrothermal environments, which represent a particularly challenging environment type for this technique. Having established the pipeline using synthetic images created from publically available spectral library data it is further validated using aerial and ground-based hyperspectral data from the same Icelandic region explored in Chapter 3.

Chapter 6 takes the SMA pipeline developed in Chapter 5 and applies it to CRISM data covering four regions on Mars, three of which have been postulated to have hosted hydrothermal systems in their history, none of which have previously been subject to quantitative mineralogical investigations. Specific issues relating to the use of CRISM imagery are discussed and the benefits of including temporally coincident high resolution HiRISE imagery in the analysis introduced.

Chapter 7 introduces a novel use of SMA that combines high spectral resolution CRISM data with high spatial resolution HiRISE data to extract for the first time a unique spectral signature for the Recurring Slope Lineae (RSL) on the slopes of the Palikir Crater.

Chapter 8 summarises the findings of this thesis and discusses further the importance of scale (both spectral and spatial) in the application of VNIR imaging spectroscopy for detecting hydrated environments on Mars. Finally suggestions for future research leading on from the work presented in this thesis are outlined.

Chapter 2: Spectral imaging, Mars and habitability

2.1: Introduction

This chapter shall cover the basic background theory and knowledge underpinning the rest of the thesis. This shall include a brief explanation and overview of Visible and Near Infrared (VNIR) reflectance spectroscopy as applied to mineral exploration; the general mineralogy of Mars as currently understood; the concept of habitability and the role it plays in martian exploration; and the use of regions of the Earth as analogues for certain environmental types on Mars to test instruments and scientific concepts.

2.2: Visible and Near Infrared (VNIR) geological reflectance spectroscopy

Spectroscopy is a broad technique that uses the interaction of electromagnetic waves with atoms, molecules, crystal structures etc. to determine certain properties of the target medium. VNIR reflectance spectroscopy refers to the particular specialisation where the incident light is in the visible and infrared range (a range that has no clear standard definition but shall in this thesis cover approximately 0.35 - 2.5 μm), and the data collected is the portion of that light that is reflected back off the surface of the target material. The reflected spectrum is then compared to the known spectrum of the incident light (in the case of planetary remote sensing this light source is the sun) showing which wavelengths of light have been absorbed by the target. Spectral features (e.g. absorption band locations, depths and widths) in the case of geological targets are attributed to specific atomic and molecular bonds within a mineral. Decades of research have gone into this field covering the identification of specific wavelength absorptions and the physical mechanism responsible for them (e.g. Clark et al., 1990; Hunt, 1977; Pieters & Englert, 1993) and the spectral signature of specific minerals. In the exploration of Mars, and in particular the search for previously habitable environments certain minerals are of key importance (see section 2.3 on Martian mineralogy), specifically those that form in the presence of liquid water and/or include O-H bonds within their crystalline structure.

2.2.1: Physics of VNIR reflectance spectra

Spectral absorptions are the result of two broad processes; molecular vibrational excitations and electronic transitions (Clark, 1999). Vibrational absorptions appear in the near infrared (NIR) and short-wave infrared (SWIR) and are primarily the result of O-H, H_2O and CO_3 molecules vibrating within the crystal lattice of a mineral (Hunt, 1977). The vibrational absorption features can be subtly altered in shape and wavelength position by the neighbouring atoms within the crystal lattice and additional atoms attached to the molecule

(e.g. the bonding of Si, Al or Mg to O-H molecules in phyllosilicates) (Bishop et al., 2008), enabling diagnosis of specific minerals as well as confirmation of the presence of one of the aforementioned elements. Each vibration has a number of fundamental modes and lower energy overtones, with the strength of the associated absorption decreasing with increasing modal number (Clark et al., 1990). In the VNIR wavelength range (as defined in this thesis) it is primarily overtone vibrational absorptions that are seen with the low modal fundamental vibrations occurring at longer wavelengths in the thermal infrared range. Important locations for vibrational absorptions are O-H around 1.4 µm and when combined with a metal ion (X-O-H bond) between 2.2 – 2.3 µm (figure 2.1d), H_2O at approximately 1.4 and 1.9 µm (figure 2.1c) and CO_3 around 2.3 and 2.5 µm (figure 2.1d) (Hunt & Salisbury, 1971).

Electronic transitions are the result of transition metal cations moving between orbital levels within minerals. Key transition metals are Fe, Ni, Cr and Mn. Iron is the most common transition metal in minerals and is responsible for major diagnostic absorptions in the 0.4 – 1.0 µm range (figure 2.1b) (Burns, 1993). The position of the cation within the crystal lattice and the identity of the neighbouring atoms and molecules shifts the exact absorption wavelength allowing for distinction between different Fe^{3+} and Fe^{2+} minerals (Clark, 1999).

2.2.2: Reflectance spectroscopy of minerals associated with hydrothermal alteration

Hydrothermal alteration assemblages typically contain a mixture of mineral types, many of which have VNIR spectra with unique diagnostic features. Primary igneous minerals and rocks on both the Earth and Mars include olivine and pyroxene. Important mineral families formed as secondary weathering and hydrothermal alteration products of these basaltic materials include phyllosilicates, carbonates, sulfates, and iron-oxides, zeolites and hydroxides.

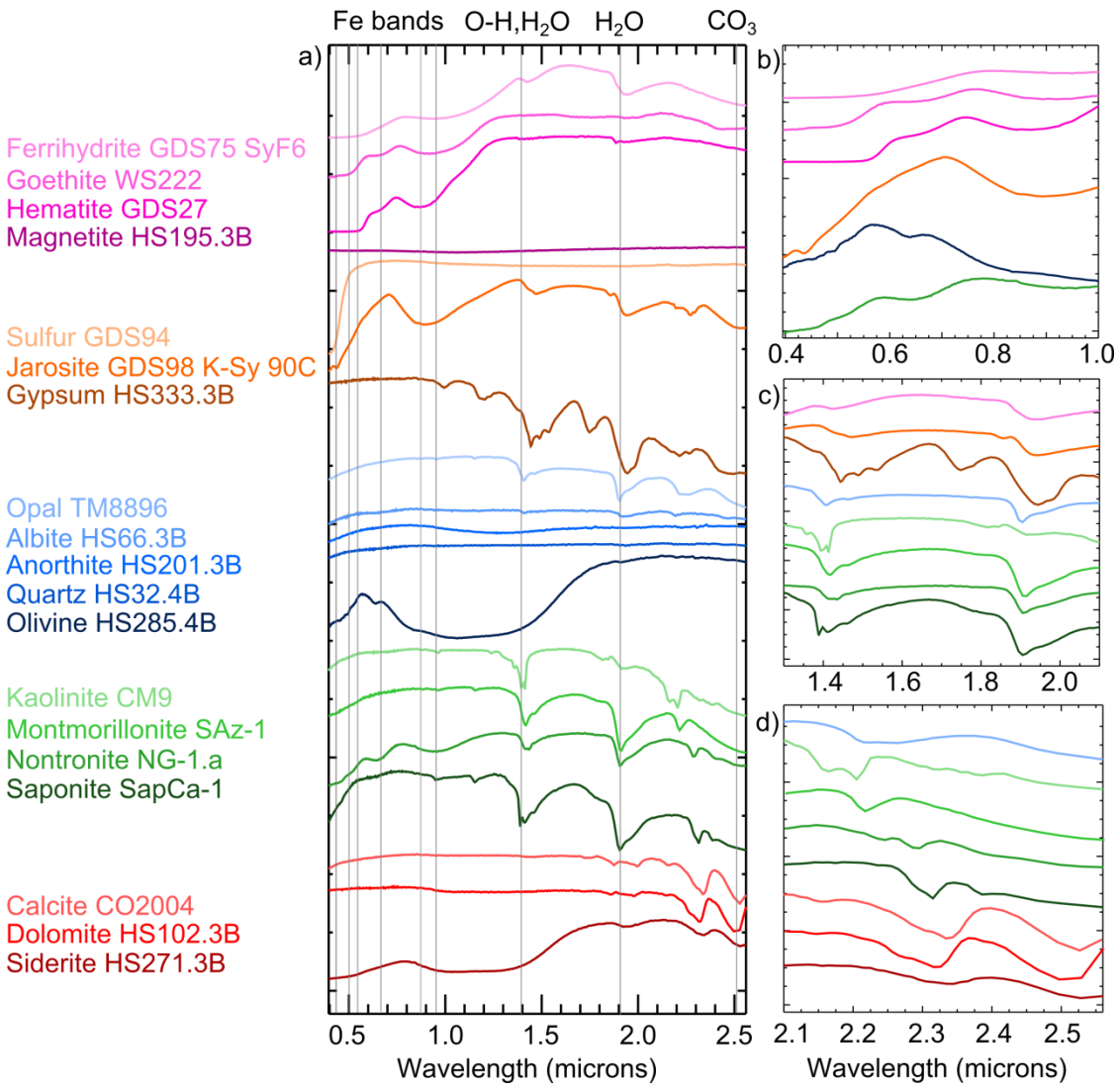

Figure 2.1: USGS Spectral library (Clark et al., 2007) *spectra of minerals common to hydrothermal environments. a) All minerals grouped according to mineral species, from the bottom upwards, carbonates (reds), phyllosilicates (greens), silicates (blues), sulfates (oranges) and iron oxides (pinks). b) The 0.4 – 1.0 µm portion of the spectrum showing the minerals with prominent Fe absorptions (from the bottom upwards, nontronite, olivine, jarosite, hematite, goethite and ferrihydrite). c) The 1.3 – 2.1 µm portion of the spectrum showing the minerals with hydroxyl and water absorptions, (from the bottom upwards, saponite, nontronite, montmorillonite, kaolinite, opal, gypsum, jarosite and ferrihydrite). Note the lack of the prominent 1.9 µm feature in the kaolinite spectrum indicating that this mineral has hydroxyl bonds but not H_2O. d) The 2.1 – 2.56 µm portion of the spectrum showing minerals with strong diagnostic features in this range (from the bottom upwards, siderite, dolomite, calcite, saponite, nontronite, montmorillonite, kaolinite and opal). In the carbonate minerals the features around 2.3 and 2.5 µm are due to the CO_3 molecule. Saponite also has an absorption around 2.3 µm but without the accompanying 2.5 µm feature enabling it to be*

clearly distinguished from the carbonates. The 2.3 µm feature in the case of saponite is due to a combination stretch of the hydroxyl molecule and the Mg/Fe-O-H bond (Clark et al., 1990). *All spectra in all figures are shifted along the y axis for clarity.*

2.2.2.1: Carbonates

Carbonates are minerals dominated by the CO_3 ion and frequently form in aqueous environments. There are no strong distinguishing carbonate bands within the visible portion of the spectrum (figure 2.1a). The near infrared (NIR) spectra of carbonates have a number of clear absorption bands whose positions and relative depths are not affected by particle size or packing, and suffer no interference from thermal emission (Gaffey, 1986). NIR is therefore an ideal spectral range to use in the identification of carbonates with the majority of the strong absorption bands occurring between 1.6 µm and 2.5 µm (Hunt & Salisbury, 1971). Slight shifts in these band positions can help distinguish between different carbonate minerals such as calcite and dolomite (figure 2.1d) (Gaffey, 1986). Carbonates that have formed with water inclusions or as hydrocarbonates will have additional bands at ~1.4 µm and ~1.9 µm due to absorptions by H_2O and O-H molecules and bonds. This second band can be broad and swamp the pure carbonate bands in that spectral region (Hunt & Salisbury, 1971) complicating the identification procedure.

2.2.2.2: Iron-oxides and hydroxides

Fe^{2+} and Fe^{3+} oxides and hydroxides including hematite, goethite, ferrihydrite and magnetite are common minerals here on Earth and Mars, forming in a variety of different environments including as hydrothermal alteration and weathering products. In the VNIR spectral range the diagnostic absorption features attributed to electronic transitions involving iron are in the 0.4 – 1.1 µm range (Hunt & Ashley, 1979). Goethite and hematite can be distinguished by the location of the major broad ≤ 1 µm band combined with the location of the absorption between 0.5 and 0.6 µm. The NIR band is centred at 0.85 µm for hematite, but shifted up to and possibly above 0.9 µm it indicates goethite or possibly jarosite (Hunt & Ashley, 1979).

2.2.2.3: Phyllosilicates

Phyllosilicates are minerals comprised of sheets of silicate tetrahedral Si_2O_5. This is a broad mineral grouping that includes a wide range of clay minerals (hydrous aluminium phyllosilicates) that commonly form as a result of weathering or low-temperature hydrothermal alteration of igneous rocks. Many of the key VNIR absorption features in this group are due to vibrational stretches involving the hydroxyl molecule and occur between 1.35 - 2.5 µm (Bishop et al., 2008) with the exact location of the absorption shifting according to the ion bonded to the hydroxyl molecule. Bands at 1.4 and 1.9 µm occur in all of these

minerals but their exact location and depth can shift depending on the nature of the mineral structure (Hunt & Ashley, 1979). A band with minima between 2.16 and 2.23 µm is due to the presence of aluminium (Hunt & Ashley, 1979). Fe^{3+}, Fe^{2+} and magnesium rich phyllosilicates can be identified by absorptions around 2.29 - 2.31 µm, 2.33 - 2.34 µm and 2.35 - 2.37 µm respectively (Bishop et al., 2008).

2.2.2.4: Silicates

Silicates are a hugely important mineral class that comprise the majority of the rocks on the Earth and the other inner solar system bodies. Mineral groups within this class include olivine, pyroxene, amphibole, quartz, zeolite and feldspar. Spectra of this mineral class can vary greatly from the high reflectivity but spectrally featureless plagioclase feldspar, to the range of olivine types with ferrous iron absorptions near 1.0 µm, differing in depth depending on iron content (Hunt & Salisbury, 1970). Pyroxenes also vary spectrally depending on their composition, with two characteristic broad bands being a Fe^{2+} ion absorption at 0.9 µm and another at 1.8 µm (Hunt & Salisbury, 1970). Both pyroxene and olivine can be difficult to uniquely identify in the VNIR spectrum as they show a large range of spectral diversity depending on exact chemical composition and particle size (Horgan et al., 2014).

2.2.2.5: Sulfates

Sulfates are minerals that contain SO_4^{2-} in their structure. They are an important secondary product in hydrothermal and evaporitic environments. A significant number of sulfate minerals are hydrous, i.e. they contain water molecules, and as such indicate the presence of liquid water during their formation. Jarosite is an Fe^{3+}, potassium sulfate with a key diagnostic absorption band centred at 0.43 µm. This band is sharp and shallow and as such can be drowned out when jarosite makes up only a small portion of the rock under observation (Hunt & Ashley, 1979). Gypsum is a common calcium sulfate dihydrite with little to distinguish it in the visible portion of the spectrum, but a number of key doublet and triplet absorption features around 1.4, 1.9 and 2.2 µm (figure 2.1a) (Hunt et al., 1971). Sulfur itself in this wavelength range is almost featureless apart from an absorption at 0.5 µm followed by a sharp increase in reflectance and a high reflectivity in the rest of the VNIR range (Hunt et al., 1971).

2.2.3: Imaging Spectroscopy

Imaging spectroscopy is a decades old technique that uses VNIR spectroscopy to produce image cubes with three dimensions, two spatial (x and y) and one spectral (λ) (figure 2.2). The first civilian Earth observation satellite to carry an imaging spectrometer was Landsat 1 launched in 1972, whose multispectral scanner had four broad spectral bands. Multispectral

scanners with less than 10 bands remain commonly used, but increasing interest is focusing on hyperspectral imagers capable of capturing a high number of contiguously spread spectral bands. Both multi and hyperspectral instruments have been of huge benefit to the exploration of Mars. Orbiting spacecraft were first sent to Mars in the 1960's and all have included cameras for capturing images of the Martian surface. A number of these have been high-resolution imagers in addition to multi and hyperspectral imaging spectrometers in the visible, near-infrared and thermal infrared. Orbiters are not the only spacecraft to be sent to Mars, a number of probes, landers and rovers have successfully reached the surface of Mars since NASA successfully landed the Viking 1 & 2 landers in 1976. Many of these missions have also included multispectral imaging capabilities although no hyperspectral imagers.

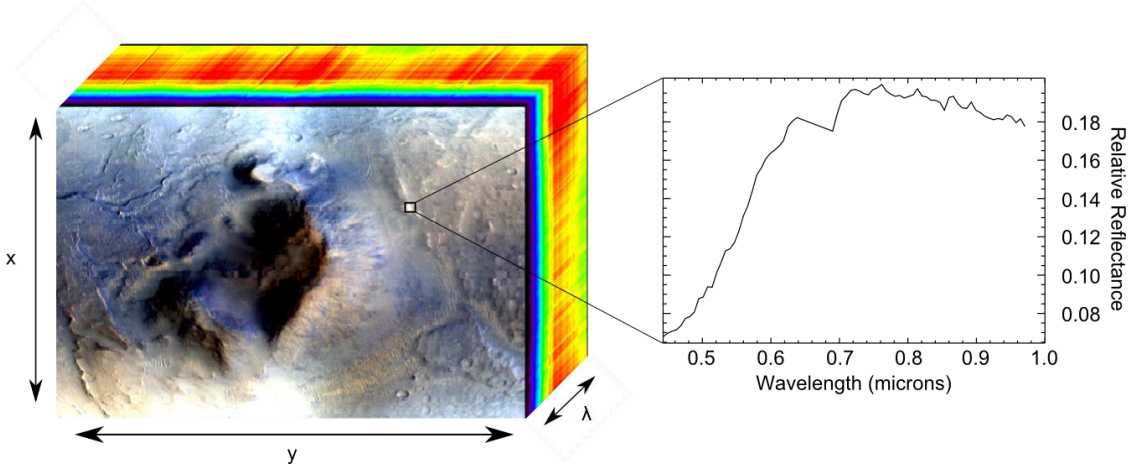

Figure 2.2: Hyperspectral imaging spectroscopy. An imaging spectrometer produces data with three dimensions as shown using an example CRISM image of the Nili Patera region on Mars; two spatial dimensions (x and y) and one spectral dimension (λ). Each individual pixel in the image has therefore a continuous spectrum as indicated.

There are currently two operational spectral imagers on the surface of Mars; Pancam on the Mars Exploration Rover *Opportunity* and Mastcam on the Mars Science Laboratory (MSL) Curiosity rover. The planned ESA/Roscosmos ExoMars rover will carry a similar spectral imaging system called PanCam, short for Panoramic Camera. Further details of these instruments are discussed in Chapter 3, section 3.2.1. There are a number of orbiting imaging spectrometers in operation around Mars, both multispectral and hyperspectral VNIR and thermal imagers. The NASA Mars Reconnaissance Orbiter (MRO) hosts both the hyperspectral Compact Reconnaissance Imaging Spectrometer for Mars (CRISM) and the three band High Resolution Imaging Science Experiment (HiRISE) camera capable of capturing images with 0.3 m/pixel resolution (McEwen et al., 2007). CRISM has a spectral coverage of 362 - 3920 nm over 544 channels split between two detectors with an average spectral

resolution of 6.55 nm and a minimum spatial resolution of 18 m/pixel (Murchie et al., 2007). Further details of CRISM are given in Chapter 6. At the time of writing HiRISE has imaged approximately 2% of the planet and CRISM has covered a similar portion of the surface at its highest spatial resolution. CRISM can also operate in a survey mode producing images with an approximate pixel size of 200 m and covering 72 channels rather than 544. In this mode it has surveyed the majority of the surface. Both of these instruments represent the highest spatial (HiRISE) and spectral (CRISM) resolution data currently available of Mars from orbit. There is one other currently operational satellite with a similar suite of instruments, ESA's Mars Express. The VNIR hyperspectral imager on board is the Observatoire pour la Minéralogie, l'Eau, Les Glaces, et l'Activité (OMEGA) which covers a spectral range from 360 - 5100 nm in 352 bands at a minimum spatial resolution of less than 500 m/pixel (Bibring et al., 2004). Also included in its payload is the four band High Resolution Stereo Camera (HRSC) that captures colour images with up to 2 m spatial resolution and allows for the production of Digital Elevation Models from stereo pairs of images.

2.3: Martian mineralogy

The surface mineralogy of Mars has been studied on both a local and global scale since the Viking landers and orbiters of the 1970's. More recent observations from the Mars Express, Odyssey and Reconnaissance Orbiter satellites, the Mars Exploration Rovers *Spirit* and *Opportunity*, and most recently Mars Science Laboratory *Curiosity* rover have increased our knowledge, and revealed a significant complexity and spatial heterogeneity to the geochemical history and present day state of the Martian surface (table 2.1). The ferric-oxide rich dust layer that covers the Martian surface (Ehlmann and Edwards, 2014; Poulet et al., 2007) obscures much of the bedrock; where exposed rock is visible data from orbiting instruments, specifically the Thermal Emission Spectrometer (TES), the Thermal Emission Imaging System (THEMIS) and OMEGA, have been used to produced large spatial scale global maps showing the locations of specific mineral species. Mineral species that have been mapped on this global scale include high and low calcium pyroxenes, ice, hydrated minerals and ferric oxides, quartz, sulfates, plagioclase, carbonates and sheet silicates (Bandfield et al., 2003; Bandfield, 2002; Bibring et al., 2005). The most abundant minerals are silicates of a basaltic to andesitic basaltic composition (Chevrier & Mathe, 2007), with high calcium pyroxenes corresponding to Hesperian terrain and low calcium pyroxenes being more prevalent in Noachian age regions. These global maps show the large scale trends evident on the surface but higher spatial resolution orbital instruments (namely CRISM) have been able to identify numerous local mineral suites and environmental types. Many of these

smaller mineral outcrops demonstrate the diversity of the aqueous history of Mars, including phyllosilicate deposits (Carter et al., 2013a; Ehlmann et al., 2011c) and hydrated sulfates (Carter et al., 2013a) and silicates (Ehlmann et al., 2009; Mustard et al., 2008) all of which form in the presence of liquid water. The phyllosilicate deposits tend to be found in the oldest Noachian terrain (Carr & Head III, 2010) with the sulfates being more prevalent in late-Noachian to early-Hesperian terrains (Carter et al., 2013a). In addition to CRISM the various landers and rovers have provided mineral identification on sub-metre to metre scales including veins of gypsum at Endeavour Crater (Arvidson et al., 2014) and Gale Crater (Nachon et al., 2014), and perchlorate salts at the Phoenix landing site (Hecht et al., 2009) and in Gale Crater (Glavin et al., 2013).

Table 2.1: Minerals detected on Mars from both orbital and ground-based observations (taken from (Ehlmann and Edwards, 2014)*, see this reference for full references to this table)*

	Class	**Group/mineral/phase**	**Formula**
Primary	Framework silicates	Olivines	$(Mg,Fe)_2SiO_4$
		Orthopyroxenes	$((Mg,Fe)_{0.95+X},Ca_{0.05-X})Si_2O_6$
		Clinopyroxenes	$(Ca,Mg,Fe)Si_2O_8$
		Plagioclase feldspars	$(Ca,Na)(Al,Si)AlSi_2O_8$
		Alkali feldspars	$(K,Na)AlSi_3O_8$
	Sulfides	Pyrrhotite	$Fe_{1-X}S$
		Pyrite/marcasite	FeS_2
	Oxides	Magnetite	$Fe_{3-X}Ti_XO_4$
		Ilmenite	$FeTiO_3$
Secondary	Oxides	Hematite	Fe_2O_3
		Goethite	$FeO(OH)$
		Akaganeite	$Fe(O,OH,Cl)$
	Phyllosilicates	Fe/Mg smectites (e.g. nontronite, saponite)	$(Ca,Na)_{0.3-0.5}(Fe,Mg,Al)_{2-3}(Al,Si)_4O_{10}(OH)_2{\cdot}nH_2O$
		Al smectites (e.g. montmorillonite, beidellite)	$(Na,Ca)_{0.3-0.5}(Al,Mg)_2(Al,Si)_4O_{10}(OH)_2{\cdot}nH_2O$
		Kaolin group minerals (e.g. kaolinite, halloysite)	$Al_2Si_2O_5(OH)_4$
		Chlorite	$(Mg,Fe^{2+})_5Al(Si_3Al)O_{10}(OH)_8$
		Serpentine	$(Mg,Fe)_3Si_2O_5(OH)_4$

	High-charge Al/K phyllosilicates (e.g. muscovite, illite)	$(K,H_3O)(Al,Mg,Fe)_2Al_XSi_{4-X}O_{10}(OH)_2$
Other hydrated silicates	Prehnite	$Ca_2Al(AlSi_3O_{10})(OH)_2$
	Analcime	$NaAlSi_2O_6{\cdot}H_2O$
	Opaline silica (n > 0), quartz (n = 0)	$SiO_2{\cdot}nH_2O$
Carbonates	Mg/Ca/Fe carbonates	$(Mg,Fe,Ca)CO_3$
Sulfates	Kieserite ($MgSO_4{\cdot}H_2O$); szomolnokite ($FeSO_4{\cdot}H_2O$);Fe^{2+}-, Fe^{3+}-, and Mg-polyhydrated sulfates	$(Fe,Mg)SO_4{\cdot}nH_2O$
	Gypsum (n = 2), bassanite (n = 0.5), anhydrite (n = 0)	$CaSO_4{\cdot}nH_2O$
	Alunite	$KAl_3(SO_4)_2(OH)_6$
	Jarosite	$KFe_3(OH)_6(SO_4)_2$
	Not a named mineral	$Fe^{3+}SO_4(OH)$
Chlorides	Chlorides	e.g., NaCl, $MgCl_2$
Perchlorates	Perchlorates	e.g., $(Mg,Ca)(ClO_4)_2$

2.4: Environmental habitability

2.4.1: Habitability and the exploration of Mars

The search for life outside of the Earth has long been an important aspect of planetary exploration and this has largely focused on the identification of potentially and/or previously habitable environments. Habitability is not an easy characteristic to define, and it becomes harder with each passing year as we learn more about the extreme environments that life has colonised here on Earth (Amils Pibernat et al., 2007; Harrison et al., 2013; Lever et al., 2015). The NASA Astrobiology Roadmap (Des Marais et al., 2003) defines a habitable environment as one that provides extended regions of liquid water, an energy source to sustain metabolism and conditions that favour the assemblage of complex organic molecules. These criteria can obviously apply to a wide variety of environments including ones characterised by extreme properties such as high/low pH values, high/low temperatures or high/low pressures. There is much evidence throughout the history of Mars that points to the possibility of at least some regions being habitable at different times (Cousins and Crawford, 2011; Martinez-Frias

et al., 2006; Schulte et al., 2006; Ulrich et al., 2012; Westall et al., 2013). The primary habitability characteristic that has been used to identify these previously habitable regions is the presence of liquid water. During both the Noachian and the Hesperian eras, liquid water is thought to have periodically existed on the martian surface in the form of fluvial and lacustrine systems and potential oceans. The evidence for this is both structural (Tanaka et al., 2014) and mineralogical (Carter et al., 2013a) and the identified previous/potential habitable regions cover a range of environmental types. The Mars Exploration Program Analysis Group (MEPAG) completed a review of potential habitable regions on Mars with a view to identify those regions of the planet that should be granted a higher planetary protection protocol than is currently in use (Rummel et al., 2014). Areas they recommend be avoided due to the risk of contamination by/propagation of bacteria brought from Earth include the Recurring Slope Lineae (RSL) that are postulated to be the result of liquid water (McEwen et al., 2011) and large fresh impact craters that may house active hydrothermal systems (although none are currently believed to be in this state at the time of writing).

2.4.2: Hydrothermal activity on Mars

Evidence of hydrothermal activity on Mars is important from an astrobiological perspective as a hydrothermally active environment is a habitable one, providing both heat and a source of liquid water (Cousins and Crawford, 2011; Fairén et al., 2005; Schulze-Makuch et al., 2007). Low-temperature hydrothermal environments in particular are also likely to preserve any organics or biofabrics that may form, opening up the possibility of detecting past life (Summons et al., 2011). Ground-based investigations by the Mars Exploration Rovers have revealed mineralogical evidence of potential hydrothermally altered impact breccias in the Meridiani Planum (Arvidson et al., 2014; Squyres et al., 2012) in addition to high concentrations of hydrothermally generated opaline silica (Squyres et al., 2008) and assemblages of temperature dependent aqueously altered iron-rich rocks and soils (Morris et al., 2008; Schmidt et al., 2009) in the Gusev Crater. Orbital data has surveyed far greater swaths of the Martian surface than the rovers and also found evidence of hydrothermal activity. Some of this evidence is again mineralogical; in Nili Patera mounds of hydrated silica have been attributed to hydrothermal activity (Skok et al., 2010) and phyllosilicate and carbonate bearing assemblages in the coincident Nili Fossae region have been interpreted as the result of low-temperature hydrothermal activity (Brown et al., 2010; Ehlmann et al., 2011b; Viviano et al., 2013). Evidence from CRISM data of the presence of chlorite, serpentine, talc and prehnite in the Tyrrhena Terra region close to the Nili Fossae, have been interpreted as evidence of historical hydrothermal alteration (Viviano-Beck, 2015). CRISM

images covering the proposed potential MSL rover and ExoMars rover landing region of Mawrth Vallis show outcrops of smectite overlain with hydrated silica and phyllosilicates; McKeown et al. (2013) have used this evidence to suggest a complex aqueous environmental history for this region including periods of hydrothermal activity.

The coverage of Mars by high resolution spectral and spatial imagers is low, with lower resolution thermal spectrometers and medium resolution cameras providing data over much larger swaths of the surface. These datasets have enabled researchers to postulate numerous other locations of potential hydrothermal activity based on structural rather than mineralogical evidence. Hydrothermal systems can form when there is an interaction between volcanism and ice, e.g. at a subglacial volcano. Such interactions can leave behind distinctive landforms that on Mars may remain long after the ice has disappeared. The Tharsis region is home to a number of volcanoes which show evidence of historical ice activity and potential hydrothermal alteration. Kadish et al (2008) used THEMIS data in conjunction with HiRISE and other datasets to investigate the deposits on the north-west flank of Ascraeus Mons and conclude that they are indicative of volcano-ice interaction. Geological maps of the late Amazonian Arsia Mons volcano created using CTX and HRSC images show evidence of glacial activity and deposits that likely formed as a result of volcano-ice interaction (Scanlon et al., 2015, 2014). Ceraunius Tholus shows evidence of having once been crowned with a snowpack and caldera lake that melted to form the fluvial erosion features seen in MOLA and HRSC data running down the flanks of the volcano (Fassett and Head III, 2007). Hecates Tholus, a volcano in the Elysium province, shows evidence of comparatively recent glacial activity (Hauber et al., 2005; Neukum et al., 2004) and loose sediments at the base of the cone that could be the result of an ongoing mud eruption (Kangi, 2007), providing the necessary heat and water to create a transient hydrothermal system. The Cerberus Fossae are a series of fissures within the Elysium Planitia near the equator of Mars. Athabasca Valles is an outflow channel series located nearby and thought to have been created in a related event (Head III et al., 2003). This feature was considered as a potential MER landing site and as such many studies were conducted investigating the structure, composition and possible formation histories. It is one of the martian regions where periglacial structures have been tentatively identified in the form of pingos and rootless cones (Balme et al., 2009; Burr et al., 2005). These, together with the suggested rifting responsible for the formation of the Cerberus Fossae, imply subglacial hydrothermal activity. The Aromatum Chaos is a small region of chaotic collapsed ground from which the Ravi Vallis emerges (Coleman, 2005). The morphology of this area suggests it formed due to

melting of the underlying cryosphere due to volcanic activity (Leask et al., 2006), more specifically a dike intrusion creating a hydrothermal system through melting of permafrost (Craft et al., 2015), however there have been no high resolution VNIR spectroscopic studies performed to provide mineralogical evidence of this or any associated hydrothermal activity.

The advent of the HiRISE instrument has allowed for small scale topographic features to be identified across Mars that may be the result of volcano-ice interaction. Keszthelyi et al (2010) searched through the first year of HiRISE imagery to produce a catalogue of such features including rootless cones in Athabasca Valles and Cerberus Palus, pingos in Utopia Planitia and lahars on the flanks of Elysium Mons.

Hydrothermal systems are not always the result of internal planetary processes, they can also form as the result of impact processes (Osinski et al., 2013). The composition of the nakhlite martian meteorites points to a short-lived impact generated hydrothermal brine (Bridges and Schwenzer, 2012) providing mineralogical evidence for these hydrothermal systems. A prominent Martian example of an impact crater showing spectral and morphological evidence of impact induced hydrothermal activity is Toro Crater (Marzo et al., 2010) on the northern edge of the Syrtis Major Volcanic Plains.

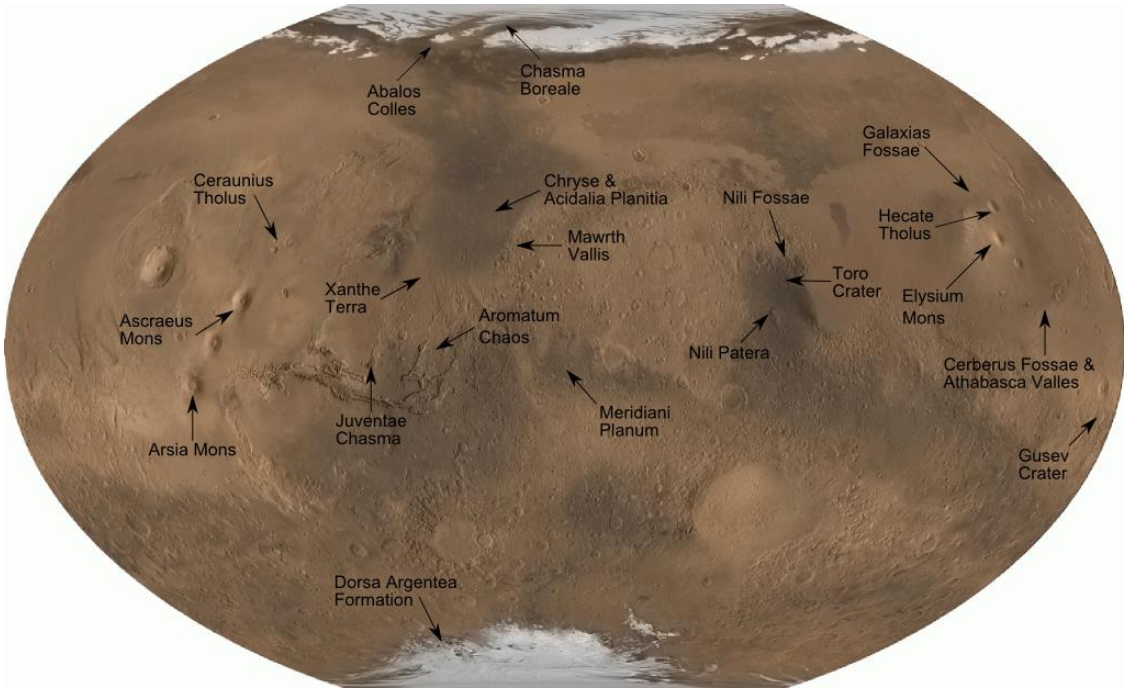

Figure 2.3: Regions of Mars identified as being previously hydrothermally active. See references in text for discussion of the evidence for each identified region.

2.5: Comparative planetology and analogue sites for Mars

Interpretation of mineralogical and structural data from Mars to extract its evolutionary history relies heavily on our understanding of regions and formations with similar characteristics here on Earth: as a result the discovery and investigation of regions on the Earth that can serve as specific Mars analogues is crucial to Mars research. Analogues can be picked for a number of different criteria. Widely used general regions include the Atacama Desert in Chile, used for its geochemical similarities and arid climate (Navarro-González et al., 2003; Wierzchos et al., 2013), Svalbard in the Arctic circle for its volcanic terrain (Treiman et al., 2002; Ulrich et al., 2011), the Dry Valleys in Antarctica for mineralogy and cold, arid climate (Bishop et al., 2012; Marchant and Head III, 2007) and the Mojave desert in the USA specifically for rover testing due to its morphological surface properties (Jolliff et al., 2002; Tunstel et al., 2002). A recent ESA commissioned catalogue gives details of these and many other analogue sites including practicalities and references to key pieces of research performed in each region (Preston et al., 2013). Analogue sites are particularly important for aiding the interpretation of remote sensing image data from Mars. They provide us with information regarding the size and scale of specific environments that can be characterised by certain sets of minerals and what these mineral suites may be.

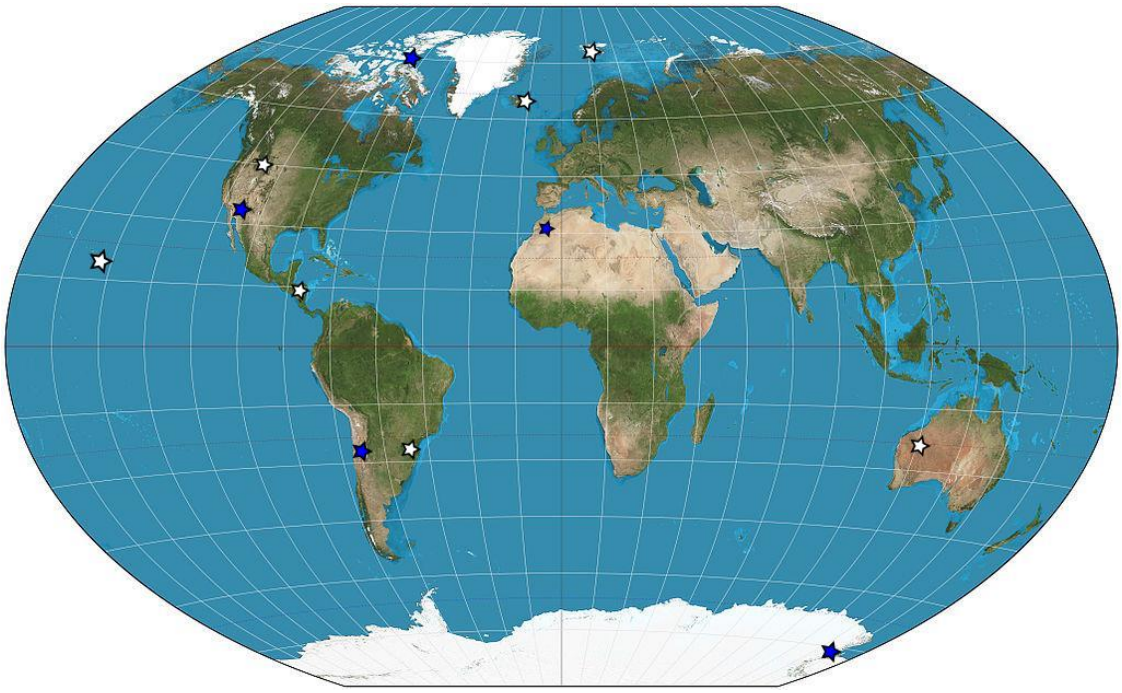

Figure 2.4: Locations used as analogues to Mars. The blue stars represent general analogue locations (Mojave desert in the USA, the Atacama desert in Chile, Haughton impact crater in the Arctic circle, the Dry Valleys in Antarctica and the Moroccan desert) and the white stars represent specifically hydrothermal analogues (Hawaii, Niciragua, the Pilbara Craton in Australia, Svalbard, Vargeão impact crater in southern Brazil, British Columbia and Iceland).

2.5.1: Earth analogues for hydrothermal systems on Mars

Hydrothermal systems on the Earth occur in submarine, subaerial and subglacial volcanic environments (see (Pirajno and van Kranendonk, 2005) for review of hydrothermal systems on Earth) as well as in impact structures. All of these types of hydrothermal systems provide potential analogues for martian paleoenvironments. The mineral depositions associated with hydrothermal systems can tell us much about the nature of the system even if it is no longer active. Of particular interest are systems where argillic alteration takes place. Hydrothermal products include alteration haloes around active vents, fumaroles, and springs, as well as the deposition of mineral ores. From the point of view of remote sensing instruments, the alteration haloes are more important as they lie on the surface whilst the potentially large ore deposits tend to be buried. From an astrobiological analogue viewpoint epithermal systems are preferable to high-temperature hydrothermal environments. Hydrothermally altered terrains on Earth have economic implications, and as such the detection and characterisation of them from aerial and satellite data is well documented (Crósta et al., 2003, 1998; Huntington, 1996; Sabins, 1999; Yang et al., 1999).

Hydrothermal analogue regions investigated specifically with respect to Mars and their likely detection with the technologies currently exploring Mars include volcanic islands and volcanic arcs in a variety of climates. *In-situ* spectroscopy studies have been carried out in Nicaragua at the Cerro Negro, Momotombo and Telica volcanoes by Marcucci et al (2013). These particular sites are analogues for small-scale, acidic-steam driven hydrothermal alteration, with a similar underlying basaltic composition to reported volcanic terrains on Mars (Morris et al., 1990). A range of acid-sulfate minerals, phyllosilicates and hydrated silica phases were identified using VNIR spectroscopy. This result demonstrated that all three can form together as part of the same hydrothermal environment, and that VNIR spectroscopy is capable of identifying them as a suite. The Pilbara Craton in Western Australia contains some of the oldest rock formations in the world and has been used as a Mars analogue for various structural types (West et al., 2010) including flood lava basalts that make up much of the ancient Martian terrain (Brown et al., 2004). Its age makes it especially compelling to astrobiologists looking to develop methods for identifying signs of early life on Mars (Philippot et al., 2009; van Kranendonk, 2006). The North Pole Dome region within Pilbara Craton is home to numerous veins of epithermal alteration products that Brown et al (2005) investigated using airborne VNIR hyperspectral instrumentation. Several alteration zones and veins were identified within 5 m/pixel data and dominant minerals identified including chlorite, serpentine and muscovite. These results were compared to ground-truth samples

and found to agree. However, all of the sub-regions investigated contained a greater variety of minerals than were identified from the aerial data alone, demonstrating one of the major limitations of remotely sensed data, namely the disparity that can exist between the spatial resolution of the remotely sensed data and the distribution of the minerals on the ground. The volcanic island chain of Hawaii has also been studied extensively as a geochemical and mineralogical analogue for a once active Mars. The islands of Hawaii are all volcanic, the product of a hotspot under the Pacific Ocean. As a result they are made of basaltic lavas and the soils that form from them comprise of basaltic minerals and their alteration products, namely silicate clays, oxides and volcanic ash (Morris et al., 1990). Numerous laboratory based studies have focused on the alteration of basaltic tephra and the analysis of the Hawaiian soil using various instruments that have or will be included on Mars rovers and landers including VNIR, Mid Infrared (MIR), X-Ray Diffraction (XRD), and Raman and Mossbauer spectroscopy (Bishop et al., 2007; Hamilton et al., 2008). Hamilton et al. (2008) investigated a series of altered basaltic tephras from Mauna Kea using VNIR and MIR spectroscopy concluding that the key absorption features easily allow differentiation between altered and unaltered samples. In addition the specific type of alteration, hydrothermal alteration under acid-sulfate conditions, was deducible from the presence of jarosite and alunite. The Vargeão impact crater in southern Brazil is one of the few impact structures on the Earth suitable for use as a martian analogue. Yokoyama et al. (2015) identified evidence of an impact induced hydrothermal system at this crater and demonstrated that the mineral assemblages formed were discernible using laboratory-based VNIR imaging spectroscopy on collected samples. Field based identification using imaging spectroscopy was not attempted.

Subglacial hydrothermal environments are the result of volcanic activity beneath a glacier. They are especially relevant as a Mars analogue type with the surface of Mars bearing many signs of both volcanism and glaciation, often in the same area (Cousins et al., 2013). Here on Earth there are widespread examples of subglacial volcanism, predominantly near the poles in Antarctica (Smellie and Skilling, 1994), British Columbia (Edwards et al., 2002) and Iceland (Cousins and Crawford, 2011; Cousins et al., 2013; Warner and Farmer, 2010). Iceland in particular has attracted the focus of the Mars and Astrobiology research communities due to its relatively recently emplaced volcanic basalts, sparse vegetation and surface waters and glaciation; an environment thought to be similar to Noachian Mars (Ehlmann et al., 2011a). Ehlmann et al (2012) studied a suite of neutral to alkaline hydrothermally altered basalts using laboratory techniques including XRD analysis and VNIR and TIR (Thermal Infrared)

spectroscopy. Cousins et al (2013) performed *in-situ* field analysis of waters and mineral alteration products in freshly exposed subglacial hot springs and their immediate surroundings using VNIR spectroscopy (400 – 1000 nm). Field spectroscopy was found to be a useful component in identifying and characterising this type of environment but the limited wavelength range available was a problem. Many of the minerals identified in later laboratory analysis have their diagnostic spectral features further into the infrared making a 400 - 2500 nm spectrometer the far preferable instrument for *in-situ* identification.

2.5.2: Field trials of Mars rover instruments in analogue sites

Analogue sites are also key to the development of new exploratory instruments, in particular instruments that will form part of the payload of a rover or lander. A major aspect of the development of any piece of new rover, as a whole and as individual instruments, is field testing and analogue sites are the ideal locations for this. Prior to sending a rover to Mars each instrument in its payload is tested both individually and as a composite system, in the laboratory and in field tests designed to simulate the conditions it will experience on Mars. Over the course of 1999 to 2001 researchers working on the MER rover design and development performed a number of field tests. These involved prototypes of specific instruments and were designed to test different aspects of the mission using a prototype rover named FIDO (Schenker et al., 2001). Field tests using FIDO were undertaken at Silver Lake, California in 1999, Black Rock Summit, Nevada in 2000 and Soda Mountains, California in 2001. The Marsokhod field test in 1999 at Silver Lake focused on field spectroscopy using a three band (650, 740, 855 nm) Pancam simulator and a hyperspectral Analytical Spectral Devices (ASD) FieldspecFR spectrometer with a spectral range of 350 – 2500 nm (Johnson et al., 2001). Newsom et al (2001) used the 1999 field trial specifically to see if the rover and field spectroscopy could be used to detect signs of life. One of the samples analysed had a clear chlorophyll signature that was found to be due to a layer of endolithic bacteria just beneath the surface of the rock in question. The ASD spectrometer was capable of picking this up and the Pancam was useful in identifying the rock as worthy of further study due to a greenish tinge that was evident in the composite RGB image created from its three band data. The 2000 Black Rock test used the same three band Pancam simulator as well as an Infrared Point Spectrometer (IPS) covering 1.3 - 2.5 µm (Arvidson et al., 2002). Curiously this IPS is nothing like any of the instruments that were planned initially or finally to go on the MER's although it shares many similarities to the Infrared Spectrometer for ExoMars (ISEM) that will form part of the ExoMars payload (Korablev et al., 2014). The final MER Pancam configuration was subject to extensive laboratory testing as detailed in Bell et al (2003) and

underwent a number of in-house field tests that have not been published. The ExoMars PanCam has been involved in a number of analogue field trails most extensively as part of the Arctic Mars Analogue Svalbard Expedition (AMASE) series of campaigns to Svalbard (Amundsen et al., 2010; Cousins et al., 2009; Schmitz et al., 2008; Steele et al., 2010). The AMASE field trials have also included numerous instruments from the MER and MSL scientific payloads.

2.6: Summary

VNIR reflectance spectroscopy is a well-established, non-destructive technique for the identification of minerals. Multi- and hyperspectral imaging spectrometers enable this identification to be undertaken from potentially great distances. This has made them invaluable instruments in the continued exploration of Mars. Regions of Earth that share similar properties to regions of Mars over the course of its lifetime have been utilised to ensure the spectral imaging data returned from Mars is being correctly interpreted. One of the key driving forces behind the exploration of Mars is the identification of previously habitable environments, the first step in the search for extra-terrestrial life. Hydrothermal environments are suitable and relevant candidates for habitable environments. VNIR spectroscopy has been shown to be capable of identifying such an environment and numerous regions of Mars have been postulated to have hosted hydrothermal environments in the planets history.

The following chapters will expand on the use of specific VNIR imaging technologies to identify hydrothermally altered regions and investigate the limitations both spectral and spatial scale can inflict on this task.

Chapter 3: ExoMars PanCam and hydrothermal alteration in Iceland*

3.1: Introduction

This chapter shall begin with the finest spatial and coarsest spectral scales dealt with in this thesis. The ExoMars rover will carry a large suite of instruments when it is sent to Mars in 2018, one of which is the PanCam, a stereoscopic, VNIR multispectral camera system. The PanCam will be the 'eyes' of the rover enabling its operators and scientists to make deductions about the environments and minerals it will encounter and plan the most efficient and salient deployment of the rovers contact instruments, in particular the drill which will collect subsurface samples to be passed to the analytical payload for examination for signs of habitability and life. The role of PanCam is thus a crucial one and it is imperative to establish that it is capable of providing the necessary data that will allow the rover operators to correctly identify potentially habitable environments and the ideal drill deployment location. This chapter shall detail the results of a unique field trial of an ExoMars PanCam emulator in Námafjall, a hydrothermally active region in the north-east of Iceland. Whilst Námafjall is not a direct analogue for any of the final four candidate ExoMars landing sites it is a region with a rich diversity of relevant alteration species (Ehlmann et al., 2012). The spectral accuracy of the multispectral data shall be validated; the utility of the data products produced to positively identify the environment established, and key analysis techniques identified in preparation for data that shall ultimately be returned from Mars.

3.2: Background

3.2.1: PanCam and ground-based spectral imagers on Mars

The ExoMars PanCam concept is inherited from previous cameras included on numerous martian rovers, most recently both of the Mars Exploration Rovers (MER) - *Spirit* and *Opportunity* (Bell III et al., 2003). The MER Panoramic Camera system (Pancam) is a multispectral, stereoscopic dual camera system designed to provide images that would allow the rover operators to assess the topography and geological context of the regions they were traversing as well as provide multispectral data to deduce mineralogical properties of the surface. The basic concept of this instrument was based on the earlier Imager for Mars Pathfinder (IMP) that had been a component of the Mars Pathfinder lander (Smith et al.,

* The bulk of this Chapter including all images has been published as Harris, J.K., Cousins, C. R., Gunn, M., Grindrod, P. M., Barnes, D., Crawford, I., Cross, R. E., Coates, I. A., Remote detection of past habitability at Mars-analogue hydrothermal alteration terrains using an ExoMars PanCam emulator. 2015, Icarus, 252, 284-300

1997). The most recent NASA mission, the Mars Science Laboratory rover *Curiosity* has a similar instrument in the form of the MastCam (Grotzinger et al., 2012). The unsuccessful ESA Beagle 2 lander was also equipped with a PanCam based on the earlier IMP and MER Pancams (Griffiths et al., 2005). The ExoMars rover PanCam build directly on the Beagle 2 PanCam heritage (Griffiths et al., 2006).

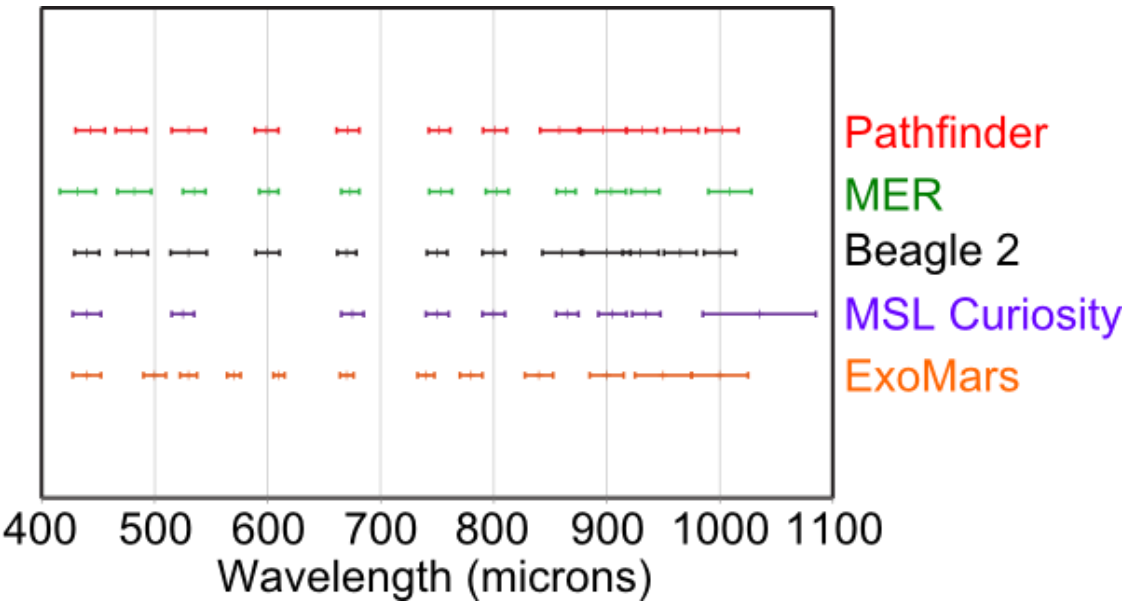

Figure 3.1: PanCam narrowband geology filter wavelengths and bandpass widths at FWHM from recent Mars landers and rovers.

The MER Pancam, the IMP and the ExoMars PanCam are all comprised of two identical wide angle cameras on either end of an optical bench. In front of each camera in these three systems is a filter wheel with a selection of filters including three broadband visible filters to enable the construction of RGB images, and narrowband filters to build coarse spectra covering approximately 0.4 – 1.0 µm. The Mastcam system is slightly different with each of the two cameras having a different angular field-of-view (FoV) from each other and a Bayer filter for RGB images as well as a filter wheel containing narrowband filters. One of the key differences between the various Pancam-type imaging systems is the exact central wavelengths and band widths of these narrowband filters and how many there are (figure 3.1 and table 3.1). Each of the missions to feature a Pancam-type system has had slightly different mission goals and subsequently slightly different requirements from their multispectral imager. MER *Spirit* and *Opportunity* were primarily focused on characterising the Fe-bearing rocks and soils in the regions they were exploring. MSL *Curiosity* is aiming to assess the past and present habitability of Gale crater where orbital data points towards the

presence of large quantities of liquid water in its history (Grotzinger et al., 2012). ExoMars however will be even more life focused with goals including actively searching for signs of past or present life and assessing the variety within the geochemical environment of its landing site (Griffiths et al., 2006). Cousins et al (2012) conducted a thorough study of the different mineral types likely to be found by the rover based on these mission goals and as a result proposed a new filter set designed to optimise the variety of mineral types identifiable with ExoMars PanCam. The field trial presented in this Chapter is the first trial of this new filter set.

Table 3.1: PanCam geology filter wavelengths and bandpass widths (given as Full Width Half Maximum (FWHM)) from recent Mars landers and rovers.

Pathfinder		**MER**		**Beagle 2**	
Filter (nm)	FWHM	Filter (nm)	FWHM	Filter (nm)	FWHM
443	6	432	32	440	22
479	27	482	30	480	28
530	30	535	20	530	32
599	21	601	17	600	21
671	20	673	16	670	17
752	19	753	20	750	18
801	21	803	20	800	20
858	34	864	17	860	34
897	41	904	26	900	42
931	27	934	25	930	32
966	30	1009	38	965	29
1002	29			1000	28
MSL		**ExoMars (FERRIC)**		**AUPE-2**	
Filter (nm)	FWHM	Filter (nm)	FWHM	Filter (nm)	FWHM
440	25	440	25	438	24
525	20	500	20	500	24
675	20	530	15	532	10
750	20	570	12	568	10
800	20	610	10	610	10
865	20	670	12	671	10
905	25	740	15	740	13

935	25	780	20	780	10
1035	100	840	25	832	37
		900	30	900	50
		950	50	950	50
		1000	50	1000	50

Final flight ready versions of rover instruments cannot be used in the field here on the Earth. Therefore in order to test the configuration of the ExoMars PanCam and ensure the data that will be returned are capable of meeting the instrument science goals an emulator is used to conduct field trials in Mars analogue sites (see Chapter 2 section 2.5.2 for further details of field trials of previous Mars rover cameras and spectrometers). The Aberystwyth University PanCam Emulator (AUPE-2) is a dedicated ExoMars PanCam emulator that has been constructed with commercial off-the-shelf cameras to replicate (as closely as possible) the data sets that will be acquired from the ExoMars PanCam. It comprises of two wide angle (39 x 33°) cameras (WACs) placed 50 cm apart along an optical bench, which in turn is fixed to a pan-tilt unit (Pugh et al., 2012). In front of each WAC is a filter wheel with 11 filter positions. Both filter wheels contain three broadband colour filters centred at 660 nm, 550 nm and 460 nm, a luminance filter covering the visible region of the spectrum and an empty filter slot for panchromatic imaging. Split evenly between the two WAC filter wheels and filling the remaining filter positions are 12 narrowband 'geology' filters spanning 440 - 1000 nm (see table 3.2 for filter centre wavelengths and bandwidths). The filters are all hard coated interference filters comprised of thin film stacks on glass substrates. In addition to the WACs, a high resolution camera (HRC) with a FoV ~ 5° is mounted in the centre of the optical bench, which provides close-up high resolution images of targets within the WAC FoV, consistent with the ExoMars PanCam (Coates et al., 2012). The HRC used in AUPE-2 provides only greyscale images unlike the ExoMars HRC that will provide colour images.

Table 3.2: Technical specifications of the current configuration of the ExoMars PanCam and the Aberystwyth University PanCam Emulator (AUPE-2). WAC filter bandpasses are given as Full Width Half Maximum (FWHM) values.

	AUPE-2 (Gunn, 2013)	**ExoMars Panoramic Camera**
Wide Angle Cameras (WAC)		
Model	Manta G-504B	WAC
Image type	Mono (8-12 bit)	Mono (10 bit)
Sensor	Sony ICX655	Cypress STAR 1000 APS
Field of view	39° x 33°	38.3 x 38.3 (h x v)°
Focal length	12 mm	21.85 mm
Image resolution	1024 x 1024	1024 x 1024
Aperture	f/11	f/10
Toe-In (cross over distance)	2.8° (5 m)	2.8° (5 m)
WAC Filter Wheels and their centre wavelengths and FWHM bandwidths [a, b]		
LWAC - Geology 1	438 (24)	440 (25)
LWAC - Geology 2	500 (24)	500 (20)
LWAC - Geology 3	532 (10)	530 (15)
LWAC - Geology 4	568 (10)	570 (12)
LWAC - Geology 5	610 (10)	610 (10)
LWAC - Geology 6	671 (10)	670 (12)
RWAC - Geology 1	740 (13)	740 (15)
RWAC - Geology 2	780 (10)	780 (20)
RWAC - Geology 3	832 (37)	840 (25)
RWAC - Geology 4	900 (50)	900 (30)
RWAC - Geology 5	950 (50)	950 (50)
RWAC - Geology 6	1000 (50)	1000 (50)
LWAC – Blue broadband	440 (120)	440 (120)
LWAC – Green broadband	540 (80)	540 (80)
LWAC – Red broadband	640 (100)	640 (100)
RWAC – Blue broadband	440 (120)	440 (120)
RWAC – Green broadband	540 (80)	540 (80)
RWAC – Red broadband	640 (100)	640 (100)
LWAC	545 (290) - Visible	925 (5) – Solar
LWAC	Empty – Panchromatic	935 (5) – Solar

RWAC	545 (290) – Visible	450 (5) – Solar
RWAC	Empty - Panchromatic	670 (5) – Solar
High Resolution Camera		
Model	Mantra G-146B	HRC
Image type	Mono (8-12 bit)	Mono (10 bit)
Sensor	Sony ICX267AL	Cypress STAR 1000 APS
Field of view	4.8°	4.8°
Focal length	58 mm	180 mm
Resolution	1024 x 1024	1024 x 1024
Aperture	f/11	f/14.4-20

[a]Final distribution and position of filters not yet determined. All filter centre wavelengths and bandpasses (in brackets) given in nm, with bandpasses at Full Width Half Maximum.

[b]Geology filter centre wavelengths and bandpasses from Cousins et al. (2012).

3.2.2: Námafjall and Iceland as a Mars analogue site

Hydrothermal and glaciovolcanic terrains have been postulated to exist across Mars throughout its history (Keszthelyi et al., 2010; Schulze-Makuch et al., 2007) and are known to exist here on Earth where they provide a habitat for number of different extremophile species (Cousins et al., 2013). Hydrothermally altered environments tend to be comprised of a wide variety of mineral assemblages, and with especial relevance to PanCam many of these mineral groupings have key spectral features in the 400 – 1000 nm wavelength range (Cousins et al., 2012). Iceland with its cold climate and active volcanic and geothermal systems provides an ideal analogue location for testing the ability of PanCam to identify hydrothermally altered environments (Ehlmann et al., 2012).

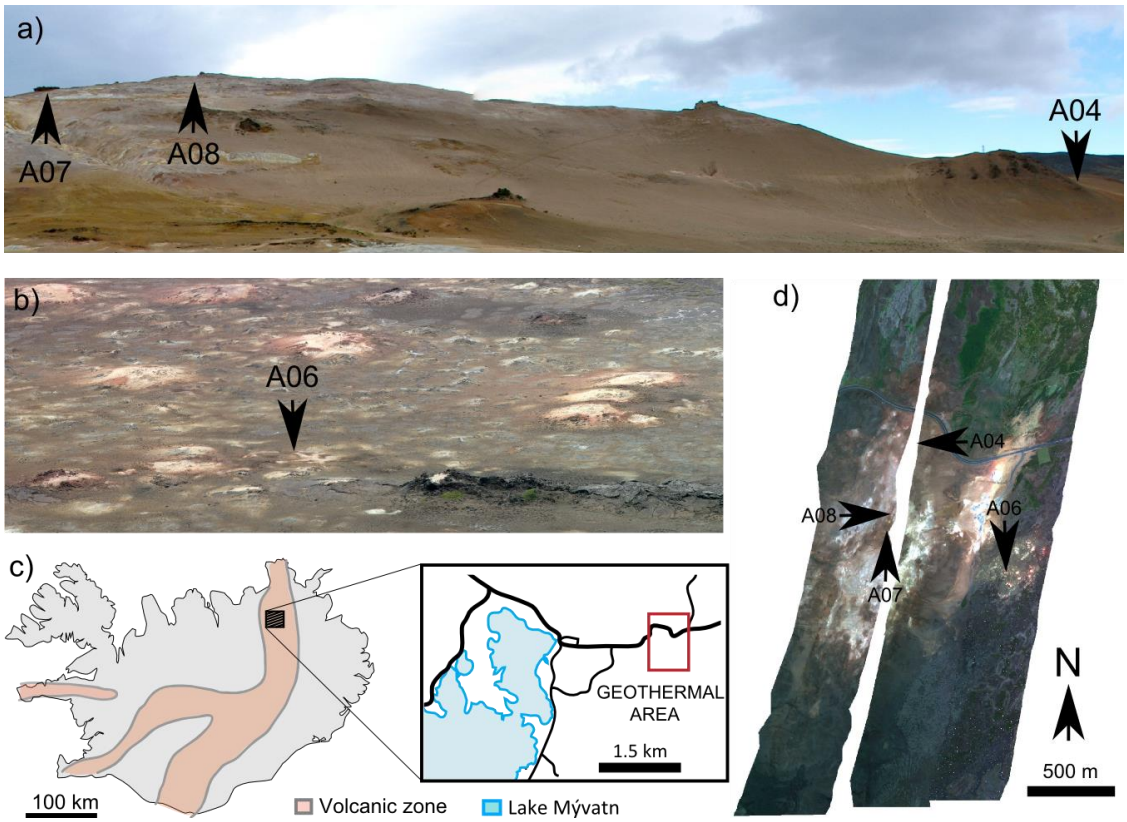

Figure 3.2: Localities used for field-testing the ExoMars PanCam emulator "AUPE-2". a) Volcaniclastic ridge where sites A04_Tuff, A07_Pillow, and A08_Vein are located, as viewed from site A06_Soils; b) Altered Holocene subaerial basaltic lava flows where site A06_Soils is located (as viewed from the summit of the ridge in (a); c) Map of Iceland showing the location of Námafjall within the northern volcanic zone - map inset shows the location of the Námafjall geothermal area; d) Colour composite sections of NERC ARSF Eagle swath data with all 4 sites shown (see Chapter 5, section 5.6.1 for full explanation of the NERC ARSF imagery).

AUPE-2 was deployed in Námafjall, a geothermal region in the northeast of Iceland, (figure 3.2) between 27/06/13 and 03/07/13. Námafjall forms part of a graben within the active rifting zone of Iceland together with the nearby Krafla volcano. The area is characterised by basaltic Pleistocene and Hologene subaerial lava flows (Thordarson and Hoskuldsson, 2002) and subglacially-erupted volcaniclastic deposits and pillow lavas. The prominent Mt. Námafjall is comprised of a glaciovolcanic hyaloclastite ridge (Gudmundsson et al., 2010). Aqueous alteration of basaltic substrates in this region has produced discrete patches of diverse alteration mineral assemblages, including sulfate-phyllosilicate-ferric oxide rich soils and gypsum veins. The region is still geothermally active with the majority of the fields being high temperature, high sulfur and acidic pH (Gudmundsson and Arnórsson, 2005). Such a site

is an ideal Mars analogue site in terms of its formational history and mineralogy (Preston et al., 2013). The primary aim of this field campaign was to test the ability of AUPE-2 to: i) detect the type and variety of mineral deposits produced in this environment and ii) compare the multispectral data products generated with the new filter set (Cousins et al., 2012) with a field spectrometer to ensure their fidelity. Four different target areas were selected to capture the variety of structural and geochemical features that typify this type of environment (figures 3.2 and 3.3). Three sites were along the top of a glaciovolcanic móberg ridge: A04_Tuff (65°38'42''N, 16°49'01''W), a collapsed series of hydrovolcanic sediment layers; A07_Pillow (65°38'24''N, 16°49'15''W), a weathered outcrop of subglacial pillow basalts, and A08_Vein (65°38'27''N, 16°49'13''W), a heavily altered series of geothermal soils surrounding a number of intrusive gypsum veins. The fourth site, A06_Soils (65°38'15''N, 16°48'21''W) was situated on a flat plain beneath the ridge and comprises a number of mostly inactive low mounds of semi-consolidated geothermally altered soils.

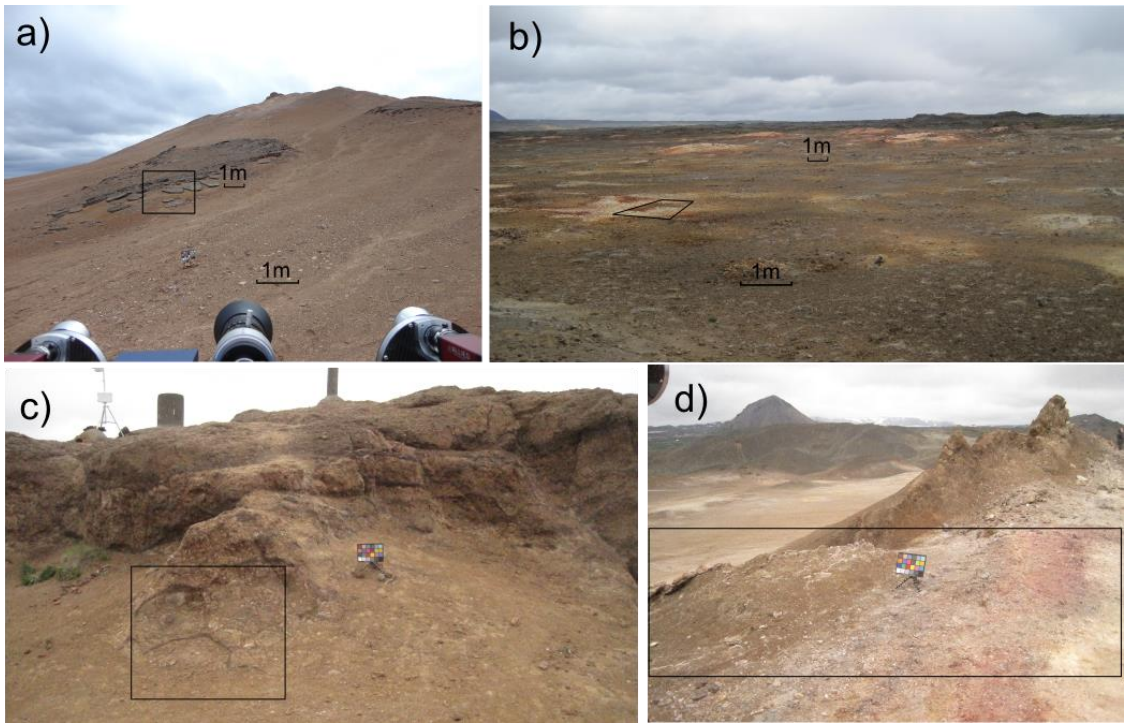

Figure 3.3: Field photographs showing target sites. a) A04_Tuff with similar structure in the top right. b) A06_Soils (box, middle left) with surrounding similar soils and low mounds. c) A07_Pillow, the calibration target in this photo is not in the same position as figure 3.7, that region of the image is the front section of the pillow formation as highlighted. d) A08_Vein showing exposed nature of target. Black boxes indicate approximately the regions imaged by AUPE-2 in figures 3.5 (3.3a), 3.6 (3.3b), 3.7 (3.3c) and 3.8 (3.3d).

3.3: Data collection and processing

3.3.1: AUPE-2

AUPE-2 was deployed *in-situ* at field localities, and a calibrated Macbeth ColorChecker© classic colour chart (X-rite) was included in one WAC image from each scene panorama to enable radiometric calibration of the AUPE-2 multispectral image data. All distances between AUPE-2 and outcrops were measured from the centre of the AUPE-2 optical bench to the centre of the calibration target (table 3.4). For all data acquisition, the AUPE-2 optical bench was positioned 2 m above the ground, consistent with the ExoMars rover configuration. AUPE-2 data were collected between 10:30 and 14:40 local time under uniform grey skies to minimise the atmospheric column the sunlight passed through and ensure consistent illumination during each dataset whilst eliminating the risk of specular reflections. The incidence and emission angles for each target region are highly dependent on local topography and vary within each scene. These conditions were largely dictated by the time and weather constraints inherent to fieldwork in Iceland but are also comparable to the use of MER Pancam on Mars (Farrand et al., 2007). ExoMars PanCam operations are still to be finalised but will be similar to those used in this work and by the MER Pancam team.

AUPE-2 multispectral data were processed using Exelis Visual Information Solutions ENVI 4.8 and IDL software (Exelis Visual Information Solutions, Boulder, Colorado) into relative reflectance calibrated image cubes following the calibration pipeline presented in Barnes et al., (2011), two cubes for each frame, one for each WAC. This pipeline encompassed flat-fielding, dark frame subtraction, removal of detector bias and the calculation of relative reflectance calibration factors from the in-scene Macbeth ColorChecker© (see Appendix I for full pipeline and associated IDL code written to facilitate the processing used in this work). These final image cubes give R* values, where R* is defined by Reid et al., (1999) as "the brightness of the surface divided by the brightness of an RT [*Radiometric Calibration Target*] scaled to its equivalent Lambert reflectance." Region of Interest (ROI) spectra were extracted from these processed cubes using ENVI version 4.8. ROI footprints ranged in size from 20 (A04_Tuff), 40 (A06_Soils; A08_Vein) to 160 (A07_Pillow) pixels. Mean spectra were calculated over each ROI to be plotted with error bars representing the standard deviation over the pixels within each ROI. Footprint pixel sizes varied depending on the scale of variation in the scene and the distance of AUPE-2 from the target but all correspond to spatial footprints of approximately 1 cm radius. Principal Components Analysis (PCA) was performed

on the ROI AUPE-2 spectra taken from the four sites (n=20). Additionally PCA images were generating using the PCA tool resident in ENVI version 4.8 for each site.

3.3.2: Ocean Optics Jaz Spectrometer

Immediately following imaging of outcrop targets with AUPE-2, corresponding 400 – 1000 nm reflectance spectra of ROIs were acquired using an Ocean Optics Jaz portable spectrometer. The Jaz spectrometer is a folded path diffractive grating spectrometer capable of detection of light in the range 370 – 1030 nm. An order sorting filter is integrated into the system to block higher grating orders. The Jaz was used with an ISP-REF integrating sphere contact probe (used in 8° incident/total hemispherical reflectance geometry) with an internal light source and a 10 mm diameter sample port. In the field the spectrometer was allowed to warm up for a minimum of five minutes to ensure the spectral stability of the light source. Prior to each target measurement a dark current spectrum was taken by completely covering the probe aperture using a spectrally flat, black surface and ensuring no external light could enter. Following this a white spectrum was taken using a block of Spectralon©, a standard calibrated surface designed to be both spectrally flat and 100% reflective across this wavelength range. These were used to calibrate the signal prior to target measurement. These dark and white spectra were saved internally by the spectrometer software to radiometrically correct the target spectra but were then automatically discarded. Target surfaces were chosen based on observable variability in the area to ensure the variety in the scene was captured. In the case of soils the probe aperture was pressed into the surface to ensure no light leaking in from the sides. For solid rock surfaces the flattest surface available was chosen and any sections that could leak in external light were blocked by hand. The Jaz software internally averaged 10 spectra in real time for each measurement to minimise errors. Each of these was automatically displayed on the operating laptop screen allowing any change in the target spectra to be monitored and if necessary the probe repositioned. A minimum of three spectra were displayed on the screen before taking a measurement to ensure the signal had stabilised.

3.3.3: X-Ray Diffraction and laboratory VNIR spectroscopy of rock and soil samples

Rock and soil samples were retrieved immediately following a field spectrometer measurement from each ROI target for all outcrops imaged with AUPE-2. These were divided into two aliquots, one of which was powdered and sieved to < 210 μm and the other left in its original consolidated state. The powdered samples were analysed using X-Ray Diffraction (XRD) to determine bulk mineralogical composition of ROI targets, while both the powdered and original samples were analysed using an ASD FieldSpec Pro spectrometer (spectral range

350 - 2500 nm with a spectral resolution of between 1.4 and 2 nm) at the Natural Environment Research Council Field Spectroscopy Facility (NERC FSF) at the University of Edinburgh using a contact probe attachment with a FoV radius of 10 mm. The Fieldspec Pro in comprised internally of three spectrometers, a VNIR (350 – 1050 nm) diffraction grating spectrometer with a 512-channel silicon photodiode single detector array with an order separation filter overlain. The two SWIR spectrometers (900 – 1850 nm and 1700 – 2500 nm respectively) are concave holographic grating scanning spectrometers with a single InGaAs detector each. The scanner measures each wavelength sequentially rather than simultaneously as the VNIR spectrometer does. The collection technique used for this instrument followed the instructions provided by the FSF (MacArthur, 2007). The optimisation routine (internal instrument calibration) was run either between every 6th target/sample or every 30 minutes (whichever was shorter) and a white reference captured before each target measurement from a calibrated block of Spectralon©. A minimum of two stable spectra displayed in real time were acquired before a target spectrum was captured to ensure a stabilised measurement. The internal averaging was set to 50 measurements to ensure a reasonable signal to noise ratio.

XRD analysis was carried out as per Cousins et al., (2013, 2012) using a Bruker D8 Advance XRD with a Vantec 1 detector at Aberystwyth University, calibrated using a corundum standard. For analysis of phyllosilicates, additional XRD analysis was conducted at Birkbeck, University of London using a Philips PW 1730 Diffractometer using Cu Kα radiation. The powdered samples for this analysis were prepared using standard methods described by Merriman and Peacor, (1999) to ensure preferential orientation of the phyllosilicates. This preparation involved mixing the existing sieved powders with distilled water and centrifuging prior to removal of excess liquid. The resulting slurry was emplaced onto frosted glass slips and allowed to dry overnight prior to analysis. In both cases, sample spectra were compared to database mineral spectra using the International Centre for Diffraction Data database, and the RRUFF database (Downs, 2006).

3.3.4: Spectral Parameters

Spectral parameters are algorithms that can be utilised to emphasise features indicative of key minerals, bulk composition, or lithology in spectral data. These parameters are usually selected to pick up on a unique spectral feature that can be used to identify the mineralogical identity of the reflective surface of a particular target of interest. These have been used to analyse MER Pancam data (Farrand et al., 2008, 2006) and form a major component in the standard analysis chain of CRISM data (Pelkey et al., 2007; Viviano-Beck et al., 2014). For the

analysis of AUPE-2 data in this work a set of parameters has been created based on the work of Anderson and Bell (2013), Cousins et al. (2012) and Farrand et al. (2008) (table 3.3). The algorithms for band depth and spectral ratio normalise the data allowing values from different instruments to be directly compared. The spectral slope calculation does not normalise the data in this way and therefore spectral slope values from different instruments cannot be directly compared. However, broad similarities should still be evident such as a negative or positive gradient. Spectral Parameters were calculated across entire multi/hyperspectral images and the results plotted as false-colour images for analysis.

3.3.5: Principal Components Analysis (PCA)

Principal Components Analysis (PCA) is a data interrogation technique that emphasises the variance in highly correlated multivariate datasets and is commonly used in spectral and remote sensing studies (Campbell, 2006; Davis, 1986; Richards and Jia, 1999). It involves an orthogonal transformation of linearly correlated data into a new coordinate frame where the greatest variance lies along the 1st coordinate (PC1), the 2nd greatest variance along the 2nd coordinate (PC2) etc. This technique produces a visual representation of the level of spectral variability within a given dataset enabling the analyst to make a first pass at creating spectral classes. PCA has been shown to be useful in the analysis of multispectral imagery in Farrand et al. (2008) using data from the MER Spirit Pancam. It is used in this Chapter to assess the level of variance within regional datasets from AUPE-2, and investigate how well this correlates with the variance of the sites as defined using visual, compositional and environmental criteria.

Table 3.3: Spectral parameters designed for AUPE-2 WAC multispectral data

Name	Description	Rationale/Related Characteristic
BD532	Depth of absorption band centred at 532 nm $1-(R_{532}/[(0.53*R_{500})+(0.47*R_{568})])$	Identifies ferric minerals, in particular hematite and related to degree of oxidation
S532-610	Slope between 532 and 610 nm $(R_{610}-R_{532})/(610-532)$	Ferric minerals and dust
BD900	Depth of absorption band centred at 900 nm $1-(R_{900}/[(0.455*R_{840})+(0.545*R_{950})])$	Strength of NIR absorption, related to ferric minerals
S740-1000	Slope between 740 and 1000 nm $(R_{1000}-R_{740})/(1000-740)$	Strength and position of NIR absorption linked to ferrous minerals
S950-1000	Slope between 950 and 1000 nm $(R_{1000}-R_{950})/(1000-950)$	Linked to hydrated minerals
R740/1000	740:1000 nm ratio R_{740}/R_{1000}	Ferrous minerals
R671/438	671:438 nm (red:blue) ratio R_{671}/R_{438}	Ferric minerals and dust
BD610	Depth of absorption band centred at 610 nm $1-(R_{610}/[(0.600*R_{568})+(0.400*R_{671})])$	Can indicate goethite development and be influenced by olivine vs pyroxene
BD950	Depth of absorption band centred at 950 nm $1-(R_{950}/[(0.500*R_{900})+(0.500*R_{1000})])$	Related to hydrous minerals, some clays and silicates
S438-671	Slope between 438 and 671 nm $(R_{671}-R_{438})/(671-438)$	Related to degree of oxidation

3.4: Results

For each of the four sites analysed using AUPE-2 datasets were collected as summarised in table 3.4.

Table 3.4: Summary of data collected in-situ

Site	AUPE dataset (# of images in panorama)	Distance of tripod foot from calibration target	Number of in-situ Jaz spectra	Number of rock/soil samples	Comment
A04_Tuff	1 (4) 2 (1)	7.75 m 3.30 m	- 5	- 4	Same area from different distance, ROI's extracted from set 2
A06_Soils	1 (2)	0.60 m (1.56 m from PTU)	6	6	
A07_Pillow	1 (1) 2 (1)	8.10 m 2.10 m	- 4	- 4	Same area from different distance, ROI's extracted from set 2
A08_Vein	1 (3)	2.90 m	5	6	

A summary of contextual mineralogical and spectral data for all site ROI units identified in the rock and soil samples is given in table 3.5. Broadly, alteration and secondary minerals identified in the ASD laboratory VNIR spectra (figure 3.4) include hematite, goethite, nontronite, montmorillonite, gypsum, and sulfur. Ferrihydrite, maghemite, and various zeolites also appear as minor constituents. Sample XRD analysis is consistent with the laboratory VNIR results, revealing alteration phases to include all the above, but also kaolinite, anatase, natrojarosite, trace calcite and quartz. AUPE-2 data for each of the four sites is described and interpreted in the following sections.

Table 3.5: Summary of site ROIs, their mineralogy, and VNIR spectral features (also see figure 3.4)

	Unit	Bulk mineralogy (XRD, *VNIR*)	VNIR reflectance absorption features (µm)
A04_Tuff, 65°38'42''N, 16O49'01''W			
A04_001	Grey slab	smectite, plagioclase, augite, kaolinite *olivine, quartz*	0.48, 1.09 (broad), 1.41 (small) 1.92, 2.20, 2.29
A04_002	Alteration soil	kaolinite, smectite, iron oxide, quartz, augite, plagioclase *chabazite, montmorillonite, nontronite*	0.49, 0.65 (small), 0.96 (broad), 1.42, 1.91, 2.21, 2.29, 2.39
A04_003	Grey slab	plagioclase, smectite, kaolinite, quartz *olivine, quartz*	0.47, 0.65 (small), 1.07 (broad), 1.41, 1.92, 2.21, 2.30
A04_005	Alteration soil	mordenite, alunite, nontronite, iron oxide *nontronite, montmorillonite, ferrihydrite, goethite*	0.49, 0.65 (small), 0.963 (broad), 1.42, 1.91, 2.21, 2.29, 2.39
A06_Mound, 65°38'15''N, 16°48'21''W			
A06_001	Bright-toned unit	sulfur, anatase *nontronite, montmorillonite*	0.44, 0.97, 1.42, 1.77, 1.92, 2.22-2.26
A06_002	Bright-toned unit	sulfur, zeolite *sulfur*	0.40 (major), 0.92, 1.41, 1.91, 2.22
A06_003	Dark red unit	hematite, natrojarosite, augite, sulfur (trace) *hematite*	0.53, 0.90, 1.41, 1.47, 1.91, 2.21, 2.27
A06_004	Bright-toned unit	sulfur, zeolite *sulfur*	0.40 (major), 0.96 (broad), 1.42, 1.91, 2.22
A06_005	Dark red unit	natrojarosite, sulfur, zeolite *goethite, montmorillonite*	0.49, 0.93, 1.42, 1.47 (tiny), 1.91, 2.22, 2.27, 2.47
A06_006	Bright-toned unit	sulfur *nontronite, montmorillonite*	0.44, 0.48, 0.91, 1.16 (tiny), 1.41, 1.77, 1.91, 2.22, 2.26, 2.47

A07_Pillow, 65°38’24’’N, 16°49’15’’W			
A07_001	High albedo nodule	calcite, plagioclase, mordenite *zeolite*	1.05, 1.42, 1.92, 2.21, 2.30, 2.40
A07_002	Dark quench rind	smectite, calcite, stilbite *nontronite, chabazite*	0.49, 0.99, 1.43, 1.78, 1.92, 2.29, 2.40
A07_003	Pillow core interior	plagioclase, smectite, stilbite, iron oxide *nontronite*	0.42, 0.48 (minor), 0.65 (minor), 1.02, 1.42, 1.92, 2.19, 2.30, 2.39
A07_004	Pillow core interior	plagioclase, smectite, stilbite, kaolinite *nontronite*	0.42, 0.48, 0.60 (shoulder, minor), 1.03, 1.42, 1.78 (minor), 1.92, 2.20, 2.30, 2.40
A08_Veins, 65°38’27’’N, 16°49’13’’W			
A08_001	Dark red unit (mineral vein)	gypsum *gypsum*	0.42, 0.49, 1.19, 1.45, 1.49, 1.54, 1.75, 1.95, 2.22, 2.27, 2.42
A08_002	Dark red unit	plagioclase, smectite, zeolite, iron oxide, opal-a *goethite, nontronite*	0.49, 1.01, 1.43, 1.92, 2.21, 2.29, 2.40
A08_003	Brown soil	hematite, gypsum, smectite *hematite, gypsum*	0.54, 0.89, 1.45, 1.49, 1.54 (both minor), 1.75, 1.94, 2.21, 2.27, 2.43
A08_004	Brown soil	hematite, alunite, gypsum, smectite, zeolite *hematite, gypsum*	0.53, 0.90, 1.44, 1.77, 1.93, 2.21, 2.46
A08_005	Brown soil	gypsum, hematite, smectite, zeolite *gypsum, goethite*	0.52, 0.65, 0.91, 1.45, 1.49, 1.54, 1.75, 1.94, 2.21, 2.27, 2.43
A08_006	Peach soil	Gypsum, zeolite, smectite, hematite *gypsum, montmorillonite*	

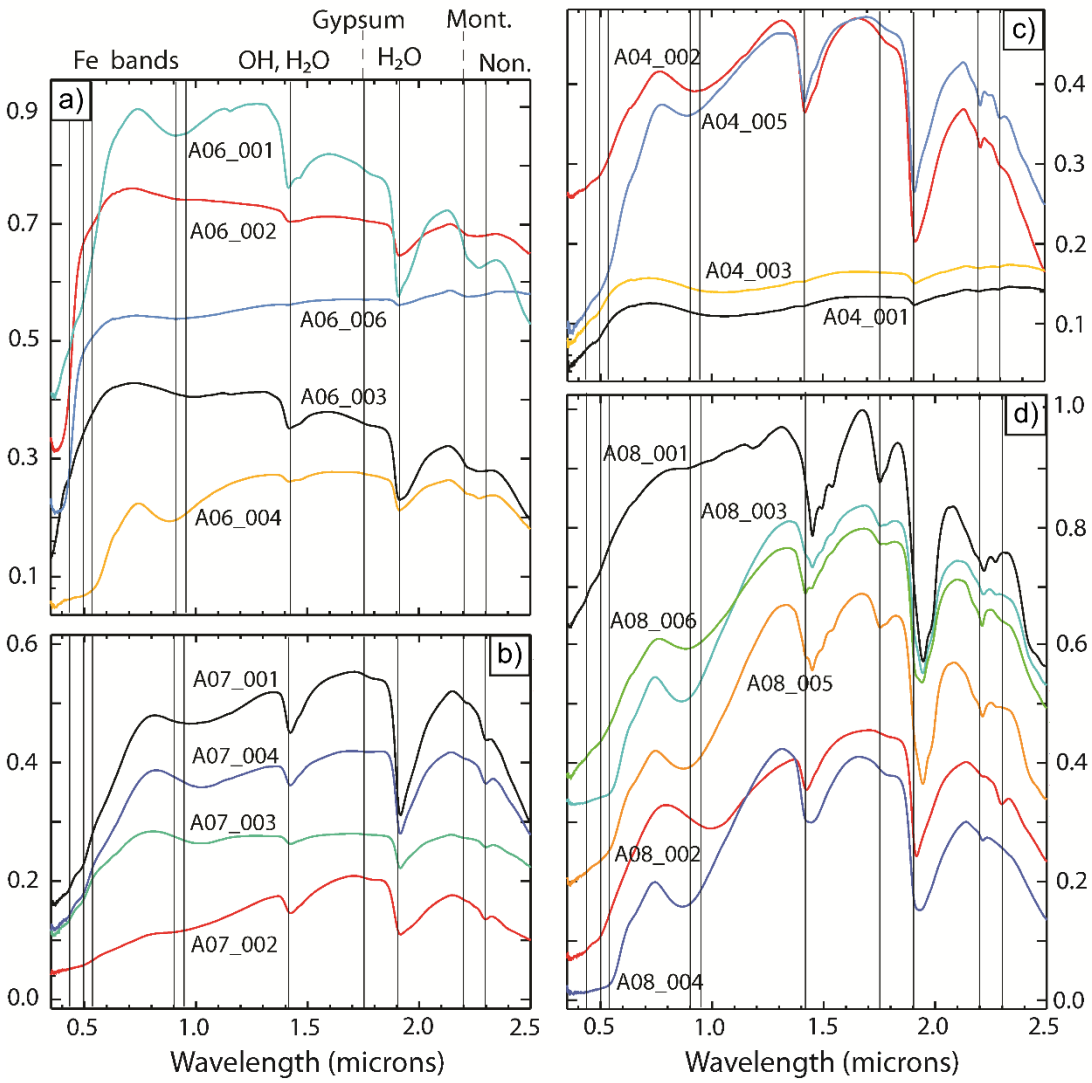

Figure 3.4: Laboratory ASD VNIR reflectance spectra of AUPE-2 ROI target samples. Individual sample names follow the format 'Site#_ROI#'. Absorption lines are shown for Fe crystal field bands, vibrational bands relating to H_2O and O-H, and key absorption bands for gypsum, montmorillonite (mont.) and nontronite (non.).

3.4.1: A04_Tuff

This outcrop was imaged first from a distance of 7.75 m (figure 3.5a) as a 4 x 1 RGB panorama, followed by a single field of view (FoV) full multispectral image set from a distance of 3.3 m. The outcrop and similar nearby deposits are comprised of layered, semi-competent circular collapse features ranging in size from 5 - 15 m in diameter, surrounded by unconsolidated geothermal soils (figure 3.5b). The edges of these circular collapse features have weathered and fragmented along sedimentary bedding planes into slabs approximately 10 – 80 cm across. Near-horizontal bedding planes and individual slabs, are visible in the LWAC RGB colour mosaic (figure 3.5b). This outcrop is less oxidised than the surrounding

soils, exhibiting a low-albedo, spectrally flat reflectance profile (ROIs A04_001 and A04_003, figure 3.5c) consistent with the grey surface colour of this lithology. This differentiation is clearly emphasised in the narrowband red:blue ratio (R671/438) spectral parameter image (figure 3.5e), highlighting the steeper ferric absorption slope of the soils. Spectrally, the site forms three distinct units (figures 3.5c and 3.5e): the sedimentary grey slab unit (ROIs A04_001 and A04_003), and two alteration soil units (A04_002 and A04_005) surrounding the grey slab unit. Despite the homogenous visible colour of the alteration soils, they show a clear variation in the ratio between red and blue (R671/438), highlighting those regions with a higher proportion of ferric minerals. In addition, the same R671/438 spectral parameter image further reveals the sedimentary layering in the grey slab unit, even in areas where the colour image shows only shadow (figure 3.5e).

AUPE-2 R*spectra measured from ROIs A04_001 and A04_003 within the grey slab unit show a consistent match in spectral profile to the *in-situ* reflectance spectrometer data (figure 3.5c). The only deviation in reflectivity is seen at the 950 nm band, with the AUPE-2 R* spectra showing a sharp increase in reflectance at this wavelength. Overall, the grey slab unit spectra have a low albedo and are flat and featureless in this wavelength range. Conversely, ROIs A04_002 and A04_005 from the surrounding alteration soils both show an Fe^{3+} absorption in the NIR in both R* and *in-situ* reflectance spectra, suggesting the presence of iron-oxide mineral species or nanophase material. These NIR absorptions in the R* spectra are not as broad as the *in-situ* reflectance measurements, beginning at the 832 nm filter rather than at 780 nm in the *in-situ* spectra. The R* spectrum for ROI A04_005 also captures the red shoulder seen in the *in-situ* spectrum at 640 nm, although due to the difference in spectral resolution it is captured at the 671 nm filter. Again the R* spectrum displays a negative slope between 950 nm and 1000 nm that is not seen in the corresponding reflectance spectral data.

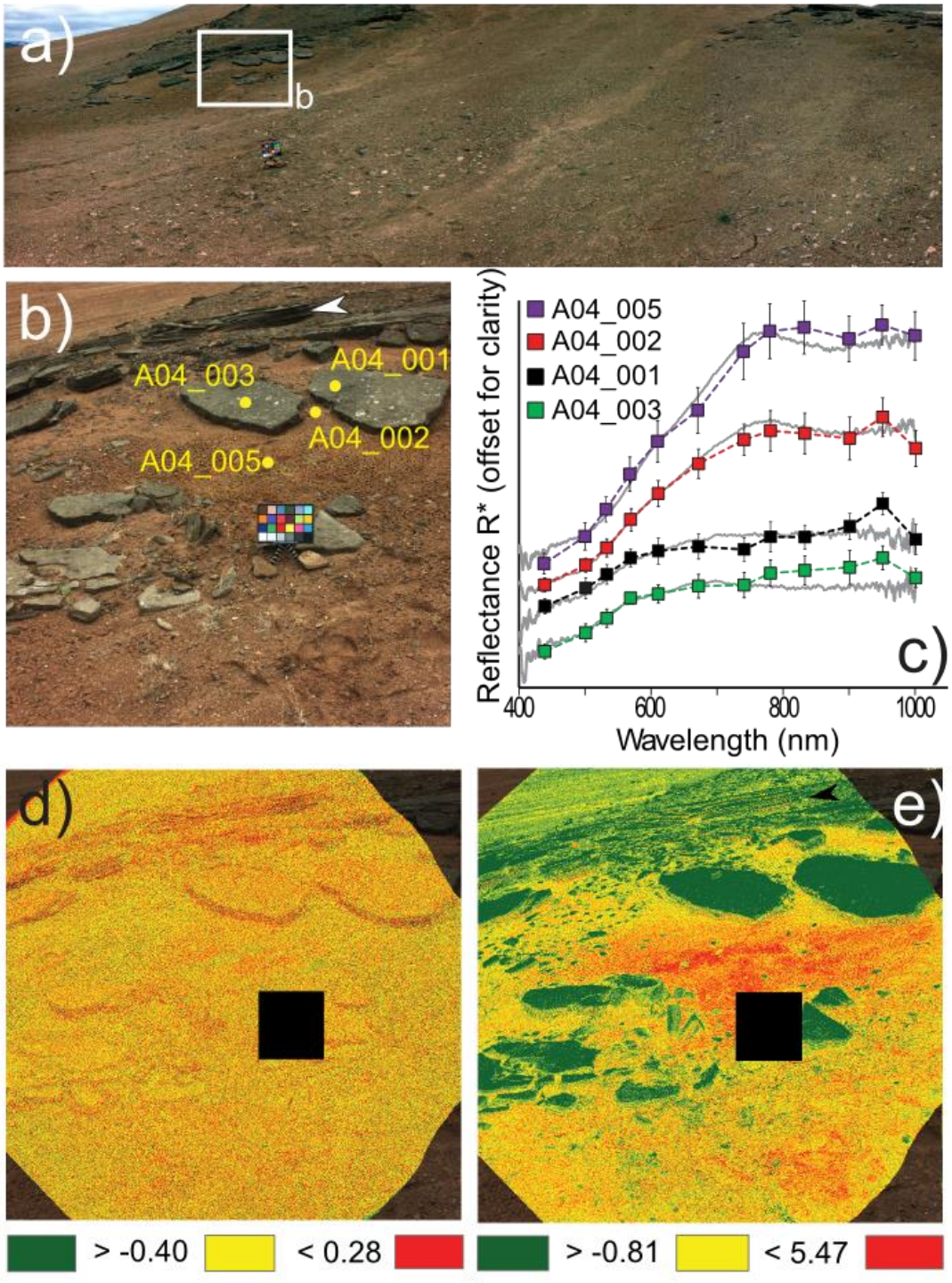

Figure 3.5: AUPE-2 datasets for site A04_Tuff. a) LWAC colour panorama of the outcrop (top left) and the surrounding area, with the 21.5 x 28 cm ColorChecker© for scale; b) Single LWAC FoV colour image showing location of AUPE-2 ROI targets (footprints not to scale), and arrow highlighting sedimentary bedding; c) AUPE-2 R spectra and corresponding in-situ field spectra (grey); d) LWAC spectral parameter image of the 610 nm band depth (BD610); e) LWAC spectral parameter image of the narrowband red:blue ratio (R671/438). Black boxes in d) and e) indicate the location of the ColorChecker©.*

The grey slab unit is characterised by finely-layered volcaniclastic sediments comprising of unaltered basaltic glass (sideromelane) clasts (<2 - 3 mm grain size) supported by a fine-grained amorphous grey-beige matrix, typical of volcanic sediments emplaced via hydrovolcanism. Clasts are angular and largely unsorted, suggesting deposition proximal to the source, though in some parts of the outcrop clasts form semi-defined bands of coarser and finer material, along which bedding planes form. The fine-grained matrix itself is in the early stages of palagonitisation (Stroncik and Schmincke, 2002), and has undergone little oxidation. Laboratory VNIR (350 - 2500 nm) spectra (figure 3.4) of grey slab unit ROIs A04_001 and A04_003 exhibit few absorption features in the 0.4 – 2.5 µm range, dominated only by a broad Fe^{2+} absorption centred around 1.0 µm and a minor H_2O band at 1.9 µm. Surrounding soil target ROIs A04_002 and A04_005 both show a broad Fe^{3+} absorption at 0.9 µm (consistent with the NIR absorption observed in the R*and *in situ* reflectance data) with well-defined O-H and H_2O absorptions at 1.4 and 1.9 µm respectively, together with minor absorptions at 2.2 and 2.3 µm, indicative of smectite clay minerals montmorillonite and nontronite (Bishop et al., 2008). XRD analysis is consistent with the results, showing the grey slab units to be predominantly plagioclase and smectite and the soils to be smectite and amorphous or poorly crystalline iron oxides.

3.4.2: A06_Soils

This target was imaged from a distance of 1.56 m in a 2 x 1 panorama. The LWAC colour mosaic (figure 3.6a) of this target reveals a multitude of heterogeneous, loosely-consolidated soils, which broadly form a bright-toned grey-pink unit and a low-albedo dark-red unit. These are emphasised by the narrowband red:blue ratio (R671/438) spectral parameter image (figure 3.6d). Structurally, this region appears to be comprised of one poorly consolidated unit, with no observable internal structural units. The LWAC PCA image (figure 3.6b) and the green – red slope (S532 – 610) spectral parameter image (figure 3.6e) show small scale spectral variation throughout the bright-toned unit implying a well-mixed soil composition on the sub-metre scale. Six ROI targets were selected within this outcrop, and were chosen based on visible colour variations identified within the LWAC colour mosaic. ROI A06_001 lies within the high albedo bright-toned unit, and exhibits a flat spectrum with no absorption features (figure 3.6c), potentially indicative of alteration minerals such as gypsum, opaline silica, zeolites, or magnesium sulfate (Cloutis et al., 2002; Ehlmann et al., 2012; Hunt and Ashley, 1979). The AUPE-2 R* spectra for this ROI accurately captured this spectral profile at all wavelengths as identified with the corresponding spectrometer field measurement except

for the 440nm value. The slightly steeper slope at this position is likely a result of a slight spatial mismatch between the measurements and the high variability of this target resulting in the AUPE measurement including slightly more sulfur than the *in-situ* measurement. ROI A06_004 exhibits a sharp slope in the blue followed by a broadly flat spectrum through the visible and NIR. This spectral shape is characteristic of sulfur, and like ROI A06_001, it is accurately captured by the AUPE-2 R* spectrum (figure 3.6c). The ROI A06_005 spectrum from the low albedo dark-red unit displays features consisted with ferric iron-bearing minerals, and in the visible the AUPE-2 data captures the absorption at 510 nm followed by the shoulder at 600 nm (figure 3.6c), but fails to capture the deep, broad absorption that characterises the NIR, centred at 950nm. Similarly, the R* spectrum for ROI A06_003 is consistent with the corresponding *in-situ* measured spectrum in the visible, but fails to capture the reflectance peak at 740 nm despite the presence of filters within this region.

This target sites lies within a cluster of bright-tone, high albedo alteration patches that are clearly distinct from the surrounding unaltered basaltic terrain (figure 3.3b). The interpretation of this is that the soils imaged by AUPE-2 may be representative of the neighbouring discrete alteration patches. Within the target itself, the low-albedo dark red unit (ROIs A06_003, A06_005) is comprised of a heterogeneous mix of hematite, goethite, montmorillonite, natrojarosite, jarosite, augite, sulfur, and opaline silica as determined by laboratory reflectance spectra (figure 3.4) and XRD data (table 3.5). The bright-toned unit ROIs have a less-varied mineralogy. ROIs A06_001 and A06_006 both comprise of smectite clays and sulfur, while ROIs A06_002 and A06_004 are dominated solely by sulfur. The target is interpreted to be an extinct acid fumarole patch consistent with the nearby active geothermal area, with the sulfur-rich soils representing the highest-temperature parts of the fumarole.

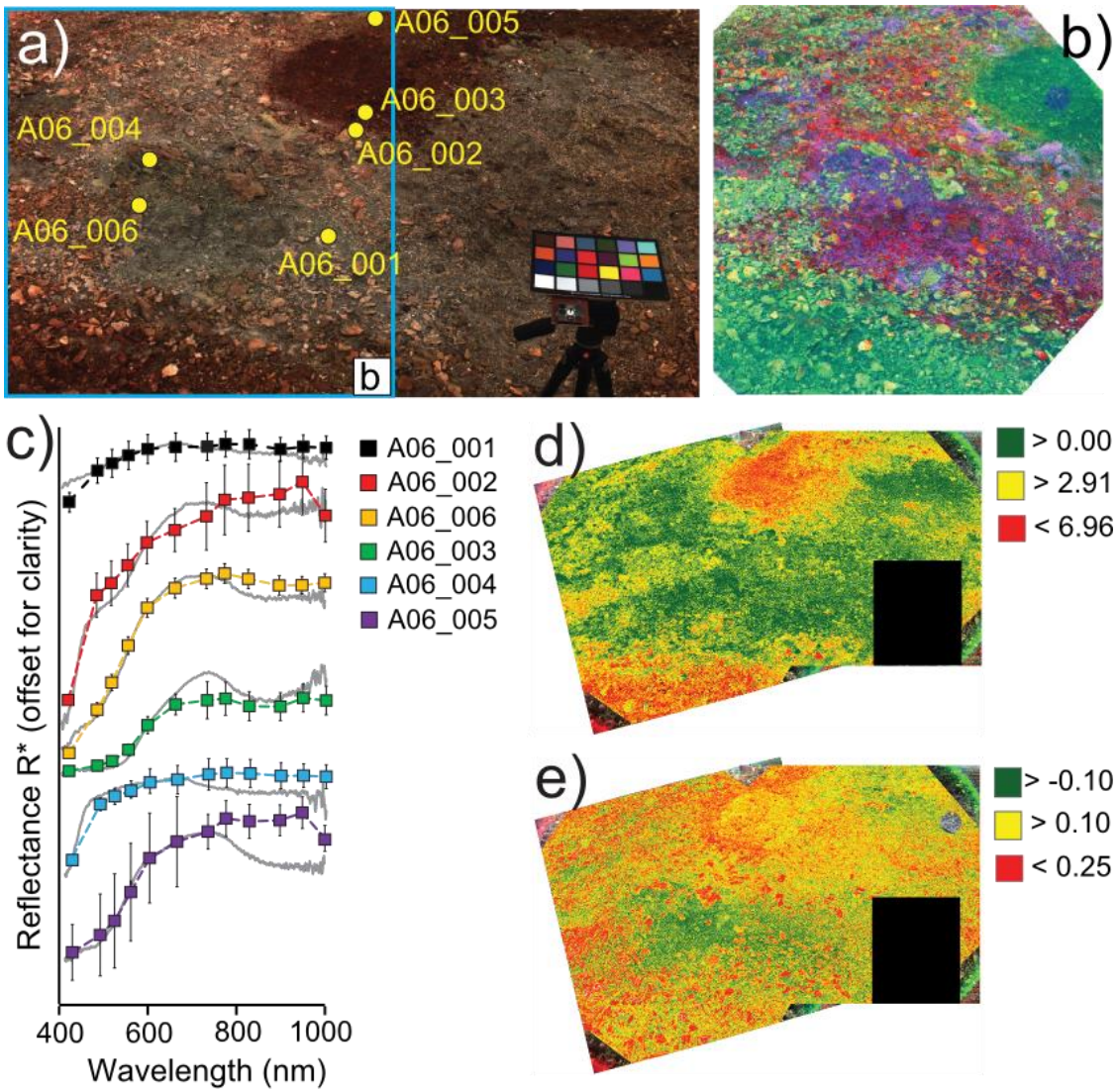

Figure 3.6: AUPE-2 datasets for site A06_Soils. a) LWAC colour panorama with the 21.5 x 28 cm ColorChecker© for scale, showing location of ROI targets (footprints not to scale) and region covered in b; b) LWAC Principal Component image (R = PC1, G = PC3, B = PC4) where red highlights white-coloured minerals, green highlights iron oxide-rich soils, and purple highlights sulfur; c) AUPE-2 R spectra and corresponding field reflectance spectra (grey); d) LWAC spectral parameter image of narrowband red:blue ratio (R671/438), e) slope between 532 and 610 nm (S532_610). Black boxes in d) and e) indicate the location of the ColorChecker©.*

3.4.3: A07_Pillow

The context LWAC colour image, taken from a distance of 2.1 m, captures the distinctive morphology and cross-sectional structure of a pillow basalt sequence (figure 3.7a). The outcrop surface is extensively weathered and altered, with the dark quench rinds of the individual pillows contrasting with the oxidised crystalline pillow core. In the PCA LWAC

image (figure 3.7c) these quench rinds stand out as bright green structures, with the more oxidised base of the outcrop displayed in purple. Millimetre sized cross-cutting mineral veins and larger nodules are strongly visible in yellow, and their emplacement does not appear to have been influenced by the existing pillow basalt structures. The HRC image (figure 3.7e) confirms the presence of the high albedo mineral veins observed in the LWAC image. These high albedo veins are also picked out as red in the narrowband red:blue ratio (R671/438) spectral parameter image (figure 3.7d), showing their distribution across the whole outcrop and not just within the footprint of the HRC target. Concentric weathering rinds are well-formed across the surface of the outcrop, and are visible in the context WAC colour and greyscale HRC images (figure 3.7a and 3.7e).

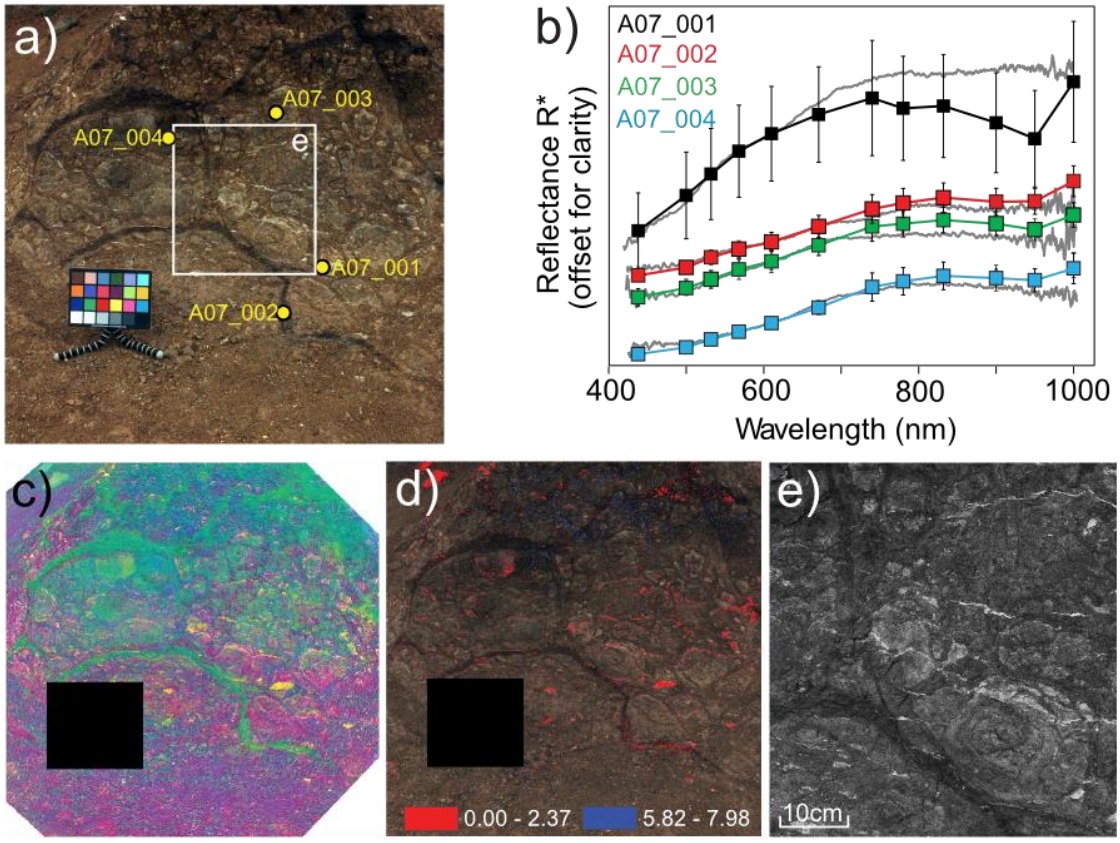

Figure 3.7: AUPE-2 datasets for site A07_Pillow. a) LWAC colour image of the outcrop face (21.5 x 28 cm ColorChecker© for scale), showing ROI targets (footprint not to scale) and HRC footprint E; b) AUPE-2 R spectra and corresponding field spectra (grey); c) PCA image (R =PC1, G = PC2, B = PC3) highlighting glass-rich quench rinds (green) and zeolite veins and nodules (yellow); d) LWAC spectral parameter image of the narrowband red:blue ratio (R671/438) showing the distribution of fine mineral veins throughout the outcrop; e) HRC image of the altered pillow cross-sections and cross-cutting zeolite mineral veins. Black boxes in d) and e) indicate the location of the ColorChecker©.*

Spectrally, ROI A07_001 from the high-albedo nodule shows the highest reflectance and the steepest visible slope (figure 3.7b) in the *in-situ* reflectance spectra. The emplacement of this deposit as secondary mineral veins, together with its high albedo and featureless spectral profile, suggests these veins likely comprise of either low temperature phases such as gypsum, zeolite, calcite or opaline silica, or higher temperature phases such as quartz. It is not possible to distinguish between these minerals from AUPE-2 multispectral data, due to the lack of absorption features within the PanCam spectral range of 440 – 1000 nm for these minerals. The R* spectral profile of this ROI agrees with the *in-situ* reflectance spectra for the visible wavelengths only. The near-infrared (NIR) part of the R* spectrum shows a deep skewed absorption from 832 to 1000 nm centred at 950 nm, which is inconsistent with the *in-situ* reflectance spectrum (figure 3.7b). The other three ROI's are measured from the pillow core interior unit (A07_003 and 004) and dark quench rind (A07_002). These are all low albedo, with a slight positive slope in the visible portion of the R* spectra and slight negative slopes in the NIR (figure 3.7b). These three are consistent (within error bars) with the corresponding *in situ* spectrometer data up to 950nm. The slight positive slope in these three AUPE-2 R* spectra from 950 to 1000 nm are not supported by the *in situ* reflectance spectra. A discrepancy at these bands is prevalent throughout the AUPE-2 dataset and is discussed more fully in section 3.5.1.

Bulk mineralogy of ROI samples determined through XRD analysis and VNIR laboratory spectra shows the altered surface of the pillow basalt outcrop to comprise of nontronite, goethite, and ferrihydrite. Basalt vesicles are infilled with zeolite amygdales, presumably originating from the same hydrothermal fluids that precipitated the mineral veins. These amygdales are not identifiable in the WAC or HRC datasets due to their small size (< 3 mm), despite their prevalence throughout the outcrop. The zeolites do however influence the laboratory reflectance spectra measured from the powdered and homogenised ROI subsamples, producing (or at least strengthening) the O-H and H_2O absorptions at 1.4 and 1.9 μm, increasing overall albedo, and producing a weak Fe^{2+} absorption at 490 nm in all samples (figure 3.4).

3.4.4: A08_Veins

A 3 x 1 LWAC panorama was acquired at this site, from a distance of 2.90 m. The region comprises exposed mineral veins surrounded by unconsolidated alteration soils (figure 3.3d). From the LWAC colour panorama, three distinct units can be identified: a structured dark red unit intercalated with higher-albedo linear ridges, a brown soil unit, and finally bright-toned alteration soils (figure 3.8a). The red:blue ratio (R671/438) spectral parameter image (figure 3.8c) highlights the spectral variety present across the whole scene. The high albedo mineral vein ridges visible within the dark red unit are positioned prominently above the surrounding unconsolidated dark-red soils. Conversely the bright-toned alteration soils to the right of the image form a distinctive 'stripe', but no structural prominence. AUPE-2 R* spectra taken from the structured dark red and brown soil units agree well in the visible with the corresponding *in-situ* reflectance spectra (figure 3.8b), but the infrared portion shows disagreement beyond 740 nm. *In-situ* reflectance spectra from ROI's A08_003, A08_004 and A08_005 within the brown soil unit all show similar features including a slope increase between 530 and 550 nm, and a very broad absorption centred at 870 nm. These features are captured by the AUPE-2 multispectral data. ROIs A08_001 and A08_002 from the high albedo mineral vein ridges and surrounding soil respectively have a featureless *in-situ* reflectance spectra, with a long shallow positive slope in the visible levelling out to a flat slope in the infrared (figure 3.8b). The corresponding R* spectra show a steeper visible slope for A08_001 and an absorption centred at 832 nm followed by a steeply negative slope from 950 - 1000 nm. This last feature is again unique to the R* spectra. AUPE-2 R* A08_001 and A08_003 also both deviate from the *in-situ* spectral measurements in the visible at 440 nm outside of the error bars. Both measurements however, do match the laboratory spectra suggesting that the *in-situ* measurements have been contaminated by dust in the field. False colour (figure 3.9a) and spectral parameter (figure 3.9b) images highlight the bright-toned mineral veins within the dark red unit, showing them to be spectrally distinct from the surrounding soils and forming long, structurally-competent deposits. HRC mosaics (figures 3.9c and 3.9d) of these features reveal the undulating morphology of these veins. Surface weathering can be seen on the exposed surfaces of the mineral veins, which has resulted in semi-rounded fragments of the deposit lying at the base of the vein (figure 3.9d). These loose fragments are also clearly picked out in the false colour image (figure 3.9a). Unlike the high-albedo cross-cutting mineral veins in the pillow basalt outcrop (A07_Pillow), these larger, more prominent veins are comprised of gypsum, as confirmed by both the laboratory VNIR spectroscopy and the XRD results. The surrounding unconsolidated altered soils are broadly similar in mineralogical composition to the soils at Site A04_Tuff, being characterised

by smectite clays and iron oxides (montmorillonite and goethite at A04_Tuff; montmorillonite and hematite at A08_Vein). The exception to this is that the soils at this site also contain gypsum, most likely weathered out from the surrounding veins.

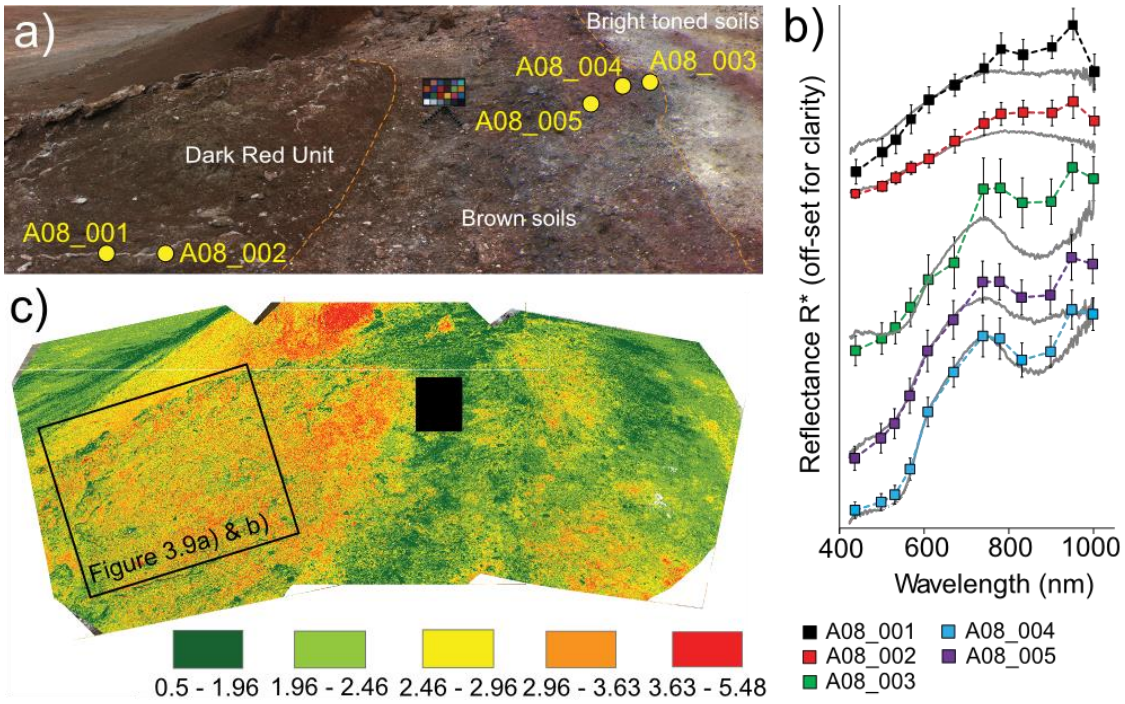

Figure 3.8. AUPE-2 datasets for site A08_Vein. a) LWAC colour panorama (21.5 x 28 cm ColorChecker© for scale) showing spectral units and ROI targets (footprints not to scale); b) AUPE-2 R spectra of the two main spectral units and corresponding field spectra (grey); c) LWAC spectral parameter panorama of the narrowband red:blue ratio (R671/438), box inset shows footprint of Figures 3.9a) and b). The black box in c) indicates the location of the ColorChecker©.*

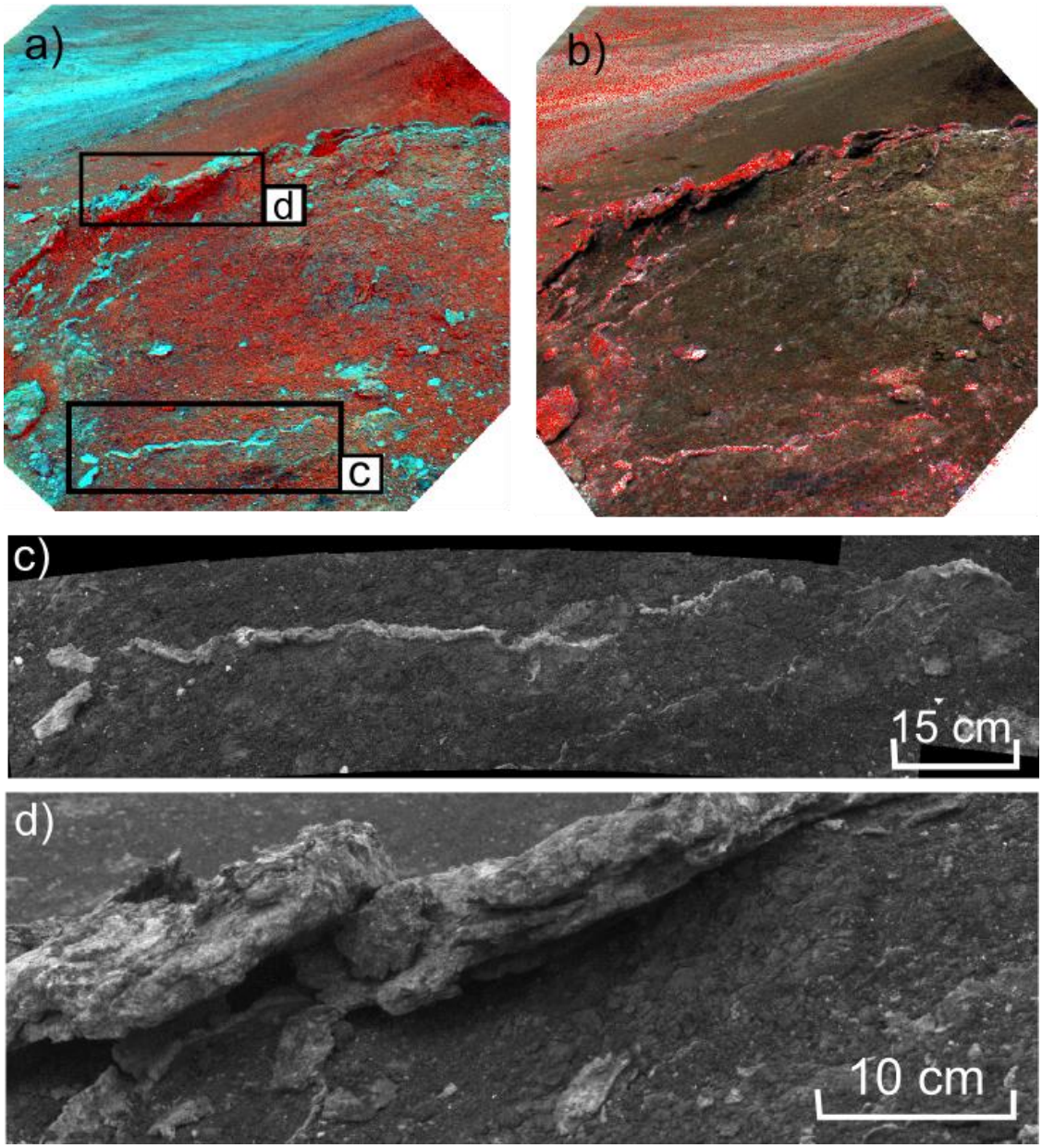

Figure 3.9: AUPE-2 datasets for site A08_Vein. a) False colour image (R = R/B ratio, G = R, B = G) showing distribution of mineral veins in the dark red unit; b) LWAC spectral parameter image of the green slope (S532_610) minus the blue to red slope (S438_671) highlighting the mineral veins; c) and d) HRC monochrome mosaics of mineral veins, arrow shows a mineral vein fragment that has been weathered out of the original vein.

3.4.5: Principal Components Analysis results

Principal Components Analysis (PCA) was performed on the 19 ROI spectra extracted from the AUPE-2 multispectral images of the four target areas. By treating these data as a single dataset it was possible to identify spectral groupings across the whole region. 99% of the PCA variance was contained within the first three principal components (91.19%, 5.88% and 1.74% respectively). By plotting these three principal components against each other a

number of clusters were identified, including the A04_Tuff grey slab unit ROIs and the A07_Pillow basalt ROIs. ROIs containing high amounts of gypsum (ROI A08_001) and sulfur (ROIs A06_002 and A06_004) appear as outliers in the PCA plots (figure 3.10) and are distinct from both the volcaniclastic/basaltic lithologies and the iron and phyllosilicate-bearing alteration soils. All gypsum containing ROIs are clustered within a single quadrant of both PCA plots. This finding corresponds well with recent work by Farrand et al. (2014) who found that gypsum veins on Cape York imaged by Opportunity proved spectrally distinct from other identified rock classes.

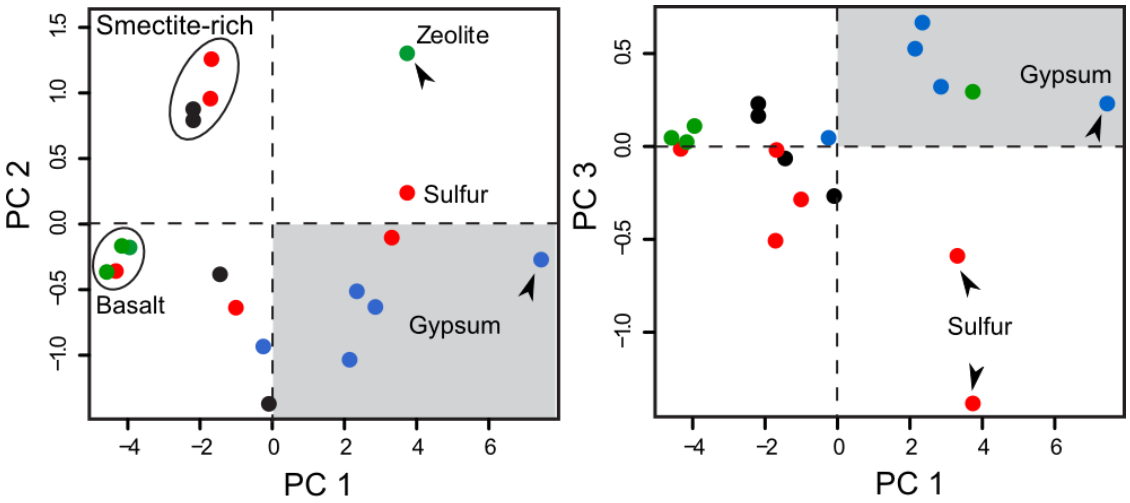

Figure 3.10: Principal Component Analysis plots showing the groupings of spectral classes as observed with AUPE-2 R data. Vertical lines divide Fe-oxide bearing targets from high albedo non-Fe oxide targets including gypsum, zeolite, and sulfur. Horizontal lines further define the quadrant for which all gypsum-bearing targets fall within (grey box). Plots include all ROIs from sites A04_Tuff (black), A06_Soils (red), A07_Pillow (green), and A08_Vein (blue).*

3.5: Discussion of results

3.5.1: Data quality and issues

3.5.1.1: NIR/RWAC spectral discrepancies

The most apparent potential flaw in the AUPE-2 multispectral data are the discrepancies between extracted R* spectra derived from the multispectral image cube acquired with the WAC geology filters and the ground-truth *in-situ* reflectance spectra (figure 3.11). Discrepancies in albedo alone between AUPE-2 R* and *in-situ* relative reflectance spectra are caused by differences in the viewing geometry between the two instruments. The AUPE-2 system viewed the ground plane at large angles, and the topography of the ground on the

decimetre scale meant that regions of interest could vary from normal incidence to almost tangential to the camera axis. In contrast the integrating sphere contact probe on the Jaz field spectrometer was placed on the surface so that the measurements were always taken at 8°. At large angles most surfaces depart significantly from Lambertian behaviour and so differences in albedo are observed in the two measurements. Without knowing the bidirectional scattering distribution of the objects in each scene it is impossible to calculate absolute reflectance values, and so the values presented for all spectral measurements here are relative reflectance values. In every case either the incidence or emission angle of the AUPE-2 R* data are different from the corresponding *in-situ* spectral measurements and so a perfect match in albedo of the coincident datasets is not to be expected.

Although a perfect match in albedo is not to be expected between the AUPE-2 spectra and the *in-situ* relative reflectance spectra it would be expected that the general spectral shapes should match. Comparisons of the two datasets once they have been scaled to match albedo at 440 nm (figure 3.11) show that there are a number of significant discrepancies in overall shape and in particular the location of absorption features. The majority of these spectral discrepancies are in the NIR and particularly at the 950 and 1000 nm filters, often producing erroneous slopes in the AUPE-2 spectra that are not present in the field spectrometer data. The *in-situ* field spectrometer results are broadly consistent with the laboratory VNIR spectra taken from the intact original surfaces of the ROI samples, confirming their validity. Therefore the observed spectral discrepancies between AUPE-2 R* spectra and the ground-truth spectra are inferred to be genuine artefacts of the AUPE-2 system. Due to this none of the NIR spectral parameters listed in table 3.3 have been used in this study.

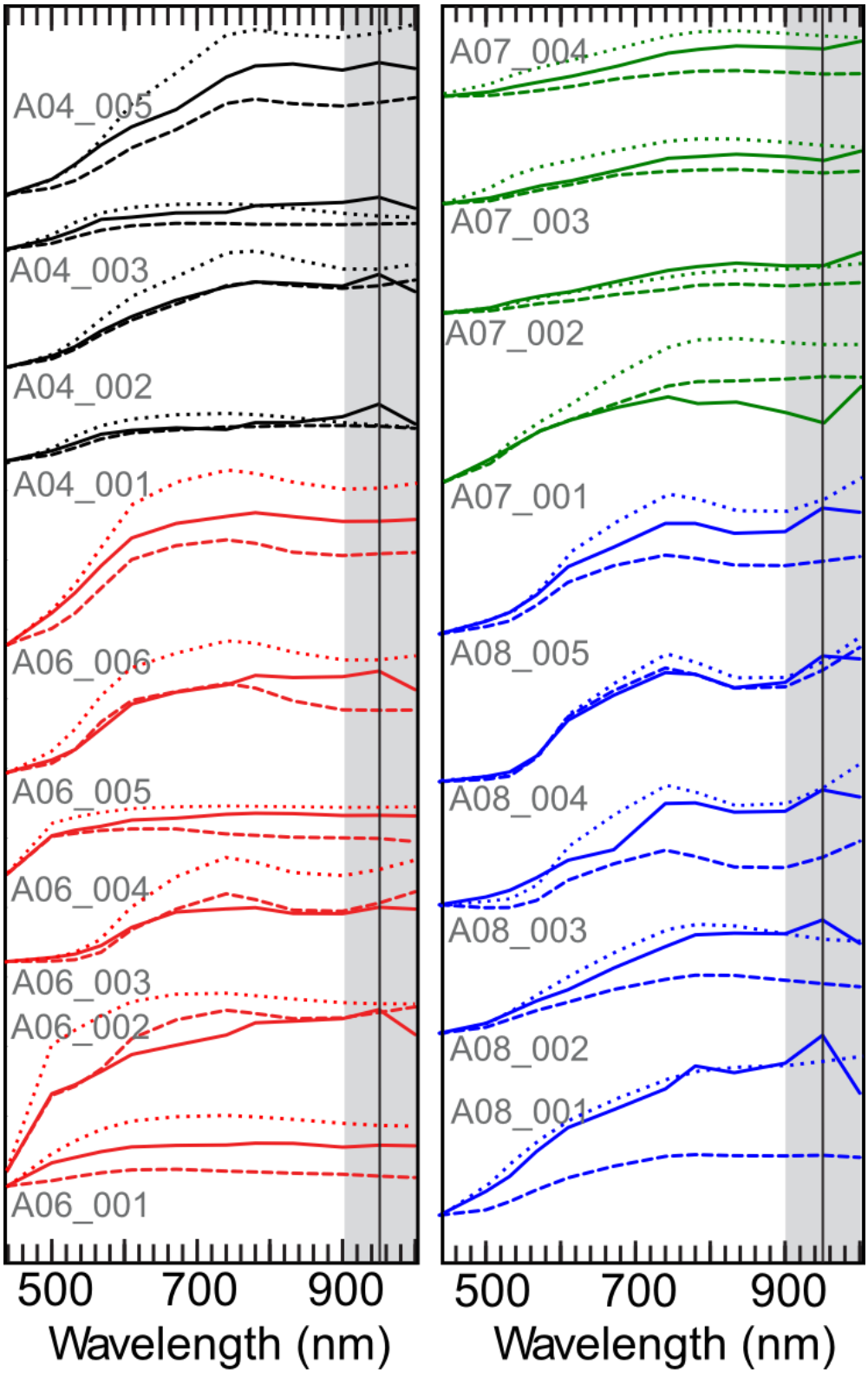

Figure 3.11: Comparison of AUPE-2 R spectra (solid line) with in-situ field spectrometer ROI measurements (dashed lines) and the ASD laboratory spectra (dotted lines) both resampled to AUPE-2 spectral bands. Solid vertical line represents the centre wavelength of the AUPE-2 950 nm filter, and grey region highlights the NIR region where hydration absorption features would be found (Rice et al., 2010).*

3.5.1.2: NIR/RWAC image artefacts

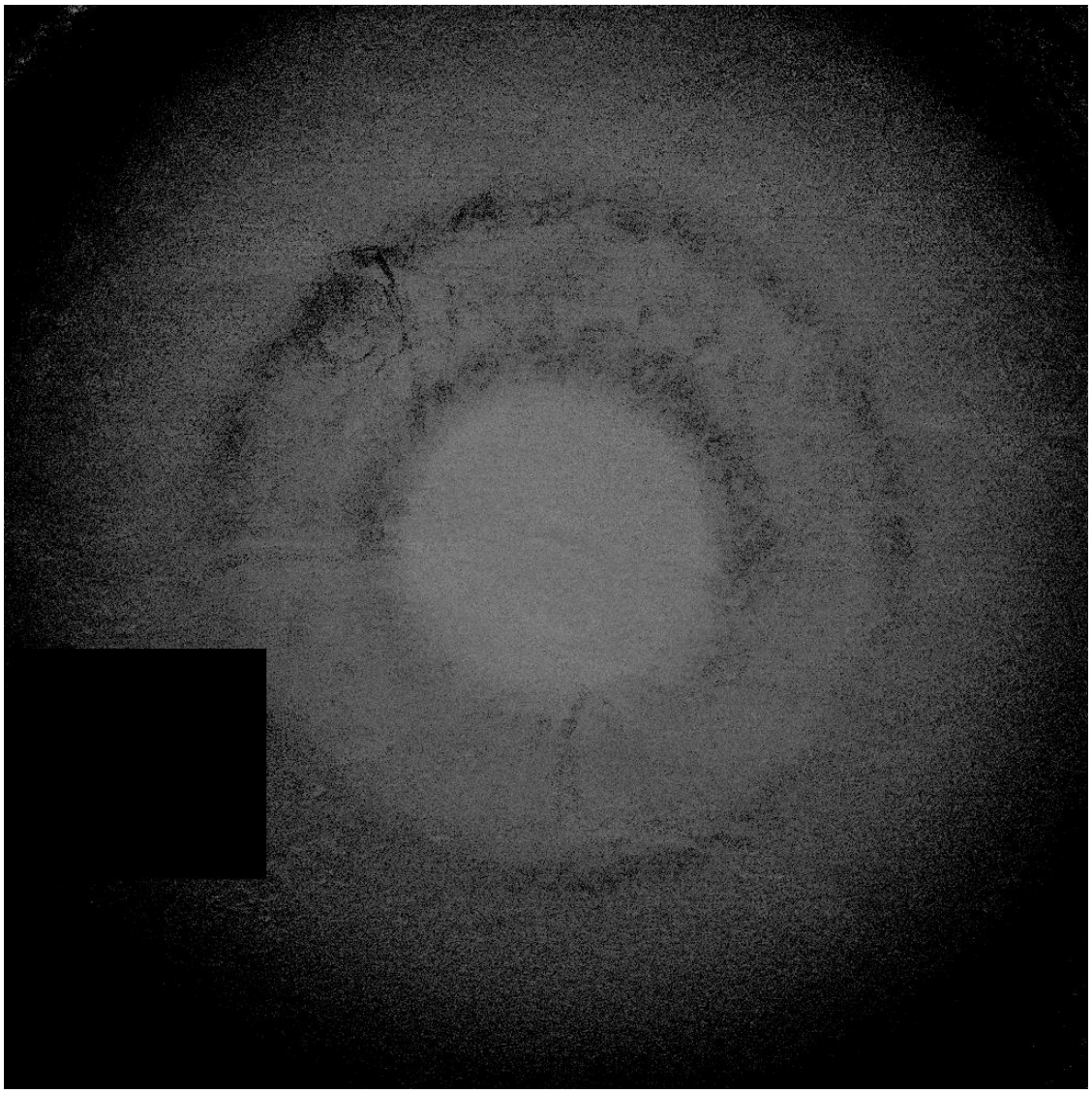

Figure 3.12: BD950 spectral parameter image from site A07_Pillow calculated using the 950 and 1000 nm filter images showing prominent concentric circle artefacts caused by internal scattering within the WAC optics. The black box indicates the location of the ColorChecker©. The same pattern is seen in all spectral parameter images calculated using the NIR/RWAC narrowband filters to a greater or lesser extent. The pattern can also be seen in the individual NIR/RWAC images but is not as pronounced.

Non-albedo differences are most evident in the NIR filters, with consistently unreliable R* values extracted from the 950 and 1000 nm multispectral data which often produced a false 'absorption' at either 950 or 1000 nm (figure 3.11). Images taken with some NIR filters (780 to 1000 nm) showed concentric artefacts which contributed to the errors in data points at these wavelengths (figure 3.12). The concentric artefacts were more prominent the longer

the filter wavelength. These artefacts are ghost images produced within the WACs optics due to a combination of the stray light performance of the lenses and the mechanism by which the light enters the optical system[†] (Dr M. Gunn, personal communication). The loss of data from the NIR end of the spectral range available to AUPE-2 (and therefore potentially the ExoMars PanCam) is of particular importance due to the location of the H_2O and O-H absorption bands around 950 nm (Rice et al., 2010). Given the utility of the 950 - 1000 nm absorption slope band parameter in identifying hydrated mineral species and mapping their distribution across a scene (Rice et al., 2010; Vaniman et al., 2014), it is imperative that this issue is resolved in the final flight-ready version of PanCam.

3.5.1.3: Stereo field-of-view (FoV) limitations

The WACs are separated by a distance of 50 cm laterally along the optical bench, to allow the acquisition of stereo images and subsequent 3D rendering of a target. However, while this provides vital structural information, this means that the two WACs are not viewing exactly the same scene - there are regions in the LWAC FoV that do not fall within the RWAC FoV and *vice versa*. This is an issue that has been faced by all stereo cameras on previous rover missions, however in the case of the ExoMars PanCam, this baseline separation of the WACs is significantly higher: 50 cm compared to 30 cm used for the MER Pancam (Bell III et al., 2003). In addition, slight vignetting from the multispectral narrowband filters in the AUPE-2 system leads to unusable data in the corners once the images have been converted into R* values (*e.g.* figure 3.6d and 3.6e). This vignetting will not be an issue for the ExoMars PanCam due to differences in the filter and camera detector design. The final percentage of the scene that is covered by both WACs and gives usable, calibrated multispectral reflectance data is approximately 85%, although this varies with target distance. The use of multiple frames to build up a panorama can go some way to alleviating this lack of overlap.

3.5.1.4: AUPE-2 vs ExoMars PanCam

AUPE-2 data were collected as 8-bit images. The final ExoMars PanCam will collect 10-bit images. The ExoMars PanCam data will therefore have a higher level of sensitivity than the AUPE-2 data presented in this Chapter. With respect to the ROI data presented here however any differences due to bit depth will be negligible when compared to the level of standard deviation within an ROI due to the averaging over numerous pixels. In the case where individual pixels are processed, i.e. when creating and interpreting Spectral Parameter

[†] For a fuller explanation of the cause of these concentric artefacts see Harris et al. (2015). The explanation provided in this paper was the result of work performed by M. Gunn and R. Cross at the University of Aberystwyth.

images, this difference in sensitivity may become apparent with subtler variations in band depth and slope becoming clearer. However it is equally possible that the extra sensitivity will just introduce more noise in the imagery. Even with the Spectral Parameter images a single pixel would never be taken as evidence of the presence of a particular feature and its neighbours would always be considered. In this way erroneous outliers are ignored and therefore the slight difference in sensitivity brought about due to pixel depth differences between AUPE-2 and the ExoMars PanCam are moot.

The major difference between AUPE-2 and the ExoMars PanCam is in the internal geometry of the camera and the optical design of the lenses. It is this difference that is thought to be responsible for the stray light artefacts evident in the NIR filter images. This is an issue that was outwith the scope of this piece of work but that shall be investigated more thoroughly once a breadboard model of the ExoMars PanCam becomes available.

3.5.2: Deduction of hydrothermal alteration and environmental type

Full suites of AUPE-2 data were collected from four discrete sites within a 1 km^2 region. Each of the four sites showed unique structural or mineralogical features demonstrating the level of variation that can be found over small (centimetres to tens of metres) spatial scales. In particular the mineral variation was on a spatial scale (< m's) that would be below that of orbiting instruments such as CRISM (see Chapter 6 for fuller explanation and discussion of CRISM). The engineering constraints on PanCam limit both the spectral range and resolution. Whilst research has been undertaken to identify the most efficient and flexible combination of narrowband 'geology' filters for hydrated mineral terrains (Cousins et al., 2012), subtle spectral features are inevitably missed and definitive identification of unique minerals is rarely achievable with the PanCam wavelength range alone. However, even within this constraint it is still possible to identify some of the key minerals in this environmental type, including sulfur and iron-oxides, based on AUPE-2 data multispectral imagery alone. The use of statistical clustering techniques such as PCA demonstrates that spectral units can be identified across distinct sites allowing for a wider geological interpretation of the entire region in addition to that of each individual target site. The HRC imagery proved invaluable in detecting key small-scale textural features. This was especially important in identifying the gypsum veins seen at site A08_Veins. The gypsum spectral signature is not uniquely identifiable in the PanCam wavelength range but a hydrated band is in theory detectable with these filters (see section 3.5.1.2 for discussion of why this hydration absorption at ~950 – 1000 nm was not found). The key component that allowed the identification of these veins

was the high resolution HRC images that exposed their millimetre scale texture. Together with the colour imagery and the spectral data this enabled a positive and accurate identification. The WAC multispectral data also revealed some structural features not immediately obvious in the RGB images. In particular the centimetre-scale layers seen in the grey slab units at site A04_Tuff were obscured in shadow in the RGB image but became clear in the R671/438 spectral parameter image. Such sedimentary layers are an important target for Mars surface exploration having been identified at Gale Crater by MSL *Curiosity* as part of a putative past hydrated environment (Grotzinger et al., 2014). In the Námafjall dataset these layers, when viewed in the mineralogical and larger scale structural context point towards a period of hydrovolcanism in the regions history.

AUPE-2 (and PanCam) can acquire a range of data all of which can be used to provide a wealth of spatially-resolved geological information at scales of centimetres to tens or even hundreds of metres. When taken together these data can be used to identify a hydrothermally altered environment such as the one investigated at Námafjall.

3.6: Future work

This field campaign has demonstrated the ability of PanCam to positively identify a hydrothermally altered environment; however this is just one environmental type that may be encountered in the search for habitability on Mars. Further field tests in different types of environment are required. These further field trial locations should be chosen to reflect the four shortlisted ExoMars landing sites, all of which are concentrated on Noachian aged terrains with significant phyllosilicate deposits and potential sedimentary layers (Loizeau et al., 2015). The problems with the NIR filters and the internal optical scattering must be addressed by the instrument engineers to ensure the same issue does not hamper the final flight-ready version of PanCam. Further analysis techniques should be explored including (but not limited to) Spectral Mixture Analysis (Farrand et al., 2013; Parente et al., 2009, and Chapters 5 - 7 of this thesis) and hierarchical clustering (Farrand et al., 2014, 2013).

3.7: Summary

This Chapter detailed the deployment of an ExoMars PanCam emulator at a hydrothermally altered glaciovolcanic site in Iceland. The spectral data collected by AUPE-2 was validated against *in-situ* reflectance spectra and the in scene mineralogical identifications verified with rock and soil samples. Using the entire AUPE-2 data suite it was possible through the use of RGB composites, Principal Components Analysis, spectral parameters and ROI spot spectra to accurately deduce the environmental and geological history of the region investigated. This work is the first time an ExoMars PanCam emulator has been deployed in this type of

environment, and the first time the final 'geology' filter set has been field trialled in any setting. A serious image artefact affecting the NIR geology filters was discovered hampering the detection of some key spectral features including the hydration absorption band at 950 – 1000 nm. It is thought this flaw is a flaw in the prototype and will not affect the final flight-ready model but this remains to be established. The limitations of the spectral resolution and the utility of the high spatial resolution of the imagery were discussed.

Chapter 4: Spatial scale, sub-pixel information and Spectral Mixture Analysis

4.1: Introduction

This Chapter shall introduce the concept of Spectral Mixture Analysis (SMA), discussing the historical and state-of-the-art algorithms that have been developed, the current limitations and unanswered questions regarding the applicability of the technique and previous applications of SMA to martian studies. The need for a method that can extract details from orbital VNIR images at a sub-pixel level is laid out with emphasis on the importance of this method being as accessible as possible to the planetary science community who may not have the necessary time and/or expertise to write their own algorithms or have access to proprietary software and programs.

4.2: Issues of spatial scale in spectral analysis on Earth and Mars

Mineralogical data for the surface of Mars are primarily collected through satellite spectroscopy in the visible and near infra-red (VNIR) through to the thermal infra-red. Whilst rovers and landers have been equipped with other instruments that are capable of definitive classifications of mm/cm-scale features, these are severely restricted in the amount of the surface they can cover. Satellite coverage of the planet on the other hand, covers the entire surface at various spatial and spectral scales. These scales place major restrictions on the level of structural and compositional detail achievable with these orbiting instruments. Whilst grey scale and three band colour (blue/green – red - infrared) images are being returned with spatial resolutions as high as ~0.3 m^2 (McEwen et al., 2007) by HiRISE on the Mars Reconnaissance Orbiter (MRO), hyperspectral VNIR data is routinely limited to 15 – 19 m^2 pixels at best (Murchie et al., 2007) via the CRISM instrument, also on MRO. The HiRISE images confirm that there are features and geological units on the surface of the planet at a spatial scale obscured within the hyperspectral data pixels in regions unexplored by ground-based instruments. The mineralogical make-up of the surface at this scale could provide the key piece of evidence for correctly characterising various habitable palaeoenvironments postulated to have once existed on Mars. What is needed is a method for extracting sub-pixel information from these hyperspectral images. This is especially crucial in areas which have potentially been hydrothermally active, where the tell-tale mineral alterations can be on the scale of metres or even less.

Spectral remote sensing has been used to create land cover classification maps for decades here on Earth since the launch of the first Landsat satellite (Nalepka et al., 1971). This is

based on using spectral signatures within the image pixels to identify the materials on the ground. These spectra are then interpreted using the assumption that each pixels worth of ground cover is composed of only one material, a so-called “pure” pixel, and the reflectance radiation detected by the instrument has not interacted with any other material once it has left the surface. This frequently erroneous or at least over-simplified assumption has not prevented reasonably accurate and useful composition maps from being produced from instruments collecting data with only a small number of discrete and broad wavelength bands (Campbell, 2006; Richards and Jia, 1999). A major disadvantage to these broadband multispectral instruments (such as in the long running NASA Landsat series of satellites) besides the often erroneous pure pixel assumption, is that such coarse spectra do not provide the necessary spectral resolution to differentiate between numerous target materials, especially in a mineralogical context (e.g. different types of phyllosilicate) regardless of the spatial resolution. With the introduction of hyperspectral imagers, i.e. imaging spectrometers with hundreds of narrow contiguous bands, such spectral features are now detectable, and if the spatial resolution is good enough to provide pure pixels these can be definitively mapped. If however the spatial resolution is larger than the spatial variance scale of the surface being imaged these subtle spectral features can be swamped or masked and the ability to break a spectral signature into its constituent spectra becomes desirable (Keshava and Mustard, 2002).

4.3: Spectral Mixture Analysis

Spectral Mixture Analysis (SMA) is the general term used to describe the many methods, techniques and algorithms that have been, and are still being, developed to extract sub-pixel spectral information from hyperspectral data (Keshava and Mustard, 2002). This information includes the number of individual materials present in the scene (‘endmembers’ as they shall be referred to for the remainder of this thesis), the spectral signature of each of these endmembers and the abundance of each in every individual pixel.

There are two general theories to how spectra can be mixed within the area covered by a pixel; linearly or non-linearly. The first (and most mathematically and physically simple) is linear mixing. This assumes that the mixing of the reflected radiance from each material happens at the detector and therefore each surface material is spatially distinct from the others as shown in figure 4.1.

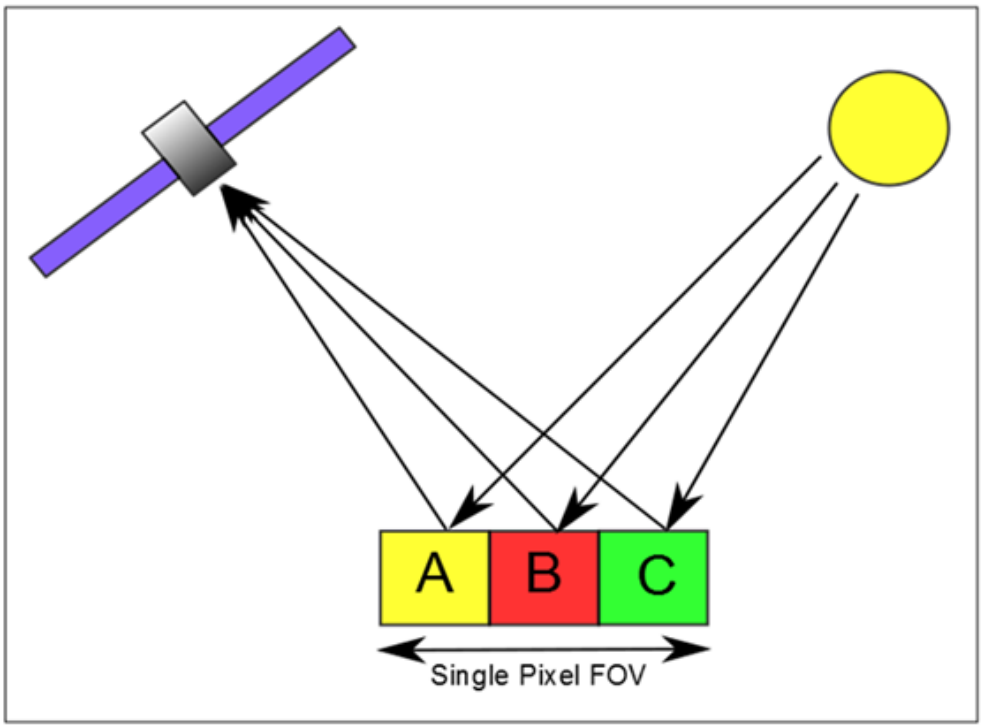

Figure 4.1: Linear spectral mixture model, three materials (endmembers) within the pixel field-of-view (FoV) illuminated by the sun and detected by a satellite. The spectra of each endmember remains distinct from the others until it reaches the detector at which point they are mixed together to form a single signal. The detector pixel spectrum is therefore linearly related to that of the three endmembers and their relative abundances within the pixel.

The final spectrum **x** is therefore a linear mixture of the spectral endmember from each material covered by the pixel and can be expressed as

$$\boldsymbol{x} = \sum_{i=1}^{p} a_i \boldsymbol{r}_i + \boldsymbol{\varepsilon} = \boldsymbol{R}\boldsymbol{a} + \boldsymbol{\varepsilon} \tag{4.1}$$

Where **x** is the L x 1 pixel spectrum vector with L spectral bands, **R** is the L x p matrix whose columns are the L x 1 pixel endmember spectra ($\mathbf{r}_i$ where i=1,…,p) and p is the number of endmembers, **a** is the p x 1 vector whose entries a_i (i=1,…,p) are the abundances of the endmembers and **ε** is the L x 1 noise vector encompassing all the additive noise inherent in the observation from both the environment and the detector itself. This theory assumes that each endmember is spatially distinct from the others and that there is no multiple scattering of radiation between the endmember materials. To make the linear mixture model physically meaningful two constraints must be applied to the inverse unmixing. The first is the abundance non-negativity constraint (ANC) which requires that $a_i \geq 0$, the second is the abundance sum-to-one constraint (ASC) that requires $\sum_{i=1}^{p} a_i = 1$.

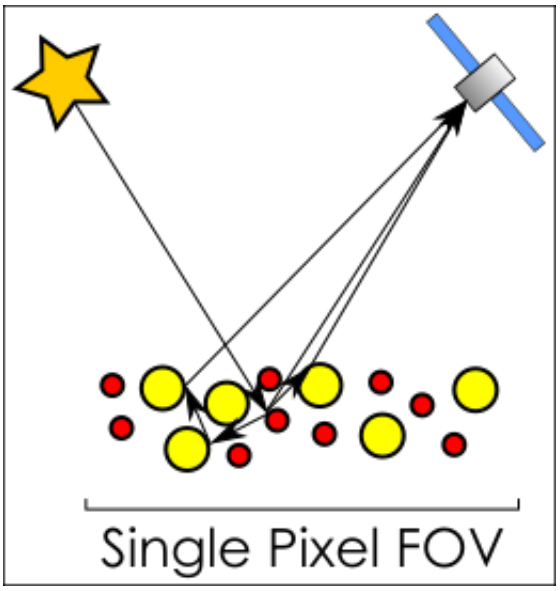

Figure 4.2: Intimate/non-linear spectral mixing scenario with two intimately mixed endmember particles (red and yellow). The incoming radiation interacts with both endmembers potentially multiple times before it is reflected back to the sensor.

The materials that constitute the pixel however may not be clearly separate from each other and may be more intimately mixed or consist of a number of layers of different materials. This is almost certainly the case in geological scenes where mixed soils and sedimentary layers are a common occurrence. In these cases a non-linear mixing model must be considered that can take into account possible multiple scatterings and spectral mixing prior to the radiation reaching the detector (figure 4.2). This is a much more complicated scenario that can involve an infinite number sequence of powers of products of reflectances (Borel and Gerstl, 1994). A number of models have been created to try and deal with the more realistic non-linear mixture model, however for the majority of real cases the far simpler linear mixture model is considered an acceptable approximation (Bioucas-Dias et al., 2012). Various non-linear approaches have included using Radiative Transfer Theory to model the interaction of photons with the particles in the pixel (Hapke, 2012; Shkuratov et al., 1999). This however is an incredibly complex problem that requires knowing numerous properties of the materials in the scene that are frequently either unconstrainable or unknowable in practice. Even if all the necessary data is available the computational cost of performing this calculation across an entire scene is prohibitive. Other techniques that are gaining increased attention include using machine learning neural networks (Licciardi and Del Frate, 2011) and kernel methods (Broadwater et al., 2009) to bring down the computational cost of non-linear models.

Detection of the type of endmember mixture in a pixel (i.e. linear or non-linear and if the latter which non-linear model) is an obvious issue that has had little attention, with most authors choosing to assume a specific mixing model prior to analysis based on *a priori* knowledge of the data in question, computational and temporal contraints and an acknowledgement that some errors are expected as a result of this assumption. The exact quantification of the level of error introduced through the common use of a linear model on data that may be at least partially non-linear is not fully quantified in the literature with different authors reporting different values depending on the scene in question. The Polynomial Post-Nonlinear Model (PPNM) of Altmann et al. (2013b) and the Kernelised Fully Constrained Least Squared (KFCLLS) algorithm of Broadwater and Banerjee (2011) have both been put forward as methods for identifying nonlinearly mixed pixels within a scene but only if the mixing within those pixels is best modelled by the relevant mixture model presented. Identification of mixture type is still a challenge to be solved.

Regardless of the mixture model that best represents a specific spectral mixture there are three main steps in the spectral unmixing pipeline; 1) establish the number of endmembers present in the dataset, 2) establish the spectral signature of each endmember and 3) calculate the amount of each endmember present in each pixel. Each of these steps represents a unique problem for which numerous algorithms have been developed, although a number of the algorithms that will be discussed in the following sections combine steps 2 and 3.

In the case of a geological scene and in particular a hydrothermally altered environment each of these steps is a non-trivial problem for a number of reasons including: i) textural differences within a single mineral can result in spectral differences, ii) spectral similarities between chemically similar minerals can make discrimination difficult, and iii) noise must be differentiated from signal even if the SNR is low.

4.3.1: How many endmembers are present?

The first step in the unmixing chain is to estimate p, the number of endmembers present. Identifying the number of land cover classes present in a scene is a common problem encountered when creating classification maps with remote sensing imagery (Campbell, 2006). Common solutions are to use Maximum Noise Fraction transformation (MNF) (Green et al., 1988) or Principal Components Analysis (PCA) (Smith et al., 1985) to reproject the data into an eigenvector space where the noise and signal can be separated out as specific bands in the transformed dataset. However, neither of these algorithms identifies the underlying

number of endmembers, merely the minimum number of bands in the transformed MNF or PCA space required to capture the non-noise related variation present.

A number of different algorithms to estimate this subspace dimensionality in mixed signals have been developed over the years in different disciplines and applications. Examples of algorithms developed specifically for application to hyperspectral images include the Harsanyi-Farrand-Chang (HFC) method, Hyperspectral Signal Subspace Identification by Minimum Error (HySIME), Eigenvalue Likelihood Maximization (ELM) and Outlier Detection Methods (ODM). The Harsanyi-Farrand-Chang (HFC) method (Chang and Du, 2004) based on Neyman-Pearson threshold detection statistics and also referred to in the literature as Virtual Dimensionality (VD). This algorithm generates eigenvalues from the image correlation and covariance matrices. The number of eigenvalues from each is equal to the spectral dimensionality of the dataset. The eigenvalues can therefore be used as an alternative dimension space. If there is only noise contained in a particular component then the corresponding correlation and covariance eigenvalues should be equal to each other. A Neyman-Pearson test is then applied to test the similarity within an operator defined threshold, the number of times the test fails across the dataset is taken as the number of endmembers present, or the Virtual Dimensionality of the image. The Hyperspectral Signal Subspace Identification by Minimum Error (HySIME) algorithm (Bioucas-Dias and Nascimento, 2008) is an unsupervised eigen decomposition method that runs automatically without the need for any tuning parameters, unlike the HFC method. HySIME first estimates the signal and noise correlation matrices of a dataset. A least-squared minimum error threshold method is then used to select the eigenvectors from these matrices that best represent the signal subspace or number of endmembers present. The authors of HySIME use a multiple regression theory-based method for estimating the noise within the image dataset however this is not prescriptive and the method for performing the noise estimation step is at the discretion of the analyst. The Eigenvalue Likelihood Maximization (ELM) algorithm (Luo et al., 2013) uses the distribution of the eigenvalues of the correlation and covariance matrices of the signal data and their differences. In a similar manner to the HFC algorithm the ELM compares the corresponding correlation and covariance eigenvalues from each data point in an image. If these are identical then they are considered to be representing only noise. If the correlation matrix eigenvalue is larger than the corresponding eigenvalue from the covariance matrix then it is taken as representing an actual signal. The total number of eigenvalue pairs that meet this second description gives the image endmember dimensionality. Unlike the HFC this algorithm is parameter free and therefore can be run as

an unsupervised method. The Outlier Detection Methods (ODM) (Andreou and Karathanassi, 2014) is a recently developed method that is based on the idea that the bulk of an image is noise and any outliers are the actual signal. It is made up of three steps. Firstly as with HySIME the noise in the image matrix is estimated. Following this the data is transformed into a noise-whitened subspace. Now that the data is in a noise defined transformation outliers representing non-noise signal can be identified using interquartile range (IQR) outlier detection methods. The number of outliers identified represented the signal dimensionality and the number of endmembers in the image scene. ELM and HFC both assume the spectral mixture is linear. HySIME and ODM make no such explicit assumption and the authors of HySIME specifically mention that it should work just as well on linear or non-linear mixtures.

4.3.2: What are the endmember spectra?

Once the number of endmembers has been determined, either through the use of an EDA such as the ones detailed in section 4.3.1, through prior knowledge of the scene or through use of an accompanying higher resolution image, the next step is to establish the spectral signature of each endmember. Assuming that no ground-based, *in situ* spectra exist for the scene in question there are two major methods for this. The existence of extensive spectral libraries have lead some analysts to use these data as image endmembers (e.g. Goudge et al., 2015), selecting the best fit spectral library spectra for a mixture based on a specified mixture model. There are a number of limitations to this approach. Firstly some *a priori* idea about the types of minerals present is needed. Secondly although basic absorption positions and major spectral features (e.g. the sharp blue slope of sulfur) should be present in both laboratory and *in situ* spectral measurements there can be significant differences in overall spectral shape and albedo across the spectrum. These differences between the laboratory spectra, normally taken from mineralogically pure, powdered and dried samples and the *in situ* spectra can be a result of textural variation (Clark, 1999), differences in incidence and emission angle (Hapke, 2012) and varying water content and other contaminants that can affect the overall spectral shape.

The alternative to using existing laboratory spectra is to extract the endmembers from within the image data themselves. The extraction of mixed signals from within a single dataset is a long-standing issue that has been the focus of much research within the signal processing community (Belouchrani and Amin, 1998; Belouchrani et al., 1997; Cao and Liu, 1996; Lee et al., 1997; Thi and Jutten, 1995). Over the years numerous different techniques specifically for extracting endmembers from within hyperspectral images have been developed. These differ in computational cost, basic theoretical underpinnings, and whether they are supervised or

unsupervised (i.e. whether they can be performed purely by an automated computer program or if operator intervention is required). Numerous review articles have been written covering the wide breadth of algorithms that have been developed, detailing their uses, complications and limitations (Bioucas-Dias et al., 2012; Dobigeon et al., 2014; Heylen et al., 2014; Keshava and Mustard, 2002; Plaza et al., 2011; Quintano et al., 2012; Somers et al., 2011) and the list of Endmember Extraction Algorithms (EEAs) is continually growing.

4.3.2.1: Endmember extraction from linear mixtures

One of the major groups of EEAs (and one of the oldest) are built around the assumption that for every endmember present in a scene there is at least one 'pure' pixel in the image. With a high enough spatial resolution for some types of environment this is not an unrealistic assumption. Orthogonal Subspace Projection (OSP) (Harsanyi and Chang, 1994), the Pixel Purity Index (PPI) (Boardman et al., 1995) and Vector Component Analysis (VCA) (Nascimento and Dias, 2005) are all based on the premise of reprojecting each spectrum in the dataset along new vectors and identifying the extreme pixels. In OSP and VCA the scene pixel vector with the maximum length within the initial projection space is identified as the first endmember, where the projection space has a dimensional size of the number of data points in each spectrum. The second endmember is then the image pixel with the maximum length when projected along the space orthogonal to the first. This process is iterated until the user specified number of endmembers required is reached. Others, mostly notably Chang and collaborators (Chang, 2005; Jiao et al., 2010) have continued to investigate this method and expand on its utility. The PPI is based on a similar premise but first runs the dataset through an MNF transformation to separate out the noise from the data and in doing so reduce the dimensionality and therefore the computational burden of the data. These data are then reprojected along random unit vectors n times with the pixels that fall on the extreme end of each vector noted. These "extreme" pixels are considered to be "pure" unmixed endmembers. This is not an unsupervised approach however, as at this stage the operator is required to identify the final set of endmembers (Quintano et al., 2012) from those suggested by the algorithm. PPI has become one of the classic techniques for endmember extraction thanks to its inclusion in the standard ENVI package. An unsupervised version of PPI was introduced in 2006 by Chang and Plaza (2006) which produces similar results to PPI but at a lower temporal cost. N-FINDR is another 'pure' pixels based method that works by calculating a volume space as opposed to the vectors calculated in the previous algorithms (Winter, 1999). The basic premise is based around finding the pixels in N[‡] spectral

[‡] where in this case N is the same as the variable L that is used throughout this thesis

dimensions that form the p number of vertices of a volume simplex with the maximum possible volume encompassing all the pixels (figure 4.3a). The algorithm starts by selecting a given number of random pixels to act as the initial set of endmembers. The volume that encompasses these pixels in the image projection space is calculated and each endmember replaced with another random pixel spectrum. The volume is calculated again and if it has increased that pixel replaces the initial endmember. This is repeated until the maximum volume is found. The N spectral dimensions are defined by the hyperspectral detector used and this can lead to a high dimensionality making this a computationally complex task. To bring down this cost dimension reducing transformations can be used to shrink the original datacube such as MNF or PCA (Plaza et al., 2011).

The assumption that there will be at least one spectrally pure pixel within an image corresponding to each endmember is not always realistic. This is particularly true in numerous geological environments including hydrothermally altered ones, and when dealing with the large spatial resolution data returned from Mars. There are a number of algorithms that have been developed to try and extract endmembers when the pure pixel assumption is violated. These algorithms are still founded upon the assumption of linear mixing. The most common approach of the non-pure pixel EEAs is based on the calculation of a bounding volume simplex around the scene dataset where the vertices of the simplex are the endmembers. This is similar to the approach used by pure pixel based algorithms such as N-FINDR, with the difference being that the vertices don't have to be existing spectra in the dataset (figure 4.3b). Algorithms based upon this premise include Minimum Volume Constrained Negative Matrix Factorization (MVC-NMF) (Miao and Qi, 2007), Simplex Identification via Split Augmented Lagrangian (SISAL) (Bioucas-Dias, 2009), Minimum Simplex Volume Analysis (MVSA) (Li and Bioucas-Dias, 2008; Li et al., 2015) and Robust Minimum Volume Enclosing Simplex (RMVES) (Ambikapathi et al., 2011). The primary difference between MVC-NMF and the other three algorithms mentioned is that the other three all allow violations of the positivity constraint in order to minimise the volume fit. Whilst this can lead to a smaller volume it has the down side of potentially introducing unreal values into the extracted endmembers. This is particularly an issue with noisy data. The main difference between SISAL, MVSA and RMVES is the mathematical method used to minimise the bounding simplex volume, with SISAL and MVSA using augmented Lagrange multipliers to solve a sequence of convex optimizations, and RMVES using quadratic programming solvers. The Iterated Constrained Endmembers (ICE) (Berman et al., 2004) and its updated version Sparsity Promoting Iterated Constrained Endmember detection (SPICE) (Zare and Gader,

2007) are based on a similar premise to those outlined above but rather than minimising the volume that contains all of the points, this pair of algorithms minimise the sum of the squared distances between the vertices. Bioucas-Dias et al (2012) found that MVC-NMF and SISAL performed better than the pure pixel based methods VCA and N-FINDR when mixed pixels were present. However neither was able to identify realistic endmembers in the case of an image composed entirely of highly mixed pixels, although both produce good results in the case of a dataset with truncated fractional abundances. Lin et al. (2015) investigated the accuracy of these minimum volume enclosing simplex (MVES) algorithms from a theoretical point-of-view and found that they all hold up well in the absence of pure pixels provided the mixing is not too heavy.

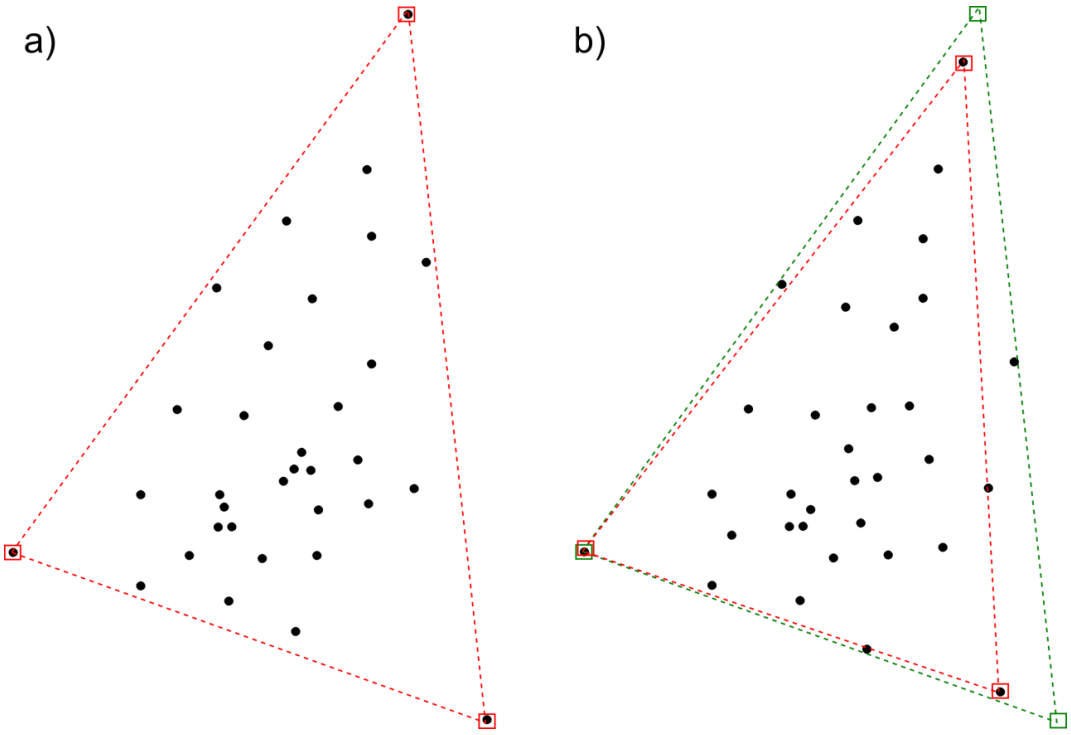

Figure 4.3: Examples of identifying endmembers from a simple linearly mixed 2D dataset with three endmembers. a) a pure pixel example, the black dots represent each pixel in the dataset, the red squares are the three extreme pixels that form the vertices of a bounding simplex encompassing all of the pixels in the image. b) an example this time without pure pixels, the red simplex that would be identified if the pure pixel assumption was enforced doesn't encompass all of the pixels, the green squares and the simplex formed by them does encompass all of the pixels but the vertices are not themselves existing points within the dataset.

4.3.2.2: Endmember extraction from non-linear mixtures

All of the EEA's discussed so far rely on the underlying assumption of a linear mixing model. The linear assumption in the MVES algorithms takes the form of straight edges between the endmember vertices. If non-linear mixing is present however, these edges may be better represented by convex (Close et al., 2012) or concave (Keshava and Mustard, 2002) lines. Attempts to integrate a non-linear mixing model to a pure pixel simplex volume algorithm have been recently presented by Heylen et al. (2011). This work demonstrated accurate results, provided there are pure pixels, through the use of curved space to account for the non-linear simplex edges.

Methods based on Bayesian statistics have been developed both to estimate a scene's endmembers and assign abundance fractions to them within the same algorithm (Altmann et al., 2013a; Dobigeon et al., 2008; Gleeson et al., 2010; Schmidt et al., 2010). The key benefit of the Bayesian methods is that they can allow for a certain amount of non-linearity in the mixing and don't necessarily require the presence of pure pixels.

4.3.3: How much of each endmember is present?

The Endmember Extraction Algorithms described in section 4.3.2 provide a qualitative analysis of what materials a scene is comprised of. In the final step in the SMA chain, the Abundance Estimation Algorithms (AEA), provide quantitative information, returning an estimation of the abundance of each endmember within each pixel of the scene. The classic/standard method for doing this assumes the spectral mixture is best represent by the linear mixing model (Keshava and Mustard, 2002). A number of variants exist with slight differences mostly on the constraints imposed on the algorithm. Heinz and Chang (2001) published a fully constrained linear least squares (FCLLS) version (obeys both ANC and ASC) that uses a least-squared error minimisation routine whilst simultaneously enforcing both the ANC and the ASC on the resulting solution for each pixel in the image. This algorithm has become the standard algorithm to compare new versions against (see following references to these newer versions).

As discussed in the previous section the likelihood of a purely linear mixture within a geological scene is slim and non-linear methods have been explored (Dobigeon et al., 2014; Heylen et al., 2014). The type of non-linearity associated with soils and sands is most likely highly intimate and therefore best modelled via a radiative transfer-based multiple scattering model such as the Hapke equation (Hapke, 2012, 1981) or the Shkuratov model (Poulet and Erard, 2004; Shkuratov et al., 1999). The Hapke equation models the scattering of light from a particulate surface and requires values for a number of physical parameters including

number of particles per unit volume, average geometric cross section of the particles, their extinction, scattering and absorption efficiencies and their phase functions. There are a number of assumptions regarding these physical parameters inherent within the Hapke model and it is not without its criticisms. Chief amongst these are discrepancies in the single-scattering phase function used to describe multiple scattering scenarios, approximations of anisotropies related to incidence and emergence angles and shadow effects in multiple scatterer scenes (Shkuratov et al., 2012). Supporters of the model argue that all radiative transfer models are approximations and that the criticisms listed do not distract from the models ability to produce reasonable accurate results in the majority of cases (Hapke, 2013). Due primarily to its relative simplicity the Hapke model is the dominant theory used by the planetary science community (Poulet et al., 2002). The model is considered valid for particulate mixtures of similar grain sizes and shapes and where the grain sizes are significantly larger than the wavelengths used (Mustard and Pieters, 1989). In practice the required parameters are incredibly difficult to determine (particularly the variation across the grain size and shape), meaning that approximations and best estimates must be used. The Hapke model approximation equation is given as:

$$R(i,e) = \left[\frac{w}{4(\mu+\mu_0)}\right][\{1 + B(g)\}P(g) + H(\mu)H(\mu_0) - 1] \quad (4.2)$$

Where *R(i,e)* is the reflectance at incidence angle *i* and emission angle *e*, *w* is the single scattering albedo (SSA), $\mu = cos(e)$, $\mu_0 = cos(i)$, $H(\mu)$ is Hapke's approximation to Chandrasekhar's multiple scattering equation and is given by $(1 + 2\mu) / (1 + 2\mu\gamma)$ where $\gamma = (1 - w)^{1/2}$, B(g) is the backscatter phase function and P(g) is the single particle phase function (figure 4.4) . This equation can be further approximated as:

$$R(i,e) = \left[\frac{w}{4(\mu+\mu_0)}\right][H(\mu)H(\mu_0)] \quad (4.3)$$

This approximation is considered valid provided three criteria are met: i) none of the endmembers are high albedo substances (Guilfoyle and Althouse, 2001) (a problem when applied to hydrothermal alteration environments where a number of the common minerals are high albedo substances), ii) B(g) = 0 (holds as long as the phase angles involved are >15°) and iii) P(g) = 1 (holds if we assume that the particulate surface scatters isotropically). One of the consequences of the Hapke equation is that a non-linear mixture of reflectance spectra

corresponds to a linear mixture of the same spectra converted to single scattering albedo (SSA) (Broadwater et al., 2009). Provided the already listed assumptions hold, in addition to knowing the emission and incidence angles of the light and assuming a homogenous particle size it is possible to convert the reflectance mixed spectral data into SSA data and apply the FCLLS algorithm to it to calculate the endmember abundances (Goudge et al., 2015; Mustard and Pieters, 1989, 1987; Stack and Milliken, 2015).

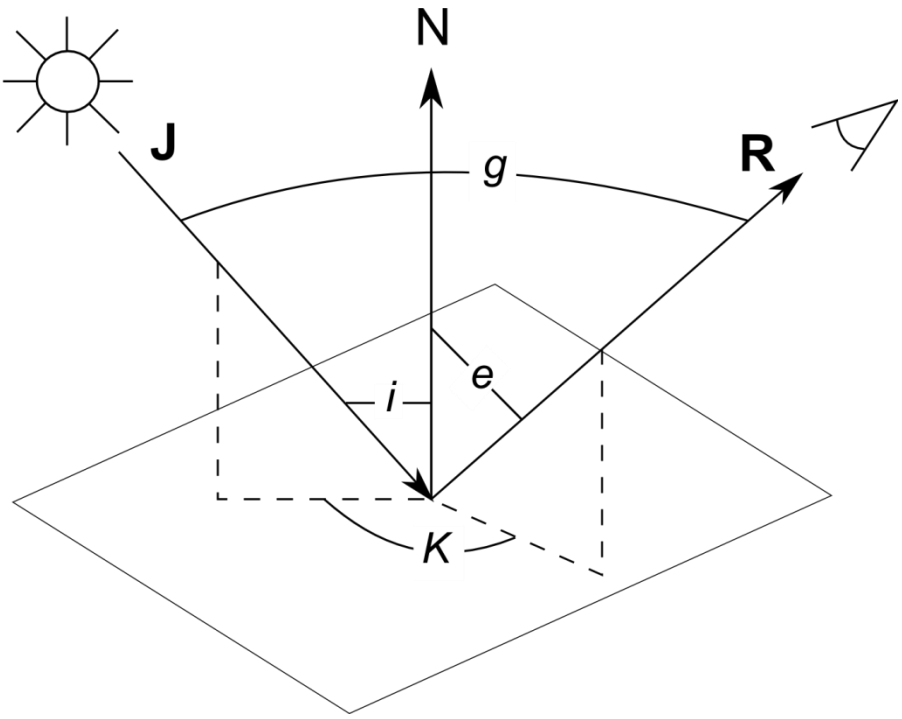

Figure 4.4: The basic geometry involved in the bidirectional reflectance Hapke model and equation 4.2 where e = angle of emission, i = angle of incidence, g = the phase angle, K = the azimuth angle between the planes of incidence and reflection, J = the incident radiation and R = the reflected radiation that reaches the sensor.

The Hapke conversion to SSA has also been combined with Kernel Methods, machine learning algorithms used in computer sciences for pattern analysis, to automate and increase the speed of this task. Kernel Methods can be run as supervised, unsupervised and semi-supervised routines. These have recently attracted some attention from the remote sensing community as a tool for performing SMA due to their ability to handle large complex datasets and combine both linear and non-linear spaces. In addition kernel algorithms benefit from not requiring exact knowledge of the non-linear model by which the scattering is occurring (Dobigeon et al., 2014). The most well-known Kernel Method is the Support Vector Machine (SVM). A number of different kernels exist with simple ones including the Radial Basis Function (RBF) (Broadwater et al., 2009). Broadwater et al. (2009) used this kernel type

together with a Support Vector Data Description (SVDD) endmember extraction routine to kernelise the FCLLS of Heinz and Chang (2001). This was tested against three simulated images containing both pure and linearly and non-linearly mixed spectra taken at the RELAB facility. The results were compared against those calculated using the non-kernel, FCLLS algorithm and found to be slightly more accurate in terms of fractional abundance estimation. The algorithm was then tested using the AVIRIS Cuprite Nevada image (NASA JPL) used by numerous other SMA researchers. These results were compared to both ground truth maps and results from the N-FINDR algorithm used together with a linear least squares unmixing algorithm. The resulting abundance maps compare well with the ground truth maps and unlike the N-FINDR algorithm no "noise" endmembers are returned. They acknowledge however that the Gaussian RBF used is not optimal for unmixing hyperspectral images and suggest instead a more physics based kernel (i.e. one based on a radiative transfer model) which when tested was found to provide better results than the RBF based kernel. Further work performed by the same lead author (Broadwater and Banerjee, 2011) sought to extend this kernelised FCLLS algorithm and test it against a real world dataset with imperfect *a priori* knowledge of endmembers and imperfect atmospheric correction. The algorithm was of use in identifying where non-linear pixels existed in the data. However as pointed out in Dobigeon et al. (2014) Broadwater's approach does not actually take into account non-linear interactions between materials and instead treats the non-linear pixels as distortions of the spectral signature of each endmember present. A similar approach has been attempted using a reproducing Hilbert space kernel by various researchers including Imbiriba et al. (2014) and Chen et al. (2013) who report smaller pixel reconstruction errors when compared to the FCLLS model. The optimal kernel for use in hyperspectral unmixing is still an open question.

Neural networks are increasing in popularity for various different types of pattern classification and image analysis problems. They can incorporate non-linear functions but do have the downside of potentially high computational cost. Adaptive resonance theory (ART) (Lui et al., 2004) and multilayer perceptron (MLP) (Foody, 1996) are two classes of neural networks that have been used for non-linear unmixing models.

One thing that all the authors in the literature agree upon is that using a non-linear model to calculate endmember abundances rather than a linear model greatly increases the computational complexity and temporal cost. There appears to be no quantitative agreement however on how great an increase this is or what the alternative increase in error is from using the simpler linear model. A major point with this comes from the inherent

complexity of real scenes that do not strictly conform to either the linear mixture models or any of the non-linear mixture models. Additionally, without a method for accurately establishing the mixture model that best represents a scene it is difficult to estimate the level of error that is introduced from using one model over another. It is for this reason that most researchers assume the linear model as it is easier and quicker to work with. Chapter 5 will investigate this matter further.

4.4: Spectral Mixture Analysis applied to Mars

SMA as an analysis technique is still in its research and development phase; however its very inclusion in commercial products such as the image processing software ENVI suggests that it is considered robust enough to have become a standard tool in an image analyst's toolbox. There is however, a lack of non-commercial hyperspectral imagery covering the Earth, which means that most of the scientific literature using SMA is concerned with developing new algorithms for one of the three unmixing steps rather than exploiting the existing ones in different environments and to answer different scientific questions. This data constraint is not a problem for Mars researchers however, with both CRISM and OMEGA continuing to generate hyperspectral images of the surface that are made freely available. Despite this plethora of data, there has been little published making use of SMA in the exploration of Mars. One of the earliest attempts at spectral unmixing was with 6 band images returned from the Viking Landers (Adams et al., 1986). The Pancam on the *Spirit* Mars Exploration Rover returns 11 band VNIR images which Farrand et al (2006) analysed using SMA, together with other spectral analysis techniques to identify which areas within the scene were dust free and spectrally unique. Ceamanos et al (2011) investigated how well a range of SMA algorithms worked using CRISM imagery over the Russell Crater megadune located in the Noachis quadrangle of Mars. The same data was used to evaluate a non-linear principal component based algorithm by Licciardi et al (2012) that incorporated the use of neural networks. A similar study by Themelis et al (2012) compared three supervised unmixing algorithms including a Bayesian *a priori* maximum probability estimator (MAP) using an OMEGA image. Another study by Schmidt et al (2010) used an OMEGA image to test their implementation of an unsupervised Bayesian Point Source Separation algorithm (BPSS) for endmember selection and abundance estimation. Parente et al (2011) presented a new automated algorithm for endmember extraction specifically for use with CRISM images. This paper is short and clearly just an introduction to their technique but it does present promising results. To date however no longer version has been published. The conversion of reflectance data to Single Scattering Albedo (SSA) detailed in Mustard and Pieters (1989 and

1987) has recently been applied to analysis of CRISM and TES data over the Kashira crater by Goudge et al. (2015) using laboratory spectral library data combined with individual pixel spectra to identify kaolin-group deposits. The Modified Gaussian Model (MGM) (Sunshine et al., 1990) deconvolves absorption bands caused by transition electrons, and estimates the modal abundances of the constituent minerals. It was developed for the analysis of primary mafic mineralogy (i.e. pyroxene and olivine) spectra and therefore is ideally suited for analysis of the bulk mineralogy of Mars. It is based on the physics of electron transition absorptions and not the vibrational absorptions that make up the major diagnostic bands in hydrated minerals. It works through identification and fitting of the large broad absorptions caused by Fe transitions as Gaussian distributions and has proven accurate for binary and ternary mineral mixtures (Clénet et al., 2011). It can help to emphasis weak spectral variations across a scene that are related to spatial variation in mineral composition (Clénet et al., 2013) and differentiate between different compositions of pyroxenes (Sunshine and Pieters, 1993) and olivines (Sunshine and Pieters, 1998) in laboratory spectroscopy data. However it is not a suitable algorithm for application to scenes with high p values (i.e. more than three endmembers) or those dominated by non-mafic igneous rocks. Its sensitivity to numerous input parameters makes it a temporally expensive algorithm meaning it is most appropriately applied to individual spectra rather than large datasets and image cubes (Horgan et al., 2014). Table 4.1 lists a selection of papers published to date utilising SMA processes (other than exclusively MGM) to quantitatively analyse VNIR martian data. These papers cover only a portion of the different SMA algorithms that have been developed, and a tiny proportion of the Martian surface and the potentially suitable data available for processing.

Table 4.1: SMA Algorithms used to analyse Mars spectral imagery

SMA Algorithm	**Paper(s)**
PCA & FCLLS	(Adams et al., 1986)
BPSS & FCLLS	(Ceamanos et al., 2011; Douté et al., 2011; Schmidt et al., 2010)
VCA & FCLLS	(Ceamanos et al., 2011; Douté et al., 2011; Parente et al., 2011)
N-FINDR & FCLLS	(Ceamanos et al., 2011; Douté et al.,

	2011; Parente et al., 2011)
MVC-NMF & FCLLS	(Ceamanos et al., 2011; Douté et al., 2011)
MVES/SISAL & FCLLS	(Ceamanos et al., 2011; Douté et al., 2011)
MELSUM/MESMA & FCLLS	(Combe et al., 2008; Gou et al., 2014; Wendt et al., 2009)
PPI & ASC-LLS	(Farrand et al., 2013, 2006; Parente et al., 2011)
FCLLS + Hapke SSA conversion	(Goudge et al., 2015)
Spectral Library + FCLLS & MGM	(Le Deit et al., 2008)
Non-linear principal components analysis (NLPCA)	(Licciardi et al., 2012)
Factor Analysis and Target Transformation (FATT) + Hapke SSA conversion	(Liu and Glotch, 2014)
ELM + VCA + ANC-LLS	(Luo et al., 2012)
ICA + BPSS	(Moussaoui et al., 2008)
Nonnegative Matrix Factorization	(Parente et al., 2009b)
SMACC & FCLLS	(Parente et al., 2011)
Parente CRISM Endmember Algorithm & FCLLS	(Parente et al., 2011)
Spectral library + LinMin	(Schmidt et al., 2014)
Bayesian MAPs	(Themelis et al., 2012)
Sparse Bayesian Unmixing	(Thompson et al., 2009)

The standard method used for identifying minerals on the surface of Mars is to identify specific Spectral Parameters across entire CRISM and/or OMEGA images at a time (see Chapter 3, section 3.3.4 for explanation of Spectral Parameters). Spectral Parameters are a quick and simple method for searching and identifying the presence of specific minerals, e.g. if you only want to map the locations of carbonates. However there are drawbacks. Firstly as

each spectral parameter is only calculating one feature be it a band depth or slope, they can only identify minerals for which there is one uniquely identifying feature or at very least a mineral type that all share the same unique feature. Secondly, minerals will generally only be identified if they are the dominant mineral in the pixel meaning that many minor, but potentially interesting, minerals can go unnoticed. Finally mixing and in particular non-linear mixing of spectra can diminish and weaken some key spectral features if they occupy a similar wavelength range to a more dominant feature, making it less likely that they will be extracted using Spectral Parameters alone. Spectral Unmixing (or at least blind endmember extraction) can be used as one way of ensuring that the smaller minerals are still identified whilst taking into account the entire spectrum of each endmember and not just a single feature.

4.5: Applicability, availability and accessibility of SMA

A common theme in the most recent developments in SMA is the increasing use of complex algorithm types and machine learning. Whilst accurate results are being returned through the use of neural networks, machine learning, kernels and Bayesian statistics, they all require a high level of computational skill and time. Without the collaboration of signal process engineers and computer scientists these techniques are out of reach for many geological and planetary scientists. The less computationally expensive algorithms such as the geometric EEAs have a long pedigree and have been shown to return accurate results in many situations, however the majority discussed in the literature have not been made publically available for use by other members of the remote sensing community. Additionally despite the wide range of algorithms developed and tested against Earth imagery few of these have been applied to martian data, with a number of the martian SMA studies using algorithms developed and used exclusively in those publications (see table 4.1 for examples).

There are some key differences between the hyperspectral images returned from Mars compared to those covering the Earth, namely the lack of vegetation and anthropogenic structures, and the different atmosphere the radiation passes through. Whilst the first of these differences does mean that a large subsection of the SMA algorithms developed with Earth Observation in mind are inappropriate for application to Mars (i.e. all developed with vegetation and large bodies of water in mind), all of those developed for geological exploration should in theory be applicable. The difference in atmosphere should not affect the applicability of any of the algorithms as in the case of both Earth and Mars imagery the effects of the atmosphere must be removed before SMA processing takes place. It is a valuable task therefore to identify the SMA algorithms for each of the three steps in the chain that are i) publically available in an easily accessible and executable format that does not

require access to numerous expensive proprietary pieces of software, and ii) suitable to the potential types of geological environment that may be found on Mars even if they have not previously been applied to martian data. This important issue shall be the focus of the following chapter with specific emphasis on hydrothermally altered environments.

4.6: Summary

The spatial resolution of imaging spectroscopy data can have significant ramifications for the level of information extractable from the dataset. This is particularly the case with data from the martian instrument CRISM, whose pixel resolution of 18 m^2 is such that much of the mineralogical diversity on the surface can be obscured. The extraction of sub-pixel information through the family of techniques known collectively as Spectral Mixture Analysis has been presented with emphasis on its use in geological applications. The three primary steps in the SMA pipeline have been discussed along with the major existing algorithms for performing each action. The application of SMA to martian data has been presented and previous studies discussed. The lack of availability of suitable SMA algorithms for a planetary scientist without the necessary time, programming skills or proprietary software was acknowledged. It is this lack that the following chapter will address.

Chapter 5: Development of a best practice, publically available Spectral Mixture Analysis pipeline for the detection of small scale hydrothermal surface alteration

5.1: Introduction

This chapter shall cover the development of a full supervised spectral unmixing routine, tested and optimised for the specific complexities inherent in a hydrothermally altered environment. From a spectral point of view a hydrothermal environment contains a number of specific complexities. These features make the use of spectral unmixing more attractive for the analysis of such areas but also more challenging. Of special interest are the following factors:

- Large numbers of endmembers - Keshava and Mustard (2002) state that the number of endmembers that can be practically determined/distinguished is 3 - 7 but hydrothermal areas can have many more over a small (metres to 10's of metres) area.
- If specifically dealing with small scale regions then there may not be many pixels covering the region of interest (in the case of CRISM even a large region around $1km^2$ may only be covered by a few thousand pixels and a region of hydrothermal surface alteration can be considerably smaller than this).
- The types of minerals typically produced in hydrothermal alteration environments exhibit significant spectral variation due to textural and mineralogical variations, e.g. the spectral signature from phyllosilicates can alter due to varying water content, and differences in average particle size also produces spectral differences in all mineral types. Additionally mineralogically similar minerals, e.g. iron oxides, can be spectrally similar in the VNIR wavelength range.
- These environments tend to feature unconsolidated soils as well as lithified rocks and stones and as such the spectral mixing is best modelled as an intimate non-linear mixture, or at least a combination of linear and non-linear mixing.

These features make spectral unmixing challenging but they also make other spectral analysis mapping techniques, such as spectral parameter analysis, less reliable if quantitative information is required. Whilst techniques such as Minimum Noise Fraction transformation (MNF) and Principal Components Analysis (PCA) can still be used to produce mineral maps despite these complications, the end results they give are still based upon reading each pixel

as a single pure endmember transformed into a new dimensional space, and thus require interpretation in an attempt to attach a physical reality to the different extracted endmembers. Additionally neither of these techniques allow for quantitative evaluation of the scene at a sub-pixel level.

Much of the work that has been undertaken in the development of spectral unmixing algorithms has focused on only one of each the three steps involved (see Chapter 4 for further details and definition of the three steps), or has been developed for a generic environment and therefore not been tested at the extremes that can exist, meaning that the limitations on the applicability of this technique are not well understood. A hydrothermal environment is one such extreme. Additionally, although many papers describe various novel unmixing related algorithms, few of these algorithms have been made available to the end-user community who may have neither the necessary time nor skills to write a computer program based on the descriptions given in the literature. For these reasons it is necessary to investigate what algorithms have been made available as open source code covering all three steps in the unmixing chain and test them in the face of hydrothermal conditions to determine a best practice full unmixing pipeline to add to the suite of analysis tools available to remote sensing geologists. In order to achieve this, a number of synthetic images were generated using data from publically available spectral libraries, each image designed to test the sensitivity of the algorithms to each of the complexities detailed above and gain a better understanding of the limitations of SMA and whether or not it is an applicable technique for analysis of a complex hydrothermal environment.

5.2 Synthetic images

Images were constructed using publically available library spectra. Unless otherwise stated pure single mineral spectra were used as endmembers. Random abundances were generated according to a Dirichlet distribution (Kotz et al., 2000) with the additional constraint that no single pixel be composed of more than 80% of an individual endmember. Noise was added to each image as Gaussian non-zero white noise with varying Signal to Noise Ratio (SNR) in 10 dB steps between 15 – 55 dB (where SNR dB = 20log(SNR(λ))). Endmember minerals were chosen based on minerals commonly found in hydrothermally altered surface environments, although in the case of non-linear mixtures the limited number of spectra available required a loosening of this constraint. Spectra were taken from either the USGS spectral library (Clark et al., 1993) supplied as one of the spectral libraries with ENVI 4.8 or the RELAB spectral library (Pieters and Hiroi, 2004). Plots of the endmembers in each image are given in Appendix II.

Table 5.1: details of the synthetic images used in section 5.4. p = number of endmembers, L = number of spectral bands, N = number of pixels/datapoints

Image #	Mix type	N	p	L	Spectra/endmembers	Spectral library	Test?
2a	Linear	8100	6	420	Hematite: GDS27, FE2602, HS45.3 Olivine: NMNH137044.b, KI3005, KI3054	USGS	High spectral variation within single mineral type due to interspecies variation
2b	Linear	8100	6	420	Hematite: GDS69.c, GDS69.d, GDS69.e Olivine: GDS70.a, GDS70.b, GDS70.c	USGS	High spectral variation within single endmember due to textural variance
3a	Linear	8100	4	420	Hematite: GDS27, FE2606 Goethite: WS219, WS220	USGS	Spectral and chemical similarity between endmembers
3b	Linear	8100	4	420	Montmorillonite: CM27, CM26 Nontronite: SWa-1.a, SWa-1.b	USGS	Spectral and chemical similarity between endmembers
4	Non-linear	8096	4	211	Olivine, Magnesite, Enstatite, Anorthite (see Mustard & Pieters, 1989 for full description of this dataset)	RELAB	Intimate non-linear mixtures
5	Linear + non-linear	8100	4	211	Olivine, Magnesite, Enstatite, Anorthite (see Mustard & Pieters, 1989	RELAB	Combination of linear and non-linear mixing

					for full description of this dataset)		
5b	Linear	8100	4	211	As 5	RELAB	Testing of effect of SSA conversion on linear mixtures
7a	Linear	8100	3	420	Opal TM8896 Montmorillonite CM27 Goethite WS220	USGS	Number of endmembers present
7b	Linear	8100	7	420	As 7a plus: Kaolinite CM9 Stilbite HS4B2.3B Gypsum SU2202 Jarosite GDS24 Na	USGS	Number of endmembers present
7c	Linear	8100	15	420	As 7b plus: Nontronite SWa-1.a Sulfur GDS94 Augite WS592 Andesine HS142.3B Hematite GDS27 Rutile HS126.3B Quartz HS32.4B Montmorillonite SWy-1	USGS	Number of endmembers present
10a.1	Linear + non-linear	8100	12	211	Kaolinite + Opal JB-JLB-81* Ferrihydrite + nontronite JB-JLB-80* Pyroxene + Hematite MX-EAC-018 Quartz + Alunite XT-CMP-016 Olivine + Magnesite XO-CMP-01* Olivine + Enstatite XO-	RELAB	Combination of intimate non-linear mixing, and high p value

					CMP-01* Olivine + Anorthite XO-CMP-02* Olivine + Anorthite + Enstatite XO-CMP-030		
10a.2	Linear + non-linear	290	12	211	As image 10a	RELAB	Combination of intimate non-linear mixing, high p value and low number of pixels, N.
10b	Linear + non-linear	8100	10	211	Kaolinite + Opal JB-JLB-81* Ferrihydrite + nontronite JB-JLB-80* Quartz + Alunite XT-CMP-016 Olivine + Magnesite XO-CMP-01* Olivine + Enstatite XO-CMP-01* Olivine + Anorthite XO-CMP-02* Olivine + Anorthite + Enstatite XO-CMP-030	RELAB	Combination of intimate non-linear mixing, and high p value

5.3: SMA related algorithms used in this work

There are numerous programming languages and packages commonly used by the signal and image processing communities including Matlab, IDL, R and Python. In order to maintain consistency in the final pipeline a single language was chosen to perform each step. Matlab was chosen as a commonly used and relatively simple language, it was also the language that most of the publically available algorithms for each of the three steps have been made available in.

5.3.1: Endmember Dimensionality Algorithms (EDA)

The first step in the unmixing pipeline is to determine the number of endmember present in the scene. Four algorithms were selected for inclusion in this study; Harsanyi-Farrand-Chang (HFC), Hyperspectral Signal Subspace Identification by Minimum Error (HySIME), Eigenvalue Likelihood Maximization (ELM) and the Outlier Detection Methods (ODM) all of which are described in more detail in Chapter 4. Of the four algorithms HFC is available within numerous spectral processing programs and packages. The version used in this work can be found within the Matlab package *Endmember Induction Algorithms Toolbox for MATLAB* distributed by the Universidad del Paas Vasco, Spain. Matlab code for HySIME is provided by the authors of the algorithm and can be found at http://www.lx.it.pt/~bioucas/code.htm. ELM and ODM were not publically available at the time of this study and Matlab code was written based on their description papers (Andreou and Karathanassi, 2014; Luo et al., 2013). This code can be found in Appendix III.

The four algorithms can be divided into two categories; algorithms that produce a definitive final numerical result and algorithms that produce a graph that must then be interpreted by the analyst. HFC and HySIME are both examples of the former type and ELM an example of the latter. ODM claims in its description paper (Andreou and Karathanassi, 2014) to be of the former type but this was not borne out in this work. My version of the code produced a graph from which the correct p value could be easily interpreted when applied to a simple dataset but was slightly more ambiguous when dealing with a complex image (figure 5.1). In no case was the single numerical value returned the correct one, consistently returning a much greater number than the correct p value. As it is only the final quoted value that is in error the flaw in the program must be in this final step where the authors have applied a simple interquartile range statistic. The synthetic test data the algorithm authors' use is not explicitly specified and so could not be verified in this work. However the plots of the final algorithm product prior to the IQR step produced in this work appear to match the pattern shown in the same plots in the description paper (Andreou and Karathanassi, 2014) and do produce the correct p value when applied to non-complex data. Efforts to contact the authors of the algorithm to investigate this discrepancy came to nothing and so all ODM values quoted in this and subsequent chapters have been read from the plot produced by my Matlab routine (see figure 5.1 for example plots).

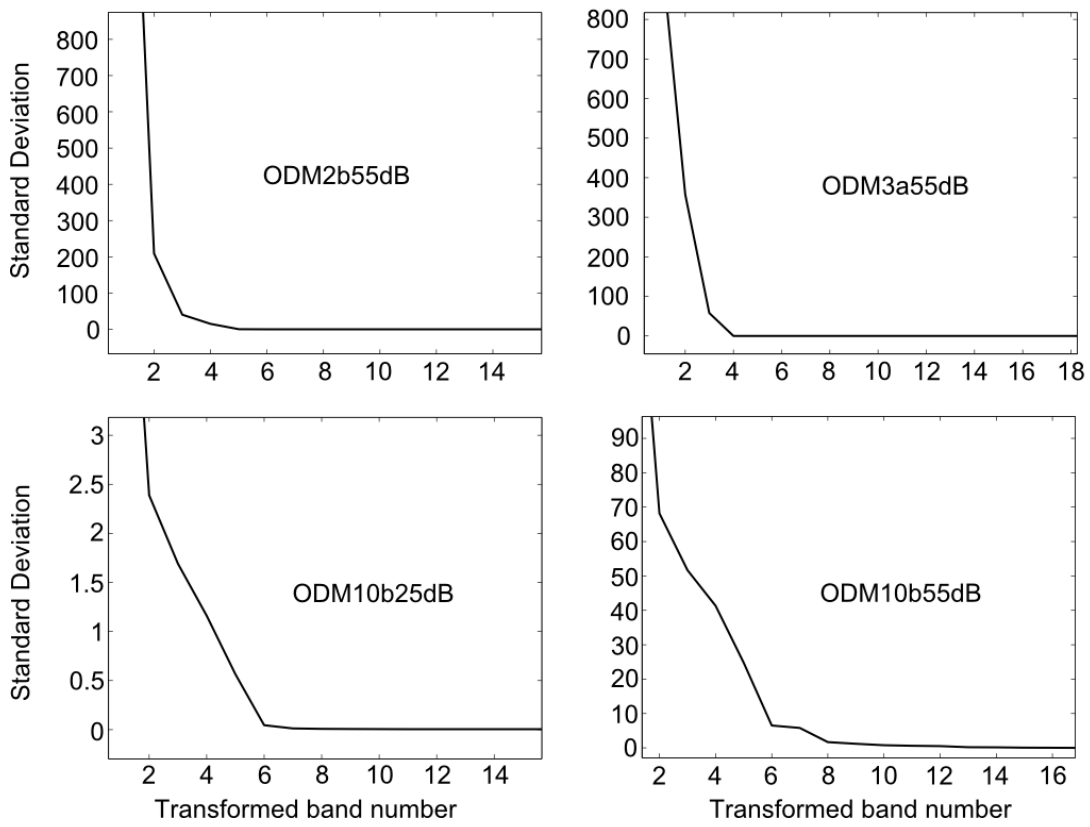

Figure 5.1: Example ODM output plots showing the Euclidean Distance between the standard deviation values of the noise whitened transformed data versus band number (see Andreou and Karathanassi, 2014 *for full explanation of these plots). The point at which the plot plateaus represents the number of endmembers present, p. In a low noise case with a low p value such as image 3a (ODM3a55dB) this value is easily identified correctly as p = 4. However this value is less obvious with higher p values as seen in ODM10b25dB and ODM10b55dB where in both cases the plot continues to slightly but significantly decrease after an initial sharper plateau point at a p value lower than the correct one.*

The accuracy of these four algorithms will be evaluated based solely on whether or not they produce the correct p value. In terms of the accuracy of this value in a setting where the real p value is unknown some diagnostic output to be used as a confidence or quality flag would be useful. For the ODM and the ELM algorithms the final graph produced gives some qualitative indication of the complexity of the problem and as the p value comes from an interpretation of these the harder they are to interpret the lower the level of confidence in the answer. HySIME also produces a graph as part of its final output from which the program reads the final p value (figure 5.2). The program read the minimum of the Mean Squared Error line as the p value, as with the ODM and ELM graphs the more ambiguous this appears to the analyst can give a qualitative assessment of the accuracy of the result. HFC gives no

output beyond the p value. However as the operator has to specify the false-probability alarm parameter that HFC runs with using a number of different values for this can give an indication of the confidence that should be assigned to the results. If the returned p value is the same for a number of false-probability parameters this could be an indication that the result is robust. It should be noted that in none of the four algorithms discussed are these quality indicators identified as such by their authors who instead validate their algorithms purely on the basis of how often they return the correct value for known scenes.

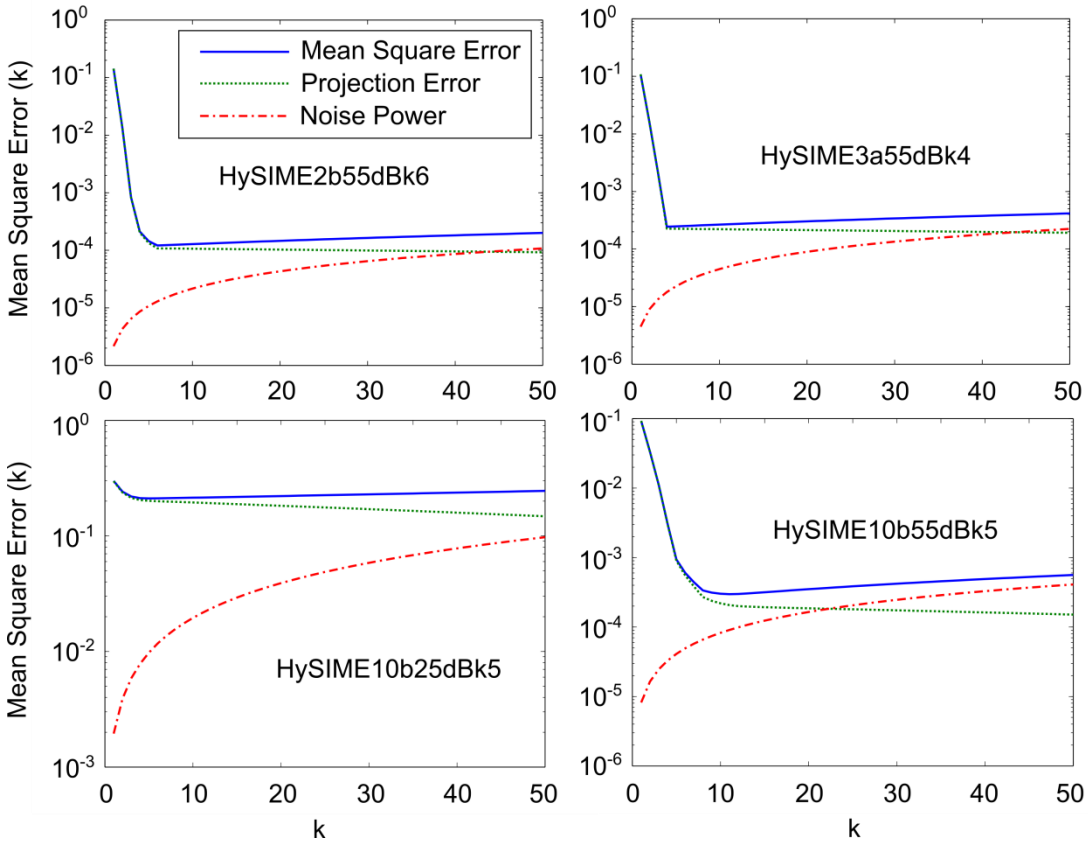

Figure 5.2: Example HySIME output plots showing the means squared error values plotted against the k eigenvalue index number (see (Bioucas-Dias and Nascimento, 2008) for a full explanation of these plots). The minimum of the solid blue line represents the p value, the number of endmembers estimated by the algorithm. In a simple case such as that for image 3a with SNR 55 dB the value is clear with a sharp minimum. In the other more complex cases this minimum is more ambiguous.

5.3.2: Endmember Extraction Algorithms (EEA)

Once the number of endmembers in a scene has been established the next step is to extract the individual spectral signatures of each of these endmembers. This is possibly the step that has seen the greatest concentration of effort in the signal processing community. For a

thorough description of the wide range of algorithms developed see Chapter 4 and the referenced review articles within. Few of the documented algorithms however have been made publically available. In this work I have looked at four algorithms; VCA, SISAL, RMVES, and ICE. A copy of SISAL is publically available for Matlab via the author's website (http://www.lx.it.pt/~bioucas/code.htm). A Matlab version of RMVES was also acquired via the algorithm author's website (http://mx.nthu.edu.tw/~tsunghan/Source%20codes.html). The Matlab code for running ICE was generated by modifying the version of the SPICE program written by Alina Zare copyright at the University of Missouri and the University of Florida (http://engineers.missouri.edu/zarea/2013/09/code-sparsity-promoting-iterated-constrained-endmembers/). The VCA Matlab code was included in the SISAL software package download referenced previously.

A significant difference between the four algorithms is their dependence on the presence of 'pure' pixels. Both VCA and ICE assume that for each endmember there is at least one 100% pure pixel in the dataset being analysed. SISAL and RMVES make no such assumption. All four are based on the assumption of a linear mixture model.

None of these algorithms include an estimation of error on the extracted endmembers or any other statistical diagnostic output. SISAL includes in its output the eigenvalues of the normalised input matrix which can be used to give an indication of how difficult the problem is. This however is not necessarily an indication of the accuracy of the resulting extracted spectra.

5.3.3: Abundance Estimation Algorithms (AEA)

This is arguably the most computationally difficult step in the spectral unmixing pipeline, especially when non-linearity is present, and as such it is the step with the fewest documented algorithms. The only publically available algorithms in Matlab language are the Modified Gaussian Model (MGM) (Sunshine et al., 1990) and the Fully Constrained Linear Least-Squared (FCLLS) algorithm (Heinz and Chang, 2001). The MGM, as discussed in Chapter 4 section 4.4, is designed specifically for the deconvolution of mafic minerals and therefore not appropriate for the unmixing of a complex hydrothermal scene. This leaves the FCLLS as the only AEA available for this study. The version used in this work is available within the *Matlab Hyperspectral Toolbox* by Isaac Gerg which can be downloaded from github. This algorithm assumes that the spectral mixture is a purely linear one and as previously discussed this is not a valid assumption for a hydrothermally altered scene. The FCLLS algorithm produces no statistical quality flag with which to evaluate the accuracy of the results,

outputting only the estimated abundance matrix based upon the input image and endmembers. Additionally, it is not clear from the literature the amount of error that can be expected when applying it to complex non-linear data with numerous other variables to be taken into consideration, and therefore it is worth establishing this.

An additional step can potentially be added to enable FCLLS to take into account non-linearity. All of the algorithms so far described use relative reflectance value data (RR). Converting this data into Single Scattering Albedo (SSA) as described in Chapter 4, section 4.3.3, should convert the non-linear RR data into linearly mixed SSA data, allowing the FCLLS to be used in such a way that encompasses the non-linearity of the spectral mixture.

5.4: Results of testing the SMA algorithms on synthetic images

Each of the algorithms listed in section 5.3 were applied to the synthetic images detailed in table 5.1 where appropriate. Tables listing the full results of each test are given in Appendix IV with key results discussed below.

5.4.1: Endmember Dimensionality Algorithm (EDA) Results

Each of the four EDA algorithms (ELM, HFC, HySIME, and ODM) was applied to the synthetic images listed in table 5.1. Each image was constructed to test the sensitivity of each algorithm to one of the specific complexities listed at the beginning of the Chapter.

5.4.1.1: Number of endmembers (high p value)

Images 7a, 7b, and 7c were all designed to investigate the ability of each algorithm to cope with increasing p value using minerals typically found in basaltic hydrothermally altered environments. All four algorithms gave accurate results with linear mixtures of 3 and 7 endmembers (images 7a and 7b). At p = 15 the results were more mixed with HFC consistently underestimating the number of endmembers present regardless of the level of noise in the dataset. The other three algorithms all gave accurate results provided the SNR of the data was at least 35 dB. At lower SNR all three underestimated the value of p. Images 4, 5 and 10a.1 all looked at different numbers of endmembers where the mixing was at least partially non-linear. Images 4 and 5 had only 4 endmembers and the only algorithm that calculated this correctly was the ODM. At a higher p value (image 10a.1, p = 12) none of the algorithms were able to consistently extract the correct value; however, ODM gave the closest results with estimates ± 1 or 2 of the correct value depending on the SNR in the image (figure 5.5).

5.4.1.2: Number of pixels (low N value)

Images 7a and 7b were run with varying values of N from 1000 to 10,000. For these linear mixtures all algorithms estimated the correct number of endmembers regardless of the level of noise with one exception. This exception was HySIME which greatly overestimated the p value for the lowest N value.

5.4.1.3: Inter-endmember spectral variation

Images 2a, 2b, 3a and 3b were all constructed to test the algorithm's sensitivity to inter-endmember spectral variation. Images 2a and 2b focused on two spectrally and mineralogically distinct endmember minerals with the inter-endmember variation being due to either slight geochemical variations between different samples of the same mineral type (2a) or spectral variation due entirely to particle size differences between two aliquots of the same samples (2b). Images 3a and 3b used mineralogically similar pairs of endmembers (two iron-oxides and two smectites respectively). Image 3a incorporated further variation due to geochemical differences within a single species and image 3b incorporated spectral variation due to particle size differences. Both of these types of variation are expected to exist in a real environment, in particular the spectral variation due to particle size or other structural and textural variables. There are two levels of result here that could both be considered correct; i) the correct number of different spectra that have gone into the mixtures (i.e. 6 in images 2a and 2b and 4 in images 3a and 3b) and ii) the correct number of mineral species (i.e. 2 in all four images). In every case except image 3b, regardless of SNR, HFC failed to identify either correct p value. HySIME consistently estimated the higher potential p value provided the SNR was at least 35 dB. This demonstrated a high sensitivity to inter-endmember variability. ODM struggled with both versions of image 2, estimating p values between the two correct ones, however, with images 3a and 3b it consistently returned the higher p values. As an algorithm it is clearly sensitive to inter-endmember variability but not to as high a degree as HySIME resulting in some variation being missed. ELM, the only remaining algorithm returned the correct higher p value in every case provided the SNR was 35 dB or higher.

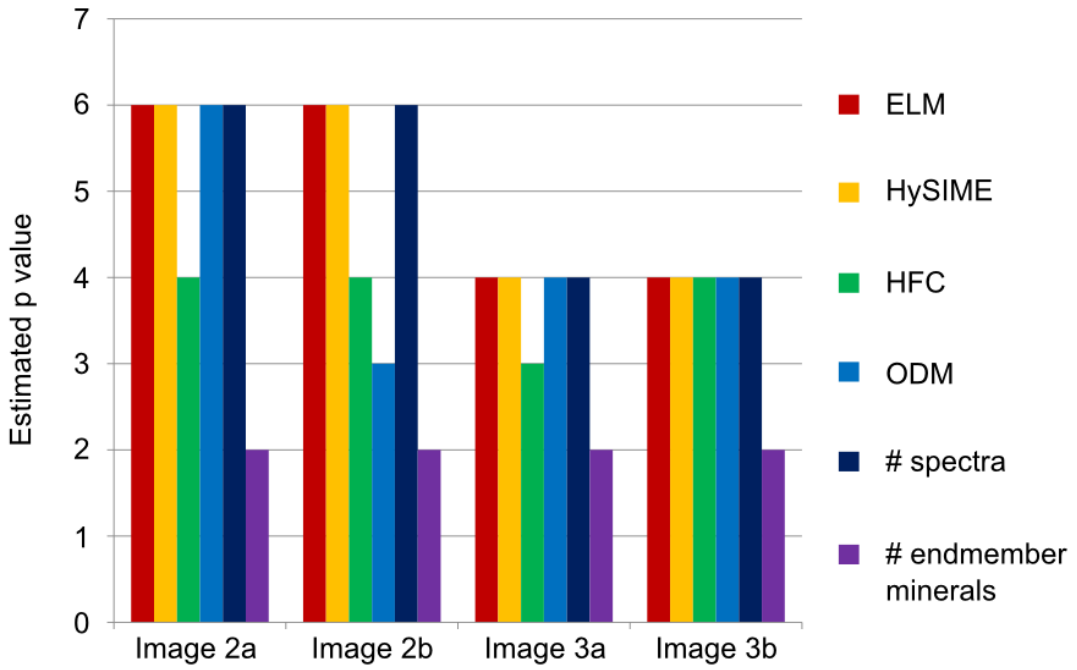

Figure 5.3: Results of modal value across the SNR range investigated of EDAs results applied to images 2a, 2b, 3a, and 3b at SNR 15 – 55 dB. HySIME and ELM are the only algorithms that consistently extract the p value correctly identifying the number of spectra in every image when SNR ≥ 25 dB. None of the algorithms correctly identified the number of endmember minerals which in every case was lower than the number of endmember spectra used in the spectral mixture. This figure does obscure the failure of all algorithms at the highest level of noise (SNR = 15 dB) in at least one of the images analysed.

5.4.1.4: Non-linear mixing

This is perhaps the most important variable and the most challenging to test. Producing non-linear mixtures from single mineral spectra that correspond to a realistic mixture model is computationally expensive, could potentially skew the results away from general non-linearity to only being relevant to the specific mixture model used, and was ultimately beyond the time available to this study. The alternative solution is to use library spectra produced from real mineral mixtures. Both the USGS and RELAB spectral libraries contain a number of spectra taken from physical mixtures that are suitable for this task, but the vast majority either do not specify the exact abundances of the constituent minerals or are mixtures of at most 3 minerals. Working within these restrictions images 4 and 5 were created with only 4 endmembers to test the sensitivity to intimate non-linear mixing. The spectra used in these images were created for use in Mustard and Pieters (1989, 1987), early papers on SMA of intimate mixtures. Only ODM was able to correctly identify the number of

endmembers present. The other three algorithms all routinely overestimated the number of endmembers with higher p values returned the higher the SNR value of the image (figure 5.4). HFC consistently underestimated the number and both HySIME and ELM both under and over-estimated the value of p depending on SNR. Images 10a.1 and 10b were constructed using a higher number of endmembers (p = 12 and 10 respectively), and with such high p values none of the algorithms correctly estimated p. The values returned by ODM had the smallest spread around the correct value across the range of SNR values (figure 5.5).

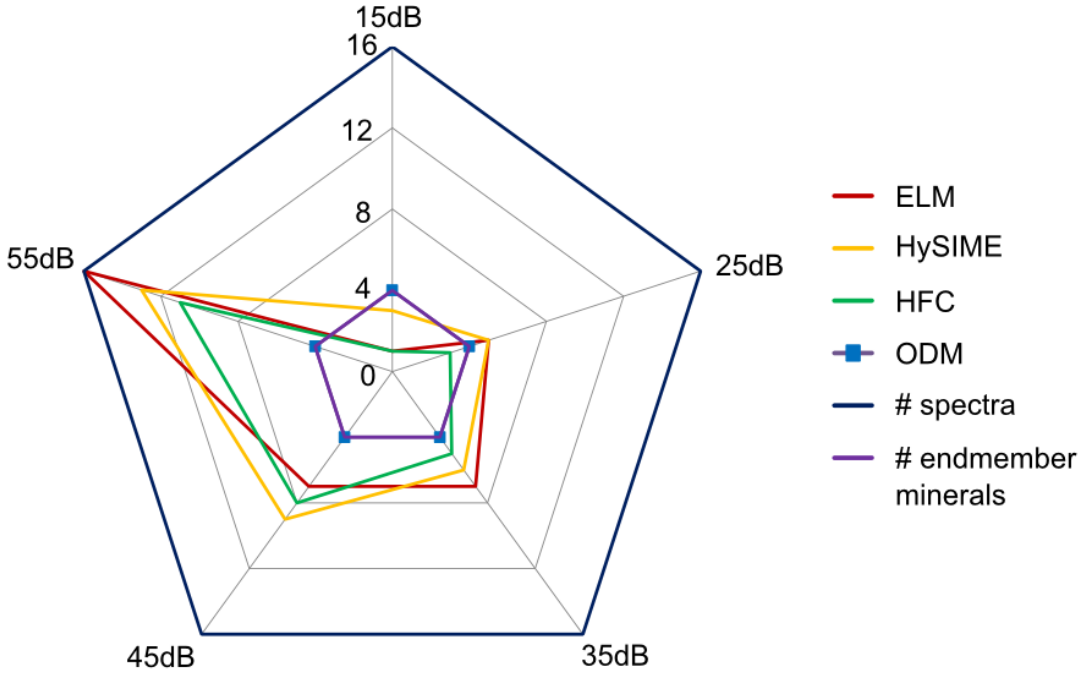

Figure 5.4: Results of the EDAs applied to image 5 at all SNR levels where the radial axis shows estimated p value. ODM was the only algorithm to consistently estimate the correct p value of p = 4. The other three algorithms all estimated increasingly higher p values the lower the level of noise present (and therefore the higher the SNR dB value).

5.4.1.5: Optimum EDA

Computational run time can also be a factor in choosing an algorithm for any calculation and whilst all four did take different amounts of time none took more than a few seconds even with the largest, most complex datasets. Taking into account a scene with every complexity examined none of the algorithms was consistently accurate (figure 5.5). All showed sensitivity to noise emphasising the importance of using data that is a clean as possible. The two that returned the most accurate results for the highest number of the examined variables were

HySIME and ODM, with ODM having the advantage of more accurate and precise results when applied to a non-linear mixture (figure 5.5). The higher sensitivity of HySIME to inter-endmember species variation when applied to a real world scene is in most cases a disadvantage. The inter-endmember species variation can come from a number of factors as previously discussed, and the factor responsible for variation in a hyperspectral image is highly unlikely to be determinable from this data alone. For this reason it is more important to estimate the number of minerals present rather than the number of slightly different forms each of those minerals is present in. The higher number of endmembers thus returned would be an unnecessary complication and potentially greatly increases the amount of time and work needed to conduct a full unmixing routine and correctly interpret the results.

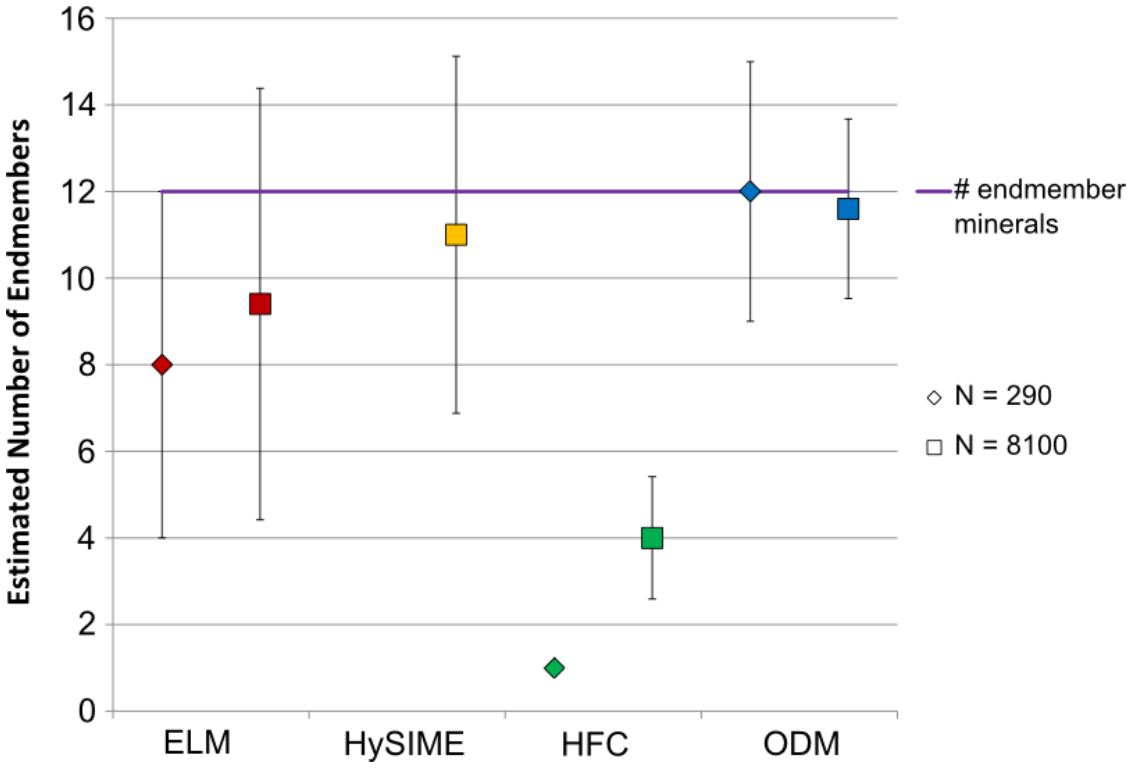

Figure 5.5: Results of EDAs applied to image 10a at two different values of N, 290 and 8100. The error bars represent the spread of results returned across the SNR levels investigated with the point showing the mean value. The N = 290 HySIME value spanned 132 – 17 (15 – 55 dB) and as such has been excluded from the plot. HFC consistently underestimated the p value and the ELM estimates span a large range. The ODM estimates were the most noise invariant with the higher N value generating the most precise and accurate results.

An additional constraint other than those already noted above or explicitly by the algorithm's authors was discovered for both HySIME and ODM. Both algorithms rely on an accurate estimation of the noise present in the data as their first step. The code for estimating this

noise provided with HySIME and also used for ODM requires that N ≥ L otherwise the calculated noise correlation matrices are non-singular and the resulting values unreliable. For a hydrothermal scene that may only include a few hundred pixels this could be an issue depending on the spectral resolution of the detector being used. CRISM has 544 spectral channels but it is possible that any hydrothermal area being investigated could be covered by fewer pixels than this making it necessary to either remove bands or resample to a coarser spectral resolution.

In the case of both HySIME and ODM a qualitative assessment of the accuracy of the result can be provided by looking at the output graph. The sharpness and clarity of the HySIME minimum and the ODM plateau points both give an indication of the quality of the p value extracted, where the harder the respective point is to identify the more caution the result should be treated with. If the p value is into double figures the confidence in the algorithms result decreases, although the level of noise left in the dataset and the mixture type have a more significant effect on the accuracy of the final result.

5.4.2: Endmember Extraction Algorithm (EEA) Results

The four EEAs (ICE, RMVES, SISAL, and VCA) were tested using the correct p value to give best case scenario results. The accuracy of the resulting endmembers were evaluated using the Spectral Angle Mapper algorithm (SAM) (Kruse et al., 1993). This commonly used algorithm calculates the angle between two spectra when mapped as vectors in L-dimensional space. By treating the spectra as vectors SAM is largely invariant to albedo differences. The smaller the SAM value the more spectrally similar the two endmembers. Additionally, when using large p values and non-linear mixtures an attempt was made to identify every endmember extracted using the Spectral Analyst tool in ENVI 4.8 which enables identification through comparison to spectral library entries. Even if an extracted endmember isn't identical to the input endmember if it is identifiable as the correct mineral then it is still a useful and valid result. This would be a standard supervised routine used to identify extracted endmembers in a real situation. One important caveat regarding this tool is the necessity of the presence of at least one example spectrum of a mineral endmember being present in the spectral libraries used to identify the endmembers. If there is no example spectrum or if the mineral in question can have significant interspecies variation and this isn't represented in the available libraries then it can be mis- or unidentified. Tables detailing full SAM results from all tests discussed below are given in Appendix IV.

5.4.2.1: Number of endmembers (high p value)

All four of the algorithms gave increasingly poor results with increasing number of endmembers. At p = 15 (image 7c) RMVES generally gave the lowest SAM values across the noise range, with the SISAL results a close second, however even at 35 dB SNR mismatches between the extracted and pure input endmembers were apparent that would lead to misidentification of at least one of the minerals present. Once non-linearity was introduced at a high p value (image 10a.1, p = 12) none of the algorithms were able to extract 12 correctly identifiable spectra. For each algorithm the SAM results were comparable across the SNR levels with VCA and ICE giving poor results (high SAM values) regardless of the noise and RMVES and SISAL giving lower SAM values at all noise levels. The identifiability of the extracted endmembers, however, did still correspond to noise with higher SNR giving endmembers that were more readily and accurately identified that the lower SNR images.

5.4.2.2: Number of pixels (low N value)

None of the algorithms appeared to be significantly affected by decreasing the number of pixels in the image. The previous step in the unmixing process (EDA) requires that $N \geq L$ and therefore this variable isn't considered an issue for the EEA step in the pipeline.

5.4.2.3: Inter-endmember spectral variation

Images 2a, 2b, 3a and 3b were all run with the higher p values associated with them (p = 6, 6, 4 and 4 respectively). This was both to test if the algorithms could correctly differentiate between the similar endmembers and also because this was the p value that was commonly extracted by the EDAs. At high SNR values (35 dB and greater) all four algorithms managed to extract the correct endmembers and discriminate the sometimes subtle differences between the minerals and the different versions of each mineral. At lower SNR values all of the algorithms returned some erroneous endmembers, e.g. at 25 dB SISAL and RMVES both returned two olivine and four hematite spectra for image 2b rather than the correct three olivine and three hematite. Across the noise range no single algorithm consistently gave the lowest SAM values but SISAL and RMVES gave the best results overall when both SAM values and positive mineral identification were considered.

5.4.2.4: Non-linear mixing

A version of image 4 was created without the 80% pixel purity restriction as the already mixed input spectra guaranteed a maximum purity of 95%. All algorithms extracted the correct endmembers with reasonable SAM values with SISAL consistently giving the lowest values. A version of image 5 with the 80% pixel purity constraint returned similar results with SISAL and RMVES again giving the lowest SAM results at all SNR values. Images 4 and 5

contained only four endmembers however and they were all quite spectrally distinct. Images 10a.1 and 10b with significantly higher p values (p = 12 and p = 10 respectively) returned poorer results. This was to be expected as even with a purely linear mixture it had already been shown with image 7c that all four algorithms struggled with high p values. VCA and ICE gave such poor visual results that calculating SAM values and attempting to identify minerals was not attempted. SISAL and RMVES gave reasonable SAM values at high SNR but even at 55 dB at least one endmember in both images was either unidentifiable or misidentified (figure 5.6). When looking solely at the identifiability of the extracted endmembers the SISAL data gave the strongest results, especially when there was a reasonable level of noise in the data (figure 5.6). The endmembers that both algorithms struggled with the most were the spectrally flat minerals; in the case of image 10b the quartz and magnesite spectra (figure 5.6) with the difficulty increasing with overall albedo. The algorithms compensated for this by extracting an additional match to one of the other endmembers to make up the correct number of endmembers and adjusting the relative albedos of the extracted endmembers in comparison to the input endmembers.

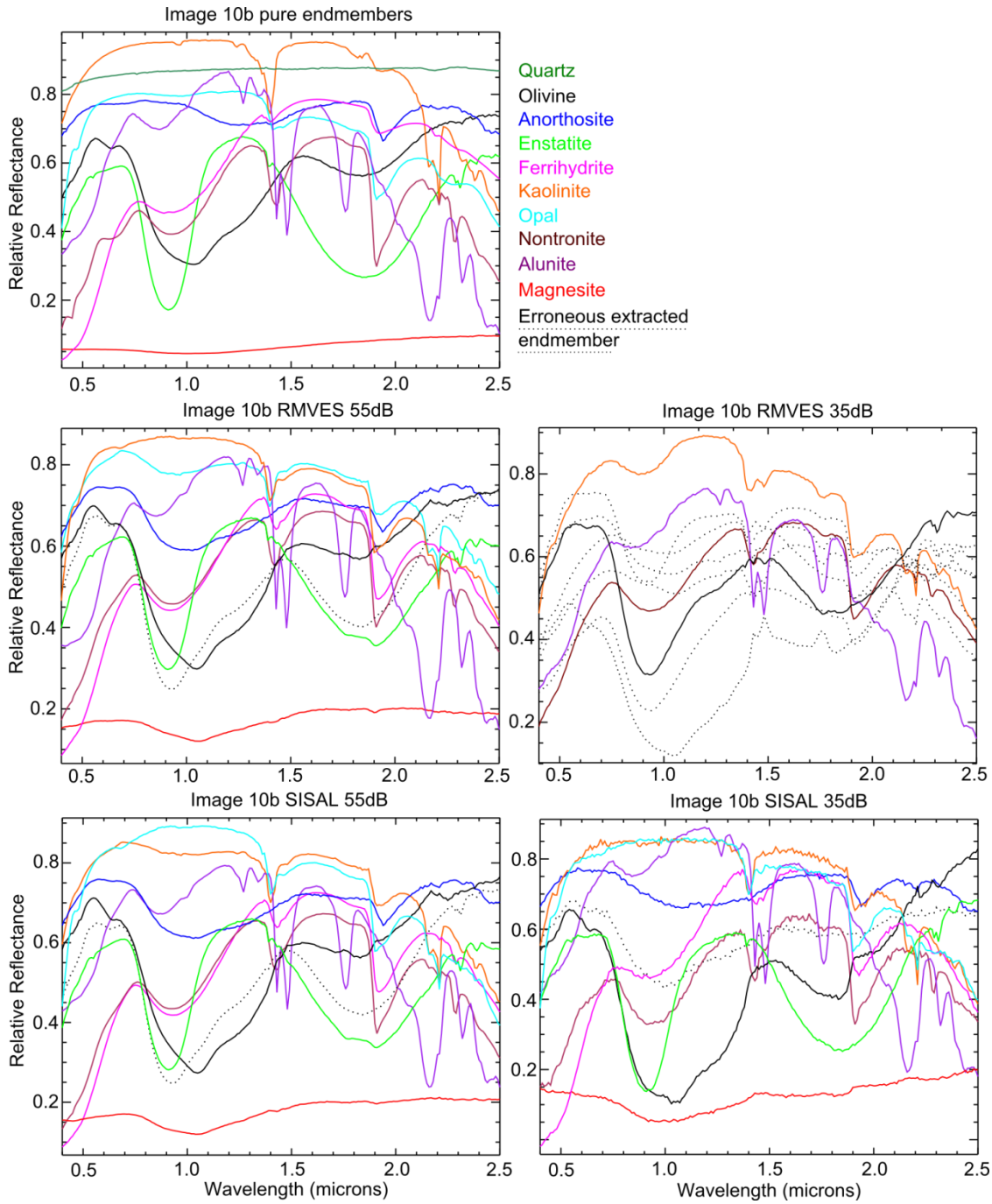

Figure 5.6: Image 10b endmembers extracted by SISAL and RMVES algorithms from versions with 35 dB and 55 dB SNR. At 55 dB both algorithms give comparable results failing to correctly extract just one endmember, the high albedo, and spectrally featureless quartz. The magnesite spectrum extracted by both has slightly exaggerated features but these are not enough to prevent correct identification. When the noise increases to 35 dB a clear difference between the two algorithms is obvious. Now SISAL returns the clearly superior results, again only failing to correctly extract the quartz endmember. Erroneous features are also now evident in a number of the other endmembers but not to the extent that the endmembers are

unidentifiable or misidentified. Of the RMVES endmembers only four (olivine, kaolinite, alunite and nontronite) are confidently identified and even they have erroneous features. The remaining six extracted endmembers appear to be mixtures of these and the other pure input endmembers.

5.4.2.5: Optimal EEA

At the end of these tests the most consistently accurate algorithms were SISAL and RMVES. However these two algorithms are not without their issues. Neither contains a restriction on the allowed reflectance values of the extracted endmembers. As long as the mixed pixels are reconstructed with the correct values they allow for the endmembers having relative reflectance values outwith the range 0 – 1. This is unrealistic and must be corrected for when attempting to attach mineral identities to the endmembers. The Matlab RMVES code used in this work incorporates a normalisation to this 'real' reflectance value range as a final step however the SISAL code does not.

Both SISAL and RMVES work by taking a random VCA selection of endmembers and then iteratively improving upon them to better encompass the dataset. The key difference between these two algorithms is the method used for this iterative improvement. Due to the random nature of this starting point both algorithms return slightly different results each time they are run on the same dataset. If the dataset is a relatively simple one with a small p value and high dB SNR these differences between runs are marginal and insignificant. If the dataset is more complex, with a large p value, these differences can be considerable, however if they are extracting the correct endmembers each time it should be possible to match the results from different runs to each other. It was found that the results (both SAM values and mineral matches) from SISAL and RMVES could be improved by running the algorithms at least p times on a dataset and then matching endmembers across the runs and averaging over these matching sets to produce a final endmember selection. In SISAL this had the added bonus of pulling the reflectance values back towards the 'real' value range if any endmembers were outside it in some of the runs as well as removing occasional obviously erroneous features in individual endmembers.

Adding this requirement of averaging over multiple runs to both SISAL and RMVES improved the extracted endmembers from both at all SNR values. This step also exposed a major difference between the two algorithms, namely the computational complexity and associated run time. Using image 10a.1 as an example each of the SISAL runs took less than 1 second,

whereas the RMVES runs took over an hour each. Given the requirement of a minimum of p runs this gives SISAL a clear advantage over RMVES.

SISAL, in common with the other algorithms looked at in section 5.4.2, does not include as part of its output any statistical error or goodness of fit values. However given the optimum use of the algorithm outlined this sub-section, using multiple runs over the same data to build up an average set of endmember spectra, a confidence test can be devised. The complex and noisy images demonstrated a much higher variation across the matching endmembers of different runs than those from the simpler and low noise images. Therefore a qualitative quality flag can be assigned to the extracted endmembers based on the level of variance within each one across the multiple runs with a low level pointing towards more accurate results.

5.4.2.6: Wrong p value

The results discussed so far only deal with the extraction of the correct number of endmembers. However the EDA sensitivity tests showed that none of the existing algorithms can guarantee to estimate the correct p value when dealing with a complex dataset such as for a hydrothermal environment as shown in the EDA results for image 10a and 10b. It is important therefore to gauge how much of a difference using the wrong p value will have on the extraction of endmembers. For this step SISAL was tested on image 10b (p = 10) using p = 9 (one less endmember) and p = 11 (one more endmember). SISAL has already been shown to be the most reliable of the algorithms tested and it is only at high p values that the ODM algorithm failed to identify the correct p value. Rather than the SAM values, the important aspect in this case is the ability to correctly identify the extracted endmembers. For the p = 9 endmembers four of the minerals known to be present were not identifiable in the resulting endmembers. Magnesite and quartz are both spectrally flat with few features in this wavelength range, therefore based on results already discussed it is not surprising that these were not extracted. However ferrihydrite and opal were also missing and these are minerals with sufficient distinguishing spectral features to expect the algorithm to find them. The four unmatched endmembers appear to be mixtures of the actual endmembers (both those identified in the other five extracted endmembers and those not) but assuming no *a priori* knowledge of these actual endmembers they could not be identified. Using p = 11 (one more than the true value) only two minerals are not identified, quartz and opal, with the additional extracted endmember being identified as olivine. Again the quartz result is consistent with previous tests. The opal is misidentified as montmorillonite. The two have very similar spectral morphology with the key difference being the sharpness of the 2.21 µm absorption,

this feature in opal should be broad but in the extracted endmember it is sharp, more closely resembling montmorillonite. The opal was correctly identified when using p = 10. The correct p value is important to the accuracy of the EEA but if the correct value cannot be estimated with a high degree of accuracy it is better to use an overestimate than an underestimate.

It is important to note the effect of noise in the data to the successful completion of this step in the unmixing chain. Unsurprisingly all of the algorithms gave worse results when the SNR was lower. CRISM was designed to have a minimum SNR of 400 or approximately 52 dB at 2300 nm. At 400 nm the SNR is expected to be at least 100 or 40 dB provided a sufficient integration time is allowed (Murchie et al., 2007). However these values were calculated when CRISM was a new instrument. As CRISM has aged its SNR has degraded (Bultel et al., 2015) and thus an algorithm that can cope with higher levels of noise is required. SISAL has been demonstrated to cope with a SNR as low as 35 dB even when the scene is complex provided there are no highly reflective, spectrally flat minerals present.

5.4.3: Abundance Estimation Algorithm (AEA) Results

The FCLLS algorithm was tested with the synthetic images in both RR and where appropriate SSA form. The FCLLS requires both the original image pixels and the endmember spectra as inputs. The synthetic images were tested using both the input 'pure' endmembers to test the best case results, and the SISAL extracted endmembers to establish how slight errors in endmember extraction could propagate through to errors in the abundance estimation step. Errors in pixel abundance estimation are presented as the percentage of the pixel that has been assigned to the wrong endmember. The accuracy of the algorithm was therefore evaluated based on the maximum and mean endmember pixel abundance errors for each image. Tables of full test results are presented in Appendix IV.

5.4.3.1: Number of endmembers (high p value)

Linear RR images 7b and 7c were tested at 25, 35, 45 and 55 dB noise levels using the pure input endmembers and the extracted SISAL endmembers. At SNR ≥ 45 dB even with p = 15 when using the correct endmembers the FCLLS was able to extract the abundances with an average maximum pixel error below 5%. The SISAL endmembers at p = 15 gave poorer results only dipping below the 5% average maximum pixel error at 55 dB. At the lowest SNR (25 dB) the pure endmembers returned errors as high as 20% and the SISAL endmembers as high as 30% on individual pixels.

5.4.3.2: Number of pixels (low N value)

Due to the way the algorithm works (on a pixel by pixel basis) this variable will have no effect on the final outcome and has therefore not been included in the sensitivity testing for this step.

5.4.3.3: Inter-endmember spectral variation

Using images 2a, 2b, 3a and 3b two levels of accuracy were investigated for the FCLLS algorithm when applied to the RR datasets based on the two p values in each image. The abundances for each individual endmember were calculated and the pixel abundance of each mineral type was also calculated. At low SNR the average maximum error on each individual endmember was high, using the pure endmembers in image 2b it was as high as 40% at SNR = 25 dB. However, even with data this noisy when the mineral species abundances rather than the individual endmember abundances were calculated the same dataset gave an average maximum pixel error of 2%. The algorithm is assigning weight to the wrong spectral endmember but still assigning the correct total amount to each mineral species. This pattern held across all 4 images. The SISAL derived endmembers in all cases above 25 dB or above were sufficiently accurate that the abundance results showed very similar average maximum pixel errors to those reported using the pure endmembers.

5.4.3.4: Non-linear mixing

Images 5 and 5b were used to test the assumption that the FCLLS when applied to a dataset containing non-linear mixing will return less accurate abundance estimations than for the identical endmembers in a purely linear mixture. In keeping with previously reported results in the literature this assumption proved valid at all noise levels investigated when using the pure input endmembers.

5.4.3.5: SSA conversion

The conversion to SSA prior to abundance estimation has been previously investigated by Mustard and Pieters (1989, 1987) using laboratory mixtures of powdered samples. They were able to show that provided the incidence and emission angles were known and that the particles were homogenous in size that the abundance estimations using least squares unmixing were greatly improved by converting the data to SSA prior to unmixing. Their work used a small number of purely non-linear intimately mixed samples. The spectra used in their paper are available from the RELAB spectral library and the FCLLS was tested on this small dataset (N = 16) in both RR and SSA versions. The SSA converted data did return better results (an average maximum error of 25% versus an average maximum error of 59% for the RR data) however this error is still significantly larger than that reported by Mustard and

Pieters. A key difference between their work and the work presented here is that they have dealt with each spectral mixture individually using only the two or three endmembers known to be present. They have not allowed their model to consider the presence of any endmembers that were not present in each individual spectral mixture. The work presented in this Chapter treated the 16 spectra as one whole dataset and therefore the algorithm was given all 4 endmembers present as potential components of each of the 16 datapoints despite the fact that none of the 16 input spectra contained all 4 endmembers. The method by which the SMA pipeline is to be employed to real remote sensing imagery means that the data must always be treated as a whole and it is highly unlikely that the exact endmembers of each pixel could be known prior to the abundance estimation step. Therefore the conversion of non-linear mixed reflectance data to SSA may yield more accurate abundances but not to the extent suggested in the literature.

The conversion to SSA was tested against purely linear mixtures to test whether or not it could provide an improvement on these mixtures and therefore potentially be applied universally. Images 2a and 3a at all SNR levels gave poorer abundance estimates using the SSA converted datasets compared to the results from the original RR datasets. This was true for both the abundances of each individual endmember and each mineral.

The synthetic images presented in this work that encompass non-linear effects are mixtures of linear and non-linear mixing. This is considered a realistic scenario that replicates a typical hydrothermally altered scene where there may be discrete patches of mixed soils lying next to each other. Image 5 with its linear mixture of non-linear mixtures gave a higher average maximum pixel abundance error after conversion to SSA. The same result was found with image 10b, a linear mixture of non-linear mixed spectra of 10 different endmember minerals; at a relatively high SNR (45 dB) when the abundances in this image were calculated from the RR dataset the average maximum pixel error was only 8% compared to the SSA conversion of the same image that returned an average maximum pixel error of 16%. The 28 non-linearly mixed spectra that were used to construct image 10b were also unmixed as a single N = 28 dataset and this time the SSA conversion did improve the results (average maximum error of 19% versus 23%). The SSA conversion does appear to improve the abundance estimation but only in the cases where the spectral mixing is purely non-linear and therefore can be modelled using the Hapke equation. When any element of linear mixing is present the SSA conversion diminishes the accuracy of the FCLLS.

5.4.3.6: Overall Scene Abundances

The results presented so far are based on the accuracy of estimating the endmember abundance in each individual pixel in an image. However it can also be useful to know the endmember abundance across the entire dataset/scene. The overall scene endmember abundances were calculated for image 10b and image 5 to investigate if the errors introduced in an individual pixel by the non-linear mixing were cancelling each other out over the entire datasets. For image 5 the scene errors when using the 'pure' endmembers at all noise levels were no more than 7% when using either the RR or SSA versions of the image. When using the SISAL endmembers for image 5, the conversion to SSA improved the scene abundance estimates down from an error of approximately 25% to 15% across all of the noise levels investigated. Image 10b showed a slightly different pattern. Again the overall scene abundance estimates appeared reasonably invariant to the level of noise present in the data for both the pure and SISAL endmembers with the pure endmembers returning a maximum error of 6% and the SISAL endmembers a maximum error of approximately 22%. This time however, the conversion to SSA resulting in higher errors in the case of both endmember sets.

The large errors in the abundances calculated using the SISAL endmembers in the high p value images all corresponded to the most poorly extracted endmembers. In the case of image 10b none of the extracted endmembers was identifiable as quartz and instead two were identified as olivine. This led to an over estimation of the olivine present and obviously no estimate of the level of quartz present. In a small scale hydrothermally altered environment it is expected that there will be a high number of endmembers and that they will be highly mixed in both linear and non-linear combinations. Under these circumstances provided the SNR of the data is high and the endmembers have been accurately extracted then using the FCLLS on the original RR data should result in overall scene abundances within 5% of the correct value. Individual pixel abundances may be significantly worse than this. If there are only a small number of endmembers ($p \leq 5$) SSA conversion should be applied to improve upon the overall scene abundances with the understanding that the individual pixel abundance estimates may suffer as a result. The primary source of error in the AEA step regardless of any of the variables discussed in this section is the accuracy of the endmembers extracted in the EEA step. If these are not correct the estimated abundances will be inevitably significantly skewed.

5.4.3.7: Errors and timing

The FCLLS algorithm used is computationally quick, taking no longer than a few seconds for even the largest number of pixels and the largest number of endmembers. Converting to SSA adds extra analysis time but is again a computationally quick process.

The results of the abundance estimations discussed here have been evaluated against the known abundances. In a real world scenario these abundances are unknown and the FCLLS algorithm outputs no diagnostic parameter that can be used to gauge the likely error on the results. In these cases where no groundtruth data is available to validate the abundance estimates the best confidence check is to rebuild the image from the extracted endmembers and estimated abundances using equation 4.1 and calculate the RMSE between the original image spectra and the pipeline spectra. Low values and a random distribution would indicate a high level of confidence in the final pipeline results.

5.5: Optimum pipeline based on results of synthetic image tests

The final SMA pipeline based on the results discussed above is therefore:

1. Ensure there are more pixels than spectral bands
    a. Attempt to include as many spectral bands as possible if they cover a wavelength range where key spectral features are expected to be found and don't coincide with any major atmospheric interference regions.
2. Clean the dataset as much as possible removing any excess noise but without removing potentially subtle surface absorption features.
3. Use ODM and HySIME to estimate the number of endmembers present.
    a. Expect that HySIME will overestimate the p value but as both are quick algorithms use both to clarify result.
    b. It is better to have a slight overestimate of the number of endmembers than an underestimate.
    c. A qualitative assessment of accuracy can be made from the output graphs of both algorithms, for an accurate p value ideally want both graphs to have sharp turning points at the relevant point for each, a sharp minimum for HySIME and a sharp plateau point for ODM.
4. Use SISAL to extract endmembers.
    a. Run a minimum of p times and calculate the spectral angle between each run to identify the matching sets across the runs.

b. Once identified, average across matching members to get a final endmember set. At this stage any obviously erroneous spectra can be removed.
    i. A rough guide to the quality of these spectra can be established at this point by looking at the variance in each endmember set, a small variance means a more accurate extraction.
c. If needed, normalise the endmembers to within 0 – 1 reflectance range. The data produced by this step however should only be used in order to feed the spectra into a spectral analyst tool to assign a mineral identify to each endmember. The original reflectance range values should be used in the AEA step even if they are unrealistic values themselves.

5. Use FCLLS to calculate the abundances.
    a. If the number of endmembers is low ($p \leq 5$) then convert to SSA prior to this step. SSA should only be used in circumstances where the incidence and emission angles are known to a high degree of confidence.
    b. Calculate area wide abundances from resulting data as these will be more accurate than the individual pixel abundances.
6. Reconstruct image using extracted endmembers and estimated abundances and calculate RMSE error between reconstructed image and original input image.
    a. Small errors with a random pattern give confidence that the pipeline has produced accurate results.

The lack of quantitative diagnostic goodness-of-fit statistics produced for any of the outputs in the pipeline is an issue. Steps are described that can give a qualitative/relative estimate of the level of confidence that the analyst should have in the outputs at each stage. The final RMSE check can give an indication as to the overall accuracy of the pipeline but this is still mostly qualitative. The minimum 5% error to be applied to the scene wide abundances is a reflection of this uncertainty and it should be borne in mind that it is a minimum and that the abundance errors on individual pixels could be much higher.

In opposition to the earlier stated limitation of SMA by Keshava and Mustard (2002) the pipeline presented here is capable of corrected unmixing scenes with up to 15 endmembers provided a number of caveats are met: i) none of the endmembers are high albedo and spectrally flat, ii) the SNR is high (> 35 dB) and iii) the spectral contrast across the dataset is high. Non-linear mixing between the endmembers is only a significant issue in the EDA and AEA steps, and if the number of endmembers is small (5 or fewer) it is not an issue for the EDA when using ODM. The step with the highest level of uncertainty is the abundance

estimation, partly because it relies on accurate results in the previous steps, but also because it appears to be heavily influenced by the mixture model involved. With high numbers of endmembers the level of confidence on the abundance estimation of individual pixels drops but provided the above caveats are met the scene wide abundances appear to be just as accurate (potentially as low as 5% error) as for low p value scenes when using the linear mixing model even if there is non-linearity within the scene although the individual pixel abundances can suffer from much higher errors.

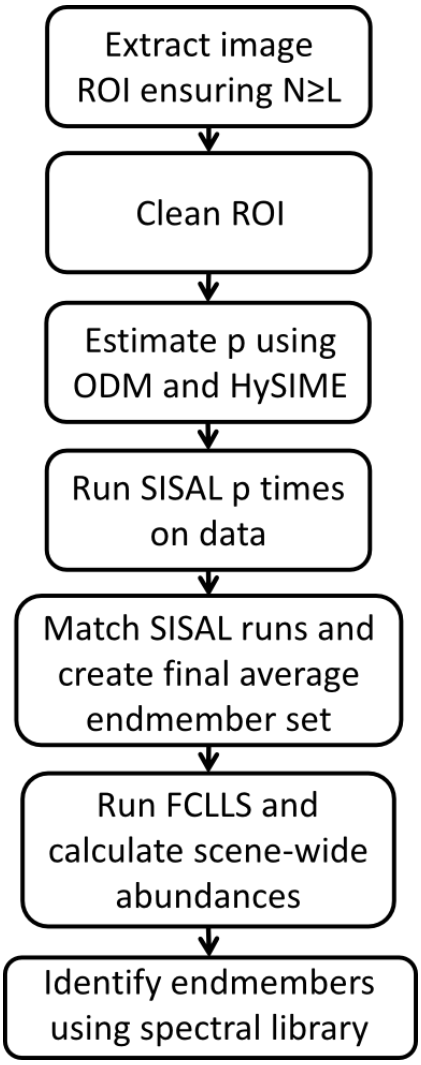

Figure 5.7: Flowchart detailing the optimum SMA pipeline for analysis of hydrothermally altered terrain.

5.6: Test on real data from Námafjall, Iceland

To fully understand the applicability and limitations of the above pipeline it is necessary to test it against real data with all of its inherent environmental and instrument noise. Two datasets were acquired covering Námafjall, the same region in Iceland dealt with in Chapter

3. The first is an aerial dataset and the second a groundbased dataset. Both datasets cover a similar spectral range and resolution. The full geological context and significance of the minerals present in this region is discussed in Chapter 3.

5.6.1: Aerial dataset[§]

Aerial datasets of the Námafjall region were acquired from the archived dataset IPY07-09 from the NERC Airborne Research and Survey Facility (ARSF), courtesy of the NERC Earth Observation Data Centre. The dataset was collected on 05/09/2008 from an altitude of approximately 1410 m using the two hyperspectral instruments operated by ARSF at the time of data collection: an AISA Eagle and an AISA Hawk. The Eagle is a VNIR hyperspectral sensor capable of collecting data spanning 400 - 970 nm at a maximum spectral resolution of 2.9 nm in a 1000 pixel swath. The Hawk covers 970 - 2450 nm at a maximum spectral resolution of 8 nm and a swath width of 320 pixels. The hyperspectral data were supplied as L1b data (non-georectified 'radiance at sensor'). The hyperspectral data was atmospherically corrected using the FLAASH module in Exelis Visual Information Solutions ENVI 4.8 (Exelis Visual Information Solutions, Boulder, Colorado) to generate ground surface reflectance values. These atmospherically-corrected datasets were then georeferenced to L3a level data using ARSF supplied software 'azgcorr' (Azimuth Systems UK, version 5.0.0, July 2005) and the supplied LiDAR DEM to a 2 m pixel resolution. The LiDAR operated by the ARSF at this time was an Optech Airborne Laser Terrain Mapper 3033. The LiDAR data was supplied as a final data product DEM supplemented with ASTER DEM data to fill any data gaps. Regions of significant atmospheric H_2O were removed from the final datasets leaving a total of 232 spectral bands.

5.6.2: Field dataset

A 2 m^2 grid was marked out over an 18 m by 18 m section of the flat altered soil plain partly imaged as A06_Soils in Chapter 3 (figure 5.8). At each 2 m intersection of the grid a spectrum was collected using an ASD Fieldspec Pro following the routine detailed in Chapter 3 section 3.3.3, adapted from the laboratory setting to the field. This grid provided a dataset to test the unmixing pipeline on and additionally demonstrated the level of mineralogical variation that could potentially be contained within a single CRISM pixel. An extra 20 spectra taken from nearby altered mounds with the same mineral composition were also included bringing the total dataset to 111 spectra. The raw data contained 2151 spectral bands. This was

[§] This paragraph is taken from Harris, J.K., Cousins, C. R., Gunn, M., Grindrod, P. M., Barnes, D., Crawford, I., Cross, R. E., Coates, I. A., Remote detection of past habitability at Mars-analogue hydrothermal alteration terrains using an ExoMars PanCam emulator., 2015, Icarus, 252, 284-300 and was written entirely by the author.

resampled to be a point every 0.02 µm spanning 0.4 - 2.5 µm, giving 106 spectral bands in total. This step was necessary for the application of the EDA step in the SMA pipeline that requires more data points than spectral bands.

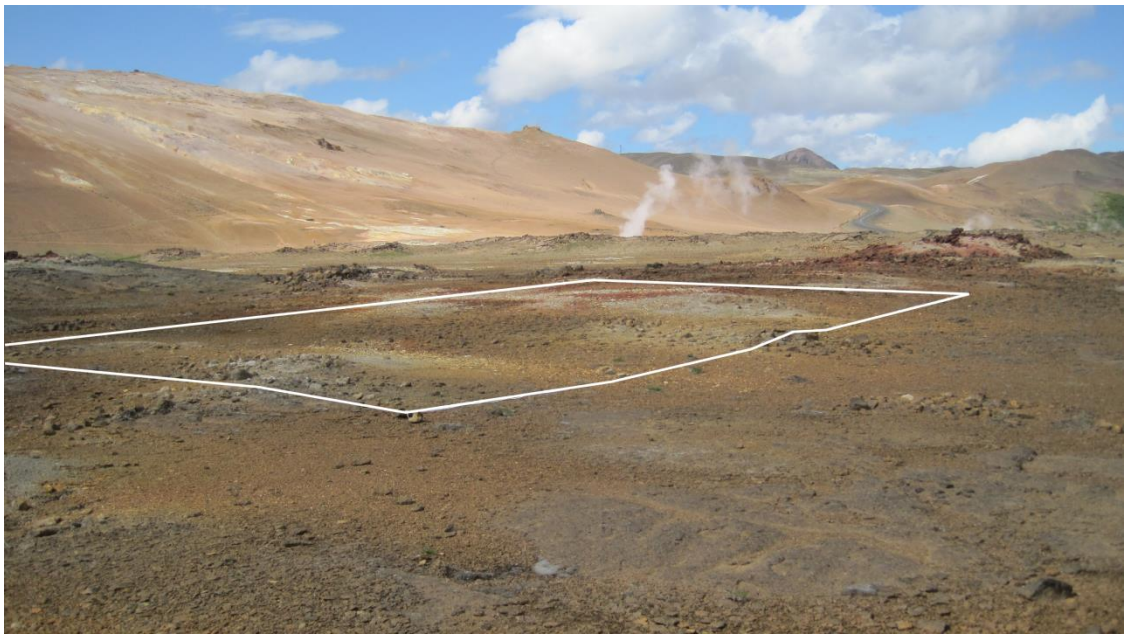

Figure 5.8: Field photo showing white outline of the 18 m by 18 m grid lain out on the flat altered plain. The top corner from this photographs point of view coincides with the ROI A06_Soils detailed in Chapter 3.

5.6.3: Groundtruth dataset

Each individual spectrum from the field dataset was examined using the Spectral Analyst tool resident in ENVI 4.8 to identify the minerals present. This identified the minerals present but gave no information regarding the abundances of each mineral in each point in the scene. In addition a number of rock and soil samples collected from within the grid and from across the plain were mineralogically analysed using qualitative XRD spectroscopy and laboratory VNIR reflectance spectroscopy. Full details of the 'groundtruthing' data collection and processing can be found in Chapter 3, section 3.3.3. The grid and associated plain region contained 12 – 14 minerals (table 5.2); gypsum, jarosite, anatase, andesine, augite, plagioclase, montmorillonite, hematite, sulfur, quartz, zeolite, goethite, kaolinite, and smectite. In some cases it was not possible to uniquely identify the specific member of a mineral species present with either the spectral or XRD analysis; this was a particular problem with samples that contained zeolite, plagioclase or smectite. This slight ambiguity is further evidence for the difficulty in uniquely identifying minerals in a hydrothermal environment, particularly using *in situ* data and technologies. A full quantitative analysis was not possible however a

rough idea of the prevalence of each mineral based on the number of samples that each mineral was present in enabled some judgement to be made as to the accuracy of the final AEA step in the pipeline.

Table 5.2: XRD and laboratory VNIR mineral identifications from the groundtruth samples collected from the altered plain region. Anatase is identified in a number of the XRD results but not in the VNIR results. Anatase is not a mineral that is contained in the USGS spectral library used in the VNIR identification process and therefore could not be identified using this method.

	Unit	**Bulk mineralogy (XRD, *VNIR*)**
A02_001	Dark red soil	gypsum, alunite, jarosite
		jarosite, nontronite
A02_002	Vesicle filled grey rock	andesine, augite, zeolite
		jarosite, goethite
A02_003	Bright alteration coating	jarosite
		jarosite
A02_004	Yellow soil	gypsum, alunite, jarosite
		nontronite, zeolite, jarosite
A02_005	White/grey soil	gypsum
		gypsum, montmorillonite
A02_006	Pink alteration coating	anatase
		saponite, zeolite
A02_007	Pink alteration coating	plagioclase
		microcline, goethite
A02_008	Dark red soil	montmorillonite, hematite
		sauconite, montmorillonite
A02_009	Alteration soil	sulfur, anatase
		sulfur
A02_010	Brown compacted soil	plagioclase
		smectite
A03_001	Grey slab	plagioclase, anatase
		microcline, perthite
A03_002	White soil	gypsum
		gypsum, zeolite

A03_003	Yellow soil	gypsum, jarosite
		jarosite, nontronite, gypsum
A03_004	Coarse grey soil	alunite, sulfur (trace)
		montmorillonite, zeolite
A03_005	Bright brittle slab	sulfur
		sulfur, microcline
A03_006	Red soil	hematite, sulfur, jarosite
		hematite, nontronite
A03_007	Brown compacted soil	plagioclase, augite
		perthite, smectite
A03_008	Brown soil	quartz, jarosite, augite, sulfur (trace)
		nontronite, ferrihydrite
A03_009	Pink alteration coating	jarosite, augite, hematite
		smectite, zeolite
A03_010	Peach alteration coating	jarosite, anatase
		nontronite, goethite
A06_001	Bright-toned unit	sulfur, anatase
		nontronite, montmorillonite
A06_002	Bright-toned unit	sulfur, zeolite
		sulfur
A06_003	Dark red unit	hematite, natrojarosite, augite, sulfur (trace)
		hematite
A06_004	Bright-toned unit	sulfur, zeolite
		sulfur
A06_005	Dark red unit	natrojarosite, sulfur, zeolite
		goethite, montmorillonite
A06_006	Bright-toned unit	sulfur
		nontronite, montmorillonite

5.7: Iceland data results

5.7.1: Aerial data

The full pipeline was applied to an ROI extracted from the aerial data (figure 5.9) at three different pixel sizes; 2 m, 4 m, and 18 m. These different pixel sizes were achieved by simple amalgamation of neighbouring pixels using a nearest neighbour technique within ENVI 4.8. The 2 m pixel image was the highest spatial resolution available of the data and the down-sampled larger pixel images were constructed to test if differences in spatial resolution would have a significant impact of the results of the unmixing pipeline. The SMA pipeline was applied to each pixel size ROI in turn. The ODM algorithm begins with an estimate of the noise present in the data and this value was largest for the 2 m pixel data. Random noise will have been slightly smoothed out in the 4 m and 18 m datasets leading to their lower noise estimation.

Table 5.3: EDA values for the aerial Iceland dataset. The ODM algorithm is returning a p value within the value range expected given the groundtruth sampling of the region. The HySIME is greatly overestimating as was expected given the structural and morphological variation on the ground.

Pixel size (# of pixels)	HySIME	ODM
2 m (17097)	54	11
4 m (4312)	68	10
18 m (282)	40	13

In every case the HySIME greatly overestimated the number of individual minerals. However it is possible that what it is picking up on is inter-mineral variation, e.g. differences in textures and particle orientations and slight geochemical variations from distinct locations across the scene. The synthetic image tests detailed in section 5.3 demonstrated that this inter-endmember variation is something that HySIME in particular is sensitive to. All of the ODM results are roughly consistent with the groundtruth data.

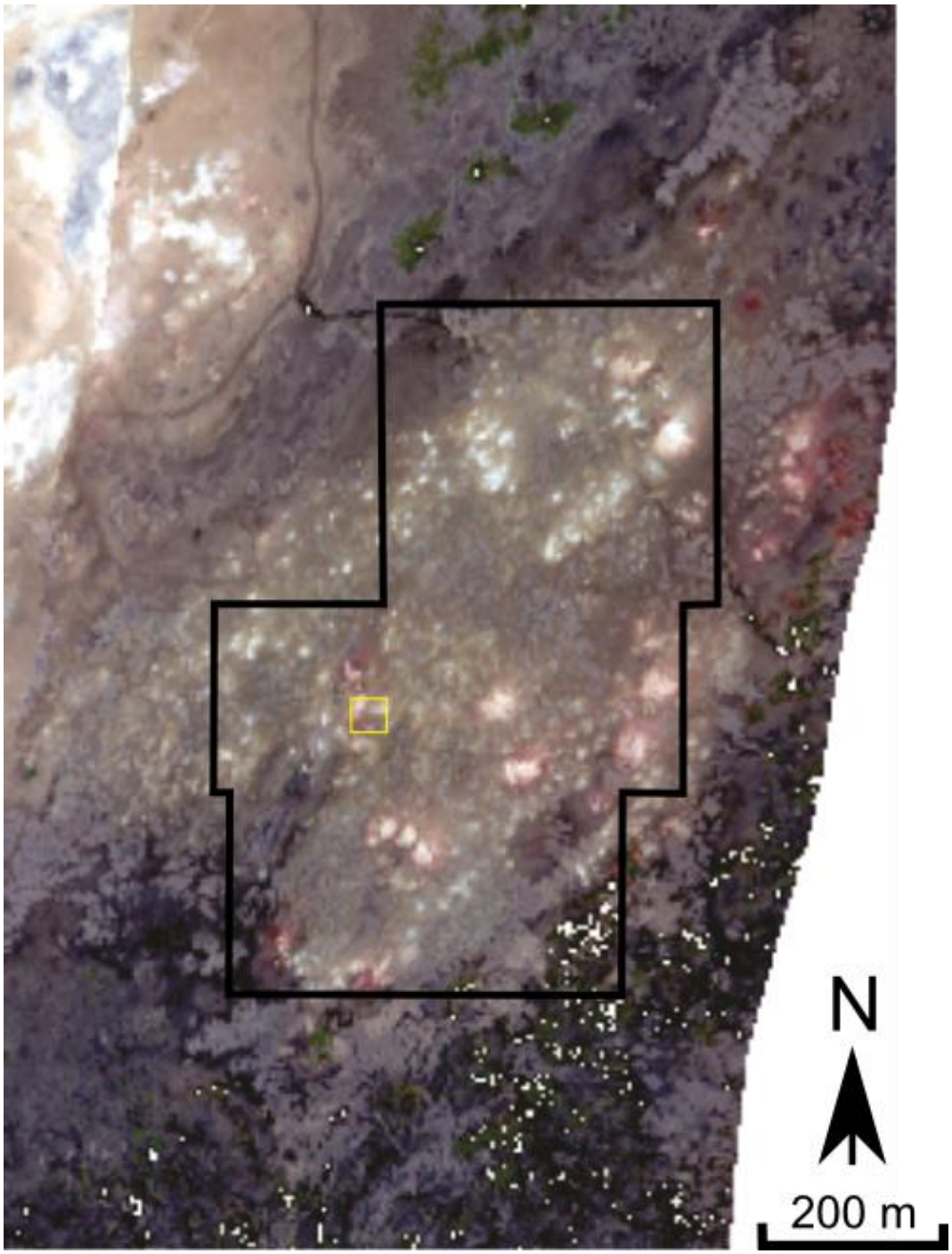

Figure 5.9: Eagle RGB (bands 638.7, 548.4, 461.4 nm) 2 m pixel image with the extracted RIO outlined in black. The yellow box indicates the location of the 18 m^2 grid of groundbased data.

The ODM p values were fed into the EEA step of the pipeline and for each pixel size all but one of the endmembers were unidentifiable (figure 5.10). Using the 2 m pixel data the only identifiable endmember is ARSF_6 which has a clear vegetation spectral signature. Vegetation's identifying spectral features are all in the 0.4 – 1 µm wavelength range unlike the majority of the minerals present in a hydrothermal environment. A number of the other

endmembers showed evidence of iron oxide in the visible portion of the wavelength range, ARSF_1, 2 and 8 in particular, but are otherwise swamped by a liquid H_2O spectral signature prevalent across the scene. Given the location, the time of year the data were collected (September) and the active hydrothermal fumaroles and pools in the local vicinity the entire scene was unsurprisingly saturated with surface water despite there being no water bodies within the ROI. The wavelength regions that would show the strong water absorptions were removed due to the risk of uncorrected atmospheric interference although the edges of these atmospheric regions still show the beginnings and endings of strong absorption features. This water saturation is seen therefore as the overall spectral shape of each realistic endmember that peaks around 0.7 - 1.0 µm and then shows a steeply negative continuum slop with increasing wavelength. This strong water signature in the infrared appears to be what is obscuring the spectral variety known to be present even at the 2 m pixel resolution. Due to the failure of the pipeline to produce identifiable results at this stage for any pixel size the final AEA step was not performed.

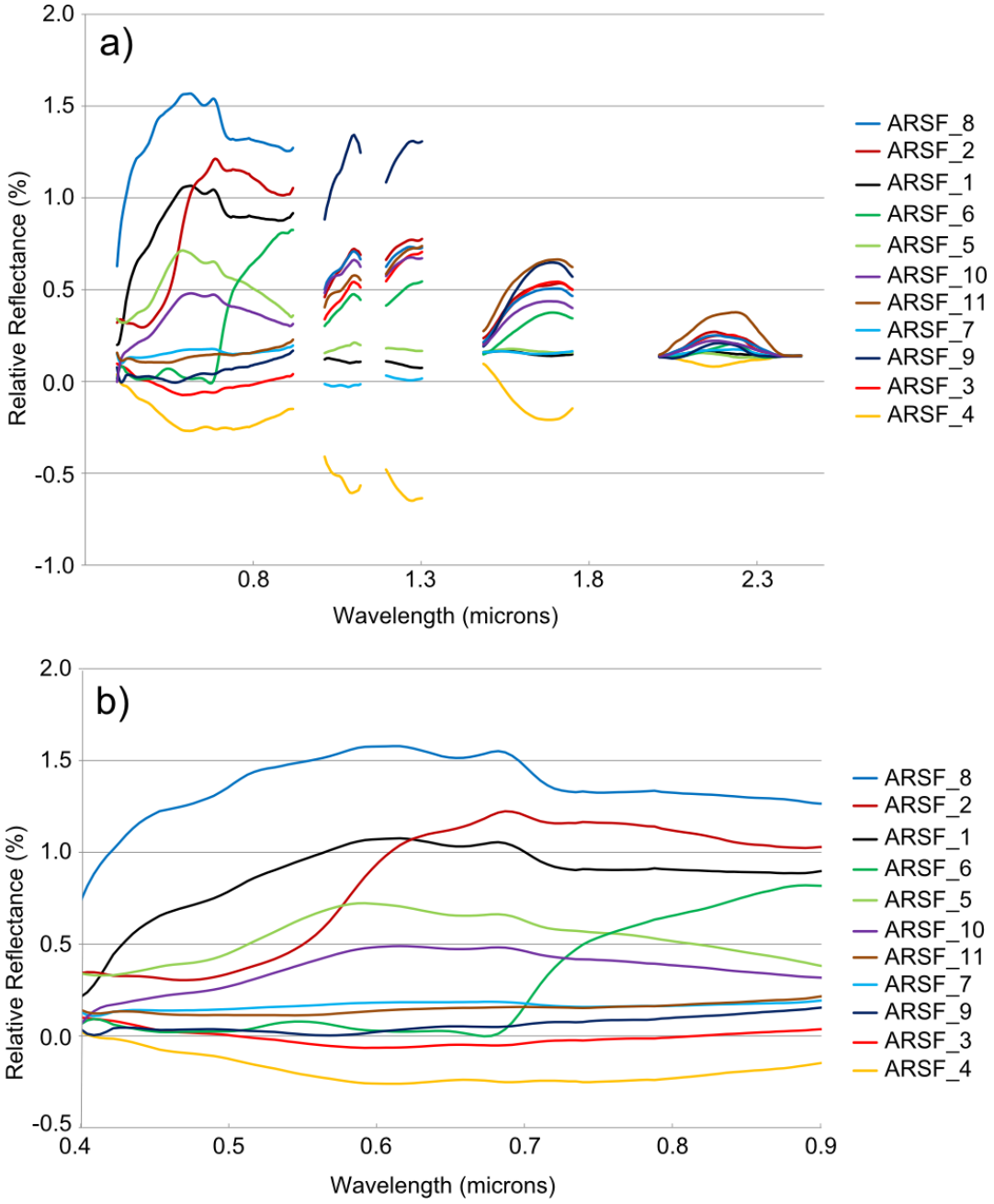

Figure 5.10: Mean SISAL extracted endmembers from the 2 m pixel ARSF ROI. a) Full spectral range, gaps show where significant regions of atmospheric interference have been removed, b) Eagle only data where the majority of the variation is seen. ARSF_8, 2 and 1 show high red:blue ratios indicating the presence of Fe-bearing minerals. ARSF_6 is a vegetation spectrum; it is the only uniquely identifiable endmember. ARSF_4 and ARSF_3 are not realistic looking spectral signatures. Similar endmembers to this set were extracted from the 4 m and 18 m ROI's. Key spectral features are expected in the 1.9 – 2.5 µm portion of the spectrum however the heavy presence of water has significantly diminished the albedo of this region and obscured any diagnostic mineral absorptions.

5.7.2: Field data

The full pipeline was applied to the N = 111 and L = 106 dataset. The EDA returned values of:

HySIME = 27

ODM = 14

Due to the small value of N this overestimate from HySIME was to be expected. The fact that it is not higher reflects the high SNR of the dataset. The ODM value is consistent with the groundtruth dataset that revealed 12 – 14 different minerals in the region. The EEA step was run using p = 14, the ODM estimated value (figure 5.11). Identification of the resulting endmembers was performed using the Spectral Analyst tool within ENVI 4.8 and the inbuilt USGS spectral library (table 5.4). Of the resulting endmembers one was unidentifiable (ASD_10) and one was judged to be an addition of the algorithm to reconcile the albedo changes across the dataset likely due to imperfectly corrected heterogeneous atmospheric components across the scene and not a real mineral endmember (ASD_4). The remaining 12 endmembers were all positively identified as minerals (or members of a mineral species) present in the groundtruth dataset (table 5.2) with the addition of opal. This mineral however was detected in samples from other ROIs in the Námafjall region (see Chapter 3, table 3.5) and is thus considered a realistic identification for this dataset given the small overall scene abundance of the opal endmember (ASD_3). One endmember was not uniquely diagnosed, potentially matching to two different minerals, opal and montmorillonite, both of which were also identified as matching to two other endmembers. In total 11 minerals were identified. The unreal endmember was removed and the remaining 13 were run through the AEA step.

The scene abundances appear to match reasonably well with the groundtruth with the dominant minerals being iron oxides and hydrated sulfates and silicates, the minerals most often identified in the grid manual analysis. The RMSE value for the entire dataset is 0.0154 with a peak in one spectral point of 0.072 and no discernible pattern with respect to the minerals known to be present in the ground samples (figure 5.12). This suggests that there is no systematic error lending confidence to the endmember extraction routine. The results of the synthetic image sensitivity tests suggest that a minimum error of 5% should be applied to these whole scene abundance results with higher errors expected in individual pixels such as the one with the high RMSE value. Again as with the aerial data nearly every endmember shows evidence of the presence of H_2O with significant absorption bands at 1.4 and 1.9 μm but without the strong negative general slope in the infrared (figure 5.11). The weather at

Námafjall in the two to three days prior to the collection of the field dataset had been dry and thus the scene was not saturated with liquid water and the absorption bands at 1.4 and 1.9 µm are interpreted as evidence of O-H and H_2O within the endmember minerals rather than liquid water in the surface. Both hematite and goethite can be formed as a direct result of hydrothermal alteration of basaltic materials, and also as a secondary mineral product due to weathering of iron rich soils and rocks. Thus the dominance of these iron oxides is interpreted as a result of the fact that the spectral data is sampling the top few microns of the surface soil where the heaviest weathering is occurring and thus picking up on both primary hydrothermally altered soils and secondary mineral production due to weathering.

Table 5.4: Endmember identifications and overall scene abundance percentages from the field data spectral dataset taken from the region highlighted in figure 5.7.

Endmember	Mineral match	Scene abundance (%)
ASD_1	Gypsum (hydrated sulfate)	9
ASD_2	Erionitmite (zeolite)	3
ASD_3	Opal (hydrated silica)	5
ASD_4	Unreal	N/A
ASD_5	Rutile (titanium dioxide)	4
ASD_6	Hematite (iron oxide)	2
ASD_7	Sulfur	2
ASD_8	Saponite (phyllosilicate)	5
ASD_9	Montmorillonite (phyllosilicate)	3
ASD_10	?	5
ASD_11	Ferrihydrite (iron oxide)	25
ASD_12	Goethite (iron oxide)	28
ASD_13	Microcline (alkali feldspar)	7
ASD_14	Montmorillonite or opal	2

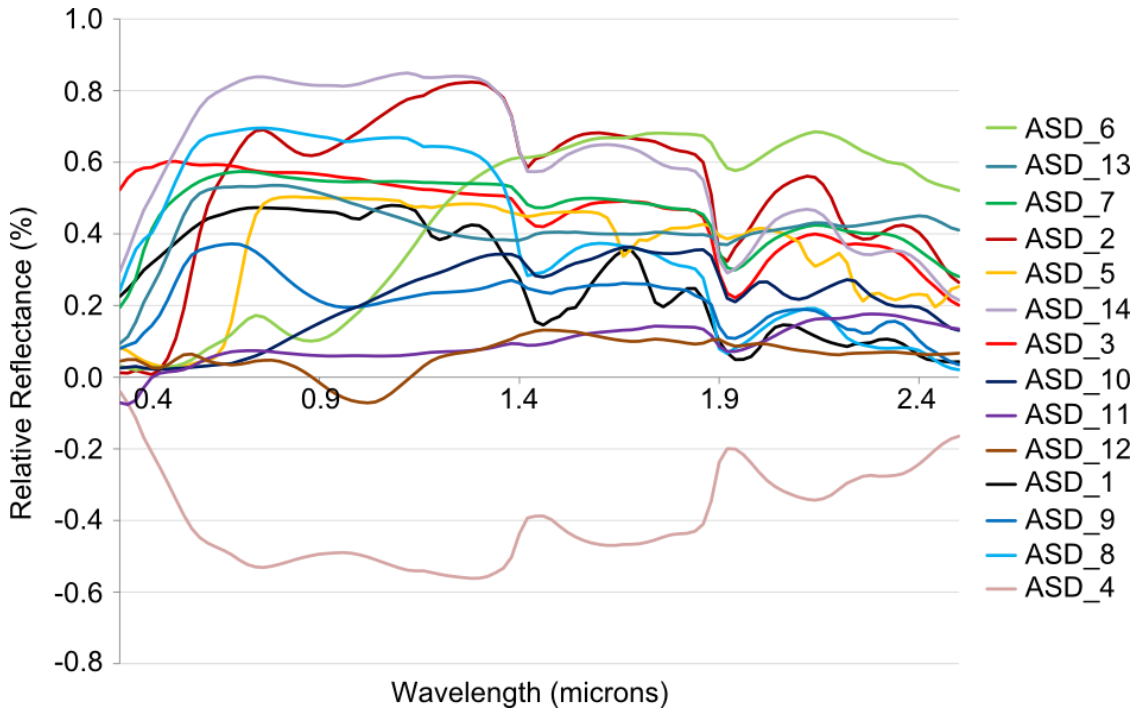

Figure 5.11: Mean SISAL extracted endmembers from ASD field spectrometer dataset prior to normalisation to the 0 – 1 reflectance range. The entirely negative endmember ASD_4 is interpreted as an artefact of the SISAL process attempting to minimise the fit error in the dataset within the p value given and was removed from the final endmember set fed into the FCLLS step. It does not match the spectral signature of any natural material in the available spectral libraries. The slightly negative absorption at ~1.0 µm in ASD_12 is a result of SISAL not constraining the extracted endmembers to the 0 – 1 relative reflectance range and is not an error; normalisation of this endmember yields a realistic spectral signature matching to goethite. Identifications of all endmembers shown are given in table 5.4.

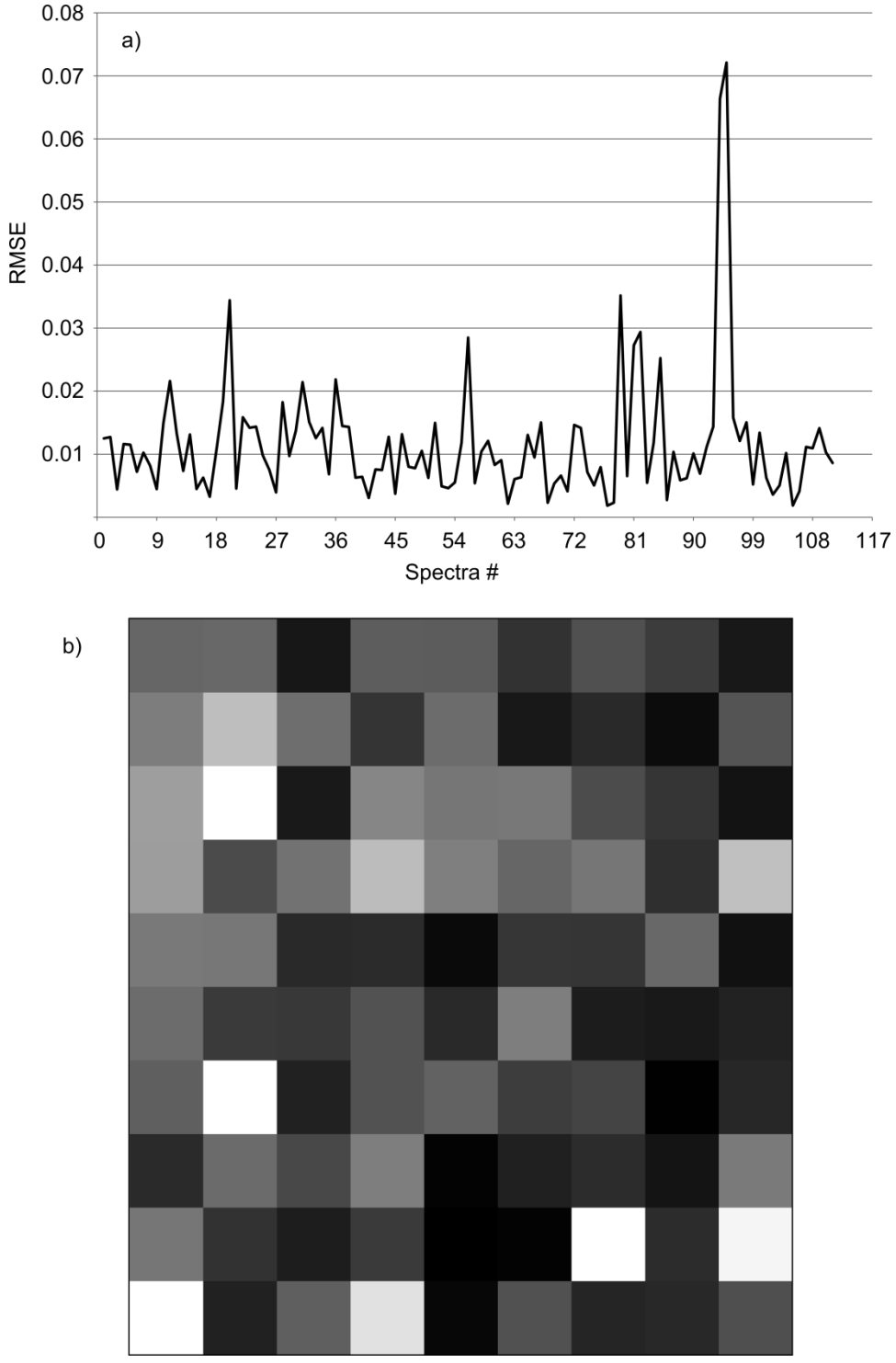

Figure 5.12: RMSE values showing the error between the original ASD dataset and the dataset reconstructed from the pipeline extracted endmembers and estimated abundances. a) a graph of the RMSE values for each point in the dataset, b) the RMSE values for the grid in the correct spatial layout showing a random distribution with the pixels with the highest error having no endmember or mineral composition in common.

5.8: Discussion of differences between synthetic sensitivity and Iceland results

There are a number of key differences between the two Iceland datasets and the synthetic images which feed into the interpretation of the results of both. The immediate difference is the environment in which they were taken. The spectral library data used in the synthetic images were collected with a similar instrument to the Iceland field data but under controlled laboratory conditions. In addition all of the spectral library samples were powdered prior to collection of their spectra (Clark et al., 2007; Pieters and Hiroi, 2004). This has been shown (Clark, 1999) to alter a mineral's reflectance spectrum, mainly with respect to general albedo and peak reflectance values. The aerial data has the added complication of significant atmospheric interference that must be dealt with. A full physics based method (FLAASH (Adler-Golden et al., 1998)) was used to remove the atmospheric contribution to the signal, but without coincident ground spectra to compare the results to it is not guaranteed that all the atmospheric signal was successfully removed. The EDA step appeared reasonably insensitive to noise (both HySIME and ODM explicitly estimate the noise present and account for it) and as such returned reasonable results for the synthetic and both the aerial and field spectrometer datasets that were largely invariant to noise. The major difference between the synthetic image results and the real scene results was seen in the EEA step. The aerial Iceland dataset showed a single overarching spectral shape due to the presence of liquid water across the scene. This was most likely due to a combination of incompletely removed atmospheric water vapour and a high level of water in the surface soils due to recent rain. This signature was so strong as to swamp any other identifiable spectral features. In the case of the field data the absorption bands due to H_20 and/or O-H were seen in every data point and in most of the extracted endmembers but the general spectral shape due to liquid water was not present and thus these hydration features were confidently interpreted as evidence of hydrated mineral species and not surface water. This overarching environmental spectral shape is not an issue that arose in the synthetic data due to the laboratory environmental setting of all of the samples. As a technique to use on Mars, a dominating liquid water signature such as seen here will not be an issue, but there is still the possibility of one general environmental signature swamping out the mineral variation on the surface. On Mars this would be the ubiquitous dust coverage (Christensen, 1988; Szwast et al., 2006). This surface and atmospheric dust is a long standing issue with any VNIR spectral imaging analysis of the surface of Mars, and there are spectral parameters designed specifically to perform a quick assessment of the level of dust coverage in an individual image (Pelkey et al., 2007; Ruff and Christensen, 2002; Viviano-Beck et al., 2014). This would enable an analyst to quickly establish if an image is suitable for the application of the SMA pipeline presented in this work.

In order for SMA to be confidently applied to martian data the level of dust in the pixels being analysed needs to be low.

5.9: Future work

Both HySIME and ODM rely on an estimation of the noise present in the dataset as a first step. The noise estimation code used in this work contained the assumption that the noise could be modelled as either Gaussian or Poisson with the option to specify which. In real data neither of these assumptions are valid with the noise typically taking on a more complex shape. Incorporating more accurate methods for estimating the noise should improve the EDA step in the pipeline. An additional step that could greatly improve the abundance estimations would be establishing a method to determine the mixing model of each pixel, whether it is an intimate non-linear mixture or a linear mixture or even a combination of the two. This is an acknowledged problem within the signal processing and remote sensing communities and some work has been attempted however the majority of the algorithms developed are based on the assumption of specific mixture models that may not be accurate in every case (Altmann et al., 2013c; Broadwater and Banerjee, 2011; Dobigeon et al., 2014; Imbiriba et al., 2014). Finally, a quantitative estimate of the error introduced in each step in the pipeline should be established.

5.10: Summary

In this chapter I have presented the development of a full spectral unmixing pipeline with specific focus on the spectral complexities inherent in small scale hydrothermally altered surface environments. A number of publically available algorithms covering each of the three steps required for full unmixing were applied to a series of synthetic images to test their sensitivity to a suite of spectral issues. At each stage the most consistently accurate algorithm was selected and any caveats with respect to its application noted. The final pipeline was then applied to two sets of hyperspectral data taken from the Námafjall region in Iceland detailed in the Chapter 3. These tests on both real and synthetic datasets demonstrated that provided the spectral image being analysed has a high SNR and no single overarching environmental signature, it should be possible to estimate the number of minerals present, extract their spectral signatures and estimate their overall scene abundance to within 5% accuracy.

Chapter 6: Application of Spectral Mixture Analysis on hydrothermally altered regions on Mars

6.1: Introduction

Chapter 5 detailed the development of a full spectral unmixing pipeline optimised for complex, small scale hydrothermal deposits utilising freely available algorithms. This approach was then validated using synthetic images constructed from spectral library data and hyperspectral data from the Námafjall region in Iceland. This chapter shall cover the application of this pipeline to regions on Mars which have been previously postulated to have experienced hydrothermal alteration. Issues of data availability and the general applicability of the pipeline to CRISM data shall also be discussed.

6.2: Data collection

The selection of potential hydrothermal deposits for analysis using the SMA pipeline developed in Chapter 5 is based on two factors; 1) selecting areas that have been found to show evidence of past hydrothermal activity either through spectral data and/or structural features and 2) the availability of CRISM coverage over these regions that is of sufficient quality (i.e. relatively dust free with a high SNR) for SMA.

6.2.1: The Compact Reconnaissance Imaging Spectrometer for Mars (CRISM)

The Compact Reconnaissance Imaging Spectrometer for Mars (CRISM) is a VNIR and shortwave infrared (SWIR) imaging spectrometer on board NASA's Mars Reconnaissance Orbiter (Murchie et al., 2007). The instrument has been operational since autumn 2006 returning thousands of hyperspectral images covering the spectral range 0.362 – 3.92 µm at 6.55 nm resolution in that time. This range is split between two internal spectrometers; the Shortwave VNIR spectrometer covering 0.362 – 1.053 µm and the Longwave IR spectrometer covering 1.002 – 3.92 µm. The incoming light is collected through a 10 cm diameter Ritchey-Chretien telescope and directed through a gold-plated nickel slit. The radiation is then fed through a beam-splitter to two Offner convex-grating spectrometers. The VNIR spectrometer is comprised of a silicon photodiode detector array with a fixed mounted filter to block higher orders from the grating. The IR spectrometer comprises an HgCdTe detector array with a fixed-mounted three-zone filter that blocks higher orders from the grating as well as thermal background radiation. Internal calibration systems monitor bias, dark current, thermal background, detector nonuniformity and behind slit responsivity. Fuller technical details can be found in Murchie et al., (2007). At 300 km altitude the spatial resolution when operated in Full Resolution Targeted (FRT) mode is 18 m/pixel (Murchie et al., 2007). This is achieved

through use of a mechanical gimbal that allows the camera to track targets on the surface as it flies overhead, removing the bulk of the image blur due to motion. CRISM data is publically available as Targeted Reduced Data Records (TRDR) processed through the internal team software (current version TRR3) to produce calibrated radiometric data in units of I/F. I/F is defined as "the spectral radiance divided by the solar spectral irradiance of the Sun at Mars distance divided by p [*p = angle of incidence*]. Another way to put it is that it is the ratio of the radiance observed from a surface to that of a perfect white Lambertian surface illuminated by the same light but at normal incidence." (Bennett et al., 2011).

CRISM was designed to have a SNR of 400 (approximately 52 dB) at 2300 nm and 100 (approximately 40 dB) at 400nm and > 2700 nm. The level of noise expected is not consistent across the instrument's spectral range, varying with wavelength. SNR estimates are based on system responsivity without any system binning and therefore include all instrument noise expected during an average target collection. However these estimates were made assuming optimal viewing geometry and the actual SNR for each measurement will vary with integration time, illumination angle and target surface reflectance (Murchie et al., 2007). Additionally as discussed in chapter 5, section 5.4.2.6 these SNR estimates were made when the instrument was new and it is expected that they will have deteriorated slightly over the years the instrument has been in service, primarily due to degradation of the cooling system (Bultel et al., 2015; Parente et al., 2010). Deterioration of the SNR due to failing of the cooling system means it is the IR section of the data that will be most affected with Bultel et al (2015) estimating that the SNR at 2300 nm in images taken in 2012 is closer to 200 than 400 whilst the SNR at 400 nm remains unchanged.

Basic processing of CRISM I/F images is possible through the CRISM Analysis Toolkit (CAT) (CRISM, 2013). CAT is a plug-in for the software ENVI written in the IDL programming language. It is a publically available toolkit and the standard method for processing CRISM images within the planetary science community. CAT contains tools to convert I/F data to radiance and perform photometric correction, remove data spikes and stripes in the images, remove the major atmospheric CO_2 contributions to the images and to georeference the images to a Mars datum. The photometric correction is particularly important as the angle of incidence can alter the general shape of a spectral reflectance signature and to a lesser extent the depth of any absorption bands. However this is only a significant effect at extreme angles far from nadir (Clark, 1999). Such angles can occur within a CRISM image due to variations in local topography. A photometric correction is performed prior to public data release that uses the MOLA global DEM dataset to correct for slope within each pixel. The

photometric correction that is performed as a tool in CAT is a simple cosine correction using the angle of incidence. This assumes a lambertian scattering behaviour from the scattering surface which has been shown to be a reasonable assumption for most low albedo martian surfaces (Bultel et al., 2015). In addition to all of these pre-processing tools CAT allows the quick production of the spectral parameters listed in Pelkey et al. (2007). CAT version 7.2.1 has been used in the work presented in this thesis.

6.2.2: Selection of hydrothermal targets

Chapter 2 discussed a number of locations on the martian surface that have been identified as regions that have hosted hydrothermal systems in their past. NASA's Planetary Data System (PDS) Geoscience node together with the CRISM data map hosted by the Applied Physics Laboratory at Johns Hopkins University (http://crism-map.jhuapl.edu/) were searched for available CRISM images over locations already postulated to have been hydrothermally altered (Cousins and Crawford, 2011; Schulze-Makuch et al., 2007; Skok et al., 2010). Data were restricted to images with both Short (VNIR) and Long (IR) detector coverage and preference given to those collected as Full Resolution Targeted (FRT) mode. CRISM images with overlapping temporally coincident HiRISE imagery were given further preference. The HiRISE images were important in enabling an initial visual inspection at a higher resolution in order to determine textural and structural features that may point towards significant spectral variation. Additionally when the HiRISE images were temporally coincident they give a quick method of estimating the level of dust present on the surface. In instances where no suitable FRT CRISM images were available covering the full spectral range, Half Resolution Targeted (HRT) images were examined for feasibility. These HRT images cover the same spectral resolution as the FRT CRISM images but with half the spatial resolution, i.e. 36 m^2 pixels versus 18 m^2 pixels.

Initial examination produced four regions of Mars with suitable CRISM coverage (figure 6.1), three of which have been investigated by previous researchers and shown to have likely experienced hydrothermal activity at some point in their history. These three regions are: 1) Aromatum Chaos [-1.03° N, 317.03° E], 2) Nili Patera [8.97° N, 67.17° E], and 3) Hecates Tholus [32.12° N, 150.24° E]. A fourth region covering a small unnamed crater was also examined [17.367° N, 291.213° E]. High energy impacts can trigger the formation of short-lived hydrothermal systems (Osinski et al., 2013), and the crater in question showed a number of interesting bright patches near the central uplift structure of the crater in HiRISE images that warranted further spectral investigation. Of the four examined regions, one CRISM image from each area was selected based on an initial visual inspection of the spatially

corresponding HiRISE and CTX coverage; this allowed for a first assessment of the potential spectral diversity present. With the exception of Nili Patera the regions analysed in this Chapter have not been subject to much, if any, previous in-depth, high resolution spectral or mineralogical analysis.

6.2.3: CRISM data processing

Once suitable CRISM images were selected they were processed to produce cleaned, atmospherically corrected, georeferenced final products. The tools necessary for standard pre-processing of CRISM images are available within the CRISM Analysis Toolkit (CAT) plugin for ENVI 4.8. All images were photometrically corrected, random data spikes were removed using the Cirrus despike tool and linear stripes due to detector pixel variations removed using the MRO Destripe tool. Finally the image cubes were map projected and a number of bands removed. The common bands removed from all four images were those identified as potentially problematic by Murchie et al (2009) and include VNIR bands < 442 nm, 644 – 684 nm, and 970 – 1023 nm, and IR bands < 1047 nm , 1648 – 1665 nm, and bands > 2660 nm. Additional bands were removed based on visual inspection for each individual image and are noted where relevant in the following region-specific discussions. Due to the size of each CRISM image smaller ROI's of approximately 1 – 2 km^2 were selected from each viable processed CRISM image based on the visual level of variability evident in spatially coincident colour (where available) HiRISE images from each region. It is these ROIs that were processed through the SMA pipeline. As discussed in Chapter 5, the higher the number of endmembers present in a scene the longer the SMA pipeline takes to perform and the lower the accuracy of the results at every stage. In the following results any band centres identified are considered to have an error of ± 0.01 μm, the average spectral sampling of the instrument (Murchie et al., 2007).

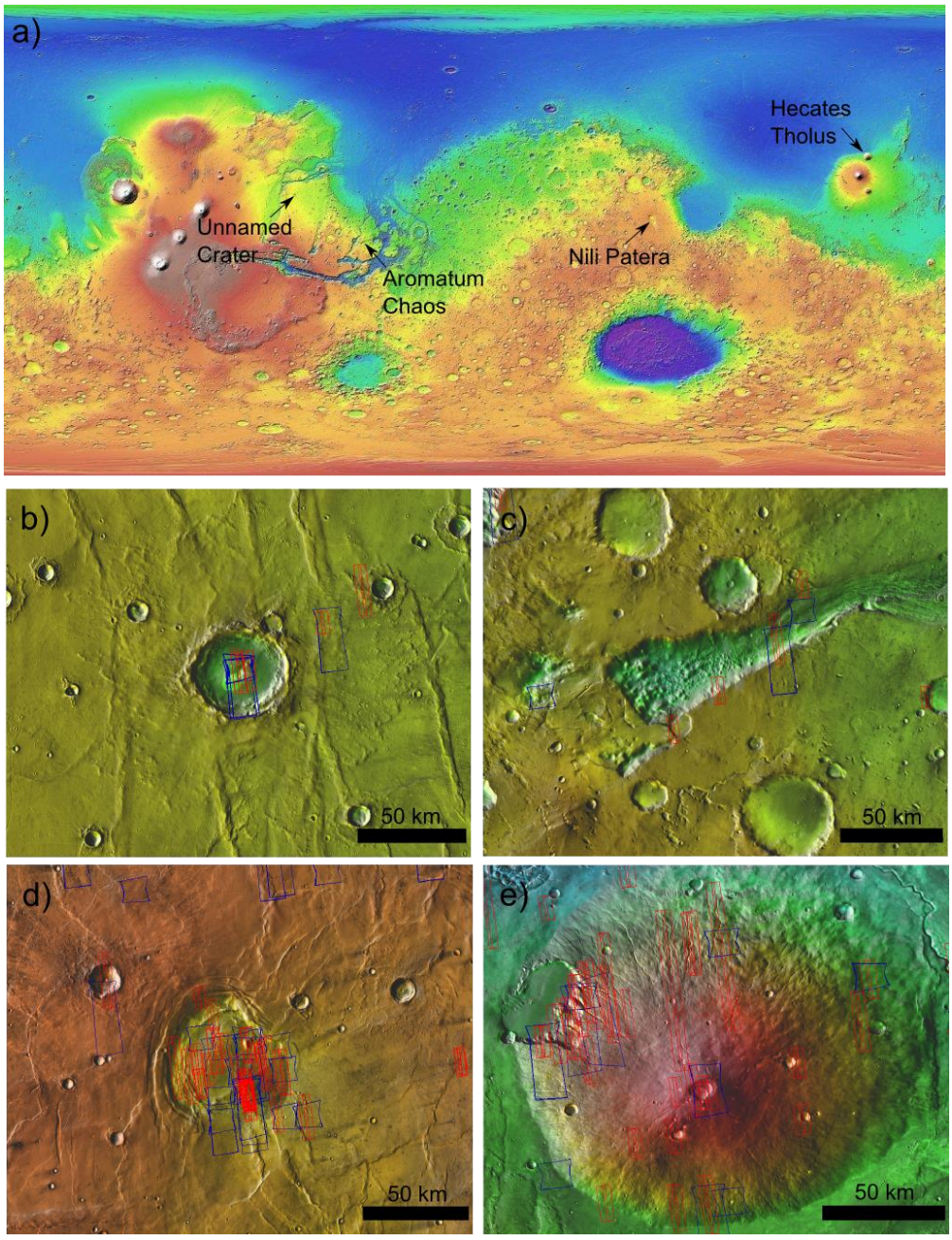

Figure 6.1: a) MOLA global coverage elevation map with locations of the four regions analysed in this Chapter. b) – e) CRISM (blue outlines) and HiRISE (red outlines) footprint coverage over the four regions taken from the JMars interface (Christensen et al., 2009) *on 13/06/15. Each image shows MOLA elevation overlain on THEMIS IR daytime temperature measurements. b) Unnamed ('Kirkcaldy') Crater, c) Aromatum Chaos, d) Nili Patera, e) Hecates Tholus. Nili Patera is well covered by both instruments, the coverage over Hecates Tholus is patchy and coincident measurements are concentrated over the collapse feature on the north-western flank of the volcano. Aromatum Chaos has very little coverage in either instrument and the coverage of the Unnamed Crater is concentrated solely on the central uplift feature.*

6.3: SMA results

6.3.1: Nili Patera

The Nili Patera caldera forms a unit of the Syrtis Major volcanic province on Mars (Fawdon et al., 2015). Early spectral imaging using the Soviet Imaging Spectrometer for Mars (ISM) on the Phobos 2 orbiter identified the Syrtis Major province as a region of high spectral variability with low homogenous global dust coverage, dominated by mafic basalts and their alteration products (Mustard et al., 1993). Later studies have focused on specific regions within the Syrtis Major complex and discovered quartz and silica rich deposits near the Antoniadi Crater (Smith and Bandfield, 2012), phyllosilicates and carbonates in the Nili Fossae region (Brown et al., 2015, 2010; Ehlmann et al., 2009), and felsic igneous rocks (Wray et al., 2013) and hydrated-silica mounds (Skok et al., 2010) within the Nili Patera caldera. These various mineral assemblages have been interpreted as evidence of significant hydrothermal activity across the region leading both Nili Fossae and Nili Patera to be put forward as rover landing sites for the NASA MSL (Ehlmann et al., 2007) and NASA 2020 Mars rover (Skok et al., 2014) missions respectively, both of which have an emphasis on habitability (Grotzinger et al., 2012; Mustard et al., 2013). As a result of these previous studies and the availability of relatively dust free CRISM images the Nili Patera region was selected as a test case for application of the SMA pipeline developed in Chapter 5. Spectral unmixing has not previously been applied to this region but the strong spectral signatures and relative lack of the homogenous martian surface dust make this region an ideal unmixing candidate, with the existing spectral studies providing an element of groundtruthing with which to interpret and validate the results.

CRISM image FRT00010628_07_IF165L/S_TRR3 was selected for unmixing analysis. This image was used in the study by Skok et al. (2010) that identified a number of hydrated-silica mounds. HiRISE image ESP_013582_185 overlaps the region covered by the CRISM image and was also used to provide some higher-resolution spatial context to aid the selection of the ROI to be unmixed (figure 6.2). A region in the south of the image was selected for SMA processing due the presence of a number of metre-scale and larger bright patches and high level of textural variation evident in the colour HiRISE image. This ROI has 5680 pixels of approximately 18 m^2. The CRISM image was pre-processed as described in section 6.2.3 with no additional cleaning performed or additional bands removed.

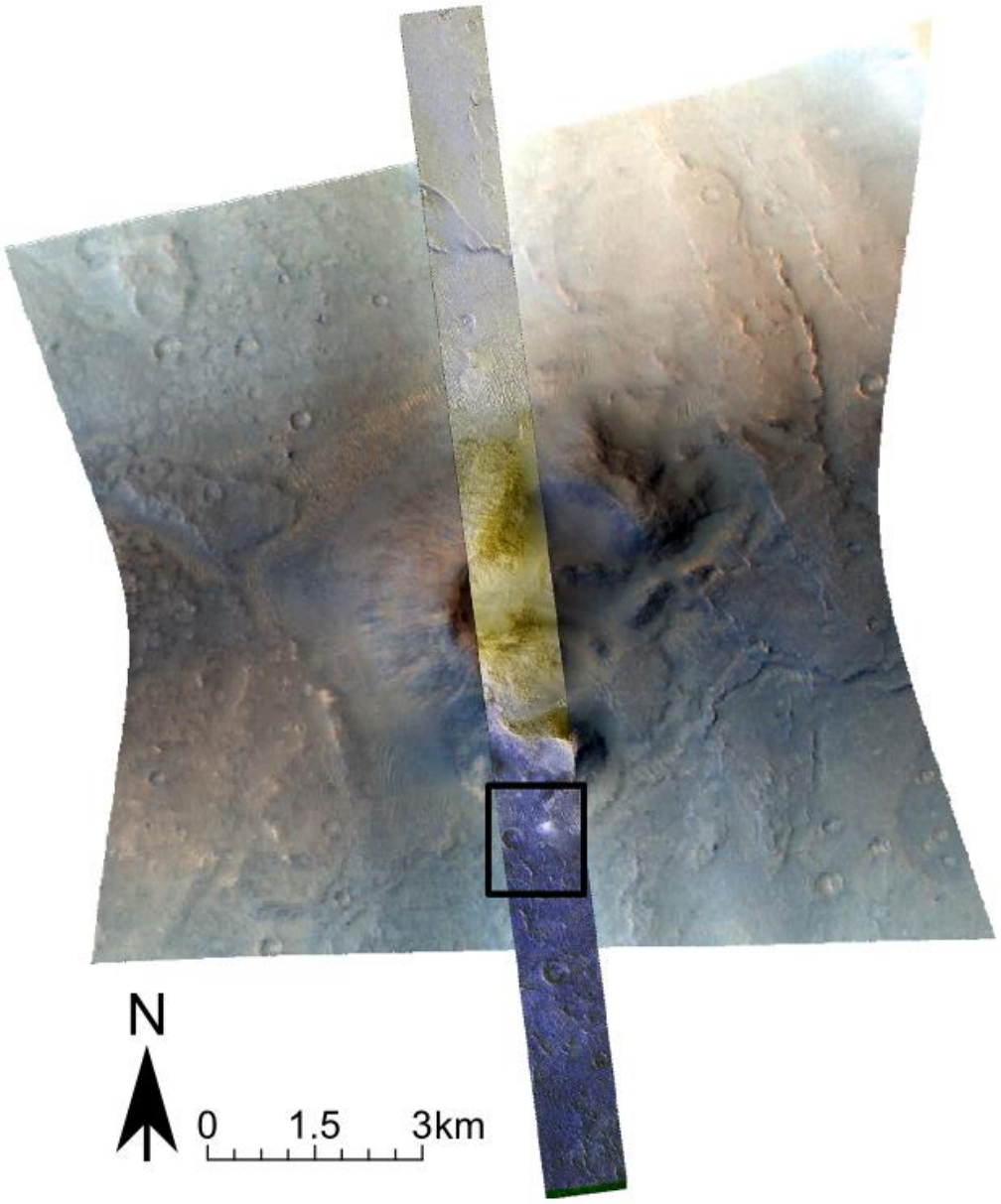

Figure 6.2: CRISM image FRT000106258_07_IFS_TRR3 RGB using bands 36, 22 and 9 with HiRISE image ESP_013582_185_COLOR overlain. The ROI selected for analysis through the SMA pipeline is outlined in black in the south of the region covered by both images.

The ODM algorithm was used to estimate the number of endmembers present in the ROI (p). It returned a p value of 13 although there were was an additional plateau point at the lower value of 8. The higher value of 13 was taken forward to the endmember extraction step in the pipeline as an overestimate is preferable to an underestimate. SISAL was then used to extract 13 endmembers. The routine was run 13 times (as explained in Chapter 5, section 5.3.2) and the results combined to create a final endmember set (figure 6.3). The variation within matching set of endmembers across the 13 runs was small lending confidence to the

accuracy of the extraction and the accuracy of the number of endmembers. Two of the endmembers were similar with the exception of one reversed feature in each centred at ~2.0 μm (a large absorption in endmember 7 and in endmember 4 a matching large reflectance 'hump'), and their abundance maps showed similar distributions with a mean pixel abundance difference of only 0.6%. This wavelength region is the location of a strong CO_2 absorption. Whilst atmospheric correction had been performed and thus should have removed almost all traces of this gas it has been shown that the volcano-scan method can leave behind a residual 'bowl-shaped' feature centred around 2.0 μm (Wiseman et al., 2014). The large reflectance 'hump' in endmember 4 is interpreted to be an attempt by the algorithm to account for surface albedo differences in the face of heterogeneously-distributed residual atmospheric CO_2 imperfectly removed by the volcano-scan method. Endmember 7 is an attempt by the algorithm to counter the inclusion of endmember 4 in higher albedo pixels. Given the level of agreement between these two endmembers abundance maps it was considered appropriate to take an average of them to remove the spurious reflectance feature. The final 12 spectra were analysed using the Spectral Analyst tool in ENVI 4.8. Both the USGS spectral library (Clark et al., 1993) and the CRISM spectral library (CRISM, 2006) were used as the necessary comparison datasets. The CRISM spectral library is the library provided by the CRISM science team specifically for comparison with CRISM spectra. The USGS spectral library provided with ENVI contains over 480 mineral spectra. This is the largest mineral spectral library provided. The endmember set all showed a common shape in the VNIR section (0.4 – 1.0 μm), and this region was not used in the identification of the endmembers. Potential identifications are listed in table 6.1. Matches to every endmember were not found in each spectral library with three endmembers going unmatched in either library. Individual visual inspection revealed no significant diagnostic features in these three from which to make a manual identification. A number of common absorptions were seen across a number of the spectra that can be quickly identified as instrument artefacts. These are the small, sharp features at ~ 0.66 μm and 1.66 μm (Murchie et al., 2009). Additionally, despite the atmospheric correction performed in the pre-processing steps the subtle triplet of absorptions within the shallow broad absorptions at ~2.01 μm are likely residual atmospheric CO_2 features that have not been fully removed (see above comments on endmembers 4 and 7). Other common subtle absorptions at 1.21, 1.31 and 2.57 μm are also uncorrected remnants of atmospheric components, primarily CO_2 (Wiseman et al., 2014). Another sharp absorption is seen in endmembers 2, 6 and 13 at 2.39 μm. A mirroring sharp reflectance peak at this same wavelength is seen in endmembers 9 and 12. An O-H combination overtone can be found at this wavelength (Ehlmann et al.,

2009), however, in this case due to the mirroring reflectance peaks it is considered an artefact of noise and not a mineralogical absorption.

Table 6.1: Nili Patera SISAL (p = 13) ENVI Spectral Analyst results matching the endmembers to spectra in both the USGS and CRISM spectral libraries. "?" indicates that no strong match was found in the specified spectral library database. In these cases the endmembers typically displayed no strongly diagnostic absorptions and could have been a match to a large number of spectral library entries. Total ROI scene abundances are also given as calculated using the Fully Constrained Linear Least Squared (FCLLS) algorithm.

#p	USGS identity	CRISM library identity	FCLLS scene %
1	?	?	8
2	opal (silica)	Siliceous sinter	4
3	?	A phyllosilicate (smectite) mixture	7
5	olivine	?	6
6	diopside	clinopyroxene	8
8	pyrite	pyroxene	9
9	?	kaolinite-serpentine	11
10	plagioclase feldspar	plagioclase/olivine mixture	8
11	?	kaolinite-serpentine or basalt	9
12	?	?	9
13	opal (silica)	?	4
4&7	?	?	14

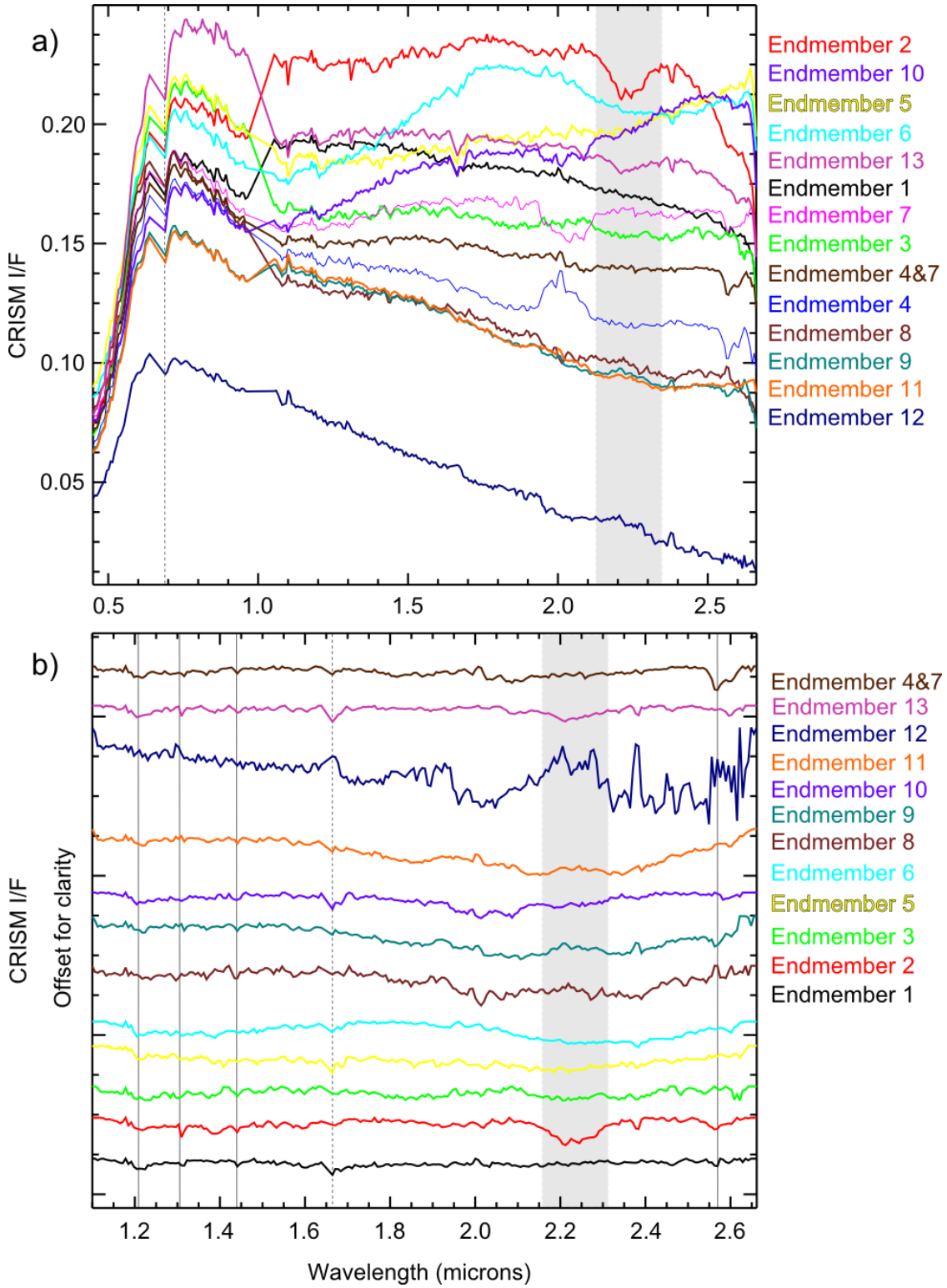

Figure 6.3: SISAL extracted endmember spectra from the CRISM ROI. a) full wavelength range endmembers, endmembers 4 and 7 show prominent mirror features centred at 2.0 µm. This feature is considered erroneous and to remove it from the final results the two endmembers have been averaged together to create a single new endmember shown in brown as endmember 4&7 in the figure. Spectra names are listed in order of highest albedo as

measured at ~2.4 µm. b) the IR section of the extracted spectra, continuum removed and offset for clarity. In both images dotted lines highlight known instrument artefacts, solid lines indicate subtle absorptions due to imperfectly removed atmospheric components and the shaded region highlights the prominent hydrated silica absorption band. The low albedo of endmember 12 leads it to show high levels of noise in the continuum removed version.

The mineral identification results listed in table 6.1 from the two spectral libraries are not always in agreement, and a number of the minerals given are not uniquely identifiable from the spectral data available. Examples of these include the plagioclase, pyrite and olivine spectra. In every case existing knowledge of the region has been used to make a suitable identification, but they should only be treated as the most likely candidates. It is also possible that a number of these endmembers are themselves still mixtures of more than one mineral; endmember 10 is a good example of this, matching in different wavelength ranges to both plagioclase and olivine spectra in the CRISM library. Looking at the abundance maps generated for each endmember strengthens the identifications of some of the endmembers (figure 6.4). Endmembers 2 and 13 have been identified as hydrated silica (opal in the USGS library) due to the broad absorption at 2.21 µm (Rice et al., 2013b; Smith et al., 2013) and in the case of endmember 2 also at 1.96 µm. They show the strongest presence in the large bright patches in the NE section of the ROI (together accounting for up to 80% abundance as shown in figures 6.4c and 6.4m respectively) that have been previously identified as hydrated silica by Skok et al. (2010). Endmember 5, identified as likely olivine, also shows its highest concentration over the major central bright patch (figure 6.4f). A number of the endmembers show abundances that appear as roughly north to south streaks (endmembers 9, 11 and 4&7). This suggests that they are picking up on uncorrected image artefacts not fully removed by the destriping step in the cleaning process, as there is no evidence of structural features in the HiRISE image that match to this pattern.

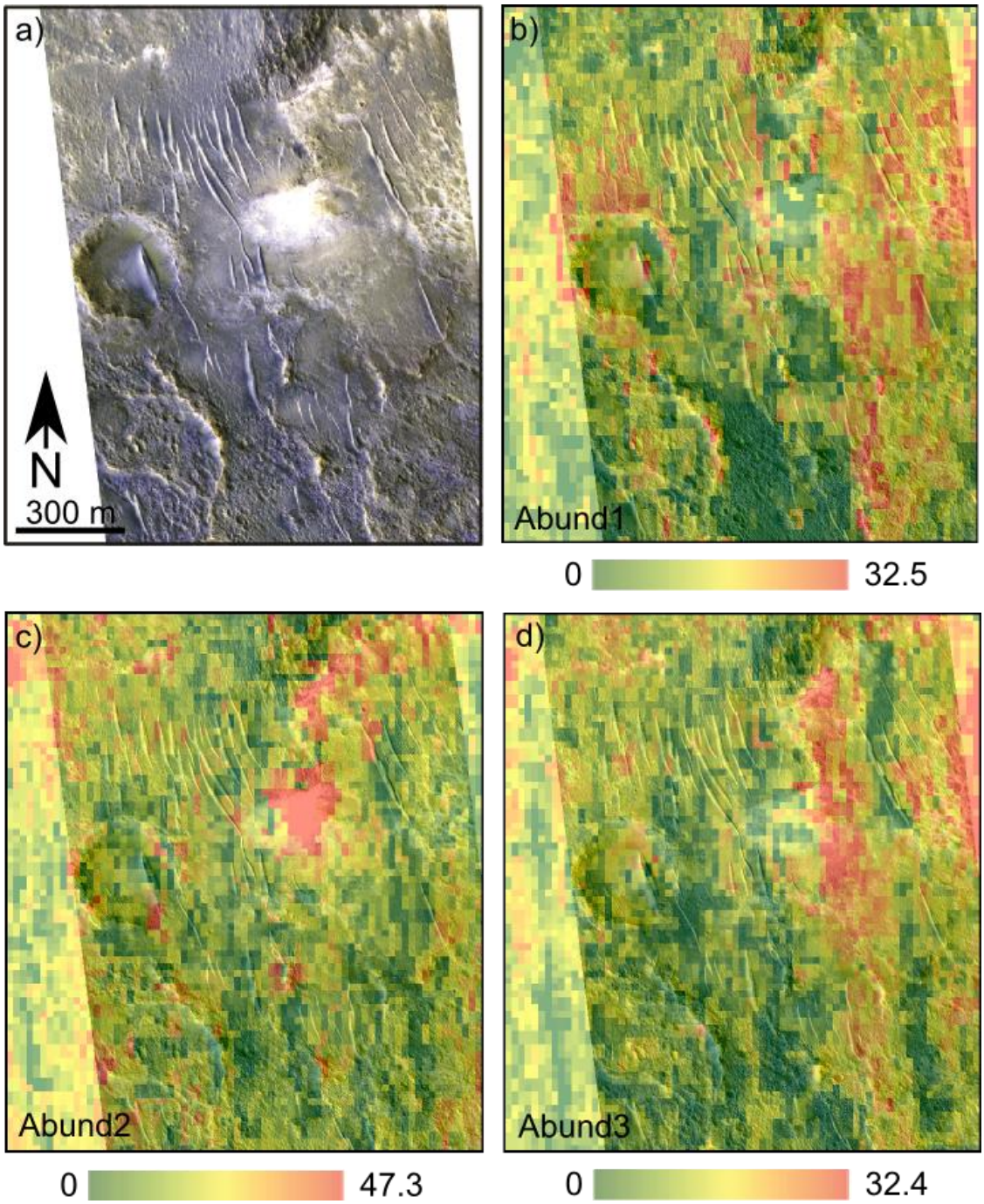

Figure 6.4: Abundance maps for SISAL extracted endmembers 1, 2 and 3 shown in figure 6.3. In each image a green to red scale is used to show increasing abundance % from green through yellow to red. a) ROI portion of HiRISE image, b) abundance map for endmember 1 (?) overlain on HiRISE image, c) abundance map for endmember 2 (opaline silica) overlain on HiRISE image, d) abundance map for endmember 3 (smectite?) overlain on HiRISE image.

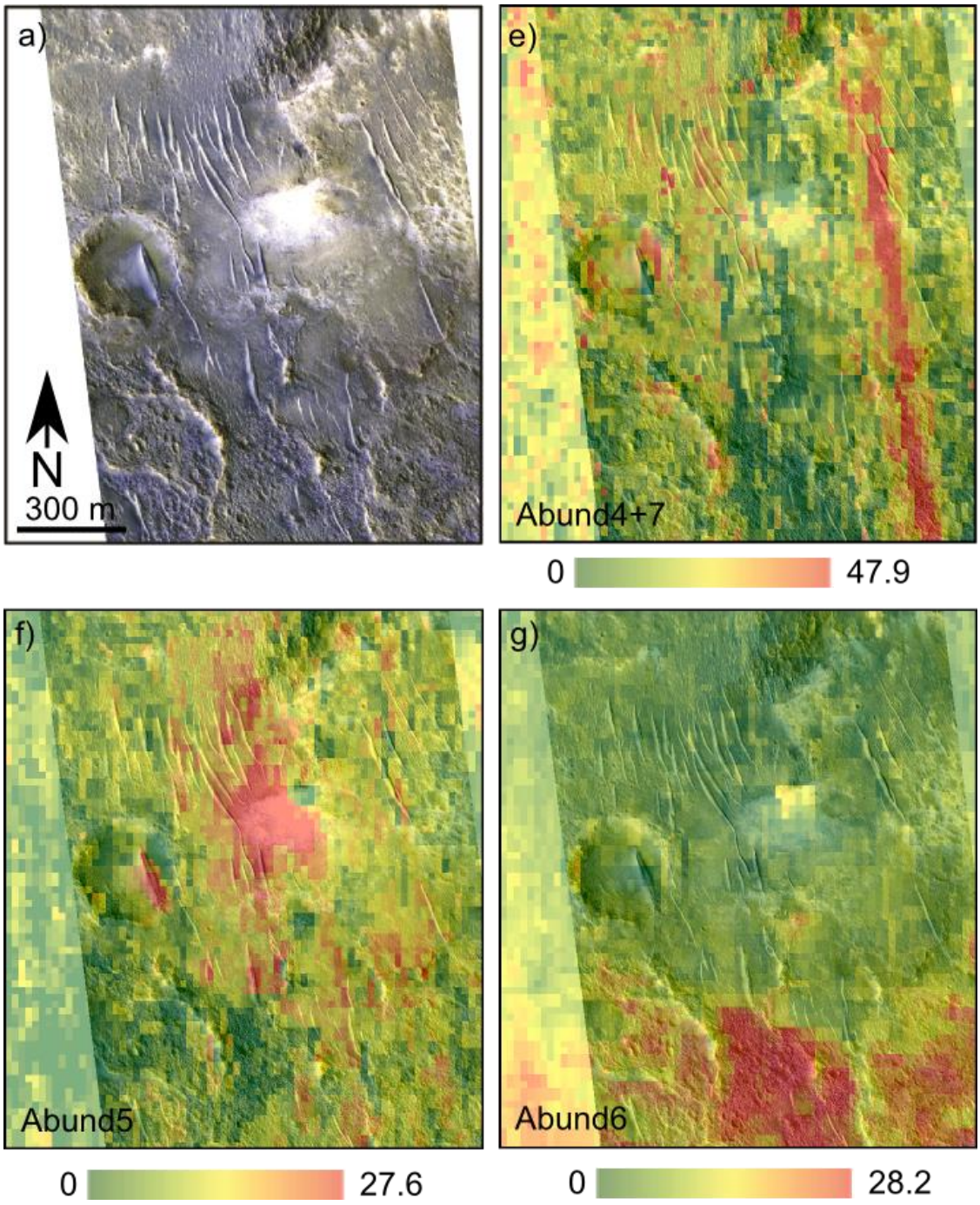

Figure 6.4: Abundance maps for SISAL extracted endmembers 4&7, 5 and 6 shown in figure 6.3. In each image a green to red scale is used to show increasing abundance % from green through yellow to red. a) ROI portion of HiRISE image, e) abundance map for endmember 4&7 (?) overlain on HiRISE image, f) abundance map for endmember 5 (olivine) overlain on HiRISE image, g) abundance map for endmember 6 (clinopyroxene) overlain on HiRISE image.

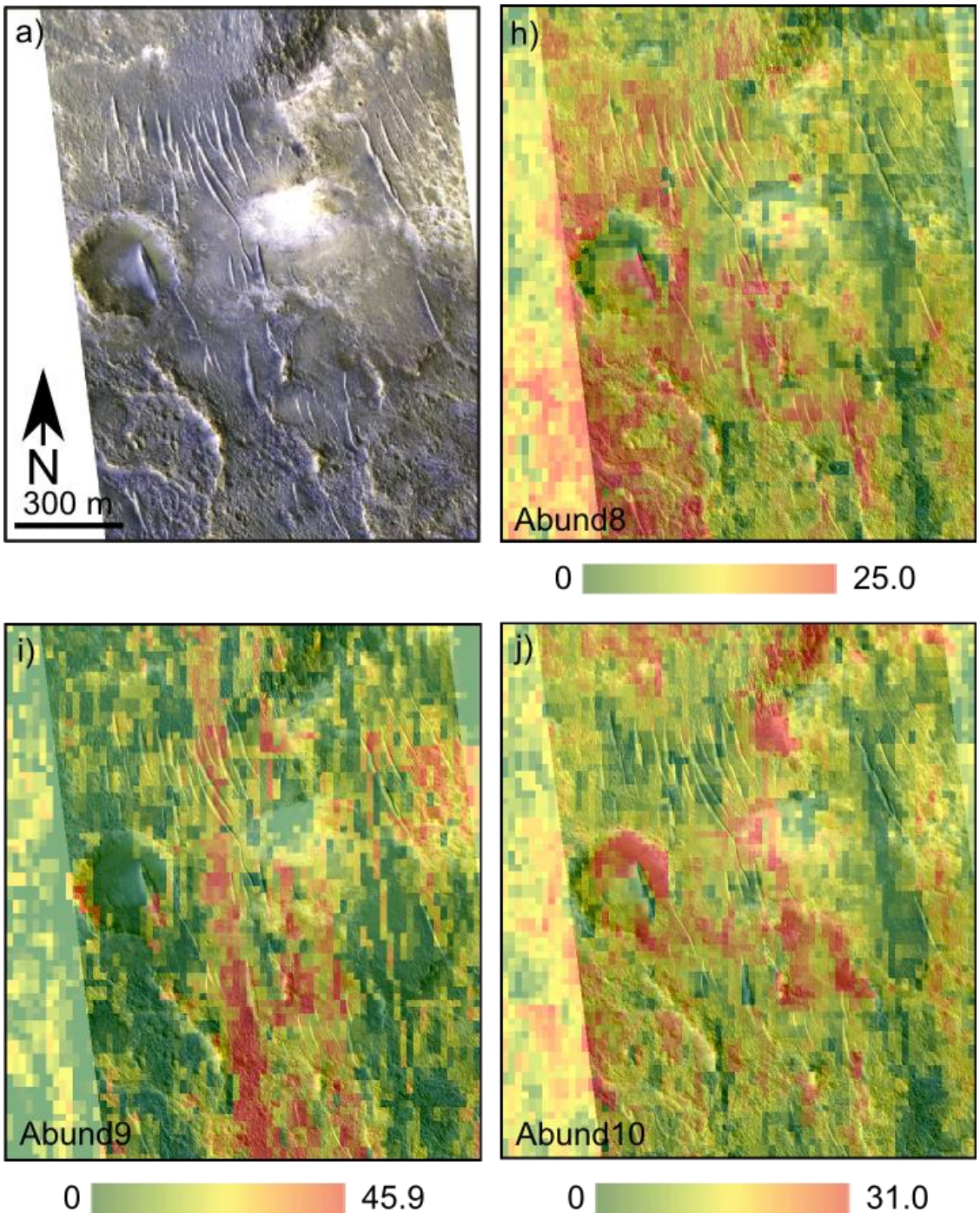

Figure 6.4: Abundance maps for SISAL extracted endmembers 8, 9, and 10 shown in figure 6.3. In each image a green to red scale is used to show increasing abundance % from green through yellow to red. a) ROI portion of HiRISE image, h) abundance map for endmember 8 (pyrite) overlain on HiRISE image, i) abundance map for endmember 9 (kaolinite-serpentine) overlain on HiRISE image, j) abundance map for endmember 10 (plagioclase) overlain on HiRISE image.

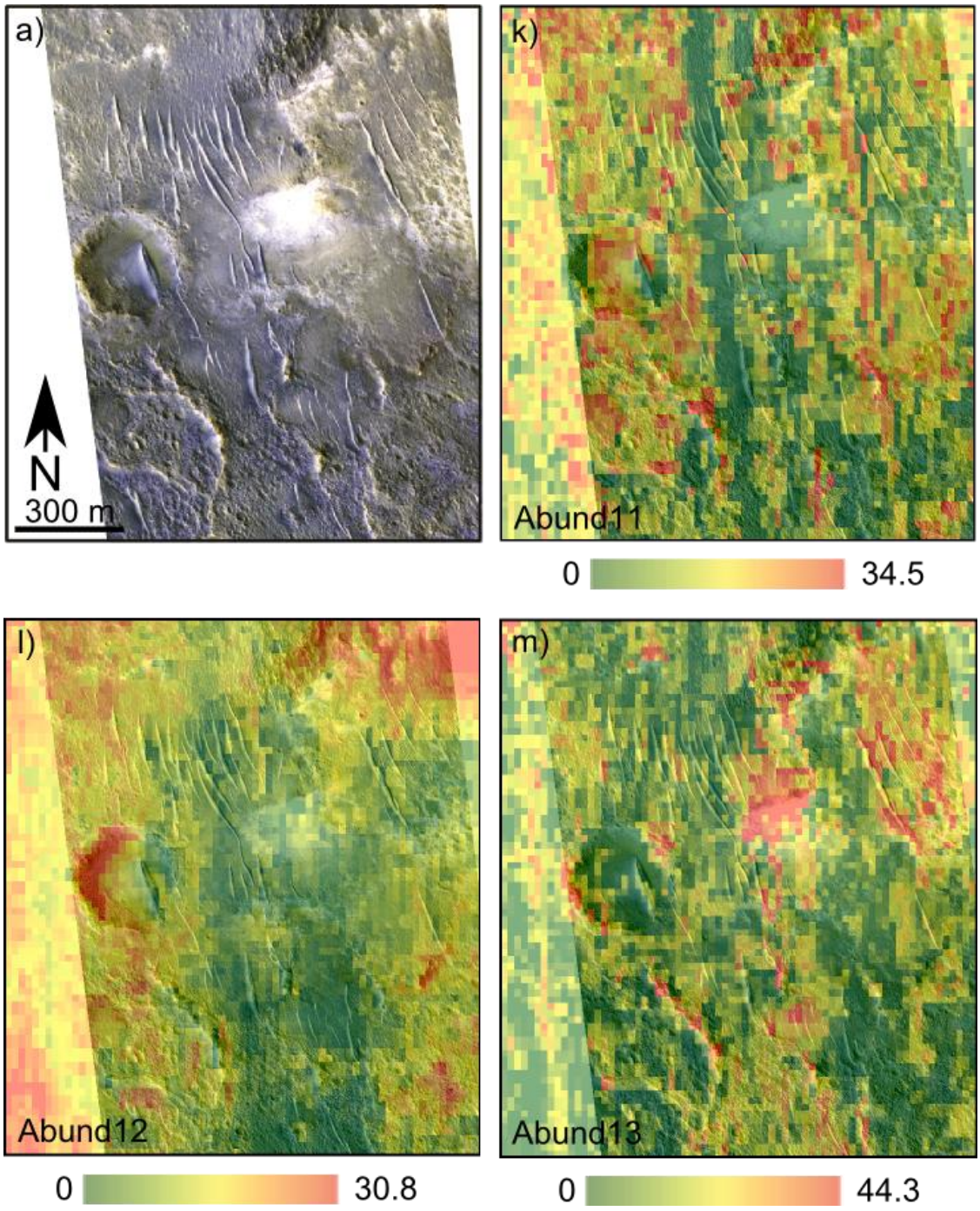

Figure 6.4: Abundance maps for SISAL extracted endmembers 11, 12 and 13 shown in figure 6.3. In each image a green to red scale is used to show increasing abundance % from green through yellow to red. a) ROI portion of HiRISE image, k) abundance map for endmember 11 (basalt) overlain on HiRISE image, l) abundance map for endmember 12 (?) overlain on HiRISE image, m) abundance map for endmember 13 (opaline silica) overlain on HiRISE image.

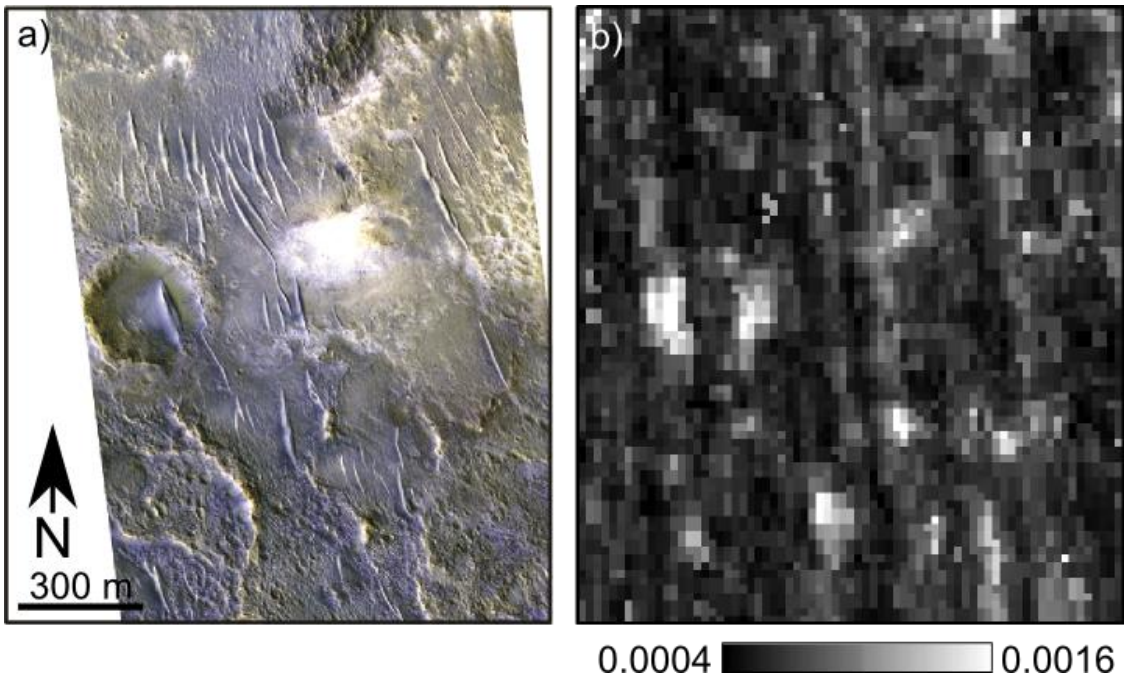

Figure 6.5: a) HiRISE image of Nili Patera ROI, b) RMSE values for the CRISM image reconstructed from the extracted endmembers and their estimated abundances.

The abundances in each individual pixel were calculated using the Fully Constrained Linear Least-Square (FCLLS) algorithm on the I/F data. Due to the number of endmembers used the data were not converted to SSA prior to this step. Total scene abundances are listed in table 6.1 and are expected to be correct to within 5% although the individual pixel abundances shown in figure 5 could be in error by as much as 15% based on synthetic image results presented in chapter 5. The reconstructed scene RMSE is 0.00063 and the plot of individual pixel RMSE shows no correlation between any of the endmember abundance maps in figure 6.4. There is a slight correlation between high RMSE values and regions that in the HiRISE image appear to have significant topographic variation but this is not a consistent observation. The random distribution of the RMSE values lends confidence to the pipeline results with the EEA step already giving a high degree of confidence as discussed above. The scene can be described as 31% unknown, 8% opaline silica, 18 – 27% phyllosilicates, 24 – 42% primary igneous products (olivine, pyroxene, and plagioclase) and 0 - 9% iron sulfide. The large fraction of unidentified material reflects the difficulties in uniquely identifying many of the primary igneous minerals and rock types within the wavelength range used in this study. Given the high concentrations of plagioclase and high-Ca pyroxene identified in the region using the 16 km/pixel Thermal Emission Spectrometer (TES) data (Bandfield, 2002) it is likely that the unidentified endmembers are one of these rock types, both of which have highly variable and slightly ambiguous spectral signatures in the VNIR making them hard to

definitively identify. The silica, phyllosilicates and iron sulfide are all minerals produced through hydrothermal alteration and weathering of primary igneous materials, which matches well with the interpretations of the previous studies already discussed, identifying this region as one that has undergone hydrothermal alteration.

6.3.2: Hecates Tholus

Hecates Tholus is the northern most of the three Elysium volcanoes and shows structural evidence of both explosive eruptions and glacial activity on its slopes dating from approximately 5 Myr (Hauber et al., 2005; Neukum et al., 2004) or as recently as 440 kyr ago (De Pablo et al., 2013). Together these observations point to the possibility of some relatively recent hydrothermal activity in the region. The general mineralogy of the volcano is assumed to be basic to ultrabasic (Hauber et al., 2005; Sgavetti et al., 2009). Global mineralogical maps constructed from 16 km/pixel TES data show some patches with an elevated abundance of sheet silicate/high silica glass, particularly over the north western collapse feature, and elevated concentrations of plagioclase at the peak of the volcano (Bandfield, 2002). CRISM coverage over the volcano is patchy and centred on glacial features on the volcano's flanks (primarily the north western collapse feature) and the central caldera (figure 6.1e). Hydrothermal systems are commonly found within volcanic calderas on the Earth (Todesco, 2008) and HiRISE coverage (ESP_017055_1975) over the Hecates Tholus volcanic caldera shows a number of metre-scale high albedo patches that warrant further spectral investigation using a coincident CRISM image. No FRT images of sufficient quality were available and thus a HRT image, HRL00007331_07_IF183L/S_TRR3, with pixels of approximately 36 m^2 was used. This CRISM image was processed as described in section 6.2.3 with no additional cleaning or extra spectral bands removed. Using the HiRISE image as a guide two ROI's were identified and extracted for analysis in the SMA pipeline (table 6.2 and figure 6.5).

Both ROI's gave a p value of 5 using ODM with clear plateau points in each output graph. SISAL was run 5 times for each ROI and in both cases the variation within each endmember matching set was low giving confidence to their accuracy.

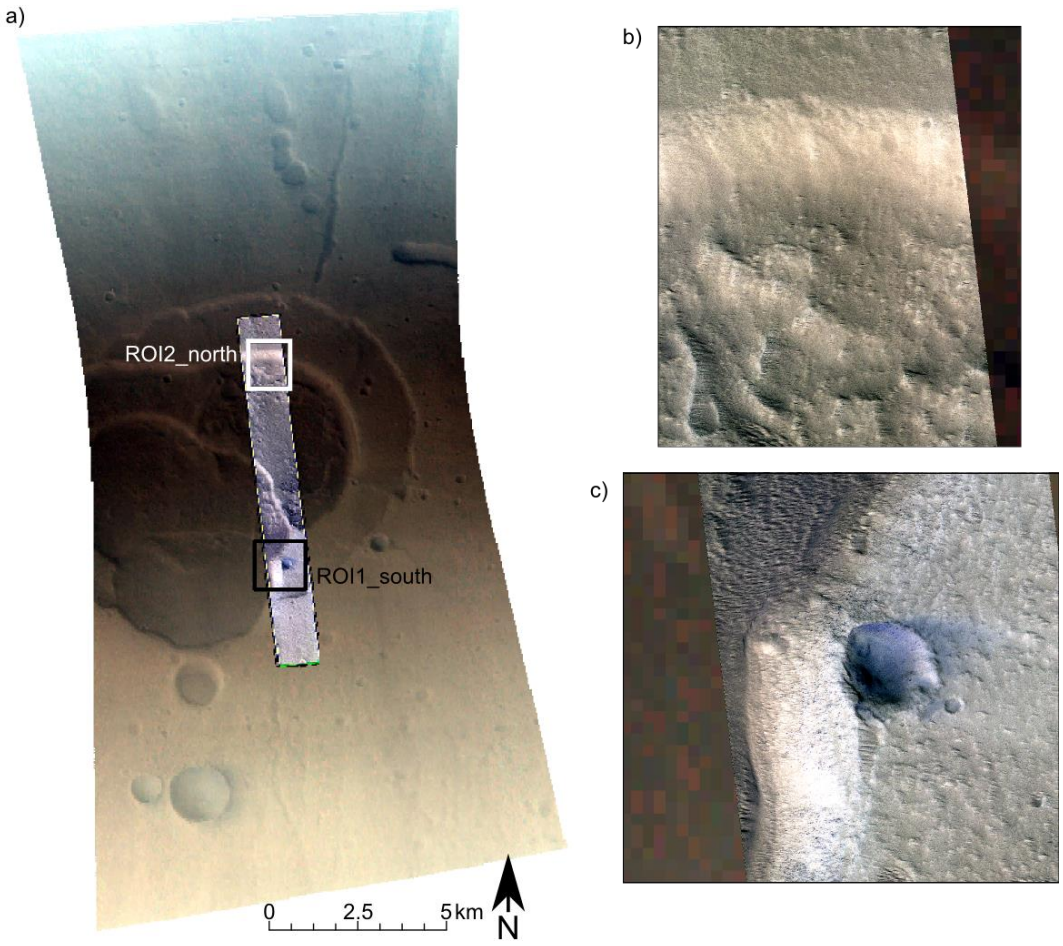

Figure 6.6: a) CRISM image HRL00007331_07_IF183S_TRR3 RGB composite of bands 43, 29 and 16 overlain with the much smaller HiRISE image ESP_017055_1975_COLOR. The black and white boxes mark the two ROI's selected for analysis through the SMA pipeline. b) ROI2_north HiRISE section showing subtle small scale spectral variation in the lower half of the ROI and the presence of small mounds and dunes. c) ROI1_south HiRISE section showing a prominent crater with a small ejecta blanket and varied small scale structure in the surrounding terrain with slight spectrally differences in the HiRISE image within two distinct albedo units.

Table 6.2: Hecates Tholus ROI's for SMA and resulting ODM p values estimating the number of endmembers present in each ROI.

ROI	# of pixels	ODM p value
ROI1_south	1584	5
ROI2_north	1225	5

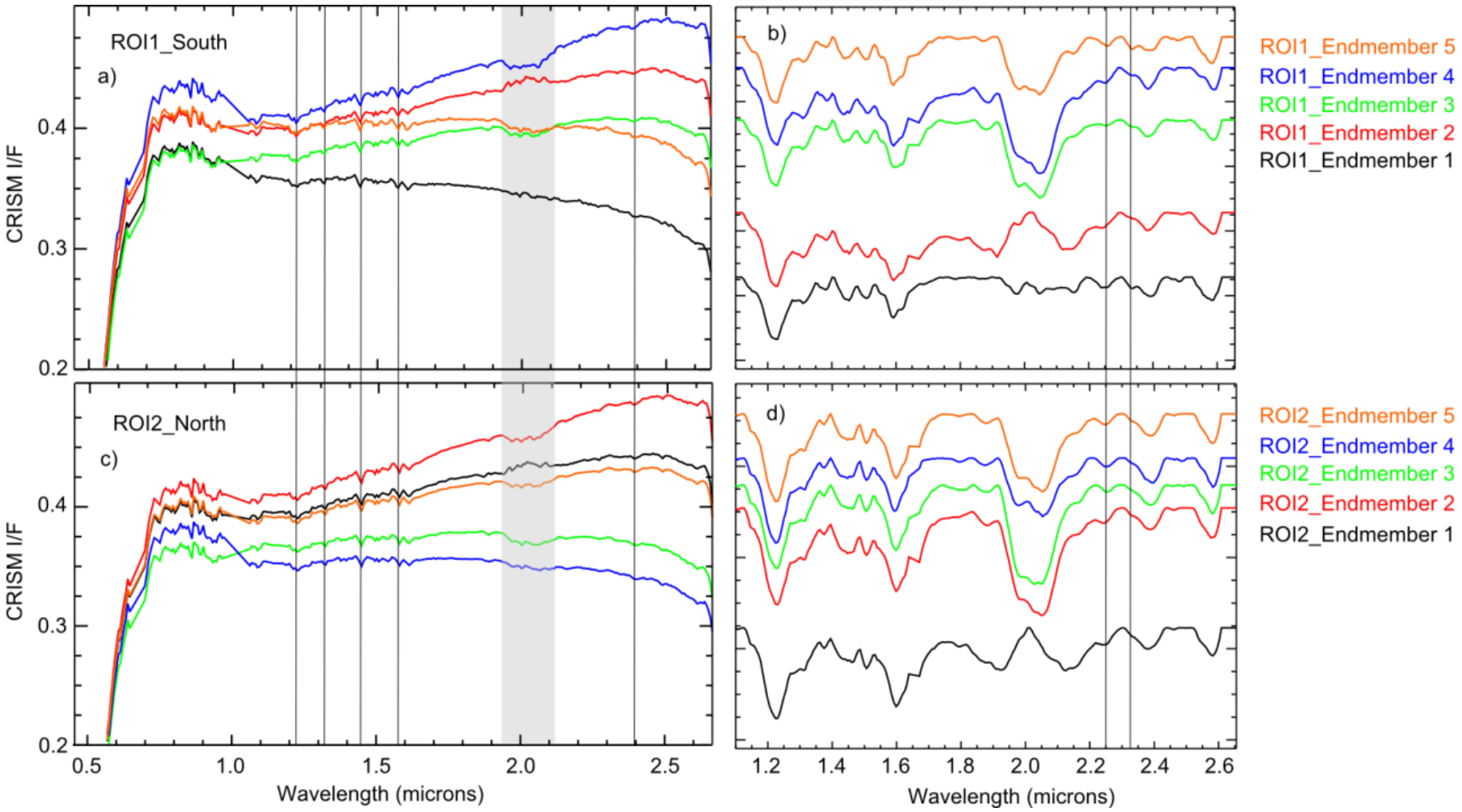
ROI1_South
a)
b)
ROI2_North
c)
d)
CRISM I/F
0.2
0.3
0.4
0.5
1.0
1.5
2.0
2.5
1.2
1.4
1.6
1.8
2.0
2.2
2.4
2.6
Wavelength (microns)
Wavelength (microns)
ROI1_Endmember 5
ROI1_Endmember 4
ROI1_Endmember 3
ROI1_Endmember 2
ROI1_Endmember 1
ROI2_Endmember 5
ROI2_Endmember 4
ROI2_Endmember 3
ROI2_Endmember 2
ROI2_Endmember 1

Figure 6.7: SISAL extracted endmembers from both ROI1_south and ROI2_north in the Hecates Tholus CRISM image. The two sets of spectra are remarkably similar to each other and show little in the way of significant variation within themselves. a) The SISAL extracted endmembers for ROI1_south, b) IR section of the ROI1_south endmembers shown with the spectral continuum removed and the resulting spectra offset for clarity, c) the SISAL extracted endmembers for ROI2_north, d) IR section of the ROI2_north endmembers shown with continuum removed and the resulting spectra offset for clarity. The vertical lines in plots a) and c) indicate the subtle absorptions common to all 10 spectra due to uncorrected atmospheric components. The two vertical lines in plots b) and d) indicate the chlorite absorptions at 2.25 - 6 and 2.33 µm, the latter of which is not present in the ROI2_north spectra. The spectra in b) and d) have been smoothed using a Savitzky-Golay filter with a window size of 11 to remove extraneous noise and emphasis the absorption features. The chlorite features are still discernible in the non-smoothed spectra confirming they are not just artefacts of the smoothing process.

The extracted endmembers from each ROI show little variation within each dataset and between each other (figure 6.7) and analysis using the Spectral Analyst tool returned no convincing diagnoses. All endmembers in both sets share a number of common features including subtle absorptions at 1.22, 1.31, 1.44, 1.57 and 2.39 µm (figure 6.7a and c). The first four of these are all atmospheric features that have been imperfectly corrected (Wiseman et al., 2014). With the exception of the 1.44 µm feature, which could also be evidence of surface CO_2 ice, all of these absorptions can be safely ignored as they do not correspond to any significant mineralogical features. Due to the presence of all these atmospheric features the 1.44 µm absorption is in this case also interpreted as atmospheric and not as a surface component. The major feature that differs between endmembers is a shallow broad absorption centred at ~2.0 µm evident in three of the endmembers in each set. Whilst this is a spectral region that must be carefully interpreted in martian spectra due to the presence of a strong CO_2 absorption, this should have been removed by the atmospheric correction step preformed in the pre-processing. However, the volcano-scan atmospheric correction method has been shown to leave behind a 'bowl-shaped' feature centred at ~2.0 µm (Wiseman et al., 2014). The shallow but broad absorption in this position in ROI1_south endmembers 3, 4, and 5 and ROI2_north endmembers 2, 3, and 5 is therefore interpreted as this particular artefact introduced by the atmospheric correction. An alternative explanation is that this could be tentative evidence of the presence of small amounts of H_2O ice (Clark, 1999). In the wavelength range used here this feature is the

strongest H_2O ice absorption, however an ice component would be expected to also show a skewed absorption at 1.5 µm. The lack of this accompanying absorption is why this feature is considered to be atmospheric CO_2 and not surface H_2O ice. The reflectance spike at ~2.0 µm in ROI1_endmember 2 and ROI2_endmember 1 is interpreted to be an artefact introduced by the algorithm to account for the heterogeneously distributed residual atmospheric CO_2 and therefore further evidence of imperfect atmospheric correction. There is also a subtle absorption in all of the endmembers at 2.39 µm (as noted above) and another at 2.25 µm in ROI2_north and 2.26 µm in ROI1_south. In ROI1_endmembers 1 and 5 this 2.26 µm feature is accompanied by an absorption at 2.33 µm. Taken together these two absorptions indicate the presence of AlMg and MgMgMg hydroxyl bonds respectively due to a chlorite mineral (Bishop et al., 2008). Chlorite forms as a hydrothermal alteration product and has been previously identified on Mars as a common component of alteration assemblages and crustal clay units (Ehlmann et al., 2011b, 2011c). The stronger 2.39 µm absorption is also an O-H combination absorption feature, seen in Mg-bearing phyllosilicates such as saponite (Smith and Bandfield, 2012), but not chlorite, suggesting that these endmembers are not pure minerals but are themselves still mixtures. The 2.33 µm feature is not seen in the ROI2_north endmembers and thus the 2.25 µm feature in these endmembers cannot be definitively confidently explained as chlorite. The presence of both the 2.25/2.26 and 2.39 µm absorptions in both ROIs points towards the widespread presence of Mg and Al-bearing phyllosilicates in this region.

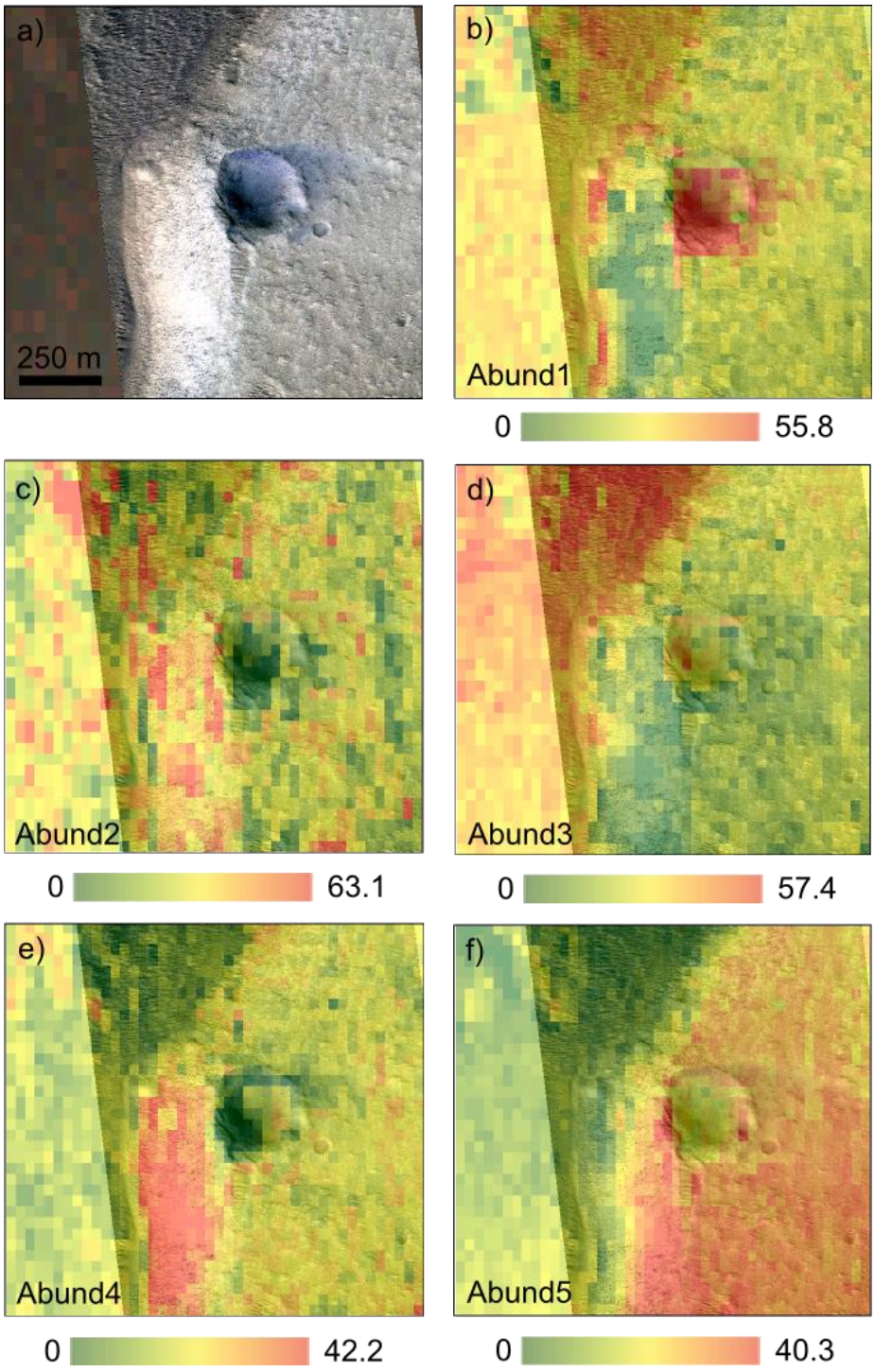

Figure 6.8A: Hecates Tholus ROI1_south FCLLS abundance maps using SISAL extracted endmembers shown in figure 6.5. A green-yellow-red scale is used to indicate increasing abundance % in each pixel. a) HiRISE image of ROI, b) abundance map for endmember 1 overlain on HiRISE image, c) abundance map for endmember 2 overlain on HiRISE image, d) abundance map for endmember 3 overlain on HiRISE image, e) abundance map for endmember 4 overlain on HiRISE image, f) abundance map for endmember 5 overlain on HiRISE image.

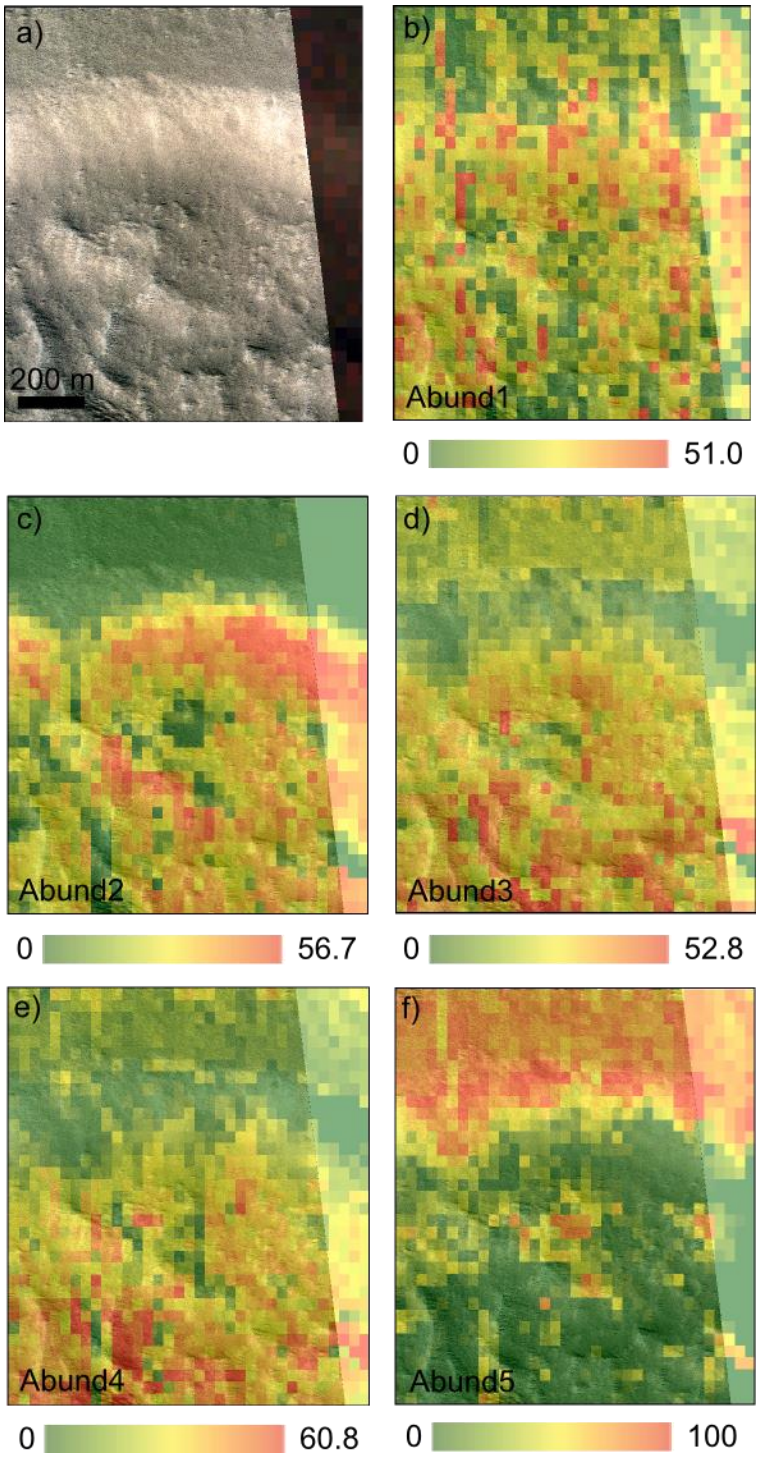

Figure 6.8B: Hecates Tholus ROI2_north FCLLS abundance maps using SISAL extracted endmembers shown in figure 6.5. A green-yellow-red scale is used to indicate increasing abundance % in each pixel. a) HiRISE image of ROI, b) abundance map for endmember 1 overlain on HiRISE image, c) abundance map for endmember 2 overlain on HiRISE image, d) abundance map for endmember 3 overlain on HiRISE image, e) abundance map for endmember 4 overlain on HiRISE image, f) abundance map for endmember 5 overlain on HiRISE image.

Table 6.3: Total scene abundance percentages for the Hecates Tholus SISAL extracted endmembers shown in figure 6.5. Total scene abundances are given with an error of ±5%. Mineral ID's are not included for all endmembers due to lack of uniquely diagnostic spectral features.

Endmember	ROI1_south	ROI2_north
1	18% (chlorite bearing endmember)	15%
2	16%	20%
3	25%	20%
4	21%	15%
5	20% (chlorite bearing endmember)	29%

Abundance maps were produced from the CRISM I/F data without conversion to SSA due to the high level of topographic variance in the scene making the incidence and emission angles for each pixel uncertain. Given the high confidence in the EDA and EEA results earlier in the SMA pipeline these scene wide abundances are expected to be correct to within 5% however errors on individual pixels could be as high as 20% based on results from similar synthetic images in chapter 5. The results predominantly map to the different albedo units in the HiRISE image (figure 6.8). For ROI1_south, endmembers 1, 3, 4 and 5 all clearly correspond to the different albedo units with the lowest albedo chlorite bearing endmember, endmember 1, showing the highest abundances in the central crater, endmember 3 showing the highest abundances in the dark NW corner of the ROI, endmember 4 (the highest albedo endmember) corresponding to the bright, highly illuminated slope to the SW of the crater and endmember 5, the second chlorite bearing endmember, mapping over the primary beige unit covering the eastern portion of the ROI. ROI1_endmember 2 shows no obvious spatial coincidence with any topographic or structural features in the HiRISE image. ROI1_endmember 2 is also the endmember that appears to be accounting for the uncorrected atmospheric CO_2 with a slight reflectance bump centred at ~2.0 µm. The atmospheric CO_2 distribution is expected to be heterogeneously distributed and not to match to any surface structural features. The effect this atmospheric CO_2 has on the albedo of each pixel will therefore not match to the differences in albedo due to surface mineralogical and structural variation. The algorithm has accounted for this by introducing a reflectance feature rather than an absorption feature in one endmember over these bands. The random nature of ROI1_endmember 2's abundance supports this interpretation. The abundance

maps for ROI2_north show a similar pattern with all maps corresponding approximately to different albedo units with the exception of that from endmember 1, the endmember that matches ROI1_south endmember 2 and is most likely representing uncorrected atmospheric CO_2 in the image and again shows a random abundance distribution within the ROI.

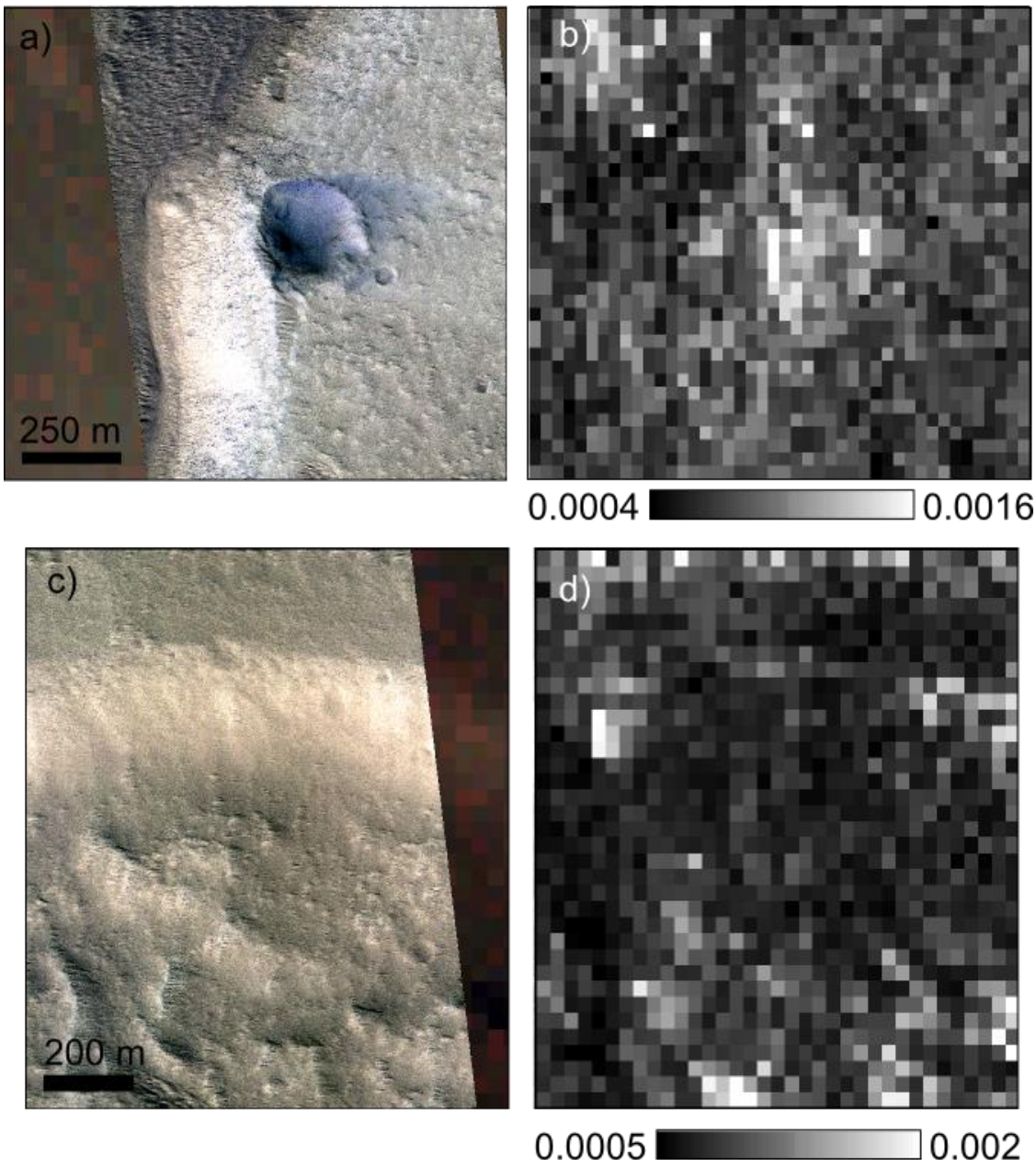

Figure 6.9: a) HiRISE image of Hecates Tholus ROI1_South, b) RMSE values for the CRISM image reconstructed from the extracted endmembers and their estimated abundances, c) HiRISE image of Hecates Tholus ROI2_north, d) RMSE values for the CRISM image reconstructed from the extracted endmembers and their estimated abundances.

The reconstructed ROI's from the extracted endmembers and estimated abundances gave scene RMSE values of 0.0006 (ROI1_south) and 0.00071 (ROI2_north). The individual pixel RMSE maps (figure showed no clear correlation between high RMSE values and any one of the extracted endmember abundance maps nor do they show any consistent coincidence with any topographic or albedo features with the exception of slightly higher RMSE values over the central crater in ROI1_south (figure 6.9a and b). These overall low RMSE values and their largely random distribution give confidence to the pipeline results.

Based on the general spectral similarity within the two ROI endmember results and the corresponding abundance maps, the unmixing is mostly picking up on textural, structural and illumination differences in this scene. There is little in the way of mineralogical variation to be seen in the SMA extracted endmembers, with the only mineral identifications being that of chlorite. The identification of chlorite, a sheet silicate, in the southern ROI supports the much lower spatial resolution TES observation of isolated, elevated sheet silicate and plagioclase concentrations (Bandfield, 2002) over the caldera. The presence of chlorite, a mineral commonly associated with hydrothermal ore deposits (Shanks III, 2010), also lends evidence to the existence of a hydrothermal system at some point in the history of this region.

The CAT pre-processing pipeline contains the optional final step of calculating the CRISM spectral parameters defined by Pelkey et al. (2007). Within the two analysed ROI's these too revealed little significant mineral variation or definitive mineral types, and where there is a discernible pattern it matches to illumination and albedo differences due to topography and texture. The chlorite identified in ROI1_south does not match to any of the spectral parameters built into CAT version 7.2.1 and was thus not picked up by this standard analysis technique.

6.3.3: Aromatum Chaos

The Aromatum Chaos depression located in the Xanthe Terra region near the north-south dichotomy boundary of Mars (figure 6.1a), shows morphological and structural evidence of an ancient flood caused by volcanic activity disrupting the cryosphere (Leask et al., 2006). Global mineralogical maps constructed using 16 km/pixel TES data show elevated abundances of sheet silicates or high silica glass and low quantities of pyroxene, plagioclase and olivine (Bandfield, 2002). No high resolution mineralogical studies have been performed, likely due to the lack of suitable data. The coverage with both CRISM and HiRISE is limited with only one coincident pair near the eastern section of the depression (figure 6.1c). HiRISE

coverage of the area shows both spectral and topographic variation in regions with coincident CRISM coverage making it a good candidate for analysis with the SMA pipeline. HiRISE image ESP_026891_1790 was used to select a region within the CRISM image FRT00024F8_07_IF165L/S_TRR3 to analyse with the SMA pipeline (figure 6.8). The CRISM image was processed as described in section 6.2.3 with the removal of additional bands spanning 1.178 – 1.198 µm and 1.716 – 1.737 µm which showed consistent, erroneous spikes across the image. The VNIR detector data was discarded as a manual inspection revealed no significant variation within these wavelengths (0.44 – 1.1 µm). The final dataset analysed contained only the IR data with 230 spectral bands (L = 230). A single ROI was selected with 8307 pixels. This CRISM image is a full resolution targeted (FRT) image meaning its pixels are approximately 18 m^2.

The ODM step in the pipeline estimated the number of endmembers present to be p = 7 with a clear plateau in the output graph at this value indicating it is an accurate estimate of the number of distinct endmembers present. This value was used to extract a final set of seven SISAL endmembers showing a number of interesting spectral features (figure 6.11) and with a low level of variance between the matching endmembers across the 7 SISAL runs suggesting they were accurately extracted. All seven endmembers have a broad skewed absorption centred at 1.5 µm and six endmembers also feature a broad absorption of varying depth centred at 2.01 µm. Whilst the broad 2.0 µm could be an artefact of the imperfect volcano-scan atmospheric correction the presence of the strong skewed 1.5 µm absorption suggests that this is a real feature due to the presence of H_2O ice (Clark, 1999; Vincendon et al., 2010). This interpretation matches the morphological interpretation of Leask et al (2006) that the chaos is a result of volcanic activity causing a flood due to melting of large amounts of ice. The varying band depths relate to the amount of ice in each endmember material, however this relationship is not a simple linear one and therefore cannot be used to quantify the amount of ice present (Milliken and Mustard, 2005). The most that can be said is that the endmembers with the deeper ice absorption bands are likely to be relatively richer in icy material than those with shallower bands. Besides these features the major spectral variation is in the overall albedo of each endmember with all of them having a very similar, mostly flat, general spectral shape. All endmembers also have subtle absorptions at 1.21 and 2.39 µm. The 1.21 µm feature is interpreted as an uncorrected remnant of atmospheric CO_2 as it was for the Hecates Tholus endmembers in section 6.3.2. The 2.39 µm feature indicates an O-H combination tone absorption (Ehlmann et al., 2009), however there are no other clear, diagnostic absorptions to determine which atom is in combination with the hydroxyl,

and subsequently which mineral is present. Endmember 4 does not have the broad 2.0 µm absorption seen in all of the others. There are two possible interpretations of this; i) this endmember contains hydroxyl but not H_2O or ii) as discussed for Hecates Tholus and Nili Patera uncorrected randomly distributed atmospheric CO_2 has been accounted for in a single endmember by introducing an increased albedo over these bands. Given the presence of other uncorrected atmospheric artefacts the second explanation is considered more probable. Other than the presence of H_2O ice there are not enough diagnostic spectral features from which to make mineral assignations to the endmembers.

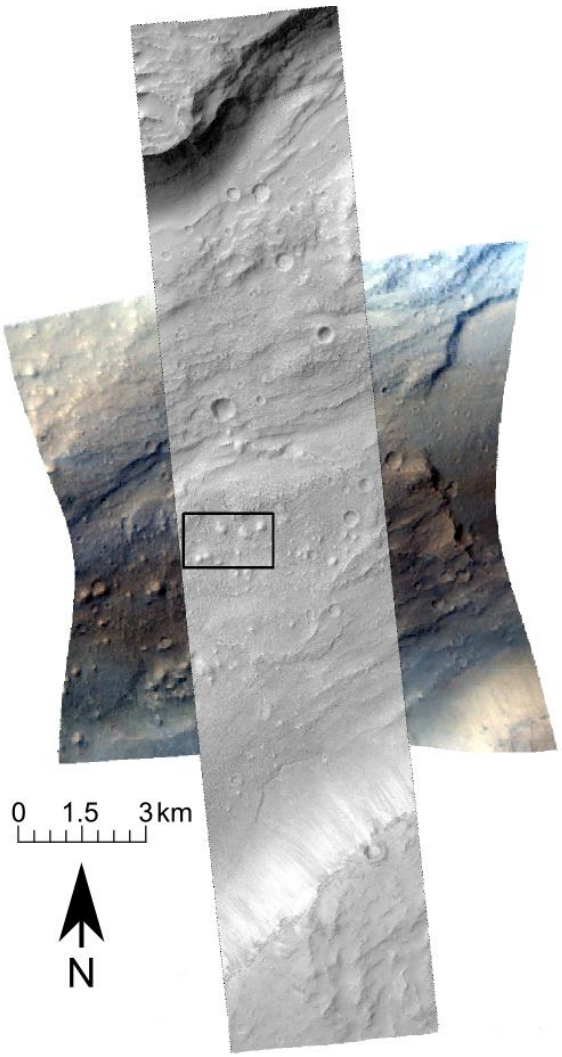

Figure 6.10 Aromatum Chaos CRISM image FRT000247F8_07_IF165S_TRR3 RGB composite of bands 43, 29, 16 and overlain HiRISE image ESP_026891_1790_RED. The ROI selected for analysis through the SMA pipeline is outlined in black near the centre of the two images.

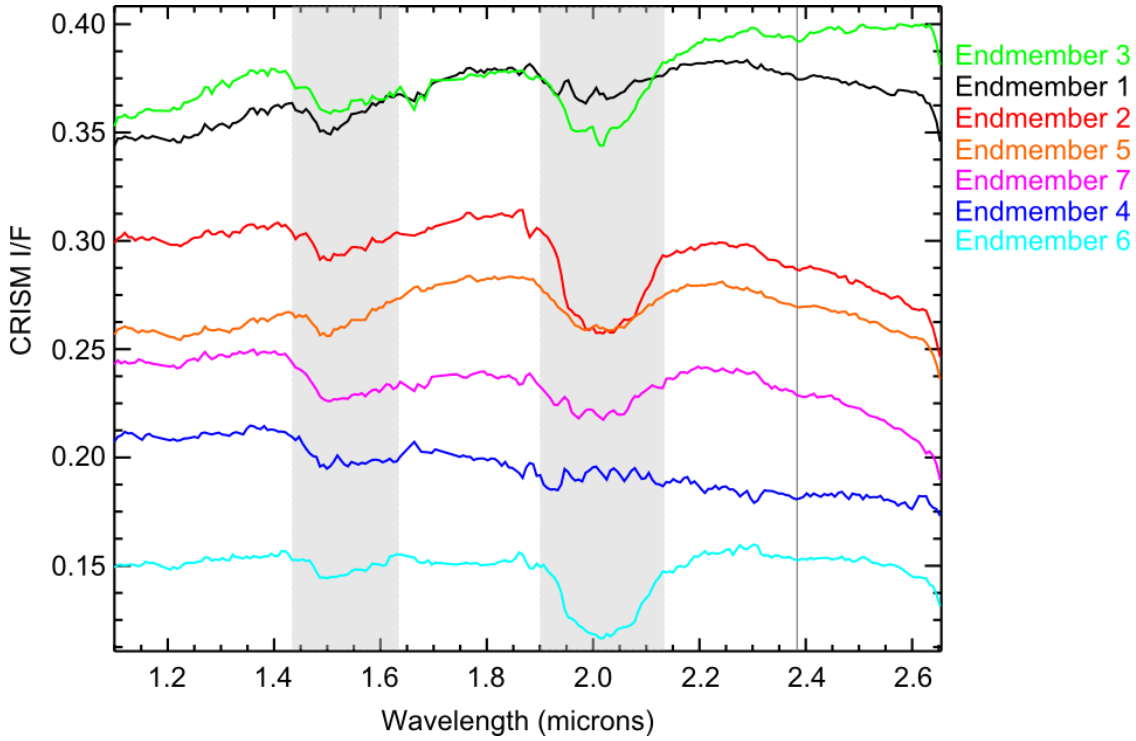

Figure 6.11: IR wavelength range of SISAL extracted endmembers from the Aromatum Chaos ROI highlighted in figure 6.8. All but one of the endmembers show strong H_2O ice absorptions at ~1.5 µm and 2.0 µm as their dominant spectral features highlighted in the figure with the grey boxes. The unspecified subtle hydroxyl combination overtone absorption is also highlighted at 2.39 µm. Endmember 4 appears to be compensating for the uncorrected atmospheric CO_2 hence its lack of absorption at 2.0 µm.

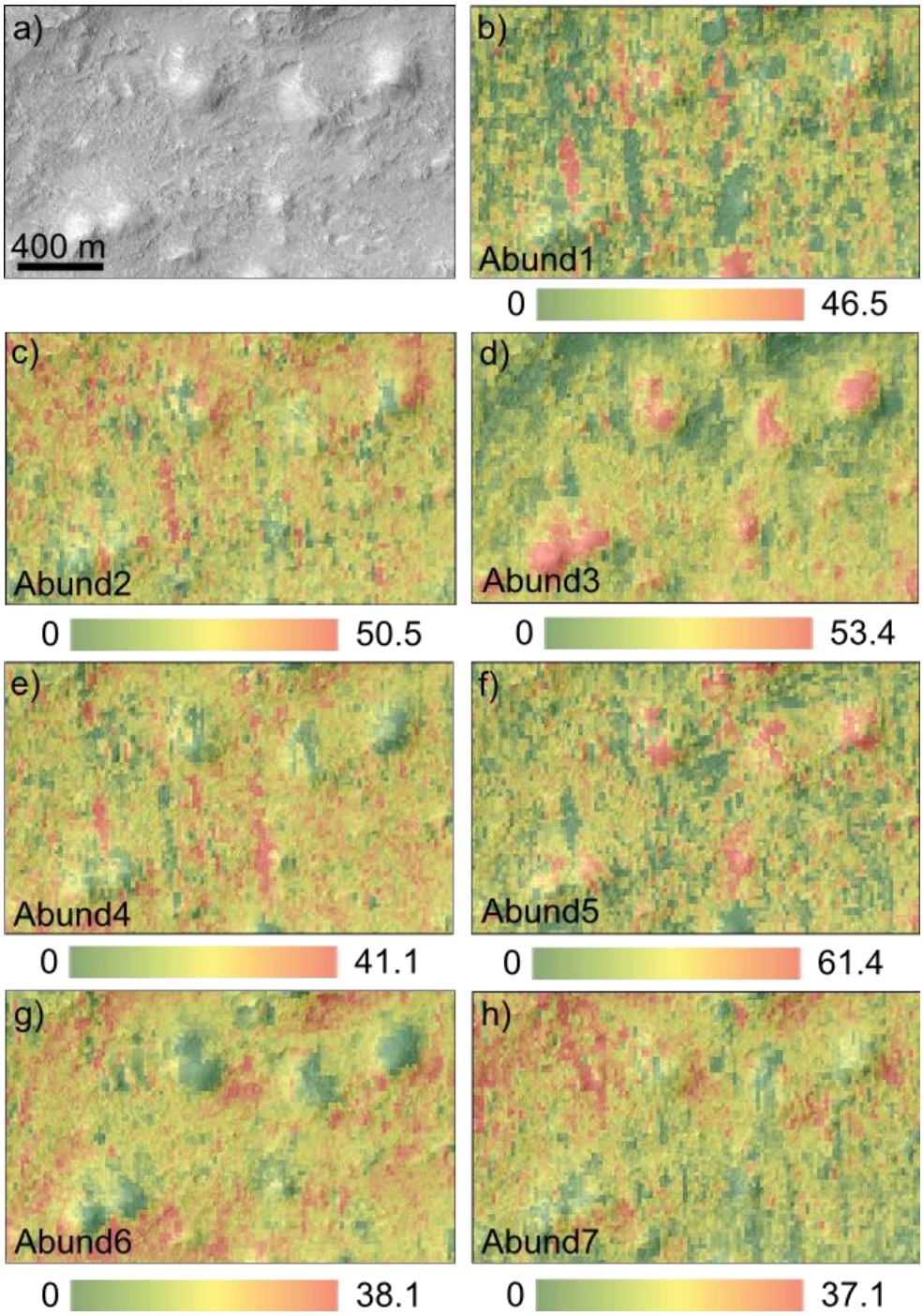

Figure 6.12: Aromatum Chaos ROI FCLLS abundance maps using SISAL extracted endmembers shown in figure 6.11. A green-yellow-red scale is used to indicate increasing abundance % in each pixel. a) HiRISE image of ROI, b) abundance map for endmember 1 overlain on HiRISE image, c) abundance map for endmember 2 overlain on HiRISE image, d) abundance map for endmember 3 overlain on HiRISE image, e) abundance map for endmember 4 overlain on HiRISE image, f) abundance map for endmember 5 overlain on HiRISE image, g) abundance map for endmember 6 overlain on HiRISE image, h) abundance map for endmember 7 overlain on HiRISE image.

FCLLS was used to produce abundance maps from the I/F data, SSA conversion was not performed due to the high number of endmembers used. Further interpretation of the extracted endmember spectra is possible based on the resulting abundance maps. The abundance maps (figure 6.12) can be grouped into three different classes; endmembers 3 and 5 show their highest abundances over the tops of the hillocks, endmembers 4 and 6 show their lowest abundances over the tops of the hillocks, (these two units are largely opposite of each other), and endmembers 1, 2, and 7 show no pattern matching to underlying morphology. Endmember 3 is the highest albedo endmember and its high abundance on the hilltops is likely a reflection of the high illumination in these regions. Endmember 6, with the lowest abundance over the hilltops is the lowest albedo endmember again lending credence to the interpretation that these endmembers are reflecting illumination differences rather than compositional differences. The interpretation given in the previous paragraph for the lack of broad 2.0 μm absorption in endmember 4 being due to a compensation for uncorrected atmospheric CO_2 would suggest a random distribution, however this is not what is seen, there is a pattern corresponding to the ROI's morphology. This is possibly another artefact of the illumination conditions with the albedo correction in these bands being needed more in the regions of low illumination.

The RMSE for the reconstructed image from the extracted endmembers and estimated abundances was 0.0011, the highest of any of the regions examined in this chapter. The CRISM image used was also the most recent, being taken in 2012, and therefore is expected to have the highest level of noise of the images examined in this chapter. The individual pixel RMSE values do not map to any obvious topographic or albedo features or any one endmember abundance lending weight to the confidence of the final pipeline results. Given the lack of unique mineral identification for the endmembers the abundance estimates (table 6.4) are perhaps of less importance than for Nili Patera or Hecates Tholus. They are still expected to be correct to within 5% with individual pixel abundances potentially having higher errors, as much as 20%.

Aromatum Chaos is located close to the equator (-1.03 N latitude) and as such it is not expected that water ice would be stable in the upper microns of the surface at this location (Carrozzo et al., 2009). The water ice spectral signature is prevalent across the ROI and doesn't correspond to any particular topographic features or structural units. An alternative interpretation of the spectra is therefore that rather than detecting water ice crystals in the upper microns of the surface, the water ice is atmospheric. Water ice is known to exist in the martian atmosphere where it forms clouds (Curran et al., 1973). Such an atmospheric

contribution would not be removed by the volcano-scan atmospheric correction method as it is only designed to remove atmospheric molecular CO_2 contributions (McGuire et al., 2009). The heterogeneous blanket distribution of the icy spectral signature would match to a thin water ice cloud layer in the atmosphere. Water ice on a planetary surface is a high albedo substance and it would be expected that any deposits significant enough to contribute to the spectral signature would be visible as bright features on the surface (Bell III et al., 1996). Whilst cloudy features are normally obvious in the RGB composite of a CRISM image (Vincendon et al., 2011) (and these were not seen in the CRISM image examined here), the lack of correlation between the icy spectral signature and any bright surface features leads to the conclusion that in this case the H_2O ice is most likely atmospheric.

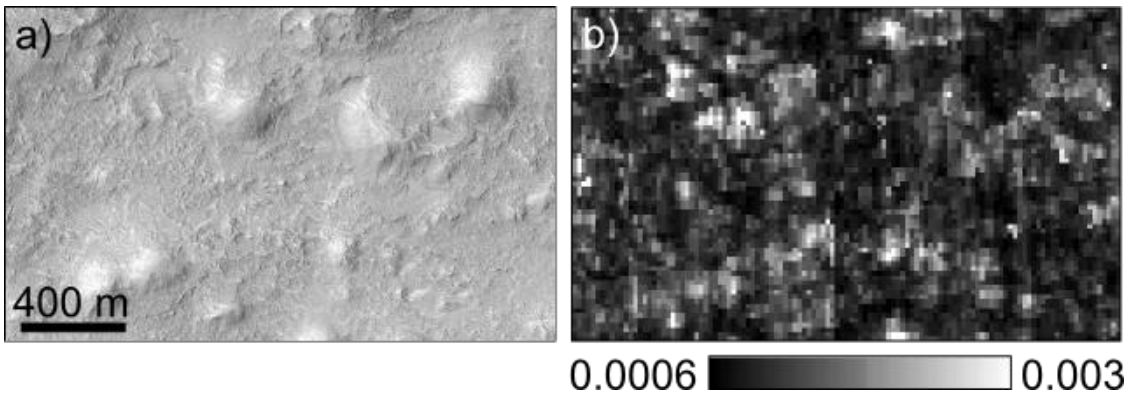

Figure 6.13: a) HiRISE image of Aromatum Chaos ROI, b) RMSE values for the CRISM image reconstructed from the extracted endmembers and their estimated abundances.

The unmixing has not revealed any variations in mineralogy, and nothing that would indicate the previous existence of a hydrothermal system. The Spectral Parameters generated as a part of the image pre-processing also revealed no significant mineral variation and the water ice absorption bands are prominent when the spectral profile of the individual pixels is examined. In this case the use of SMA has not revealed any information or details about the regions that could not be discerned using quicker and simpler methods.

Table 6.4: Aromatum Chaos SISAL extracted endmember ROI total abundance quoted with and error of ±5%, no mineral assignments are given due to a lack of spectral features making diagnostic identifications impossible.

Endmember	Scene %
1	9
2	18
3	12
4	14
5	15
6	16
7	16

6.3.4: Unnamed (Kirkcaldy) Crater (17.367 N, 291.213 E)

Impact craters are obvious features on the surface of Mars and the energy that creates them can also trigger the creation of a temporary hydrothermal environment (Osinski et al., 2013). An unnamed crater approximately 45km in diameter, centred at 17.367° N, 291.213° E in the north western corner of the Hesperian aged Lunae Planum (Warner et al., 2015) near the Sacra Fossae, has been imaged with both HiRISE and CRISM as part of the HiRISE broader science theme investigating impact processes (McEwen et al., 2007). Global mineralogical maps constructed from OMEGA VNIR spectral data show this general region to have a low pyroxene but high ferric oxide content (Bibring et al., 2006). The HiRISE image ESP_017055_1975 shows a texturally and structurally diverse terrain within the impact crater, with numerous spectrally bright patches below the resolution of CRISM that could indicate the presence of hydrothermally altered mineralogy. For this reason this crater was selected for spectral unmixing using the spatially coincident CRISM image FRT00017463_IF165L/S_TRR3. A single ROI to the south of the central uplift feature was selected containing 3976 pixels (figure 6.14). In addition to the bands removed as part of the standard processing described in section 6.2.3 spectral bands 1.178, 1.184, 1.191, 1.198, 1.2537, 1.250 and 1.263 µm were also removed due to erroneous spikes in the data at these wavelengths. For the purposes of this work this crater shall be informally referred to as Kirkcaldy Crater, a name that follows the IAU planetary feature naming conventions.

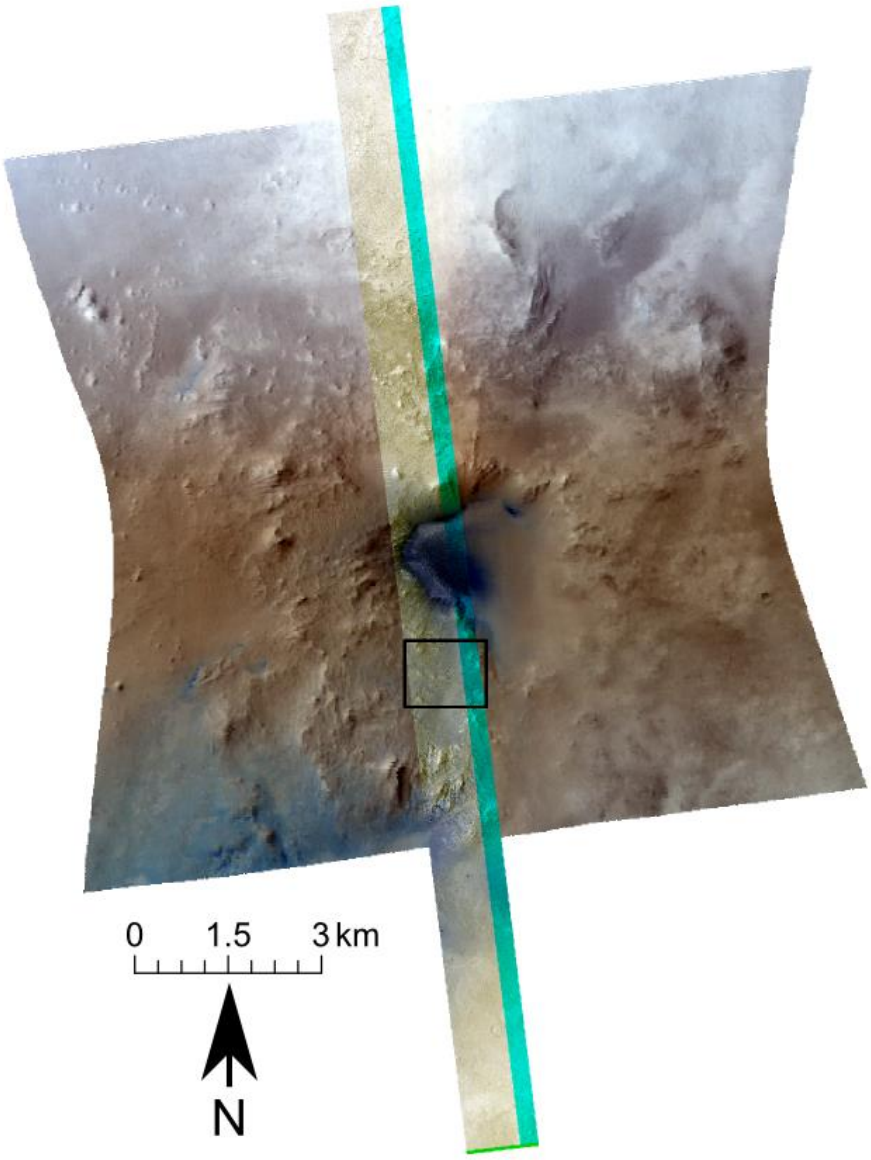

Figure 6.14: Kirkcaldy Crater CRISM image FRT00017463_07_IF165S_TRR3 RGB composite of bands 43, 29, 16 with HiRISE image ESP_017055_1975_COLOR overlain. The black box highlights the region extracted for analysis with the SMA pipeline. The blue/green line in the HiRISE image is due to a missing red CCD strip. See figure 6.13a for a larger version of the ROI outlined in the black box in this figure.

The ODM step gave a p value of 10 but this was not a clear plateau point and therefore confidence of the accuracy of this value was low. SISAL was first run with p = 10. The resulting endmembers revealed one dominated by noise (endmember 9, figure 6.15a) and another with a prominent erroneous reflection feature mirroring an absorption feature centred at ~2.03 µm (endmember 4, figure 6.15a). This feature is interpreted as an attempt by the algorithm to account fully for albedo differences and uncorrected atmospheric CO_2 as

seen in the Nili Patera and Hecates Tholus analyses. Due to the low level of confidence on the initial p value, the high variance between matching members of the 10 SISAL runs and the height of the reflectance spike without an obvious mirror endmember it was decided to increase the p value estimate to investigate if this could mitigate the erroneous feature. The p value was increased by increments of 1 until a suitably realistic set of endmembers was extracted. This iterative method was chosen to find the smallest number of endmembers that encompass the level of variation present without the inclusion of such a large erroneous feature. Using p = 12 the extracted endmembers are all realistic with a low level of variance between the matching members of the 12 SISAL runs and for these reasons considered to be acceptable final endmembers reflecting the reality of the scene (figure 6.15b). The variation in this endmember set is subtle. One major feature that is evident in the majority of the spectra is a broad absorption feature at 2.03 μm. This is interpreted to be evidence of H_2O ice when accompanied by a skewed absorption feature at 1.5 μm (Clark, 1999) as it is in a number of the endmembers. When this 1.5 μm feature is not present the broad 2.0 μm feature is attributed to uncorrected atmospheric CO_2 as it was in the Nili Patera and Hecates Tholus analyses. Other absorption features are seen across the set at 1.21 and 1.80 μm that are remnants of uncorrected atmospheric gases (Wiseman et al., 2014). A number of subtle absorptions are seen in the 2.1 – 2.6 μm range (figure 6.15c), an important wavelength range for mineralogical stretching and bending overtones (see Chapter 2). The absorption at ~2.37 seen in endmembers 4, 5, 8, 9, 10 and 12 is once again an unspecified O-H combination absorption (Swayze et al., 2014), and the 2.55 – 2.57 μm absorption in endmembers 5, 6, 8, 10 and 12 is an uncorrected atmospheric component. A subtle absorption is seen at 2.24 μm in endmembers 7, 9 and 11 and at 2.26 μm in endmembers 1, 2 and 12 in the smoothed spectra (figure 6.15c). However when viewed in the non-smoothed version (figure 6.15b) these features are no longer discernible above the general signal noise. This suggests that in this particular case these very subtle features are artefacts of the smoothing process rather than real mineralogical absorptions.

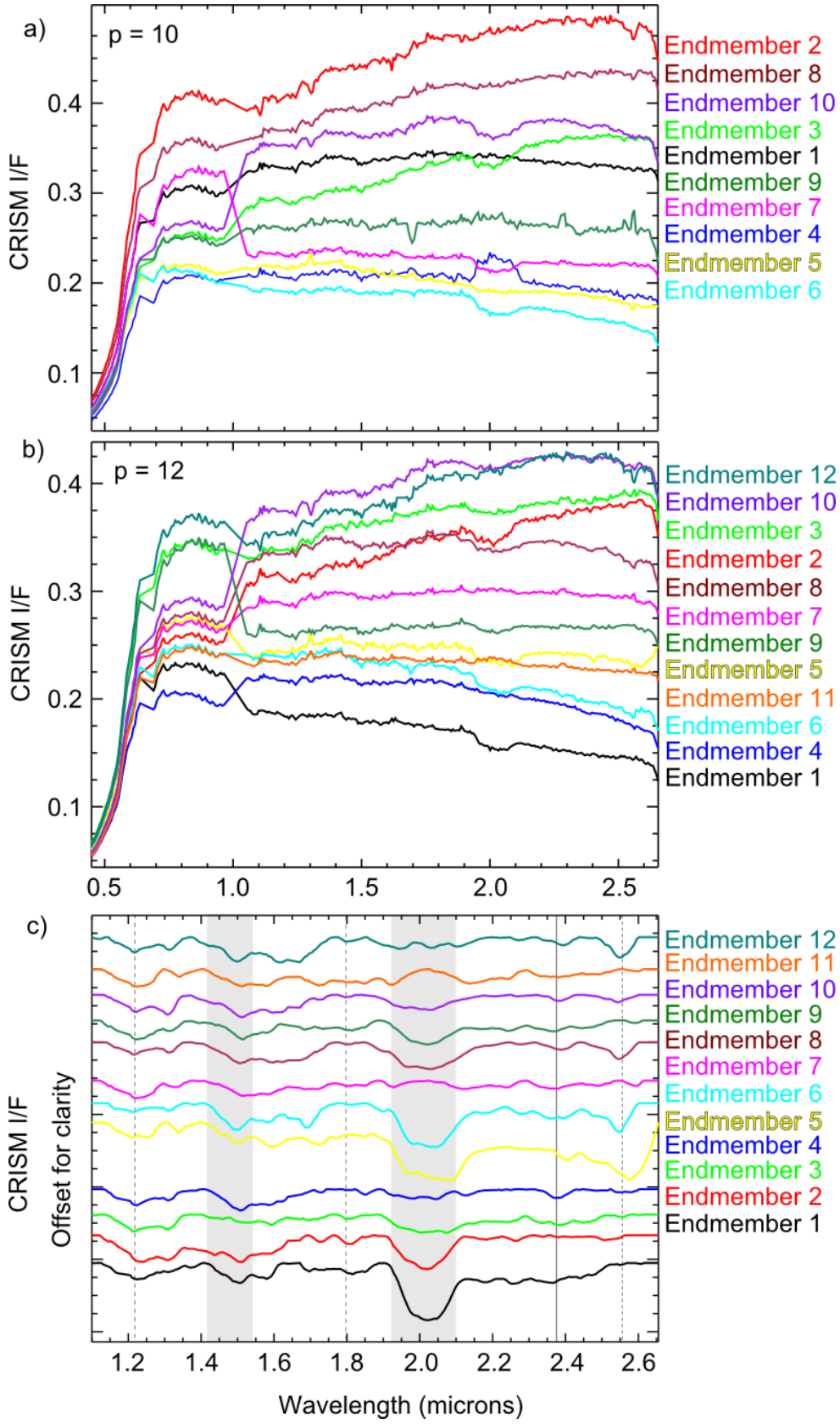

Figure 6.15: SISAL extracted endmembers from Kirkcaldy Crater ROI highlighted in figure 6.14. a) endmembers using p = 10, note the reflectance bump centred at ~ 2.0 µm in endmember 4 and the level of noise in endmember 9. b) endmembers using p = 12, the ~2.0 µm reflectance

bump has disappeared leaving behind a fully realistic endmember set, c) the IR portion of the SISAL endmembers shown in b) smoothed using a Savitzky-Golay filter with a window size of 13 to remove extraneous noise and emphasis the absorption features. Grey shaded areas indicate the location of H_2O ice absorption bands, the solid vertical line indicates the O-H combination absorption and the dotted vertical lines indicate the uncorrected atmospheric artefacts.

There is not enough variation or clear absorption features in the spectra to enable unique mineralogical identification of each individual endmember, but endmembers with an H_2O ice component were identified. The scene abundances and individual pixel abundances were calculated from the I/F data using FCLLS (table 6.5). Although the initial p value was uncertain the high level of confidence in the final extracted endmember set means that these total scene abundances are expected to be correct to within 5%. Individual pixel abundances however could be in error by as much as 15%. Approximately 46% of the scene is comprised of icy material but there do not appear to be any significant regions where this is concentrated, with different icy endmembers concentrating in different regions.

Table 6.5: Totally scene abundances and identification of icy material within the composition of the endmembers extracted from Kirkcaldy Crater ROI using p = 12. An endmember was identified as icy if it had both a clear 1.5 and a clear 2.0 µm absorption.

#	Icy Material	Scene %
1	Yes	10
2	Yes	7
3	No	8
4	No	10
5	Yes	4
6	Yes	4
7	No	18
8	Yes	8
9	Yes	9
10	Yes	4
11	No	10
12	No	8

As was seen in the unmixing results for Nili Patera a number of the endmembers (6, 8, 10 and 11) show abundance patterns as roughly north to south running streaks (figure 6.16) which are again interpreted as uncorrected instrument artefacts. The HiRISE coverage of this region shows a number of broad structural units including a dune/ripple unit in the south of the ROI orientated approximately SW – NE, a smooth unit to the east of the dunes/ripples and a similar looking unit in the north of the ROI. The rest of the ROI is comprised of small outcrops and raised sections surrounded by small bright patches below the resolution of CRISM. Endmember 1 appears to roughly correspond with the smoother sections of the scene and endmembers 2 and 4 show higher abundances in the areas with the small pale patches although these high abundances are not in identical areas. Endmember 3 also has its highest abundances in the regions with a high number of the small bright patches in the HiRISE image, predominantly along the eastern ridges of the ROI. The spectrally flat endmember 7 shows the largest abundance with concentrations to the south of the ROI and again over the smoother/sandier units.

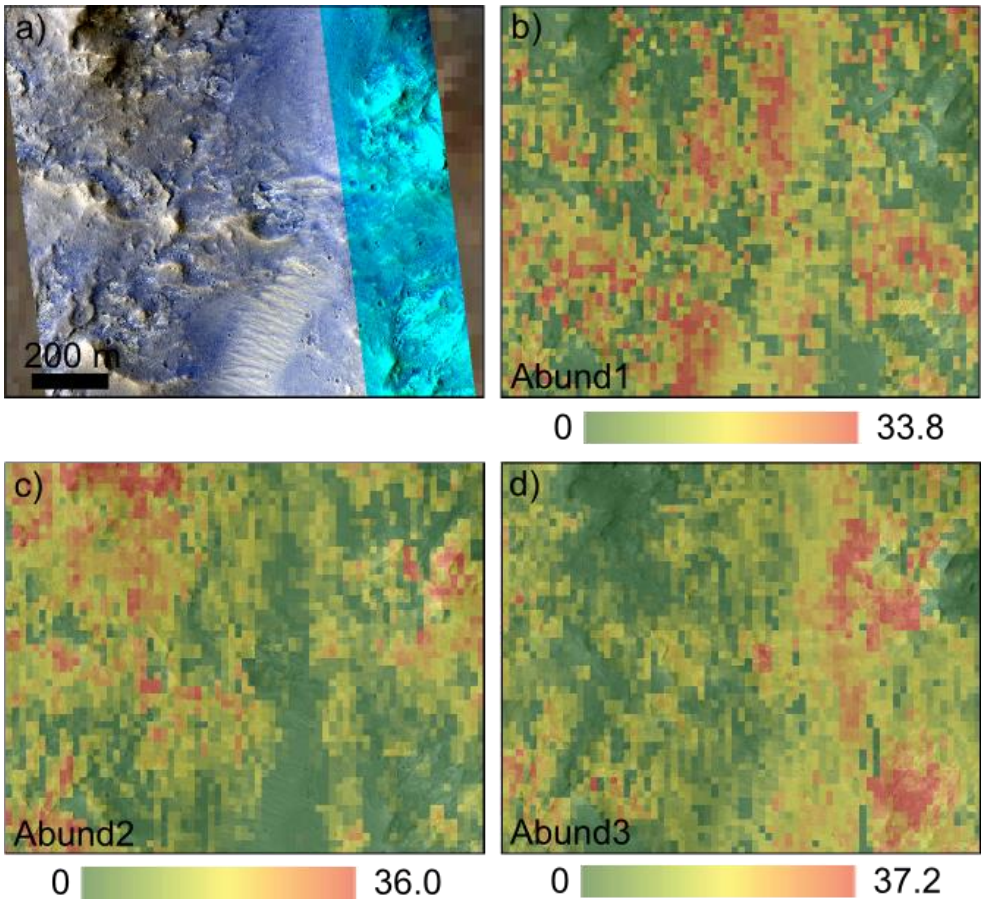

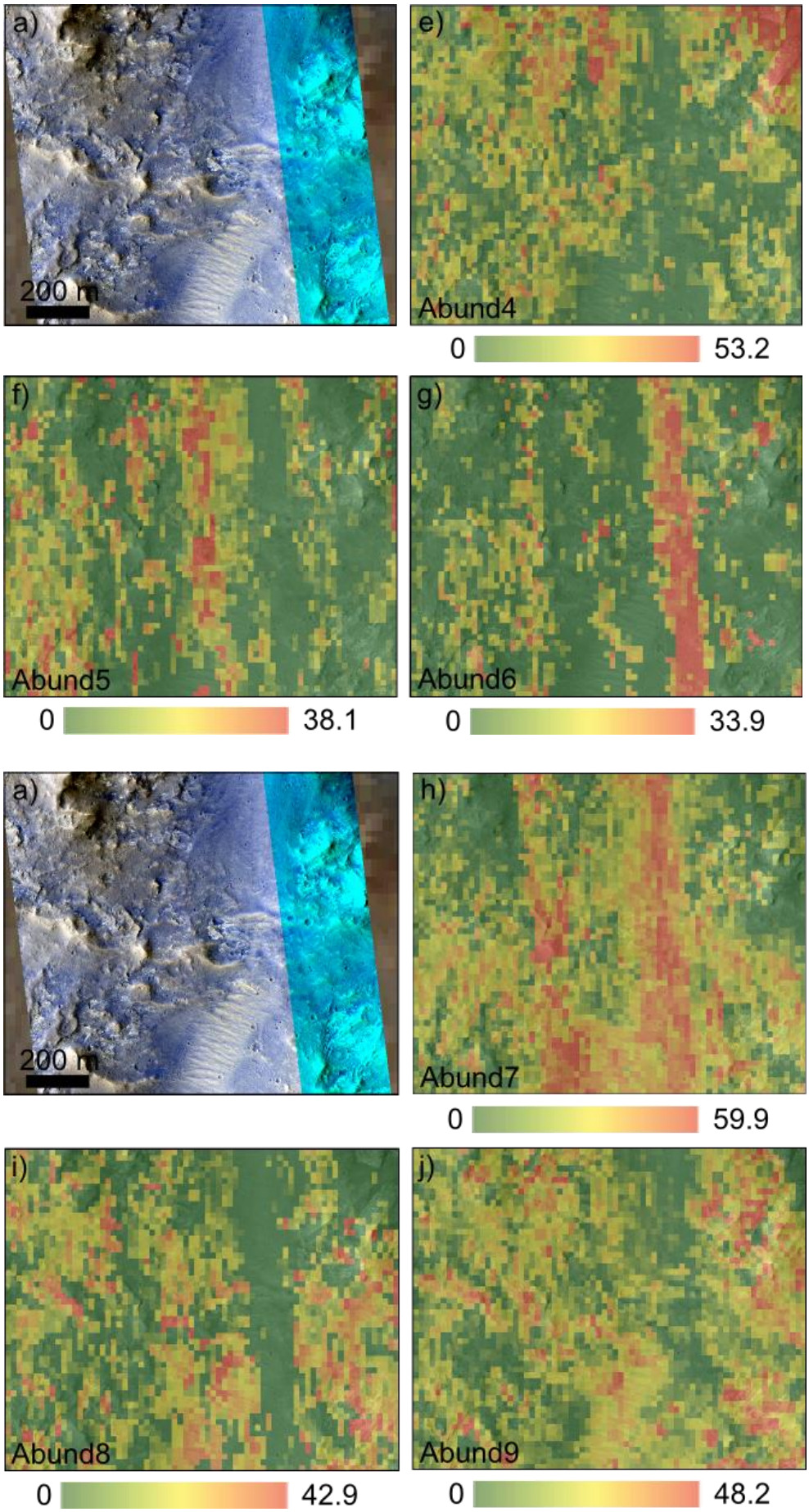
a)
200 m
e)
Abund4
0
53.2
f)
Abund5
0
38.1
g)
Abund6
0
33.9
a)
200 m
h)
Abund7
0
59.9
i)
Abund8
0
42.9
j)
Abund9
0
48.2

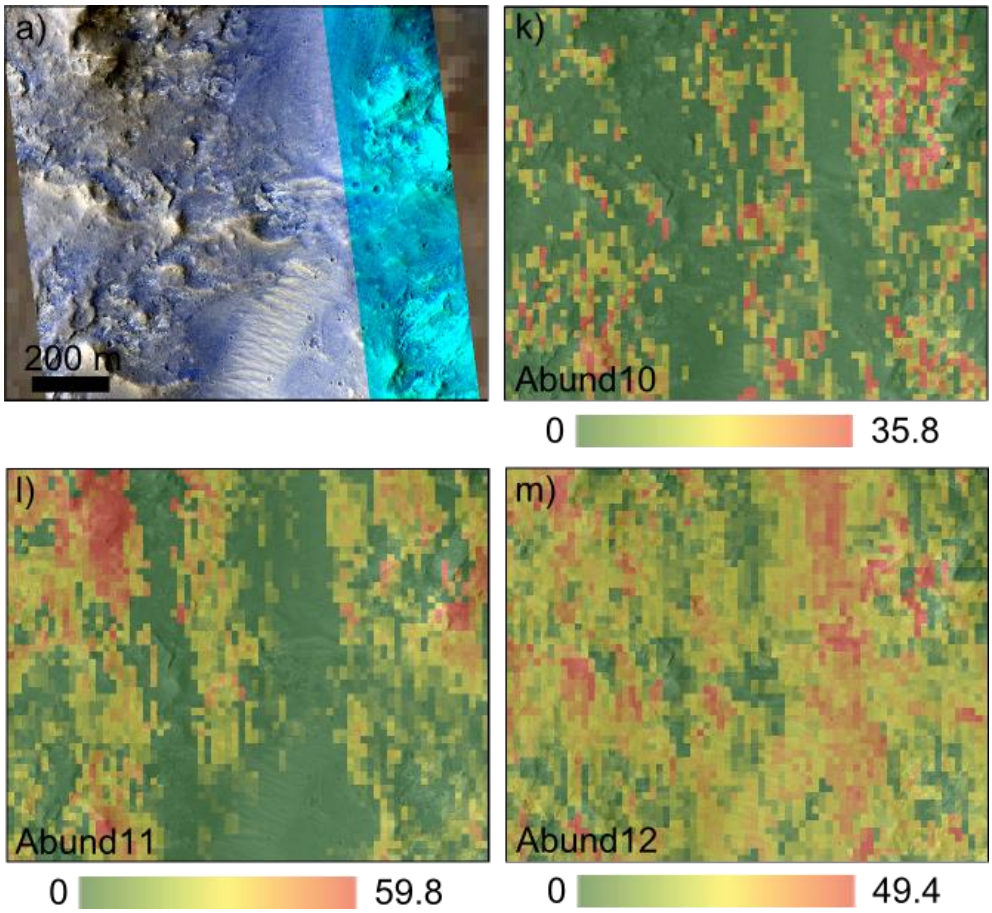

Figure 6.16: Abundance maps for Kirkcaldy Crater ROI. a) ROI portion of colour HiRISE image, b) abundance map for endmember 1 (icy), c) abundance map for endmember 2 (icy), d) abundance map for endmember 3, e) abundance map for endmember 4, f) abundance map for endmember 5 (icy), g) abundance map for endmember 6 (icy), h) abundance map for endmember 7, i) abundance map for endmember 8 (icy), j) abundance map for endmember 9, k) abundance map for endmember 10 (icy), l) abundance map for endmember 11, m) abundance map for endmember 12. All abundance maps are plotted over a greyscale HiRISE image to show spatial context.

Endmember 11 is absent in the rippled/dune unit and shows highest concentrations in the areas with high shade and visual elevation change (figure 6.16l). The highest concentrations of the small bright pale patches are in two units in the far east of the ROI, one in the northern corner and one in the southern. The endmembers that appear most abundant over these pixels with the small pale patches (endmembers 2, 3 and 4) fall into both of the broad spectral categories (icy, non-icy and non-icy respectively) suggesting they can be explained as exposed icy material surrounded by a non-icy material. The presence of the uncorrected image stripes in the abundance maps makes a clear interpretation of the results challenging.

The RMSE of the reconstructed scene using the extracted endmembers and associated estimated abundances is 0.00097 with the individual pixel RMSE values not mapping to any obvious topographic or albedo feature or any of the abundance distributions of the endmembers (figure 6.17).

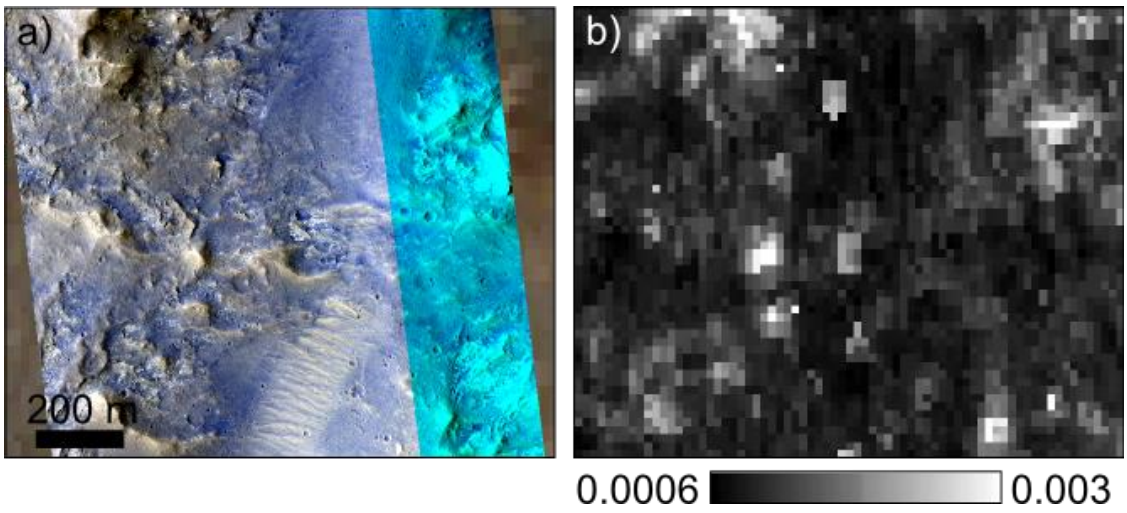

Figure 6.17: a) HiRISE image of Kirkcaldy Crater ROI, b) RMSE values for the CRISM image reconstructed from the extracted endmembers and their estimated abundances.

The potential for any H_2O ice to be atmospheric rather than surficial was discussed in section 6.3.3 with respect to similar spectral signatures extracted from Aromatum Chaos. Kirkcaldy crater is located further from the equator than Aromatum Chaos at approximately 17°N. Carrozzo et al. (2009) have previously reported detection of surface water ice at this latitude range, primarily in shaded regions, based on observations made with OMEGA of the 1.5, 2.0 and 3.0 μm absorptions. These findings have been disputed by Vincendon et al. (2010) who concluded the same observations were the result of atmospheric H_2O ice. There are traces of what could be H_2O ice clouds in the northern section of the full RGB composite CRISM image from which the analysed ROI was taken, however these do not extend to the southern regions where the ROI is located. This lack of cloud and the presence in the HiRISE image of small high albedo patches lead to a tentative conclusion that the H_2O ice detected here is surficial rather than atmospheric.

The SMA pipeline results have revealed the significant presence of slightly icy material and provided tentative spectral evidence that the small pale bright patches in the HiRISE image are a significant source of this H_2O ice. No clear spectral evidence of hydrothermal activity is revealed.

6.4: Hydrothermal region unmixing discussion

The four regions analysed above are all examples of different environments that could have at some point in their past experienced hydrothermal alteration. Nili Patera is the only region showing strong spectral, mineralogical evidence of hydrothermal alteration in the SMA results, in keeping with previous studies (Fawdon et al., 2015; Skok et al., 2010), with the other three regions generating more ambiguous results. Nili Patera and Hecates Tholus were the only regions where it was possible to assign mineralogical identities to the extracted endmembers and even these were often tentative and incomplete. This lack of diagnostic spectral identification is not necessarily a short-coming of the SMA technique, but rather a reflection of the lack of uniquely diagnostic spectral features in the wavelength range used for a number of common minerals expected in these environments. However, even with this restriction the results allowed for quantitative estimation of the presence of certain minerals that have previously only been qualitatively discussed, in particular the hydrated silica identified in Nili Patera first described in Skok et al., (2010). The identification of chlorites and Mg-bearing phyllosilicates in the northern section of the Hecates Tholus central caldera has not previously been reported as no previous high-resolution spectral studies have been performed on this region. The identification of chlorite-bearing units was not possible using the available Spectral Parameters and to manually inspect each pixel would be an unrealistic use of time. This demonstrates the utility of the SMA technique that allows a large region to be distilled down to a handful of spectra that can then be manually inspected for subtle features. The addition of high resolution colour imagery in the form of HiRISE images was vital to the interpretation of the unmixing results, enabling identification of instrument artefacts with confidence and the matching of endmembers with structural units. Even when it was not possible to assign unique mineralogical identities to individual endmembers, the SMA process allowed for some qualitative results. Aromatum Chaos and Kirkcaldy Crater both showed evidence of water ice but the interpretation of this as a component of the surface material and not thin atmospheric clouds was only possible for Kirkcaldy Crater. A tentative association for the H_2O ice with the surface composition was possible for Kirkcaldy Crater based on bright patches in the associated HiRISE image and heterogeneous icy signature distribution. Two classes of endmembers were identified in Kirkcaldy Crater, those that contained H_2O ice and those that did not. This enabled an estimate of the amount of icy material present in the ROI analysed (46%). SMA application to the Aromatum Chaos ROI revealed nothing extra beyond that which could be deduced using the CAT spectral parameters and visual inspection of the individual pixel spectra, a quicker and simpler combination of analysis techniques. Both Aromatum Chaos and Hecates Tholus showed little

spectral variation within the extracted endmembers and when they were mapped to the terrain they predominantly corresponded to larger scale albedo variations. These were also however the two regions analysed that showed the least small scale colour and albedo variation in the HiRISE coverage giving an indication that this would be the case prior to the SMA processing.

The four CRISM images used in this chapter were taken in different years and this is reflected in the results of the SMA. The two regions that yielded identifiable mineral spectra and from which the SMA technique gave new information were the two oldest images, with the Nili Patera image being taken in 2009 and the Hecates Tholus image from 2007. The image that gave the poorest results with the highest RMSE and ambiguous SMA results, Aromatum Chaos, was from 2012 and was expected to have a higher level of instrument noise than the earlier images. The lack of quantitative error statistics within the SMA pipeline makes it difficult to estimate how much error instrument noise is adding to the final results but it is clear from the work presented here that it is an important factor and that early CRISM images are preferable for SMA than more recent ones.

Two prominent issues appeared in the analysis of all four regions, both related to the pre-processing of the CRISM images. Firstly uncorrected atmospheric artefacts were found in all SMA endmember sets. In most cases these were easily identifiable as components of the atmosphere (e.g. slight absorptions at 1.21 and 2.57 µm amongst others) and didn't interfere with the mineralogical interpretation of the endmembers. The imperfect removal of the major CO_2 triplet of absorptions around 2.0 µm however could result in misidentifications. In the analysis presented here the possibility of any features around this wavelength containing a remnant of the atmosphere was considered and taken into account in the endmember diagnoses. However it would be preferable if a more accurate removal of the atmosphere could be performed. This imperfect atmospheric correction using the volcano-scan method has been previously noted by other authors and improvements suggested, but these focus only on the 2.0 µm region (McGuire et al., 2009; Morgan et al., 2011). The volcano-scan method is the only one available through CAT but it does have a number of different parameters in its run settings. These were experimented with using the Nili Patera image and the default setting of allowing the program to pick the best volcano-scan column for the image returned the spectra with the lowest visual level of potential CO_2 at the 2.0 µm region. An alternative, radiative transfer, physics-based approach, has been investigated by a number of authors who have reported improved results using a model called DISORT (Liu and Glotch, 2014; Wiseman et al., 2014, 2012). DISORT is a complex method that requires significant

time and expertise to use. It is not available as an off-the-shelf product and as such it was not utilised as a part of this study. Secondly the failure to completely remove vertical stripes in the images due to differences within the instrument detector array was also found to have a serious effect on the abundance maps of the final endmembers. In the case of Kirkcaldy Crater this made confident interpretation of the final abundance maps impossible. In every case presented the MRO destriping routine was used. CAT does provide an alternative to this in the form of the CIRRUS destriping routine. Every image described in section 6.3 was also processed using the CIRRUS routine and in each case the stripe removal with the MRO was superior. A recent paper by Carter et al (2013) detailed an alternative method to those contained in the CAT plugin for removing the vertical stripes as a part of the pre-processing stage. They reported good results, especially when faint and subtle spectral signals were expected in the CRISM images. This method has not however been made available as a public piece of code and as such was not included in this study.

6.5: Future Work

An alternative to the CAT CRISM image pre-processing routine shall be developed. A full radiative transfer based atmospheric correction such as DISORT shall be investigated as well as the destriping method presented in the Carter et al. (2013) paper. In each image only a small portion was analysed using the SMA pipeline. All regions, and in particular the Nili Patera and Hecates Tholus images, would benefit from further ROIs being analysed after a more rigorous cleaning process to ensure the removal of the vertical stripes, and the atmospheric CO_2. The abundance errors reported in this chapter are based on comparison to qualitative analysis of synthetic images with known values, a fuller quantitative estimate of error throughout the SMA pipeline with specific attention paid to the error contribution of CRISM instrument noise should be established.

6.6: Summary

This Chapter has presented test cases of the application of the SMA pipeline developed in Chapter 5 to potentially hydrothermally altered terrain on Mars. CRISM images were selected from four regions that may have hosted hydrothermal systems in their past. Small sections within each image were selected for analysis using spatially and temporally coincident HiRISE imagery and run through the SMA pipeline developed in Chapter 5. Results were varied, with clear evidence of hydrothermal alteration shown for Nili Patera together with quantitative estimates of key mineral abundances and more tentative evidence in the caldera of Hecates Tholus. Even where the SMA results were not sufficient to enable unique mineralogical identification of all endmembers, key features could still be picked out and

mapped giving an idea of their abundance across scenes. The importance of pre-processing was shown, particularly with respect to atmospheric contributions to the signal, and alternatives to the standard CAT processing tools suggested for future work.

Chapter 7: Spectral Mixture Analysis applied to Recurring Slope Lineae

7.1: Introduction

Chapters 5 and 6 demonstrated the utility of Spectral Mixture Analysis (SMA) in the identification and exploration of hydrothermally altered environments. This chapter shall detail a novel use of SMA to investigate the mineralogy of Recurring Slope Lineae (RSL), narrow seasonal features that have been potentially linked to the existence of liquid water in the shallow sub-surface of Mars and identified as potentially habitable environments (Rummel et al., 2014). The Endmember Extraction Algorithms (EDA) and Abundance Estimation Algorithms (AEA) utilised in Chapter 6 shall be used on hyperspectral data from CRISM together with spatially and temporally coincident high resolution imagery from the HiRISE instrument.

7.2: Recurring Slope Lineae (RSL)

The hydrothermal environments discussed in Chapters 5 and 6 are just one example of small scale potentially hydrated and previously habitable regions on the surface of Mars. Another example of a potentially hydrated and habitable environment (Rummel et al., 2014) that has been gaining increasing attention in the last five years are regions containing Recurring Slope Lineae (RSL). Recurring Slope Lineae (RSL) are transient streak-like features that have been identified on steep equatorial facing slopes in the southern mid-latitudes of Mars (McEwen et al., 2011) and more recently in the northern mid-latitudes and equatorial regions (McEwen et al., 2014). Multiple HiRISE images taken over different martian seasons show RSL as dark streaks that grow and darken with the summer months and shrink back again with the winter. They can be tens of metres in length but are only 1 - 5m in width (McEwen et al., 2011), meaning they are visible in HiRISE imagery but are below the spatial resolution of any of the imaging spectrometers currently operational around Mars, including CRISM. As such, the exact geochemical nature and formation mechanism of RSL have yet to be determined. One leading explanation is that they are the result of near surface liquid brines, resulting from either melting and subsequent release of a subsurface frozen brine source (Chevrier and Rivera-Valentin, 2012; McEwen et al., 2011), or release of water through deliquescence of hydrated salts (Kossacki and Markiewicz, 2014) with increased surface temperatures during spring and summer months. Similar terrestrial features have been identified in Antarctica (Levy, 2012) and Alaska (Hooper and Dinwiddie, 2014), and were found to be the result of seasonal melting of permafrost. Liquid water is not stable at the martian surface but the addition of salts could lower the freezing, melting and sublimation points of brines

sufficiently to allow them to exist as transient liquids on the surface of present day Mars (Hanley et al., 2012). Evidence of the chemicals necessary for such brines have been found in the martian soil by ground-based missions; in particular perchlorates have been found at both the Phoenix landing site (Hecht et al., 2009) and more recently in Gale crater (Glavin et al., 2013; Leshin et al., 2013). The exact chemical nature of these perchlorates and the brines they could form has not been established but Mg, Ca, and Na brines have all been modelled and proposed as possible martian surface brines (Chevrier et al., 2009; Cull et al., 2010; Marion et al., 2010).

7.3: RSL and Spectral Unmixing

A major impediment to the compositional investigation of RSL is their small size relative to the spatial resolution of the imaging spectrometers currently orbiting Mars, including the Observatoire pour la Minéralogie, l'Eau, les Glaces et l'Activité (OMEGA, ≥ 300 m/px) and Compact Reconnaissance Imaging Spectrometer for Mars (CRISM, ≥ 18 m/pixel). This small size means no hyperspectral pixels are comprised 100% of the surface RSL and as such there has been no unique spectral signature extracted for RSL to date. SMA would therefore be an ideal technique to further investigate RSL. Mushkin et al (2010) combined CRISM and HiRISE data to investigate the spectral properties of low-albedo slope streaks in two locations in the Olympus Mons Aureole. They used SMA to demonstrate that the streaks were not shadowing effects or mixtures of the surrounding soils but made no attempt to identify the geochemical makeup of the RSL themselves. More recently Ojha et al (2013) used CRISM imagery to investigate the spectral properties of 13 confirmed RSL sites. Spectral ratioing was employed to enhance any potential faint spectral features that could exist in pixels with RSL components. They found no evidence of water but did detect enhanced abundances of ferric or ferrous minerals in the presence of RSL. Many of the sites they investigated had spectrally limited CRISM coverage with only data from the short wavelength detector covering 0.362 – 1.053 μm. At this wavelength range many important diagnostic features including the major H_2O absorptions at ~1.4 and 1.96 μm are not covered meaning their work did not rule out the presence of water in all 13 investigated RSL sites. They also provided no evidence that the increased ferric and ferrous mineral content came from the RSL themselves and not the soils immediately surrounding them.

A new technique using SMA to extract a unique spectral signature for RSL is presented in this Chapter. The work detailed in Chapter 6 demonstrated the usefulness of coincident HiRISE and CRISM coverage in the interpretation of SMA products and this utility shall be further exploited here to provide a groundtruth image from which to interpret the SMA abundance

results. HiRISE images are necessary to confirm the existence of RSL and in some cases CRISM images were taken at the same time. Unlike the structurally complex hydrothermal environments investigated in the previous Chapters, the areas containing RSL are often simpler, containing only two or three basic units; the RSL themselves and one or two background material units surrounding the RSL. These units can be easily determined by visual inspection of the HiRISE imagery. The area covered by the RSL can be estimated from the HiRISE images. If there is temporally and spatially coincident CRISM coverage the abundance of RSL in each CRISM pixel can therefore be established. If the number of endmembers and their relative abundance has been estimated from the HiRISE imagery then there is only one step in the SMA pipeline left to perform, the endmember extraction. The remainder of this Chapter will detail an attempt to validate the use of SMA using both HiRISE and CRISM imagery to extract a spectrum for the RSL and attempt to identify their mineralogical and chemical composition.

7.4: Image preparation

Coincident pairs of HiRISE and CRISM datasets of confirmed RSL locations (Ojha et al., 2014) were acquired from the Planetary Data Systems Mars imagery archive. HiRISE images with few RSL and/or significant variation in the background material including large numbers of boulders were discarded. This left one region suitable for the SMA method proposed in this Chapter. Palikir Crater [-41.623° N, 202.282° E] is host to a particularly dense suite of confirmed RSL that are found on a slope free from large numbers of boulders (Ojha et al., 2014). The images used in this work are CRISM image FRS00029F0C_01_IF170L/S_TRR3 and HiRISE image ESP_032381_1380. The CRISM image was pre-processed using the CAT (CRISM Analysis Toolkit) v7.2.1 plugin in ENVI 4.8. First the image was converted to I/F reflectance values as described in (Murchie et al., 2009, 2007). Photometric correction to correct for angle of incidence effects was applied and atmospheric correction performed using the volcano-scan method with the updated McGuire band selection (McGuire et al., 2009). Stripes due to instrument artefacts and spikes due to noise were removed. Finally the data were map projected and georeferenced to a Mars datum. At this stage the image was examined and any remaining bands with obviously erroneous data spikes in the area of interest were removed leaving 336 spectral bands. A number of bands and band ranges in CRISM are known to return unreliable values (Murchie et al., 2009), as listed in Chapter 6, section 6.2.3. Any features in the bands listed in that section were discounted as image artefacts in the final interpretation of the SMA results.

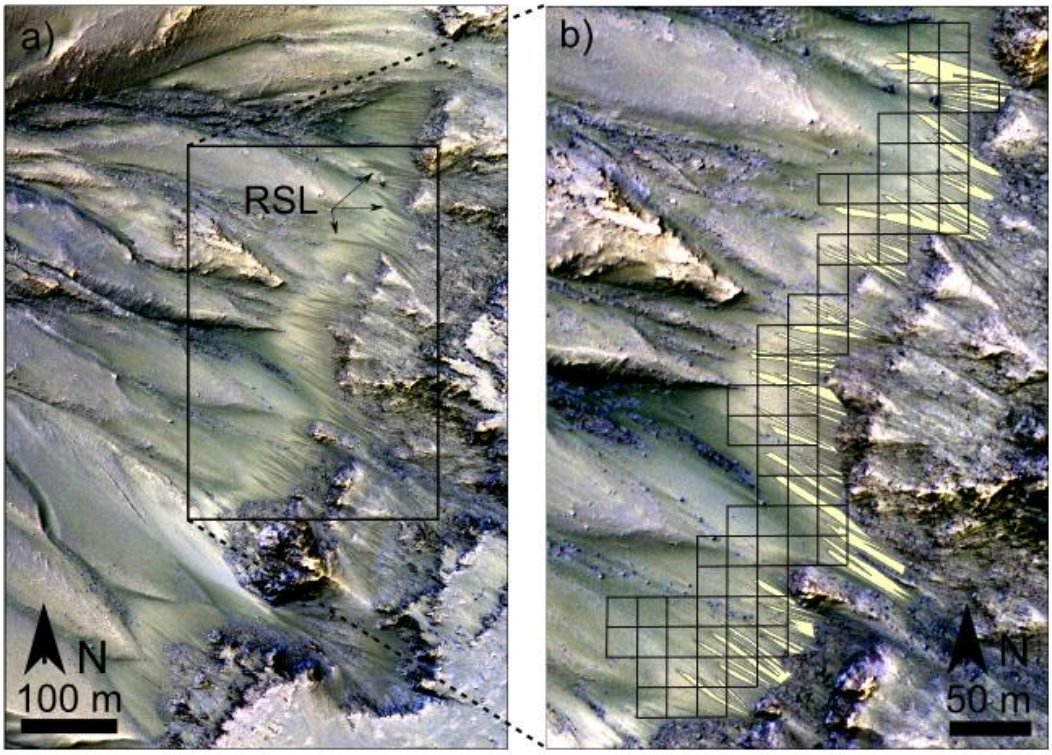

Figure 7.1: a) Section of HiRISE image ESP_032381_1380 showing prominent RSL. b) outlined section of a), RSL areas are highlighted in pale yellow and the outline of the extracted CRISM pixels is shown in black. 75 pixels are outlined in this figure however eight were discarded from the final analysis due to the presence of boulders. The three band HiRISE image has been contrast stretched to emphasise the RSL and the colour variation in the background soils.

Any slight spatial mismatches between the pair were corrected to allow for accurate co-registration of the map projected CRISM and HiRSE images. Central subsections covering the RSL locations were extracted from both processed images. The 899 nm CRISM band was then georeferenced to the NIR HiRISE band in a process similar to that used in Ceamanos et al. (2011) to co-register HiRISE and CRISM imagery in a SMA algorithm comparison study. Using a moving window of 31 pixels, tie-points were identified by matching the grey-scale values in either band. A minimum correlation value of 0.65 was enforced resulting in 30 tie-points all within the region shown in figure 7.1a with a matching root mean square error (RMSE) of 0.1989. The full CRISM subsection was then warped to the HiRISE image using a Delaunay triangulation. RSL were outlined manually in the HiRISE image and the percentage of RSL in each of the overlain CRISM pixels was calculated (figure 7.1b). These together with a number of RSL-free pixels were extracted for the spectral unmixing process giving a total of 75 pixels. Each pixel was then re-examined to ensure that no boulders or obvious extra endmembers

were present beyond the RSL and the background material, and eight pixels removed leaving a total of 67 for use in the SMA process.

Visual inspection of the HiRISE image showed albedo variation in the soils surrounding the RSL and so a p value of 3 was assigned to allow for two background soil endmembers. The extracted CRISM dataset was analysed through two EEA algorithms; RMVES and SISAL. Each EEA was run 26 times. Each of the 52 sets of extracted endmembers were run through the FCLLS algorithm to calculate the relative abundance of each endmember in each pixel. These abundance results were compared to those calculated directly from the HiRISE image. The difference between the extracted endmember abundance (a_i') and the HiRISE derived abundance measurements (a_i) were calculated as

$$E = \frac{1}{p}\sum_{i=1}^{p} \min_{j}\left(\frac{1}{N}\sum_{k=1}^{N}\left|a'_{ik} - a_{jk}\right|\right) \quad (6.1)$$

as used in Heylen et al (2011). Equation (6.1) calculates the difference in the abundance of each endmember in each pixel between the FCLLS calculated data and the HiRISE data and averages this value.

7.5: SMA results

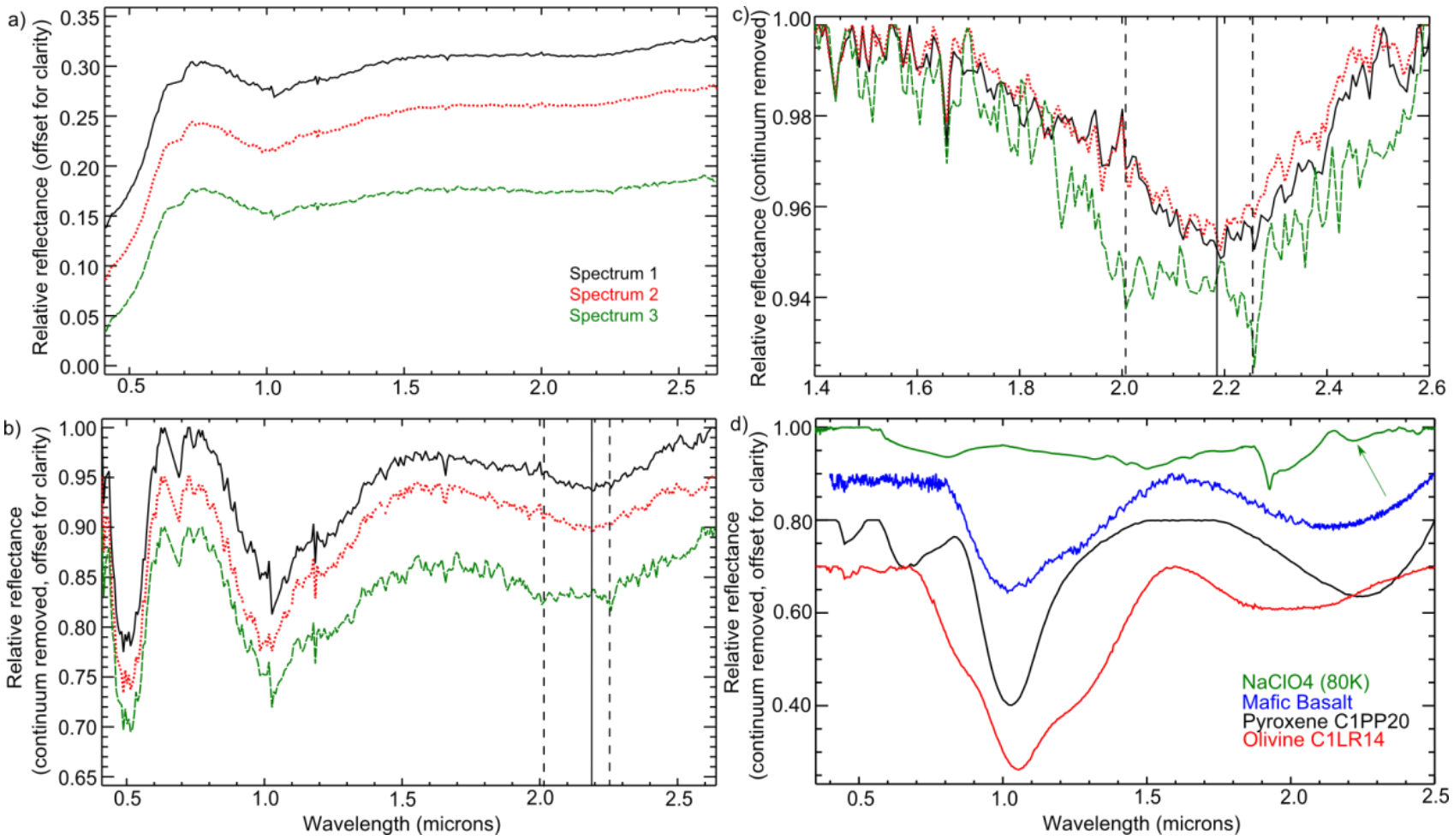

Figure 7.2: a) the extracted endmember set with the smallest E value and best fit to the HiRISE calculated abundances. Spectrum 1 (the solid black line) and Spectrum 2 (dotted red line) together account for the background soils. Spectrum 3 (the green dashed line) correlates with the RSL abundance. The background spectra have been offset by 0.05 for clarity. b) The three extracted endmembers with the continuum removed to emphasis key spectral absorption features. The solid vertical line marks the centre of the background endmembers major IR absorption and the two dashed vertical lines mark the centre of the RSL endmember's two IR absorptions. The green and red spectra have been offset by 0.05 for clarity. c) The IR portion of the spectrum only, emphasising the key absorptions, these spectra have not been offset. d) example spectra from spectral libraries offset by 0.1 for clarity, pyroxene and olivine from the Johns Hopkins spectral library and mafic basalt from the CRISM spectral library. The $NaClO_4$ spectrum taken from Hanley et al [2014] with the ~2.23 µm absorption highlighted. The other major absorption in this spectrum at 1.96 µm is an H_2O absorption band not present in the extracted endmembers.

A common spectral pattern was found in all 52 SMA runs. The primary difference between the numerous runs was the depth of the absorptions in the three spectra rather than the central wavelengths of the absorptions. The three endmembers in each run were assigned to either the RSL or the background based on their match to the pixel endmember abundances extracted from the HiRISE image. The endmember set from both the SISAL and RMVES runs with the lowest overall abundance error, E, as calculated using equation (6.1) were identical, with an E value of only 0.00029. The best fit three spectra produced by the SMA all follow the same general spectral shape but with a number of subtle differences (figure 7.2). Spectrum 1 and Spectrum 2 are identical above 1.5 µm with their primary difference being a lower general albedo in Spectrum 2 (figure 7.2) in the 0.4 – 1.5 µm range and a shift in the band centre around 1 µm, the Spectrum 2 band centred at 1.0 µm and the Spectrum 1 (figure 7.2) band centred at 1.03 µm. Spectrum 1 and Spectrum 3 show a sharp discontinuity at 1.03 µm which is an instrument artefact showing where the VNIR and IR detectors overlap (Murchie et al., 2007). This is not as evident in Spectrum 2. It is most likely masked by the 1.0 µm band centre. The combined calculated abundance for Spectrum 1 and Spectrum 2 matches well to the abundance calculated for the background material using the HiRISE image. The HiRISE image (figure 7.1) shows that the background material does become darker at the northern end of the region of interest and these two endmembers are reflecting this. This albedo difference is most likely the result of differences in particle size or length of surface exposure time rather than any mineralogical differences as reflected in the very

similar endmembers. The calculated abundances of Spectrum 3 (24% over the whole scene) were a numerical match to the RSL abundances (23% over the whole scene). Spectrum 3 has a lower albedo than the combined background spectra (Spectrum 1 and Spectrum 2), consistent with previous observations (Mushkin et al., 2010; Ojha et al., 2013). All three spectra show a strong 690 nm shoulder, however this is a well-documented instrument artefact due to a detector filter boundary at 650 nm (Murchie et al., 2007). All three endmembers also exhibit a slight absorption at 0.5 µm due to crystal field transitions in ferric iron and a broad ~1.0 µm absorption due to a crystal field transition in ferrous iron (Hunt and Ashley, 1979). The background endmembers (Spectrum 1 and 2, figure 7.2) also exhibit a broad shallow absorption centred at ~ 2.17 µm. These features together constitute a basaltic soil (Horgan et al., 2014) of pyroxene + olivine and possibly some iron oxide, a fairly typical mix for weathered martian soil (Chevrier and Mathe, 2007). The RSL endmember Spectrum 3 also has this broad 2.17 µm feature but superimposed on it are two shallow broad absorptions centred at 2.01 and 2.26 µm (figure 7.2). This suggests the RSL material is the same basaltic soil as the other two endmembers but with a minor additional component. The 2.01 µm broad absorption feature is subtle and given its location should be treated with caution as atmospheric CO_2 results in significant (but sharp) absorptions features at ~2.0 µm. These atmospheric features are seen as a triplet at approximately 1.97, 2.01 and 2.07 µm (Bernstein et al., 2005). This triplet of sharp features is evident here suggesting that the atmospheric correction may not have removed all of the atmospheric CO_2 correctly.

None of the endmember spectra show the deep absorption bands associated with hydration at ~1.4 µm and 1.96 µm. Massé et al (2014a) demonstrated in laboratory experiments that the absence of VNIR spectral signatures of water did not necessarily mean an absence of water activity. It is therefore possible that the liquid water within the brines forming the RSL sublimated shortly after exposure to the Martian surface, thereby resulting in the low-albedo features observed and the absence of water absorptions in endmember Spectrum 3. Alternatively, if we assume that the 2.01 µm feature would remain after a more robust atmospheric correction then it could be explained as a shifted hydration feature. Crystallisation of certain hydrated salts (namely $MgCl_2$ and $MgSO_4$) has been shown to cause the 1.96 µm H_2O absorption in previously wet basaltic soils to shift to longer wavelengths (Massé et al., 2014b). It does not seem unreasonable to assume this shift could be seen in the presence of other similar salts as well. This particular H_2O feature has also been shown to shift to longer wavelengths and broaden as the water freezes (Clark, 1999). Massé et al (2014b) also note that CRISM measurements are made outside the soltime during which

liquid water is stable and thus if the RSL are the result of liquid water at the surface it could have refrozen prior to the CRISM measurement.

The 2.26 µm feature is harder to interpret. Many sulfates and chlorides have absorptions in the neighbourhood of this wavelength (Bishop et al., 2014; Hunt et al., 1971) but in these mineral types this absorption is always accompanied by stronger absorptions in the 2.35 – 2.5 µm range. Such accompanying absorptions are not seen in Spectrum 3. The favoured hypothesis in the community to explain RSL is the presence of salts, in particular chlorates or perchlorates that have been previously found in the soils at various martian localities (Dundas and McEwen, 2015; Hecht et al., 2009). There has been little work however in this wavelength range investigating the spectral signatures of chlorates and perchlorates and how their absorption features may change and shift with particle size, temperature and accompanying minerals. Work by Hanley et al (2014) investigating the spectral properties of chlorates and perchlorates as they might appear under the environmental conditions of the Icy moons of the outer solar system, show that sodium perchlorate ($NaClO_4$) exhibits an absorption band at ~2.23 µm when at low temperatures without the strong ~2.4 µm accompanying feature (figure 7.2d). Earlier work by the same authors (Hanley et al., 2010) showed similar features from sodium chlorate ($NaClO_3$) with an even stronger 2.22 µm absorption. This feature however, while near to the unidentified feature in Spectrum 3 is not in the exact same location and therefore cannot be used to explain the absorption at 2.26 µm. Exploration of the literature revealed no convincing candidate to explain the 2.26 µm absorption.

7.6: Discussion of SMA results – a suitable technique for RSL?

The spectral variance in the extracted endmember set is subtle and there are numerous sources of error in the technique described that must be considered. The estimation of the RSL abundance in a CRISM pixel is dependent on the accuracy of the co-registration of the HiRISE and CRISM images. The method employed in this work provides reasonably accurate results but some error is expected (in this work this is estimated to be as a spatial displacement of up to 2 HiRISE pixels). This error in turn feeds into error in the groundtruth HiRISE estimated abundances in each CRISM pixel. Without an accurate groundtruth of the RSL abundances it is difficult to assess the accuracy of the extracted SMA endmembers and their associated FCLLS calculated abundances. The COSI-Corr program has been shown to have some promise for use in improving the accuracy of co-registering HiRISE and CRISM images (Rice et al., 2013a). This technique however, is still in the development phases and was unavailable for this study. Due to the subtlety of the spectral features present slight

errors introduced in the processing of the CRISM image can have a significant impact, as seen in the potential CO_2 absorptions left in the SMA endmembers. The volcano-scan method is the atmospheric correction method provided to the general CRISM user community but it has been shown to be less accurate than radiative transfer based methods (Wiseman et al., 2012). A number of authors have reported improved results removing the atmospheric effects in CRISM images using the DISORT radiative transfer code (McGuire et al., 2008; Wiseman et al., 2012). Atmospheric correction of CRISM data using radiative transfer modelling is however a time consuming task and it was not possible to perform as part of this study. The SMA abundance calculation was performed using the FCLLS algorithm assuming linear mixing in the scene. Whilst this is a reasonable assumption between the RSL and the background endmembers the two background endmembers in this case are likely a non-linear intimate mixture. This adds another source of error to the unmixing routine making it more difficult to assess the accuracy of the extracted endmembers. Use of conversion to SSA reflectance could improve on this source of error but the unmixing results on synthetic images presented in Chapter 5 suggest that this would not provide a significant decrease in error and could potentially make the results worse. Finally the results presented here are from just one image set, in one region. Although there exists CRISM coverage of other RSL sites it is not all coincident with HiRISE imagery, and of those that are, all others examined were unsuitable for this technique due to additional complexity, primarily in the form of boulders littering the soils around the RSL.

7.6: Future work

Despite the number of sources of error in the technique described here some intriguing results were still extracted. SMA using temporally coincident CRISM and HiRISE imagery shows promise and if the COSI-Corr and DISORT algorithms could be integrated into the image pre-processing steps the unmixing results would be substantially more robust. Understanding RLS is a high priority goal for the Mars science community and thus there is hope that more CRISM and coincident HiRISE images will be taken as long as the instruments remain operational. The remaining issue remains that of limited spectral libraries to compare the resulting endmember spectra to. This is a problem for interpretation of planetary reflectance spectroscopy data across the board and is gradually being addressed on a long-term scale within the planetary community and beyond.

7.7: Summary

This chapter has presented the results of a proof-of-concept test using SMA of CRISM data together with spatially and temporally coincident HiRISE images to determine the spectral and mineralogical signature of RSL. A CRISM and HiRISE image covering RSL on the slopes of Palikir Crater were co-registered and the SISAL algorithm used to extract spectral endmembers. The FCLLS algorithm was used to calculate the pixel abundances of these endmembers. RSL pixel abundances were also estimated from the coincident HiRISE image and these values used to match the extracted spectral endmembers to either the background medium or the RSL. The background was identified as basaltic soil. A unique spectrum was extracted for the RSL themselves. Whilst it was not possible to identify the chemical/mineralogical source of the unique spectral feature this is an issue of incomplete spectral libraries available for comparisons rather than a failing of the analysis technique. The RSL endmember featured two subtle extra features compared to the background signature; one was interpreted as tentative evidence of water ice although it may be uncorrected atmospheric CO_2 and the other remained unidentifiable. The spectral signature of the RSL is subtle and numerous sources of possible error exist primarily in the image pre-processing stage. Methods to improve the pre-processing (the atmospheric correction and the image co-registration) were suggested that if implemented would make this a promising technique for characterising the chemical nature of RSL.

Chapter 8: Conclusions

The preceding Chapters have investigated the utility of VNIR spectral imaging in the exploration and identification of small scale hydrated environments on Earth and Mars, in particular hydrothermally altered surfaces and Recurring Slope Lineae. Both environment types are of particular importance as potentially habitable environments. Two types of instrument have been investigated whose data differ in key aspects of scale; the high spatial, low spectral resolution PanCam, and the low spatial, high spectral resolution CRISM. A solution to the limitations imposed by the low spatial resolution of CRISM was investigated in the form of Spectral Mixture Analysis (SMA), focusing on its availability to the planetary science community and its applicability to mineralogically complex hydrothermally altered environments. Both the PanCam and the CRISM levels of scale demonstrated their own advantages and disadvantages. The findings of this thesis shall be summarised and discussed more fully in this final chapter.

8.1: PanCam – high spatial, low spectral resolution

The PanCam is a multispectral, stereoscopic, panoramic imaging system planned for inclusion in the 2018 ESA/Roscosmos ExoMars rover payload. The Aberystwyth University PanCam Emulator (AUPE-2), an emulator of the PanCam instrument, was field trialled in Námafjall, Iceland, a hydrothermally active region exhibiting significant mineralogical and structural heterogeneity over small spatial scales. Engineering constraints limit the spectral capabilities of PanCam to a 12 point spectrum spread between 400 – 1000 nm, a coarse spectral resolution over a less than ideal wavelength range for geological applications. Given the ExoMars science goals to identify signs of extinct and extant life, the ideal filter set to detect the broadest range of minerals likely to form in habitable environments was identified in previous work by Cousins et al. (2012). The work presented in this thesis represents the first field trial of these filters, testing their applicability to the identification of a hydrothermal environment and ensuring the fidelity of the data returned. Despite the spectral limitations, the datasets collected with AUPE-2 proved sufficient to correctly characterise the study region as a hydrothermally altered glaciovolcanic environment when the spectral data were used in conjunction with contextual WAC and HRC imaging. Whilst the majority of the minerals present could not be uniquely identified from PanCam data alone, certain key characteristics were captured including diagnostic Fe absorptions and sharp blue slopes indicating the presence of sulfur. The use of specifically designed spectral parameters and well established techniques including Principal Components Analysis proved to be quick and

efficient analysis methods; highlighting commonalities across different ROI targets within the wider area, and emphasising discrete spectral units within the multispectral image cubes. The PanCam filter set is also capable of capturing the absorption around 950 – 1000 nm related to hydrated minerals (Rice et al., 2010), however this was not reflected in the collected data. This was found to be due to a flaw in the AUPE-2 optical system that affected the longest wavelength filters. Detection of such faults is an important aspect of field trials and this early detection should allow the PanCam engineering team enough time to ensure a similar problem does not affect the final flight-ready instrument, particularly given the importance of the 900 - 1000 nm spectral region in identifying hydrated mineral deposits, as demonstrated by MER Pancam and MSL Mastcam. The major factor that enabled the accurate characterisation of the environment, despite the frequently ambiguous and sometimes flawed spectra, was that these spectra were not collected as isolated data points, but instead as high spatial resolution images. Centimetre, and in the case of the accompanying HRC images, millimetre scale textures and structures were visible providing extra information together with the necessary spatial context needed to fully interpret the admittedly limited spectral data.

8.2: CRISM and SMA – high spectral and low spatial resolution

The work presented using the PanCam showed the utility of coarse spectral resolution imagery provided the spatial resolution is high. Such data is one of the two forms of VNIR imagery available from Mars, both currently and as part of future planned missions. The other is orbital data from the CRISM and OMEGA instruments. In opposition to the PanCam data these orbital instruments return imagery with a high spectral resolution (hundreds of spectral bands) over a wide spectral range (0.362 – 3.92 μm in the case of CRISM), but with a much lower spatial resolution; CRISM has the smallest pixel size of the orbital VNIR spectrometers with a standard full resolution product producing pixels of approximately 18 m^2. The PanCam fieldwork performed at Námafjall demonstrated that a significant mineralogical and structural variation can exist within such a small area. Such variety would be smeared and obscured within the CRISM pixels and standard analysis techniques (e.g. spectral parameters or spectral ratioing) are incapable of extracting the full level of information contained within these mixed pixels, most notably the quantitative detail.

The family of techniques known as Spectral Mixture Analysis (SMA) are designed to extract qualitative and quantitative sub-pixel information from within a hyperspectral dataset. There is an extensive literature describing a wide range of SMA related algorithms, however few of these have been tested against the complexity of a hydrothermal environment or with

martian data. Additionally few have been made available as fully executable code to the wider community, effectively excluding this method from the toolbox of the general image analyst or planetary scientist. A full SMA pipeline was developed using publically available pre-existing algorithms written in the Matlab language. This pipeline was optimised for sensitivity to the complexities inherent in a hydrothermally altered surface environment. These included large number of minerals (> 10), spectral similarities between minerals and spectral differences within mineral species, and non-linear intimate spectral mixing. This pipeline was validated using synthetic images constructed from publically available spectral library data as well as hyperspectral data covering the Námafjall region from both ground-based and aerial hyperspectral instruments.

Having established the utility of SMA and the particular algorithms used to build this pipeline it was applied to CRISM data covering a number of regions on Mars postulated to have hosted hydrothermal systems at some point in their history; Nili Patera, Hecates Tholus, Aromatum Chaos and an unnamed crater informally named Kirkcaldy Crater for the purposes of this work. These analyses returned mixed results. For the first time a quantitative estimate for the amount of hydrated silica in some of the bright toned mounds previously identified as such by Skok et al. (2010) was extracted using the SMA pipeline. The presence of a chlorite-bearing unit was identified in the caldera of Hecates Tholus. This unit was not identifiable using the published CRISM spectral parameters (Pelkey et al., 2007; Viviano-Beck et al., 2014) but was quickly identified in the SMA extracted spectral endmembers. The Aromatum Chaos and Kirkcaldy crater showed evidence of significant quantities of icy material. Only in the case of Kirkcaldy crater however, was the SMA pipeline able to add extra information to this identification beyond that available from more standard analysis, with an estimate of the amount of icy material within the crater. In both cases surface water ice is not expected to be stable and the possibility of the spectral signature of ice coming from thin atmospheric clouds had to be considered. In both analyses the coincident HiRISE image combined with the endmember abundance maps allowed for an assessment of the likelihood of the ice being either atmospheric or surface. The lack of bright surface patches and the heterogeneous distribution of the icy signature in the Aromatum Chaos data pointed to the ice being atmospheric. The coincidence of the icy signatures highest abundances over areas with numerous small high albedo patches in Kirkcaldy Crater lead to a tentative diagnosis of surface ice rather than atmospheric. This use of high spatial resolution HiRISE images was also key to the analysis of the other two regions both to identify an ROI to

analyse and then to interpret the abundance maps, matching surface structures and units to the endmember abundance distributions.

A second use of SMA was also investigated combining temporally and spatially coincident HiRISE and CRISM imagery to extract a unique spectrum for the Recurring Slope Lineae (RSL) in Palikir Crater. Through accurate co-registration of the images, area pixel abundances for the RSL were calculated from the HiRISE image and used to validate the abundance calculations of the spectral signatures extracted from the CRISM image using SMA. Three spectral signatures were extracted and through pixel percentage abundance comparison identified as representing the RSL and two background materials that differed only in their albedo. The RSL signature did display a subtle spectral difference from that of the background material but it was not possible to identify the cause of the primary unique feature. This lack of identification was not a fault of the SMA process but rather a result of incomplete spectral libraries to compare the feature to. The building of spectral libraries is an ongoing task within the planetary science and mineral spectroscopy communities and it is hoped that re-analysis in the future will enable a diagnostic identification of the RSL signature to be performed. RSL are subject to ongoing monitoring and further HiRISE and CRISM images of both currently known and new RSL locations are expected over the remainder of the MRO's operational life. With improved image pre-processing the SMA technique described in this thesis could prove invaluable to the question of what is causing these transient features to form.

Analysis of CRISM images is commonly undertaken using the technique of spectral parameters. The analysis of an entire image on an individual pixel-by-pixel basis would be unrealistic and the use of spectral parameters allows for a quick search of an image for key absorption features. It is not a technique without its disadvantages however. Spectral parameters presuppose the existence of specific features and do not allow for significant variation within that feature. As was discussed in Chapter 2 key features for numerous minerals can shift based on various factors including grain size, crystalline structure and slight geochemical impurities. Numerous spectral parameters have been developed specifically for CRISM data first by Pelkey et al. (2007) with revised versions being described by Viviano-Beck et al. (2014). The analysis of Hecates Tholus demonstrated that not all mineral absorptions are featured in these two sets of parameters which could be leading minerals to go undiscovered in some images. A major advantage of SMA is that it distils potentially thousands of pixels down to only a handful. Where it would be unrealistic to examine thousands of spectra on an individual basis, the analysis of only ten is feasible. This allows for

the picking up of unusual absorptions for which no spectral parameter has been developed whilst at the same time taking into account entire spectral shape and multiple absorption features, both of which can prove crucial in identifying the mineral composition of the surface.

8.3: Importance of image pre-processing

The two different applications of SMA presented in this thesis treat the data in different ways appropriate to the environmental type being investigated and the data available. Both however revealed a number of similar issues related to the pre-processing of the CRISM images and in particular the removal of noise, both instrumental and environmental, from the images. All of the CRISM imagery used in this thesis had been processed through the CRISM Analysis Toolkit (CAT) pipeline prior to the application of the SMA algorithms. This basic processing toolbox provided by the CRISM team to the general community sadly proved inadequate in these situations, failing to completely remove both the atmospheric contributions to the data and major instrument artefacts, in particular the vertical stripes due to detector pixel response variations. These vertical stripes were not an issue in the RSL investigation but this is likely because so few pixels were utilised in that analysis. The vertical stripes did show up in the final step of the SMA pipeline in the hydrothermal region exploration for two of the four regions studied. Mineralogical concentrations in vertical swaths that did not correspond to any structural feature were seen in both the Nili Patera and the Kirkcaldy Crater abundance maps. A common method of dealing with detector pixel line artefacts that remain after CAT processing is to take spectral ratios of pixels of interest and 'neutral' pixels from the same detector pixel. This removes any common errors in the pixel due to the detector (as well as the spectral continuum) and can therefore emphasis subtle spectral features. It is of most use when only one or two particular absorption features are of interest and the 'neutral' pixel can be chosen with respect to those features. Otherwise this technique has the potential to introduce artificial features or mask other potentially interesting subtle spectral absorptions. It is also a fix that has to be applied on a pixel by pixel basis to non-georeferenced data rather than across entire images or ROIs and does not address differences between the detector pixels. In the case of SMA it is not believed by this author that such spectral ratioing is a suitable fix to the detector stripe issues for these reasons. Additionally in every image analysed imperfect atmospheric correction introduced uncertainties in the identification of surface spectral absorptions, particularly at around 2.0 μm. The atmospheric correction had been performed using the volcano-scan method using the recommended parameter settings for this tool (Morgan et al., 2009).

Alternative input parameters were experimented with and found to have no positive impact on the final output. Previous researchers have shown that this method does not remove all of the atmospheric contribution to a CRISM image (Wiseman et al., 2012). The atmospheric remnants can be subtle but when the features that are being revealed through SMA are also subtle any remaining atmosphere is an issue. Alternative methods for atmospheric cleaning have been discussed including the radiative transfer based DISORT algorithm; however all require a significant amount of time and specialist software to use, potentially placing them out of reach for some CRISM data users.

8.4: Scale, why it matters and how it can be enhanced

Two different scale resolutions have been investigated over the course of this thesis, the low spectral resolution PanCam and the high spectral resolution CRISM. In both cases the information extractable from the spectral images was greatly enhanced by the addition/combination of high spatial resolution data. In the case of PanCam this was the same data as well as the additional HRC images, and in the case of CRISM this was the HiRISE imagery. These HiRISE images enabled image artefacts to be confidently detected (i.e. the vertical stripes in the SMA abundance maps that did not correspond to any structural features) and the correct spectral signature to be assigned to sub-CRISM pixel features including the small patches of hydrated silica in the NE corner of the Nili Patera ROI and the RSL. Clearly the ideal instrument would have both high spectral and spatial resolution but in the meantime combining datasets with different scales can enhance the level of information available. This combination of different resolution data from different instruments will be available for ExoMars with PanCam being enhanced through conjunction with data from the Infrared Spectrometer for ExoMars ISEM (Korablev et al., 2014). This instrument shall return hyperspectral point spectra across the wavelength range 1.15 - 3.3 µm specifically from targets within the FoV of the PanCam. The work presented in Chapter 3 showed how ASD point spectra from in frame samples often provided the necessary data to conclusively identify the minerals present. The ISEM will perform the same task over a slightly different wavelength range, essentially expanding the wavelength range used to analyse ROIs within a PanCam scene enabling more confident mineral diagnosis to be performed than for PanCam data alone.

8.5: Future work

A number of tasks remain from this thesis that should be carried forward into further research:

1. A quantitative assessment of the error attached to each step in the SMA pipeline should be established. This would give more confidence in the results specifically in the case of CRISM data where groundtruth data is rare.

2. The inclusion of more robust atmospheric (DISORT or anther technique to be determined) and instrument artefact removal routines to the SMA pipeline is a priority. A more rigorous pre-processing pipeline shall be developed addressing these two points. This will enable more confident interpretation of the SMA results and allow for application to a wider range of environments. With greater cleaning applied to the CRISM data the SMA techniques presented in this work show the potential to return significant, new results from an existing instrument with a large backlog of data still waiting to be thoroughly examined.

3. Post inclusion of improved pre-processing methods to the SMA pipeline, further ROIs covering more of the Nili Patera and Hecates Tholus caldera region should be processed and the existing ROIs reprocessed. Both regions showed evidence of significant mineralogical variation which points towards the existence of previous hydrothermal systems. In this case of Nili Patera this work is particularly relevant in light of the area's proposal as a Mars 2020 landing site (Skok et al., 2014).

4. AUPE-2 field trials should continue, covering a wider range of potentially habitable analogue environmental types, in particular those featuring sedimentary layering and phyllosilicates that can act as analogues for the four shortlisted ExoMars candidate landing sites. Integration of an ISEM emulator or prototype into these field trials would be especially beneficiary to further investigate the utility of combining high spatial, low spectral resolution PanCam data with high spectral, low spatial resolution point spectrometer data.

5. Integration of AUPE-2 data and aerial or orbital hyperspectral data should be attempted. The ARSF data used in Chapter 5 was not of sufficient quality to attempt this in this work however better quality data may be available covering future field trial locations. The

applicability of mineralogical deductions made with the ground-based instruments to validate, or at least constrain, the extracted endmembers and estimated abundance maps shall be examined.

References

Adams, J.B., Smith, M.O., Johnson, P.E., 1986. Spectral Mixture Modeling: A New Analysis of Rock and Soil Types at the Viking Lander 1 Site. J. Geophys. Res. 91, B8, 8098–8112. doi:10.1029/JB091iB08p08098

Adler-Golden, S.M., Berk, A., Bernstein, L.S., Richtsmeier, S.C., Acharya, P.K., Matthew, M.W., Anderson, G.P., Allred, C., Jeong, L.S., Chetwynd, J.H., 1998. FLAASH, A MODTRAN4 atmospheric correction package for hyperspectra data retrievals and simulations, in: 7th Annual JPL Earth Science Workshop. JPL, pp. 98 – 104.

Altmann, Y., Dobigeon, N., McLaughlin, S., Tourneret, J.-Y., 2013a. Nonlinear Spectral Unmixing of Hyperspectral Images Using Gaussian Processes. IEEE Trans. Signal Process. 61, 10, 2442–2453. doi:10.1109/TSP.2013.2245127

Altmann, Y., Dobigeon, N., Tourneret, J.-Y., 2013b. Nonlinearity detection in hyperspectral images using a polynomial post-nonlinear mixing model. IEEE Trans. Image Process. 22, 4, 1267–76. doi:10.1109/TIP.2012.2210235

Altmann, Y., Dobigeon, N., Tourneret, J.-Y., Bermudez, J.C.M., 2013c. A robust test for nonlinear mixture detection in hyperspectral images, in: IEEE International Conference on Acoustic, Speech and Signal Processing (ICASSP). IEEE, Vancouver, pp. 2149–2153.

Ambikapathi, A., Chan, T.-H., Ma, W.-K., Chi, C.-Y., 2011. Chance-Constrained Robust Minimum-Volume Enclosing Simplex Algorithm for Hyperspectral Unmixing. IEEE Trans. Geosci. Remote Sens. 49, 11, 4194–4209. doi:10.1109/TGRS.2011.2151197

Amils Pibernat, R., Ellis-Evans, C., Hinghoferr-Szalkay, H., 2007. Life in Extreme Environments, 3rd ed. Springer.

Amundsen, H.E.F., Westall, F., Steele, A., Vago, J., Schmitz, N., Bauer, A., Cousins, C.R., Rull, F., Sansano, A., Midtkandal, I., 2010. Integrated ExoMars PanCam, Raman, and close-up imaging field tests on AMASE 2009, in: EGU General Assembly. Vienna, Austria, p. 8757.

Anderson, R.B., Bell III, J.F., 2013. Correlating Multispectral Imaging and Compositional Data from the Mars Exploration Rovers and Implications for Mars Science Laboratory. Icarus 223, 1, 157–180. doi:10.1016/j.icarus.2012.11.029

Andreou, C., Karathanassi, V., 2014. Estimation of the Number of Endmembers Using Robust Outlier Detection Method. IEEE J. Sel. Top. Appl. Earth Obs. Remote Sens. 7, 1, 247–256. doi:10.1109/JSTARS.2013.2260135

Arvidson, R.E., Squyres, S.W., Baumgartner, E.T., Schenker, P.S., Niebur, C.S., Larsen, K.W., Seelos, F.P., Snider, N.O., Jolliff, B.L., 2002. FIDO prototype Mars rover field trials, Black Rock Summit, Nevada, as test of the ability of robotic mobility systems to conduct field science. J. Geophys. Res. 107, E11. doi:10.1029/2000JE001464

Arvidson, R.E., Squyres, S.W., Bell III, J.F., Catalano, J.G., Clark, B.C., Crumpler, L.S., de Souza, P.A., Fairén, A.G., Farrand, W.H., Fox, V.K., Gellert, R., Ghosh, A., Golombek, M.P., Grotzinger, J.P., Guinness, E.A., Herkenhoff, K.E., Jolliff, B.L., Knoll, A.H., Li, R., McLennan, S.M., Ming, D.W., Mittlefehldt, D.W., Moore, J.M., Morris, R. V., Murchie, S.L., Parker, T.J., Paulsen, G., Rice, J.W., Ruff, S.W., Smith, M.D., Wolff, M.J., 2014. Ancient aqueous environments at Endeavour crater, Mars. Science 343, 6169, 1248097. doi:10.1126/science.1248097

Balme, M.R., Gallagher, C.J., Page, D.P., Murray, J.B., Muller, J.-P., 2009. Sorted stone circles in Elysium Planitia, Mars: Implications for recent martian climate. Icarus 200, 1, 30–38. doi:10.1016/j.icarus.2008.11.010

Bandfield, J.L., 2002. Global mineral distributions on Mars. J. Geophys. Res. 107, E6, 5042. doi:10.1029/2001JE001510

Bandfield, J.L., Glotch, T.D., Christensen, P.R., 2003. Spectroscopic identification of carbonate minerals in the martian dust. Science 301, 5636, 1084–1087. doi:10.1126/science.1088054

Barnes, D.P., Wilding, M., Gunn, M., Pugh, S., Tyler, L., Coates, A.J., Griffiths, A.D., Cousins, C.R., Schmitz, N., Bauer, A., Paar, G., 2011. Multi-spectral vision processing for the ExoMars 2018 mission, in: 11th Symposium on Advanced Space Technologies in Robotics and Automation - ASTRA 2011.

Bell III, J.F., Calvin, W.M., Ockert-Bell, M.E., Crisp, D., Pollack, J.B., Spencer, J., 1996. Detection and monitoring of H2O and CO2 ice clouds on Mars. J. Geophys. Res. 101, E4, 9227. doi:10.1029/96JE00689

Bell III, J.F., Squyres, S.W., Herkenhoff, K.E., Maki, J.N., Arneson, H.M., Brown, D., Collins, S.A., Dingizian, A., Elliot, S.T., Hagerott, E.C., Hayes, A.G., Johnson, M.J., Johnson, J.R., Joseph, J., Kinch, K., Lemmon, M.T., Morris, R. V., Scherr, L., Schwochert, M., Shepard, M.K., Smith, G.H., Sohl-Dickstein, J.N., Sullivan, R.J., Sullivan, W.T., Wadsworth, M., 2003. Mars Exploration Rover Athena Panoramic Camera (Pancam) investigation. J. Geophys. Res. 108, E12. doi:10.1029/2003JE002070

Belouchrani, A., Abed-Meraim, K., Cardoso, J.-F., Moulines, E., 1997. A blind source separation technique using second-order statistics. IEEE Trans. Signal Process. 45 (2), 2, 434–444. doi:10.1109/78.554307

Belouchrani, A., Amin, M.G., 1998. Blind source separation based on time-frequency signal representations. IEEE Trans. Signal Process. 46 (11), 11, 2888–2897. doi:10.1109/78.726803

Bennett, K., Scholes, D., Wang, J., Zhou, F., 2011. CRISM product primer, in: Planetary Data Systems (PDS) Geosciences Node, Orbital Data Explorer, Version 3.0, User's Manual.

Berman, M., Kiiveri, H., Lagerstrom, R., Ernst, A., Dunne, R., Huntington, J.F., 2004. ICE: a statistical approach to identifying endmembers in hyperspectral images. IEEE Trans. Geosci. Remote Sens. 42, 10, 2085–2095. doi:10.1109/TGRS.2004.835299

Bernstein, M.P., Cruikshank, D.P., Sandford, S.A., 2005. Near-infrared laboratory spectra of solid H2O/CO2 and CH3OH/CO2 ice mixtures. Icarus 179, 2, 527–534. doi:10.1016/j.icarus.2005.07.009

Bibring, J.-P., Langevin, Y., Gendrin, A., Gondet, B., Poulet, F., Berthé, M., Soufflot, A., Arvidson, R.E., Mangold, N., Mustard, J.F., Drossart, P., 2005. Mars surface diversity as revealed by the OMEGA/Mars Express observations. Science 307, 5715, 1576–81. doi:10.1126/science.1108806

Bibring, J.-P., Langevin, Y., Mustard, J.F., Poulet, F., Arvidson, R.E., Gendrin, A., Gondet, B., Mangold, N., Pinet, P., Forget, F., Berthé, M., Gomez, C., Jouglet, D., Soufflot, A., Vincendon, M., Combes, M., Drossart, P., Encrenaz, T., Fouchet, T., Merchiorri, R., Bellucci, G., Altieri, F., Formisano, V., Capaccioni, F., Cerroni, P., Coradini, A., Fonti, S., Korablev, O., Kottsov, V., Ignatiev, N., Moroz, V., Titov, D., Zasova, L., Loiseau, D., Mangold, N., Pinet, P., Douté, S., Schmitt, B., Sotin, C., Hauber, E., Hoffmann, H., Jaumann, R., Keller, H.U., Duxbury, T., Forget, F., Neukum, G., 2006. Global mineralogical and aqueous mars history derived from OMEGA/Mars Express data. Science 312, 5772, 400–404. doi:10.1126/science.1122659

Bibring, J.-P., Soufflot, A., Berthé, M., Langevin, Y., Gondet, B., Drossart, P., Bouyé, M., Combes, M., 2004. OMEGA : Observatoire pour la Minéralogie , l ' Eau , les Glaces et l ' Activité. European Space Agency.

Bioucas-Dias, J.M.B., 2009. A variable splitting augmented Lagrangian approach to linear spectral unmixing, in: 2009 First Workshop on Hyperspectral Image and Signal Processing: Evolution in Remote Sensing. IEEE, pp. 1–4. doi:10.1109/WHISPERS.2009.5289072

Bioucas-Dias, J.M.B., Nascimento, J.M.P., 2008. Hyperspectral Subspace Identification. IEEE Trans. Geosci. Remote Sens. 46, 8, 2435–2445. doi:10.1109/TGRS.2008.918089

Bioucas-Dias, J.M.B., Plaza, A., Dobigeon, N., Parente, M., Du, Q., Gader, P., Chanussot, J., 2012. Hyperspectral Unmixing Overview: Geometrical, Statistical, and Sparse Regression-Based Approaches. IEEE J. Sel. Top. Appl. Earth Obs. Remote Sens. 5, 2, 354–379. doi:10.1109/JSTARS.2012.2194696

Bishop, J.L., Franz, H.B., Goetz, W., Blake, D.F., Freissinet, C., Steininger, H., Goesmann, F., Brinckerhoff, W.B., Getty, S., Pinnick, V.T., Mahaffy, P.R., Darby Dyar, M., 2012. Coordinated analyses of Antarctic sediments as Mars analog materials using reflectance spectroscopy and current flight-like instruments for CheMin, SAM and MOMA. Icarus 224, 2, 309–325. doi:10.1016/j.icarus.2012.05.014

Bishop, J.L., Lane, M.D., Dyar, M.D., Brown, A.J., 2008. Reflectance and emission spectroscopy study of four groups of phyllosilicates: smectites, kaolinite-serpentines, chlorites and micas. Clay Miner. 43 (1), 1, 35–54. doi:10.1180/claymin.2008.043.1.03

Bishop, J.L., Schiffman, P., Dyar, M.D., Drief, A., Lane, M.D., 2007. Characterization of alteration products in tephra from Haleakala, Maui: a visible-infrared spectroscopy, Mössbauer spectroscopy, XRD, EMPA and TEM study. Clays Clay Miner. 55, 1, 1–17. doi:10.1346/CCMN.2007.0550101

Bishop, J.L., Ward, M.K., Roush, T.L., Davila, A.F., Brown, A.J., McKay, C.P., Quinn, R.C., Pollard, W., 2014. Spectral properties of Na, Ca-, Mg- and Fe-Chlorides and analyses of hydrohalite-bearing samples from Axel Heiberg Island, in: LPSC XXXXV. Houston, USA, p. 2145.

Boardman, J.W., Kruse, F.A., Green, R.O., 1995. Mapping Target Signatures Via Partial Unmixing of AVIRIS Data. Jet Propulsion Laboratory.

Borel, C.C., Gerstl, S.A.W., 1994. Nonlinear spectral mixing models for vegetative and soil surfaces. Remote Sens. Environ. 47, 3, 403–416. doi:10.1016/0034-4257(94)90107-4

Bridges, J.C., Schwenzer, S.P., 2012. The nakhlite hydrothermal brine on Mars. Earth Planet. Sci. Lett. 359-360, 117–123. doi:10.1016/j.epsl.2012.09.044

Broadwater, J., Banerjee, A., 2011. Mapping intimate mixtures using an adaptive kernel-based technique, in: 2011 3rd Workshop on Hyperspectral Image and Signal Processing: Evolution in Remote Sensing (WHISPERS). IEEE, pp. 1–4. doi:10.1109/WHISPERS.2011.6080881

Broadwater, J., Banerjee, A., Burlina, P., 2009. Kernel Methods for Unmixing Hyperspectral Imagery, in: Camps-Valls, G., Bruzzone, L. (Eds.), Kernal Methods for Remote Sensing Data Analysis. John Wiley & Sons.

Brown, A.J., Bishop, J.L., Viviano-Beck, C.E., 2015. Spectral analysis of carbonate deposits at Nili Fossae, Mars, in: LPSC XXXXVI. LPI, Houston, USA, p. 2701.

Brown, A.J., Hook, S.J., Baldridge, A.M., Crowley, J.K., Bridges, N.T., Thomson, B.J., Marion, G.M., de Souza Filho, C.R., Bishop, J.L., 2010. Hydrothermal formation of Clay-Carbonate alteration assemblages in the Nili Fossae region of Mars. Earth Planet. Sci. Lett. 297, 1-2, 174–182. doi:10.1016/j.epsl.2010.06.018

Brown, A.J., Walter, M.R., Cudahy, T.J., 2005. Hyperspectral imaging spectroscopy of a Mars analogue environment at the North Pole Dome, Pilbara Craton, Western Australia. Aust. J. Earth Sci. 52, 3, 353–364. doi:10.1080/08120090500134530

Brown, A.J., Walter, M.R., Cudahy, T.J., 2004. Short-Wave Infrared Reflectance Investigation of Sites of Paleobiological Interest: Applications for Mars Exploration. Astrobiology 4, 3, 359–376. doi:10.1089/ast.2004.4.359

Bultel, B., Quantin, C., Lozac'h, L., 2015. Description of CoTCAT (Complement to CRISM Analysis Toolkit). IEEE J. Sel. Top. Appl. Earth Obs. Remote Sens. pre-press, 99, 1–11. doi:10.1109/JSTARS.2015.2405095

Burns, R.G., 1993. Mineralogical applications of crystal field theory, 2nd ed. Cambridge University Press.

Burr, D.M., Soare, R.J., Wan Bun Tseung, J.-M., Emery, J.P., 2005. Young (late Amazonian), near-surface, ground ice features near the equator, Athabasca Valles, Mars. Icarus 178, 1, 56–73. doi:10.1016/j.icarus.2005.04.012

Campbell, J.B., 2006. Introduction to Remote Sensing, 4th ed. Taylor & Francis, London.

Cao, X.-R., Liu, R.-W., 1996. General approach to blind source separation. IEEE Trans. Signal Process. 44 (3), 3, 562–571. doi:10.1109/78.489029

Carr, M.H., Head III, J.W., 2010. Geologic history of Mars. Earth Planet. Sci. Lett. 294 (3-4), 3-4, 185–203. doi:10.1016/j.epsl.2009.06.042

Carrozzo, F.G., Bellucci, G., Altieri, F., D'Aversa, E., Bibring, J.-P., 2009. Mapping of water frost and ice at low latitudes on Mars. Icarus 203, 2, 406–420. doi:10.1016/j.icarus.2009.05.020

Carter, J., Poulet, F., Bibring, J.-P., Mangold, N., Murchie, S.L., 2013a. Hydrous minerals on Mars as seen by the CRISM and OMEGA imaging spectrometers: Updated global view. J. Geophys. Res. 118, E4, 831–858. doi:10.1029/2012JE004145

Carter, J., Poulet, F., Murchie, S.L., Bibring, J.-P., 2013b. Automated processing of planetary hyperspectral datasets for the extraction of weak mineral signatures and applications to CRISM observations of hydrated silicates on Mars. Planet. Space Sci. 76, 53–67. doi:10.1016/j.pss.2012.11.007

Ceamanos, X., Douté, S., Luo, B., Schmidt, F., Jouannic, G., Chanussot, J., 2011. Intercomparison and Validation of Techniques for Spectral Unmixing of Hyperspectral Images: A Planetary Case Study. IEEE Trans. Geosci. Remote Sens. 49, 11, 4341–4358. doi:10.1109/TGRS.2011.2140377

Chang, C.-I., 2005. Orthogonal subspace projection (OSP) revisited: a comprehensive study and analysis. IEEE Trans. Geosci. Remote Sens. 43, 3, 502–518. doi:10.1109/TGRS.2004.839543

Chang, C.-I., Du, Q., 2004. Estimation of Number of Spectrally Distinct Signal Sources in Hyperspectral Imagery. IEEE Trans. Geosci. Remote Sens. 42, 3, 608–619. doi:10.1109/TGRS.2003.819189

Chang, C.-I., Plaza, A., 2006. A Fast Iterative Algorithm for Implementation of Pixel Purity Index. IEEE Geosci. Remote Sens. Lett. 3, 1, 63–67. doi:10.1109/LGRS.2005.856701

Chen, J., Richard, C., Honeine, P., 2013. Nonlinear Unmixing of Hyperspectral Data Based on a Linear-Mixture/Nonlinear-Fluctuation Model. IEEE Trans. Signal Process. 61, 2, 480–492. doi:10.1109/TSP.2012.2222390

Chevrier, V.F., Hanley, J., Altheide, T.S., 2009. Stability of perchlorate hydrates and their liquid solutions at the Phoenix landing site, Mars. Geophys. Res. Lett. 36, 10, L10202. doi:10.1029/2009GL037497

Chevrier, V.F., Mathe, P., 2007. Mineralogy and evolution of the surface of Mars: A review. Planet. Space Sci. 55, 3, 289–314. doi:10.1016/j.pss.2006.05.039

Chevrier, V.F., Rivera-Valentin, E.G., 2012. Formation of recurring slope lineae by liquid brines on present-day Mars. Geophys. Res. Lett. 39, 21, L21202. doi:10.1029/2012GL054119

Christensen, P.R., 1988. Global albedo variations on Mars - Implications for active aeolian transport, deposition, and erosion. J. Geophys. Res. 93, B7, 7611–7624. doi:10.1029/JB093iB07p07611

Christensen, P.R., Engle, E., Anwar, S., Dickenshied, S., Noss, D., Gorelick, N., Weiss-Malik, M., 2009. JMARS - A Planetary GIS, in: American Geophysical Union, Fall Meeting 2009. AGU, San Fransisco, USA, p. IN22A–06.

Clark, R.N., 1999. Spectroscopy of Rocks and Minerals and the Principles of Spectroscopy, in: Rencz, A.N. (Ed.), Manual of Remote Sensing, Volume 3, Remote Sensing for the Earth Sciences. John Wiley & Sons, New York, pp. 3–58.

Clark, R.N., King, T.V. V., Klejwa, M., Swayze, G.A., Vergo, N., 1990. High spectral resolution reflectance spectroscopy of minerals. J. Geophys. Res. 95, B8, 12653–12680. doi:10.1029/JB095iB08p12653

Clark, R.N., Swayze, G.A., Gallagher, A., King, T.V. V., Calvin, W.M., 1993. USGS, Digital Spectral Library: Version 1: 0.2 to 3.0 microns - Open File Report 93-592.

Clark, R.N., Swayze, G.A., Wise, R., Livo, E., Hoefen, T., Kokaly, R., Sutley, S.J., 2007. USGS digital spectral library splib06a: U.S. Geological Survey, Digital Data Series 231 [WWW Document]. U.S. Geol. Surv. Digit. Data Ser. 231. URL http://speclab.cr.usgs.gov/spectral.lib06. (accessed 1.1.12).

Clénet, H., Pinet, P., Ceuleneer, G., Daydou, Y., Heuripeau, F., Rosemberg, C., Bibring, J.-P., Bellucci, G., Altieri, F., Gondet, B., 2013. A systematic mapping procedure based on the Modified Gaussian Model to characterize magmatic units from olivine/pyroxenes mixtures: Application to the Syrtis Major volcanic shield on Mars. J. Geophys. Res. 118, E8, 1632–1655. doi:10.1002/jgre.20112

Clénet, H., Pinet, P., Daydou, Y., Heuripeau, F., Rosemberg, C., Baratoux, D., Chevrel, S., 2011. A new systematic approach using the Modified Gaussian Model: Insight for the characterization of chemical composition of olivines, pyroxenes and olivine-pyroxene mixtures. Icarus 213, 1, 404–422. doi:10.1016/j.icarus.2011.03.002

Close, R., Gader, P., Zare, A., Wilson, J., Dranishnikov, D., 2012. Endmember extraction using the physics-based multi-mixture pixel model, in: Shen, S.S., Lewis, P.E. (Eds.), Imaging Spectrometry XVII. SPIE, San Diego, p. 85150L. doi:10.1117/12.930288

Cloutis, E.A., Asher, P.M., Mertzman, S.A., 2002. Spectral reflectance properties of zeolites and remote sensing implications. J. Geophys. Res. 107, E9, 5067. doi:10.1029/2000JE001467

Coates, A.J., Griffiths, A.D., Leff, C.E., Schmitz, N., Barnes, D.P., Josset, J.-L., Hancock, B.K., Cousins, C.R., Jaumann, R., Crawford, I.A., Paar, G., Bauer, A., 2012. Lunar PanCam: Adapting ExoMars PanCam for the ESA Lunar Lander, in: Planetary and Space Science. pp. 247–253. doi:10.1016/j.pss.2012.07.017

Coleman, N.M., 2005. Martian megaflood-triggered chaos formation, revealing groundwater depth, cryosphere thickness, and crustal heat flux. J. Geophys. Res. 110, E12. doi:10.1029/2005JE002419

Combe, J.-P., Le Mouélic, S., Sotin, C., Gendrin, A., Mustard, J.F., Le Deit, L., Launeau, P., Bibring, J.-P., Gondet, B., Langevin, Y., Pinet, P., 2008. Analysis of OMEGA/Mars Express data hyperspectral data using a Multiple-Endmember Linear Spectral Unmixing Model (MELSUM): Methodology and first results. Planet. Space Sci. 56, 7, 951–975. doi:10.1016/j.pss.2007.12.007

Cousins, C.R., Crawford, I.A., 2011. Volcano-ice interaction as a microbial habitat on Earth and Mars. Astrobiology 11, 7, 695–710. doi:10.1089/ast.2010.0550

Cousins, C.R., Crawford, I.A., Carrivick, J.L., Gunn, M., Harris, J.K., Kee, T.P., Karlsson, M., Carmody, L., Cockell, C.S., Herschy, B., Joy, K.H., 2013. Glaciovolcanic hydrothermal environments in Iceland and implications for their detection on Mars. J. Volcanol. Geotherm. Res. 256, 61–77. doi:10.1016/j.jvolgeores.2013.02.009

Cousins, C.R., Griffiths, A.D., Schmitz, N., Paar, G., Barnes, D.P., 2009. Wide Angle Camera testing during the 2009 AMASE expedition for the ExoMars PanCam instrument. EPSC Abstr. 2009 4, 813.

Cousins, C.R., Gunn, M., Prosser, B.J., Barnes, D.P., Crawford, I.A., Griffiths, A.D., Davis, L.E., Coates, A.J., 2012. Selecting the geology filter wavelengths for the ExoMars Panoramic Camera instrument. Planet. Space Sci. 71, 1, 80–100. doi:10.1016/j.pss.2012.07.009

Craft, K.L., Lowell, R.P., Potter-McIntyre, S., 2015. Aromatum Chaos: Heating up, melting ice, and letting it flow - A preliminary analysis, in: LPSC XXXXVI. LPI, Houston, USA, p. 2999.

CRISM, S.T., 2013. CRISM Analysis Toolkit.

CRISM, S.T., 2006. CRISM Spectral Library.

Crósta, A.P., De Souza Filho, C.R., Azevedo, F., Brodie, C., 2003. Targeting key alteration minerals in epithermal deposits in Patagonia, Argentina, using ASTER imagery and principal component analysis. Int. J. Remote Sens. 24, 21, 4233–4240. doi:10.1080/0143116031000152291

Crósta, A.P., Sabine, C., Taranik, J. V., 1998. Hydrothermal Alteration Mapping at Bodie, California, Using AVIRIS Hyperspectral Data. Remote Sens. Environ. 65, 3, 309–319. doi:10.1016/S0034-4257(98)00040-6

Cull, S.C., Arvidson, R.E., Catalano, J.G., Ming, D.W., Morris, R. V., Mellon, M.T., Lemmon, M.T., 2010. Concentrated perchlorate at the Mars Phoenix landing site: Evidence for thin film liquid water on Mars. Geophys. Res. Lett. 37, 22, L22203. doi:10.1029/2010GL045269

Curran, R.J., Conrath, B.J., Hanel, R.A., Kunde, V.G., Pearl, J.C., 1973. Mars: Mariner 9 Spectroscopic Evidence for H2O Ice Clouds. Science (80-.). 182, 4110, 381–383. doi:10.1126/science.182.4110.381

Davis, J.C., 1986. Statistics and Data Analysis in Geology, 2nd ed. John Wiley & Sons.

De Pablo, M.A., Michael, G.G., Centeno, J.D., 2013. Age and evolution of the lower NW flank of the Hecates Tholus volcano, Mars, based on crater size-frequency distribution on CTX images. Icarus 226, 1, 455–469. doi:10.1016/j.icarus.2013.05.012

Des Marais, D.J., Allamandola, L.J., Benner, S.A., Boss, A.P., Deamer, D., Falkowski, P.G., Farmer, J.D., Hedges, S.B., Jakosky, B.M., Knoll, A.H., Liskowsky, D.R., Meadows, V.S., Meyer, M.A., Pilcher, C.B., Nealson, K.H., Spormann, A.M., Trent, J.D., Turner, W.W., Woolf, N.J., Yorke, H.W., 2003. The NASA Astrobiology Roadmap. Astrobiology 3, 2, 219–35. doi:10.1089/153110703769016299

Dobigeon, N., Tourneret, J.-Y., Chang, C.-I., 2008. Semi-Supervised Linear Spectral Unmixing Using a Hierarchical Bayesian Model for Hyperspectral Imagery. IEEE Trans. Signal Process. 56, 7, 2684–2695. doi:10.1109/TSP.2008.917851

Dobigeon, N., Tourneret, J.-Y., Richard, C., Bermudez, J.C.M., McLaughlin, S., Hero, A.O., 2014. Nonlinear Unmixing of Hyperspectral Images: Models and Algorithms. IEEE Signal Process. Mag. 31, 1, 82–94. doi:10.1109/MSP.2013.2279274

Douté, S., Ceamanos, X., Luo, B., Schmidt, F., Jouannic, G., Chanussot, J., 2011. Validation of spectral unmixing algorithms applied on CRISM/MRO hyperspectral images, in: 2011 3rd Workshop on Hyperspectral Image and Signal Processing: Evolution in Remote Sensing (WHISPERS). IEEE, pp. 1–4. doi:10.1109/WHISPERS.2011.6080903

Downs, R.T., 2006. The RRUFF Project: an integrated study of the chemistry, crystallography, Raman and infrared spectroscoy of minerals, in: Program and Abstracts of the 19th General Meeting of the Internationa Association. Kobe, Japan, pp. O03–13.

Dundas, C.M., McEwen, A.S., 2015. Slope activity in Gale crater, Mars. Icarus 254, 213–218. doi:10.1016/j.icarus.2015.04.002

Edwards, B., Russell, J., Anderson, R., 2002. Subglacial, phonolitic volcanism at Hoodoo Mountain volcano, northern Canadian Cordillera. Bull. Volcanol. 64, 3-4, 254–272. doi:10.1007/s00445-002-0202-9

Ehlmann, B.L., Bish, D.L., Ruff, S.W., Mustard, J.F., 2012. Mineralogy and chemistry of altered Icelandic basalts: Application to clay mineral detection and understanding aqueous environments on Mars. J. Geophys. Res. 117, E11. doi:10.1029/2012JE004156

Ehlmann, B.L., Edwards, C.S., 2014. Mineralogy of the Martian Surface. Annu. Rev. Earth Planet. Sci. 42, 1, 291–315. doi:10.1146/annurev-earth-060313-055024

Ehlmann, B.L., Mustard, J.F., Bish, D.L., 2011a. AQUEOUS ALTERATION OF BASALTIC LAVAS IN ICELAND: AN ANALOGUE FOR NOACHIAN MARS., in: LPI - Analogue Sites for Mars Missions. Houston, USA, pp. 4–6.

Ehlmann, B.L., Mustard, J.F., Clark, R.N., Swayze, G.A., Murchie, S.L., 2011b. Evidence for low-grade metamorphism, hydrothermal alteration, and diagenesis on mars from phyllosilicate mineral assemblages. Clays Clay Miner. 59, 4, 359–377. doi:10.1346/CCMN.2011.0590402

Ehlmann, B.L., Mustard, J.F., Harvey, R.P., Rampey, M., 2007. Traversing the Noachian-Hesperian contact: Syrtis Major volcanics to Nili Fossae phyllosilicates, in: 2nd MSL Landing Site Workshop.

Ehlmann, B.L., Mustard, J.F., Murchie, S.L., Bibring, J.-P., Meunier, A., Fraeman, A.A., Langevin, Y., 2011c. Subsurface water and clay mineral formation during the early history of Mars. Nature 479, 7371, 53–60. doi:10.1038/nature10582

Ehlmann, B.L., Mustard, J.F., Swayze, G.A., Clark, R.N., Bishop, J.L., Poulet, F., Des Marais, D.J., Roach, L.H., Milliken, R.E., Wray, J.J., Barnouin-Jha, O.S., Murchie, S.L., 2009. Identification of hydrated silicate minerals on Mars using MRO-CRISM: Geologic context near Nili Fossae and implications for aqueous alteration. J. Geophys. Res. 114, E2. doi:10.1029/2009JE003339

Fairén, A.G., Dohm, J.M., Uceda, E.R., Rodriguez, A., Baker, V.R., Fernández-Remolar, D., Schulze-Makuch, D., Amils, R., 2005. Prime candidate sites for astrobiological exploration through the hydrogeological history of Mars. Planet. Space Sci. 53, 13, 1355–1375. doi:10.1016/j.pss.2005.06.007

Farrand, W.H., Bell III, J.F., Johnson, J.R., Arvidson, R.E., Crumpler, L.S., Hurowitz, J.A., Schröder, C., 2008. Rock spectral classes observed by the Spirit Rover's Pancam on the Gusev Crater Plains and in the Columbia Hills. J. Geophys. Res. 113, E12. doi:10.1029/2008JE003237

Farrand, W.H., Bell III, J.F., Johnson, J.R., Jolliff, B.L., Knoll, A.H., McLennan, S.M., Squyres, S.W., Calvin, W.M., Grotzinger, J.P., Morris, R. V., Soderblom, J., Thompson, S.D., Watters, W.A., Yen, A.S., 2007. Visible and near-infrared multispectral analysis of rocks at Meridiani Planum, Mars, by the Mars Exploration Rover Opportunity. J. Geophys. Res. 112, E6. doi:10.1029/2006JE002773

Farrand, W.H., Bell III, J.F., Johnson, J.R., Rice, M.S., Hurowitz, J.A., 2013. VNIR multispectral observations of rocks at Cape York, Endeavour crater, Mars by the Opportunity rover's Pancam. Icarus 225, 1, 709–725. doi:10.1016/j.icarus.2013.04.014

Farrand, W.H., Bell III, J.F., Johnson, J.R., Rice, M.S., Jolliff, B.L., Arvidson, R.E., 2014. Observations of rock spectral classes by the Opportunity rover's Pancam on northern Cape York and on Matijevic Hill, Endeavour Crater, Mars. J. Geophys. Res. 119, E11, 2349–2369. doi:10.1002/2014JE004641

Farrand, W.H., Bell III, J.F., Johnson, J.R., Squyres, S.W., Soderblom, J., Ming, D.W., 2006. Spectral variability among rocks in visible and near-infrared multispectral Pancam data collected at Gusev crater: Examinations using spectral mixture analysis and related techniques. J. Geophys. Res. 111, E2. doi:10.1029/2005JE002495

Fassett, C.I., Head III, J.W., 2007. Valley formation on martian volcanoes in the Hesperian: Evidence for melting of summit snowpack, caldera lake formation, drainage and erosion on Ceraunius Tholus. Icarus 189, 1, 118–135. doi:10.1016/j.icarus.2006.12.021

Fawdon, P., Skok, J.R., Balme, M.R., Vye-Brown, C.L., Rothery, D.A., Jordan, C.J., 2015. The geological history of Nili Patera, Mars. J. Geophys. Res. 120, E5, 951–977. doi:10.1002/2015JE004795

Foody, G.M., 1996. Approaches for the production and evaluation of fuzzy land cover classifications from remotely-sensed data. Int. J. Remote Sens. 17, 7, 1317–1340. doi:10.1080/01431169608948706

Gaffey, S.J., 1986. Spectral reflectance of carbonate minerals in the visible and near infrared (0.35-2.55 microns): calcite, aragonite, and dolomite. Am. Mineral. 71, 151–162.

Gaffey, S.J., 1985. Reflectance Spectroscopy in the Visible and Near-Infrared (0.35-2.55um): Applications in carbonate petrology. Geology 13, 270–273. doi:10.1130/0091-7613(1985)13<270

Glavin, D.P., Freissinet, C., Miller, K.E., Eigenbrode, J.L., Brunner, A.E., Buch, A., Sutter, B., Archer, P.D., Atreya, S.K., Brinckerhoff, W.B., Cabane, M., Coll, P., Conrad, P.G., Coscia, D., Dworkin, J.P., Franz, H.B., Grotzinger, J.P., Leshin, L.A., Martin, M.G., McKay, C.P., Ming, D.W., Navarro-González, R., Pavlov, A., Steele, A., Summons, R.E., Szopa, C., Teinturier, S., Mahaffy, P.R., 2013. Evidence for perchlorates and the origin of chlorinated hydrocarbons detected by SAM at the Rocknest aeolian deposit in Gale Crater. J. Geophys. Res. 118, E10, 1955–1973. doi:10.1002/jgre.20144

Gleeson, D.F., Pappalardo, R.T., Grasby, S.E., Anderson, M.S., Beauchamp, B., Castaño, R., Chien, S.A., Doggett, T., Mandrake, L., Wagstaff, K.L., 2010. Characterization of a sulfur-rich Arctic spring site and field analog to Europa using hyperspectral data. Remote Sens. Environ. 114, 6, 1297–1311. doi:10.1016/j.rse.2010.01.011

Gou, S., Yue, Z., Di, K., Wang, J., 2014. Mineral abundances and different levels of alteration around Mawrth Vallis, Mars. Geosci. Front. In press. doi:10.1016/j.gsf.2014.09.004

Goudge, T.A., Mustard, J.F., Head III, J.W., Salvatore, M.R., Wiseman, S.M., 2015. Integrating CRISM and TES hyperspectral data to characterize a halloysite-bearing deposit in Kashira crater, Mars. Icarus 250, 165–187. doi:10.1016/j.icarus.2014.11.034

Green, A.A., Berman, M., Switzer, P., Craig, M.D., 1988. A transformation for ordering multispectral data in terms of image quality with implications for noise removal. IEEE Trans. Geosci. Remote Sens. 26, 1, 65–74. doi:10.1109/36.3001

Griffiths, A.D., Coates, A.J., Jaumann, R., Michaelis, H., Paar, G., Barnes, D.P., Josset, J.-L., 2006. Context for the ESA ExoMars rover: the Panoramic Camera (PanCam) instrument. Int. J. Astrobiol. 5, 03, 269. doi:10.1017/S1473550406003387

Griffiths, A.D., Coates, A.J., Josset, J.-L., Paar, G., Hofmann, B.A., Pullan, D., Rüffer, P., Sims, M.R., Pillinger, C.T., 2005. The Beagle 2 stereo camera system. Planet. Space Sci. 53, 14-15, 1466–1482. doi:10.1016/j.pss.2005.07.007

Grotzinger, J.P., Crisp, J.A., Vasavada, A.R., Anderson, R.C., Baker, C.J., Barry, R., Blake, D.F., Conrad, P.G., Edgett, K.S., Ferdowski, B., Gellert, R., Gilbert, J.B., Golombek, M.P., Gómez-Elvira, J., Hassler, D.M., Jandura, L., Litvak, M., Mahaffy, P.R., Maki, J.N., Meyer, M., Malin, M.C., Mitrofanov, I., Simmonds, J.J., Vaniman, D.T., Welch, R. V., Wiens, R.C., 2012. Mars Science Laboratory Mission and Science Investigation. Space Sci. Rev. 170, 1-4, 5–56. doi:10.1007/s11214-012-9892-2

Grotzinger, J.P., Sumner, D.Y., Kah, L.C., Stack, K., Gupta, S., Edgar, L., Rubin, D., Lewis, K.W., Schieber, J., Mangold, N., Milliken, R.E., Conrad, P.G., DesMarais, D., Farmer, J.D., Siebach, K., Calef, F.J., Hurowitz, J., McLennan, S.M., Ming, D.W., Vaniman, D.T., Crisp, J.A., Vasavada, A., Edgett, K.S., Malin, M.C., Blake, D.F., Gellert, R., Mahaffy, P.R., Wiens, R.C., Maurice, S., Grant, J.A., Wilson, S., Anderson, R.C., Beegle, L., Arvidson, R.E., Hallet, B., Sletten, R.S., Rice, M.S., Bell III, J.F., Griffes, J.L., Ehlmann, B.L., Anderson, R.B., Bristow, T.F., Dietrich, W.E., Dromart, G., Eigenbrode, J.L., Fraeman, A.A., Hardgrove, C., Herkenhoff, K.E., Jandura, L., Kocurek, G., Lee, S., Leshin, L.A., Leveille, R., Limonadi, D., Maki, J.N., McCloskey, S., Meyer, M.A., Minitti, M.E., Newsom, H.E., Oehler, D.Z., Okon, A., Palucis, M.C., Parker, T.J., Rowland, S., Schmidt, M.E., Squyres, S.W., Steele, A., Stolper, E.M., Summons, R.E., Treiman, A.H., Williams, R.M.E., Yingst, R.A., Team, M.S., 2014. A Habitable Fluvio-Lacustrine Environment at Yellowknife Bay, Gale Crater, Mars. Science 343, 6169. doi:10.1126/science.1242777

Gudmundsson, Á., Mortensen, A.K., Hjartarson, A., Ármannsson, H., Karlsdóttir, R., 2010. Exploration and Utilization of the Námafjall High Temperature Area in N Iceland, in: Proceedings World Geothermal Congress 2010.

Gudmundsson, B.T., Arnórsson, S., 2005. Secondary mineral–fluid equilibria in the Krafla and Námafjall geothermal systems, Iceland. Appl. Geochemistry 20, 9, 1607–1625. doi:10.1016/j.apgeochem.2005.04.020

Guilfoyle, K.J., Althouse, M.L., 2001. A quantitative and comparative analysis of linear and nonlinear spectral mixture models using radial basis function neural networks. IEEE Trans. Geosci. Remote Sens. 39, 10, 2314–2318. doi:10.1109/36.957296

Gunn, M., 2013. Matt Gunn, Aberystwyth University PanCam Development etc. Aberystwyth University.

Hamilton, V.E., Morris, R. V., Gruener, J.E., Mertzman, S.A., 2008. Visible, near-infrared, and middle infrared spectroscopy of altered basaltic tephras: Spectral signatures of phyllosilicates, sulfates, and other aqueous alteration products with application to the mineralogy of the Columbia Hills of Gusev Crater, Mars. J. Geophys. Res. 113, E12, E12S43. doi:10.1029/2007JE003049

Hanley, J., Chevrier, B.L., Davis, R.S., Altheide, A., Francis, W.M., 2010. Reflectance spectra of low-temperature chloride and perchlorate hydrates and their relevance to the martian surface, in: LPSC XXXXI. Houston, USA, p. 1953.

Hanley, J., Chevrier, V.F., Berget, D.J., Adams, R.D., 2012. Chlorate salts and solutions on Mars. Geophys. Res. Lett. 39, 8. doi:10.1029/2012GL051239

Hanley, J., Dalton, J.B., Chevrier, V.F., Jamieson, C.S., Barrows, R.S., 2014. Reflectance spectra of hydrated chlorine salts: The effect of temperature with implications for Europa. J. Geophys. Res. Planets 119, 11, 2370–2377. doi:10.1002/2013JE004565

Hapke, B., 2013. Comment on “A critical assessment of the Hapke photometric model” by Y. Shkuratov et al. J. Quant. Spectrosc. Radiat. Transf. 116, 184–190. doi:10.1016/j.jqsrt.2012.11.002

Hapke, B., 2012. Theory of Reflectance and Emittance Spectroscopy, 2nd ed. Cambridge University Press, Cambridge.

Hapke, B., 1981. Bidirectional reflectance spectroscopy: 1. Theory. J. Geophys. Res. 86, B4, 3039. doi:10.1029/JB086iB04p03039

Harris, J.K., Cousins, C.R., Gunn, M., Grindrod, P.M., Barnes, D.P., Crawford, I.A., Cross, R.E., Coates, A.J., 2015. Remote detection of past habitability at Mars-analogue hydrothermal alteration terrains using an ExoMars Panoramic Camera Emulator. Icarus 252, 284–300. doi:10.1016/j.icarus.2015.02.004

Harrison, J.P., Gheeraert, N., Tsigelnitskiy, D., Cockell, C.S., 2013. The limits for life under multiple extremes. Trends Microbiol. 21, 4, 204–212. doi:10.1016/j.tim.2013.01.006

Harsanyi, J.C., Chang, C.-I., 1994. Hyperspectral image classification and dimensionality reduction: an orthogonal subspace projection approach. IEEE Trans. Geosci. Remote Sens. 32, 4, 779–785. doi:10.1109/36.298007

Hauber, E., van Gasselt, S., Ivanov, B.A., Werner, S., Head III, J.W., Neukum, G., Jaumann, R., Greeley, R., Mitchell, K.L., Muller, P., 2005. Discovery of a flank caldera and very young glacial activity at Hecates Tholus, Mars. Nature 434, 7031, 356–361. doi:10.1038/nature03423

Head III, J.W., Wilson, L., Mitchell, K.L., 2003. Generation of recent massive water floods at Cerberus Fossae, Mars by dike emplacement, cryospheric cracking, and confined aquifer groundwater release. Geophys. Res. Lett. 30, 11. doi:10.1029/2003GL017135

Hecht, M.H., Kounaves, S.P., Quinn, R.C., West, S.J., Young, S.M.M., Ming, D.W., Catling, D.C., Clark, B.C., Boynton, W. V., Hoffman, J., Deflores, L.P., Gospodinova, K., Kapit, J., Smith, P.H., 2009. Detection of perchlorate and the soluble chemistry of martian soil at the Phoenix lander site. Science 325, 5936, 64–67. doi:10.1126/science.1172466

Heinz, D.C., Chang, C.-I., 2001. Fully constrained least squares linear spectral mixture analysis method for material quantification in hyperspectral imagery. IEEE Trans. Geosci. Remote Sens. 39, 3, 529–545. doi:10.1109/36.911111

Heylen, R., Burazerovic, D., Scheunders, P., 2011. Non-Linear Spectral Unmixing by Geodesic Simplex Volume Maximization. IEEE J. Sel. Top. Signal Process. 5, 3, 534–542. doi:10.1109/JSTSP.2010.2088377

Heylen, R., Parente, M., Gader, P., 2014. A Review of Nonlinear Hyperspectral Unmixing Methods. IEEE J. Sel. Top. Appl. Earth Obs. Remote Sens. 7, 6, 1844 – 1868. doi:10.1109/JSTARS.2014.2320576

Hooper, D.M., Dinwiddie, C.L., 2014. Debris flows on the Great Kobuk Sand Dunes, Alaska: Implications for analogous processes on Mars. Icarus 230, 15–28. doi:10.1016/j.icarus.2013.07.006

Horgan, B.H.N., Cloutis, E.A., Mann, P., Bell III, J.F., 2014. Near-infrared spectra of ferrous mineral mixtures and methods for their identification in planetary surface spectra. Icarus 234, 132–154. doi:10.1016/j.icarus.2014.02.031

Hunt, G.R., 1977. Spectral signatures of particulate minerals in the visible and near infrared. Geophysics 42, 3, 501–513. doi:10.1190/1.1440721

Hunt, G.R., Ashley, R.P., 1979. Spectra of altered rocks in the visible and near infrared. Econ. Geol. 74, 7, 1613–1629. doi:10.2113/gsecongeo.74.7.1613

Hunt, G.R., Salisbury, J.W., 1971. Visible and Near-Infrared Spectra of Minerals and Rocks: II. Carbonates. Mod. Geol. 2, 23–30.

Hunt, G.R., Salisbury, J.W., 1970. Visible and near-infrared spectra of minerals and rocks: I Silicate Minerals. Mod. Geol. 1, 283–300.

Hunt, G.R., Salisbury, J.W., Lenhoff, C.J., 1971. Visible and near-infrared spectra of minerals and rocks IV: Sulphides and Sulphates. Mod. Geol. 3, 1–14.

Huntington, J.F., 1996. The Role of Remote Sensing in Finding Hydrothermal Mineral Deposits on Earth, in: Bock, G.R., Goode, J.A. (Eds.), Ciba Foundation Symposium 202 - Evolution of Hydrothermal Ecosystems on Earth (And Mars?), Novartis Foundation Symposia. John Wiley & Sons, Ltd., Chichester, UK, pp. 214–235. doi:10.1002/9780470514986

Imbiriba, T., Bermudez, J.C.M., Tourneret, J.-Y., Cedric, R., 2014. Detection of nonlinear mixtures using Gaussian processes: Application to hyperspectral imaging, in: IEEE International Conference on Acoustic, Speech and Signal Processing (ICASSP).

Jiao, X., Chang, C.-I., Du, Y., 2010. Orthogonal subspace projection approach to finding signal sources in hyperspectral imagery, in: ALGORITHMS AND TECHNOLOGIES FOR MULTISPECTRAL, HYPERSPECTRAL, AND ULTRASPECTRAL IMAGERY XVI. SPIE, p. 76952L–76952L–12. doi:10.1117/12.852757

Johnson, J.R., Ruff, S.W., Moersch, J., Roush, T., Horton, K., Bishop, J., Cabrol, N.A., Cockell, C., Gazis, P., Newsom, H.E., Stoker, C., 2001. Geological characterization of remote field sites using visible and infrared spectroscopy: Results from the 1999 Marsokhod field test. J. Geophys. Res. 106, E4, 7683–7711. doi:10.1029/1999JE001149

Jolliff, B.L., Knoll, A.H., Morris, R. V., Moersch, J.E., McSween Jr., H.Y., Gilmore, M.S., Arvidson, R.E., Greeley, R., Herkenhoff, K.E., Squyres, S.W., 2002. Remotely sensed geology from lander-based to orbital perspectives: Results of FIDO rover May 2000 field tests. J. Geophys. Res. 107, E11. doi:10.1029/2000JE001470

Kadish, S.J., Head III, J.W., Parsons, R., Marchant, D.R., 2008. The Ascraeus Mons fan-shaped deposit: Volcano–ice interactions and the climatic implications of cold-based tropical mountain glaciation. Icarus 197, 1, 84–109. doi:10.1016/j.icarus.2008.03.019

Kangi, A., 2007. The role of mud volcanoes in the evolution of Hecate Tholus Volcano on the surface of Mars. Acta Astronaut. 60, 8-9, 719–722. doi:10.1016/j.actaastro.2006.10.004

Keshava, N., Mustard, J.F., 2002. Spectral unmixing. IEEE Signal Process. Mag. 19, 1, 44–57. doi:10.1109/79.974727

Keszthelyi, L.P., Jaeger, W.L., Dundas, C.M., Martínez-Alonso, S., McEwen, A.S., Milazzo, M.P., 2010. Hydrovolcanic features on Mars: Preliminary observations from the first Mars year of HiRISE imaging. Icarus 205, 1, 211–229. doi:10.1016/j.icarus.2009.08.020

Korablev, O., Ivanov, A., Mantsevich, S., Kiselev, A., Vyazovetskiy, N., Fedorova, A., Evdokimova, N., Stepanov, A., Titov, A., Kalinnikov, Y., Kuzmin, R.O., Batilevsky, A.T., Bondarenko, A., Moiseev, P., 2014. AOTF near-IR spectrometers for study of Lunar and Martian surface composition, in: EPSC 2014. EPSC, Cascais, Portugal, pp. ESPC20147–371–2.

Kossacki, K.J., Markiewicz, W.J., 2014. Seasonal flows on dark martian slopes, thermal condition for liquescence of salts. Icarus 233, 126–130. doi:10.1016/j.icarus.2014.01.032

Kotz, S., Balakrishnan, N., Johnson, N.L., 2000. Dirichlet and Inverted Dirichlet Distributions, in: Kotz, S., Balakrishnan, N., Johnson, N.L. (Eds.), Continuous Multivariate Distributions. Volume 1: Models and Applications. Wiley, New York, pp. 485–527.

Kruse, F.A., Lefkoff, A.B., Boardman, J.W., Heidebrecht, K.B., Shapiro, A.T., Barloon, P.J., Goetz, A.F.H., 1993. The Spectral Image Processing System (SIPS) - Interactive visualization and analysis of imaging spectrometer data. Remote Sens. Environ. 44, 145–163.

Le Deit, L., Le Mouélic, S., Bourgeois, O., Combe, J.-P., Mège, D., Sotin, C., Gendrin, A., Hauber, E., Mangold, N., Bibring, J.-P., 2008. Ferric oxides in East Candor Chasma, Valles Marineris (Mars) inferred from analysis of OMEGA/Mars Express data: Identification and geological interpretation. J. Geophys. Res. 113, E7, E07001. doi:10.1029/2007JE002950

Leask, H.J., Wilson, L., Mitchell, K.L., 2006. Formation of Aromatum Chaos, Mars: Morphological development as a result of volcano-ice interactions. J. Geophys. Res. 111), E8. doi:10.1029/2005JE002549

Lee, T.-W., Bell, A.J., Orglmeister, R., 1997. Blind source separation of real world signals, in: Proceedings of International Conference on Neural Networks (ICNN'97). IEEE, Houston, USA, pp. 2129–2134. doi:10.1109/ICNN.1997.614235

Leshin, L.A., Mahaffy, P.R., Webster, C.R., Cabane, M., Coll, P., Conrad, P.G., Archer, P.D., Atreya, S.K., Brunner, A.E., Buch, A., Eigenbrode, J.L., Flesch, G.J., Franz, H.B., Freissinet, C., Glavin, D.P., McAdam, A.C., Miller, K.E., Ming, D.W., Morris, R. V., Navarro-González, R., Niles, P.B., Owen, T., Pepin, R.O., Squyres, S.W., Steele, A., Stern, J.C., Summons, R.E., Sumner, D.Y., Sutter, B., Szopa, C., Teinturier, S., Trainer, M.G., Wray, J.J., Grotzinger, J.P., 2013. Volatile, isotope, and organic analysis of martian fines with the Mars Curiosity rover. Science 341, 6153, 1238937. doi:10.1126/science.1238937

Lever, M.A., Rogers, K.L., Lloyd, K.G., Overmann, J., Schink, B., Thauer, R.K., Hoehler, T.M., Jorgensen, B.B., 2015. Life under extreme energy limitation: a synthesis of laboratory- and field-based investigations. FEMS Microbiol. Rev. doi:10.1093/femsre/fuv020

Levy, J.S., 2012. Hydrological characteristics of recurrent slope lineae on Mars: Evidence for liquid flow through regolith and comparisons with Antarctic terrestrial analogs. Icarus 219, 1, 1–4. doi:10.1016/j.icarus.2012.02.016

Li, J., Agathos, A., Zaharie, D., Bioucas-Dias, J.M.B., Plaza, A., Li, X., 2015. Minimum Volume Simplex Analysis: A Fast Algorithm for Linear Hyperspectral Unmixing. IEEE Trans. Geosci. Remote Sens. 53, 9, 5067–5082. doi:10.1109/TGRS.2015.2417162

Li, J., Bioucas-Dias, J.M.B., 2008. Minimum Volume Simplex Analysis: A Fast Algorithm to Unmix Hyperspectral Data, in: IGARSS 2008 - 2008 IEEE International Geoscience and Remote Sensing Symposium. IEEE, pp. III – 250–III – 253. doi:10.1109/IGARSS.2008.4779330

Licciardi, G.A., Ceamanos, X., Douté, S., Chanussot, J., 2012. Unsupervised nonlinear spectral unmixing by means of NLPCA applied to hyperspectral imagery, in: 2012 IEEE International Geoscience and Remote Sensing Symposium. IEEE, Munich, pp. 1369–1372. doi:10.1109/IGARSS.2012.6351281

Licciardi, G.A., Del Frate, F., 2011. Pixel Unmixing in Hyperspectral Data by Means of Neural Networks. IEEE Trans. Geosci. Remote Sens. 49, 11, 4163–4172. doi:10.1109/TGRS.2011.2160950

Lin, C.-H., Ma, W.-K., Li, W.-C., Chi, C.-Y., Ambikapathi, A., 2015. Identifiability of the Simplex Volume Minimization Criterion for Blind Hyperspectral Unmixing: The No-Pure-Pixel Case. IEEE Trans. Geosci. Remote Sens. 53, 10, 5530–5546. doi:10.1109/TGRS.2015.2424719

Liu, Y., Glotch, T.D., 2014. Spectral Mixture Analysis of Hydrated Minerals in Southwest Melas Chasma, in: LPSC XXXXV. Houston, USA, p. 2443.

Loizeau, D., Flahaut, J., Vago, J., Hauber, E., Bridges, J.C., 2015. ExoMars 2018: The candidate landing sites, in: LPSC XXXXVI. LPI, Houston, USA, p. 1831.

Lui, W., Seto, K.C., Wu, E.Y., Gopal, S., Woodcock, C.E., 2004. ART-MMAP: a neural network approach to subpixel classification. IEEE Trans. Geosci. Remote Sens. 42, 9, 1976–1983. doi:10.1109/TGRS.2004.831893

Luo, B., Chanussot, J., Douté, S., Zhang, L., 2013. Empirical automatic estimation of the number of endmembers in hyperspectral images. IEEE Geosci. Remote Sens. Lett. 10, 1, 24–28. doi:10.1109/LGRS.2012.2189934

Luo, B., Douté, S., Ceamanos, X., Chanussot, J., Zhang, L., 2012. Extraction of minerals on the south pole of the planet Mars by unsupervised linear unmixing of hyperspectral images, in: 2012 IEEE International Geoscience and Remote Sensing Symposium. IEEE, Munich, pp. 3050–3053. doi:10.1109/IGARSS.2012.6350782

MacArthur, A., 2007. Guide to using the ASD FieldSpec Pro in white reflectance mode in the field - version 2.

Marchant, D.R., Head III, J.W., 2007. Antarctic dry valleys: Microclimate zonation, variable geomorphic processes, and implications for assessing climate change on Mars. Icarus 192, 1, 187–222. doi:10.1016/j.icarus.2007.06.018

Marcucci, E.C., Hynek, B.M., Kierein-Young, K.S., Rogers, K.L., 2013. Visible-near infrared reflectance spectroscopy of volcanic acid-sulphate alteration in Nicaragua: Analogs for early Mars. J. Geophys. Res. Planets 118, 10, 2213–2233. doi:10.1002/jgre.20159

Marion, G.M., Catling, D.C., Zahnle, K.J., Claire, M.W., 2010. Modeling aqueous perchlorate chemistries with applications to Mars. Icarus 207, 2, 675–685. doi:10.1016/j.icarus.2009.12.003

Martinez-Frias, J., Amaral, G., Vázquez, L., 2006. Astrobiological significance of minerals on Mars surface environment. Rev. Environ. Sci. Bio/Technology 5, 2-3, 219–231. doi:10.1007/s11157-006-0008-x

Marzo, G.A., Davila, A.F., Tornabene, L.L., Dohm, J.M., Fairén, A.G., Gross, C., Kneissl, T., Bishop, J.L., Roush, T.L., McKay, C.P., 2010. Evidence for Hesperian impact-induced hydrothermalism on Mars. Icarus 208, 2, 667–683. doi:10.1016/j.icarus.2010.03.013

Massé, M., Beck, P., Conway, S.J., Gargani, J., McEwen, A.S., Schmitt, B., Patel, M., Jouannic, G., Ojha, L., Pommerol, A., 2014a. Laboratory simulation of martian recurring slope lineae (RSL): Origin and detectability of liquid brines, in: LPSC XXXXV. Houston, USA, p. 2137.

Massé, M., Beck, P., Schmitt, B., Pommerol, A., McEwen, A.S., Chevrier, V.F., Brissaud, O., Séjourné, A., 2014b. Spectroscopy and detectability of liquid brines on mars. Planet. Space Sci. 92, 136–149. doi:10.1016/j.pss.2014.01.018

McEwen, A.S., Dundas, C.M., Mattson, S.S., Toigo, A.D., Ojha, L., Wray, J.J., Chojnacki, M., Byrne, S., Murchie, S.L., Thomas, N., 2014. Recurring slope lineae in equatorial regions of Mars. Nat. Geosci. 7, 1, 53–58. doi:10.1038/ngeo2014

McEwen, A.S., Eliason, E.M., Bergstrom, J.W., Bridges, N.T., Hansen, C.J., Delamere, W.A., Grant, J.A., Gulick, V.C., Herkenhoff, K.E., Keszthelyi, L.P., Kirk, R.L., Mellon, M.T., Squyres, S.W., Thomas, N., Weitz, C.M., 2007. Mars Reconnaissance Orbiter's High Resolution Imaging Science Experiment (HiRISE). J. Geophys. Res. 112, E5, E05S02. doi:10.1029/2005JE002605

McEwen, A.S., Ojha, L., Dundas, C.M., Mattson, S.S., Byrne, S., Wray, J.J., Cull, S.C., Murchie, S.L., Thomas, N., Gulick, V.C., 2011. Seasonal flows on warm Martian slopes. Science 333, 6043, 740–743. doi:10.1126/science.1204816

McGuire, P.C., Bishop, J.L., Brown, A.J., Fraeman, A.A., Marzo, G.A., Frank Morgan, M., Murchie, S.L., Mustard, J.F., Parente, M., Pelkey, S.M., Roush, T.L., Seelos, F.P., Smith, M.D., Wendt, L., Wolff, M.J., 2009. An improvement to the volcano-scan algorithm for atmospheric correction of CRISM and OMEGA spectral data. Planet. Space Sci. 57, 7, 809–815. doi:10.1016/j.pss.2009.03.007

McGuire, P.C., Wolff, M.J., Smith, M.D., Arvidson, R.E., Murchie, S.L., Clancy, R.T., Roush, T.L., Cull, S.C., Lichtenberg, K.A., Wiseman, S.M., Green, R.O., Marti, T.Z., Milliken, R.E., Cavender, P.J., Humm, D.C., Seelos, F.P., Seelos, K.D., Taylor, H.W., Ehlmann, B.L., Mustard, J.F., Pelkey, S.M., Titus, T.N., Hash, C.D., Malaret, E.R., 2008. MRO/CRISM Retrieval of Surface Lambert Albedos for Multispectral Mapping of Mars With DISORT-Based Radiative Transfer Modeling: Phase 1—Using Historical Climatology for Temperatures, Aerosol Optical Depths, and Atmospheric Pressures. IEEE Trans. Geosci. Remote Sens. 46, 12, 4020–4040. doi:10.1109/TGRS.2008.2000631

McKeown, N.K., Bishop, J.L., Silver, E.A., 2013. Variability of rock texture and morphology correlated with the clay-bearing units at Mawrth Vallis, Mars. J. Geophys. Res. Planets 118, 6, 1245–1256. doi:10.1002/jgre.20096

Merriman, R.J., Peacor, D.R., 1999. Very low-grade metapelites: mineralogy, microfabrics and measuring reaction progress, in: Frey, M., Robinson, D. (Eds.), Low-Grade Metamorphism. Blackwell Sciences Ltd, Oxford.

Miao, L., Qi, H., 2007. Endmember Extraction From Highly Mixed Data Using Minimum Volume Constrained Nonnegative Matrix Factorization. IEEE Trans. Geosci. Remote Sens. 45, 3, 765–777. doi:10.1109/TGRS.2006.888466

Milliken, R.E., Mustard, J.F., 2005. Quantifying absolute water content of minerals using near-infrared reflectance spectroscopy. J. Geophys. Res. E Planets 110, 1–25. doi:10.1007/s00426-005-0036-0

Morgan, M.F., Mustard, J.F., Wiseman, S.M., Seelow, F.P., Murchie, S.L., McGuire, P.C., 2011. Improved algorithm for CRISM volcano-scan atmospheric correction, in: LPSC XXXXII. LPI, Houston, USA, p. 2453.

Morgan, M.F., Seelos, F.P., Murchie, S.L., Team, C., 2009. CRISM Data Users' Workshop CAT Tutorial [WWW Document]. URL http://pds-geosciences.wustl.edu/missions/mro/CRISM_Workshop_090322_CAT_MFM.pdf

Morris, R. V., Gooding, J.L., Lauer, H. V., Singer, R.B., 1990. Origins of Marslike spectral and magnetic properties of a Hawaiian palagonitic soil. J. Geophys. Res. 95, B9, 14427–14434. doi:10.1029/JB095iB09p14427

Morris, R. V., Klingelhöfer, G., Schröder, C., Fleischer, I., Ming, D.W., Yen, A.S., Gellert, R., Arvidson, R.E., Rodionov, D.S., Crumpler, L.S., Clark, B.C., Cohen, B.A., McCoy, T.J., Mittlefehldt, D.W., Schmidt, M.E., De Souza, P.A., Squyres, S.W., 2008. Iron mineralogy and aqueous alteration from Husband Hill through Home Plate at Gusev Crater, Mars: Results from the Mössbauer instrument on the Spirit Mars Exploration Rover. J. Geophys. Res. 113, E12. doi:10.1029/2008JE003201

Moussaoui, S., Hauksdóttir, H., Schmidt, F., Jutten, C., Chanussot, J., Brie, D., Douté, S., Benediktsson, J.A., 2008. On the decomposition of Mars hyperspectral data by ICA and Bayesian positive source separation. Neurocomputing 71, 10-12, 2194–2208. doi:10.1016/j.neucom.2007.07.034

Murchie, S.L., Arvidson, R.E., Bedini, P., Beisser, K., Bibring, J.-P., Bishop, J.L., Boldt, J., Cavender, P.J., Choo, T.H., Clancy, R.T., Darlington, E.H., Des Marais, D.J., Espiritu, R., Fort, D., Green, R.O., Guinness, E.A., Hayes, J., Hash, C.D., Heffernan, K., Hemmler, J., Heyler, G., Humm, D.C., Hutcheson, J., Izenberg, N., Lee, R., Lees, J., Lohr, D., Malaret, E.R., Martin, T., McGovern, J.A., McGuire, P.C., Morris, R. V., Mustard, J.F., Pelkey, S.M., Rhodes, E., Robinson, M., Roush, T.L., Schaefer, E., Seagrave, G., Seelos, F.P., Silverglate, P., Slavney, S., Smith, M., Shyong, W.-J., Strohbehn, K., Taylor, H.W., Thompson, P., Tossman, B., Wirzburger, M., Wolff, M.J., 2007. Compact Reconnaissance Imaging Spectrometer for Mars (CRISM) on Mars Reconnaissance Orbiter (MRO). J. Geophys. Res. 112, E5. doi:10.1029/2006JE002682

Murchie, S.L., Seelos, F.P., Hash, C.D., Humm, D.C., Malaret, E.R., McGovern, J.A., Choo, T.H., Seelos, K.D., Buczkowski, D.L., Morgan, M.F., Barnouin-Jha, O.S., Nair, H., Taylor, H.W., Patterson, G.W., Harvel, C.A., Mustard, J.F., Arvidson, R.E., McGuire, P.C., Smith, M.D., Wolff, M.J., Titus, T.N., Bibring, J.-P., Poulet, F., 2009. Compact Reconnaissance Imaging Spectrometer for Mars investigation and data set from the Mars Reconnaissance Orbiter's primary science phase. J. Geophys. Res. 114, E2, E00D07. doi:10.1029/2009JE003344

Mushkin, A., Gillespie, A.R., Montgomery, D.R., Schreiber, B.C., Arvidson, R.E., 2010. Spectral constraints on the composition of low-albedo slope streaks in the Olympus Mons Aureole. Geophys. Res. Lett. 37, 22. doi:10.1029/2010GL044535

Mustard, J.F., Adler, M., Allwood, A., Bass, D.S., Beaty, D.W., Bell III, J.F., Brinckerhoff, W.B., Carr, M.H., Des Marais, D.J., Drake, B., Edgett, K.S., Eigenbrode, J.L., Elkins-Tanton, L.T., Grant, J.A., Milkovich, S.M., Ming, D.W., Moore, C., Murchie, S.L., Onstott, T.C., Ruff, S.W., Sephton, M.A., Steele, A., Treiman, A., 2013. Report of Mars 2020 Science Definition Team.

Mustard, J.F., Erard, S., Bibring, J.-P., Head III, J.W., Hurtrez, S., Langevin, Y., Pieters, C.M., Sotin, C.J., 1993. The surface of Syrtis Major - Composition of the volcanic substrate and mixing with altered dust and soil. J. Geophys. Res. 98, E2, 3387 – 3400. doi:10.1029/92JE02682

Mustard, J.F., Murchie, S.L., Pelkey, S.M., Ehlmann, B.L., Milliken, R.E., Grant, J.A., Bibring, J.-P., Poulet, F., Bishop, J.L., Dobrea, E.N., Roach, L.H., Seelos, F.P., Arvidson, R.E., Wiseman, S.M., Green, R.O., Hash, C.D., Humm, D.C., Malaret, E.R., McGovern, J.A., Seelos, K.D., Clancy, R.T., Clark, R.N., Marais, D.D., Izenberg, N., Knudson, A.T., Langevin, Y., Martin, T., McGuire, P.C., Morris, R. V., Robinson, M., Roush, T.L., Smith, M., Swayze, G.A., Taylor, H.W., Titus, T.N., Wolff, M.J., 2008. Hydrated silicate minerals on Mars observed by the Mars Reconnaissance Orbiter CRISM instrument. Nature 454, 7202, 305–309. doi:10.1038/nature07097

Mustard, J.F., Pieters, C.M., 1989. Photometric phase functions of common geologic minerals and applications to quantitative analysis of mineral mixture reflectance spectra. J. Geophys. Res. 94, B10, 13619. doi:10.1029/JB094iB10p13619

Mustard, J.F., Pieters, C.M., 1987. Quantitative abundance estimates from bidirectional reflectance measurements. J. Geophys. Res. 92, B4, E617–E626. doi:10.1029/JB092iB04p0E617

Nachon, M., Clegg, S.M., Mangold, N., Schröder, S., Kah, L.C., Dromart, G., Ollila, A., Johnson, J.R., Oehler, D.Z., Bridges, J.C., Le Mouélic, S., Forni, O., Wiens, R.C., Anderson, R.B., Blaney, D.L., Bell III, J.F., Clark, B.C., Cousin, A., Dyar, M.D., Ehlmann, B.L., Fabre, C., Gasnault, O., Grotzinger, J.P., Lasue, J., Lewin, E., Léveillé, R., McLennan, S.M., Maurice, S., Meslin, P.-Y., Rapin, W., Rice, M.S., Squyres, S.W., Stack, K.M., Sumner, D.Y., Vaniman, D.T., Wellington, D., 2014. Calcium sulfate veins characterized by ChemCam/Curiosity at Gale crater, Mars. J. Geophys. Res. Planets 119, 9, 1991–2016. doi:10.1002/2013JE004588

Nalepka, R.F., Horwitz, H.M., Hyde, P.D., 1971. Estimating Proportions of Objects from Multispectral Data.

NASA JPL, n.d. AVIRIS f970619t01p02r02 [WWW Document]. URL http://aviris.jpl.nasa.gov/data/free_data.html (accessed 12.7.13).

Nascimento, J.M.P., Dias, J.M.B., 2005. Vertex component analysis: a fast algorithm to unmix hyperspectral data. IEEE Trans. Geosci. Remote Sens. 43, 4, 898–910. doi:10.1109/TGRS.2005.844293

Navarro-González, R., Rainey, F.A., Molina, P., Bagaley, D.R., Hollen, B.J., de la Rosa, J., Small, A.M., Quinn, R.C., Grunthaner, F.J., Cáceres, L., Gomez-Silva, B., McKay, C.P., 2003. Mars-like soils in the Atacama Desert, Chile, and the dry limit of microbial life. Science 302, 5647, 1018–1021. doi:10.1126/science.1089143

Neukum, G., Jaumann, R., Hoffmann, H., Hauber, E., Head III, J.W., Basilevsky, A.T., Ivanov, B.A., Werner, S.C., van Gasselt, S., Murray, J.B., McCord, T., 2004. Recent and episodic volcanic and glacial activity on Mars revealed by the High Resolution Stereo Camera. Nature 432, 7020, 971–979. doi:10.1038/nature03231

Newsom, H.E., Bishop, J.L., Cockell, C.S., Roush, T.L., Johnson, J.R., 2001. Search for life on Mars in surface samples: Lessons from the 1999 Marsokhod rover field experiment. J. Geophys. Res. 106, E4, 7713–7720. doi:10.1029/1999JE001159

Ojha, L., McEwen, A.S., Dundas, C.M., Byrne, S., Mattson, S.S., Wray, J.J., Massé, M., Schaefer, E., 2014. HiRISE observations of Recurring Slope Lineae (RSL) during southern summer on Mars. Icarus 231, 365–376. doi:10.1016/j.icarus.2013.12.021

Ojha, L., Wray, J.J., Murchie, S.L., McEwen, A.S., Wolff, M.J., Karunatillake, S., 2013. Spectral constraints on the formation mechanism of recurring slope lineae. Geophys. Res. Lett. 40, 21, 5621–5626. doi:10.1002/2013GL057893

Osinski, G.R., Tornabene, L.L., Banerjee, N.R., Cockell, C.S., Flemming, R., Izawa, M.R.M., McCutcheon, J., Parnell, J., Preston, L.J., Pickersgill, A.E., Pontefract, A., Sapers, H.M., Southam, G., 2013. Impact-generated hydrothermal systems on Earth and Mars. Icarus 224, 2, 347–363. doi:10.1016/j.icarus.2012.08.030

Parente, M., Bishop, J.L., Bell III, J.F., 2009a. Spectral unmixing for mineral identification in pancam images of soils in Gusev crater, Mars. Icarus 203, 2, 421–436. doi:10.1016/j.icarus.2009.04.029

Parente, M., Bishop, J.L., Bell III, J.F., 2009b. Spectral unmixing for mineral identification in pancam images of soils in Gusev crater, Mars. Icarus 203, 2, 421–436. doi:10.1016/j.icarus.2009.04.029

Parente, M., Clark, J.T., Brown, A.J., Bishop, J.L., 2010. End-to-End Simulation and Analytical Model of Remote-Sensing Systems: Application to CRISM. IEEE Trans. Geosci. Remote Sens. 48, 11, 3877–3888. doi:10.1109/TGRS.2010.2050000

Parente, M., Mustard, J.F., Murchie, S.L., Seelos, F.P., 2011. Robust unmixing of hyperspectral images: Application to Mars, in: Geoscience and Remote Sensing Symposium (IGARSS). Vancouver, pp. 1291–1294.

Pelkey, S.M., Mustard, J.F., Murchie, S.L., Clancy, R.T., Wolff, M.J., Smith, M., Milliken, R.E., Bibring, J.-P., Gendrin, A., Poulet, F., Langevin, Y., Gondet, B., 2007. CRISM multispectral summary products: Parameterizing mineral diversity on Mars from reflectance. J. Geophys. Res. 112, E8. doi:10.1029/2006JE002831

Philippot, P., van Kranendonk, M.J., van Zuilen, M., Lepot, K., Rividi, N., Teitler, Y., Thomazo, C., Blanc-Valleron, M.-M., Rouchy, J.-M., Grosch, E., de Wit, M., 2009. Early traces of life investigations in drilling Archean hydrothermal and sedimentary rocks of the Pilbara Craton, Western Australia and Barberton Greenstone Belt, South Africa. Comptes Rendus Palevol 8, 7, 649–663. doi:10.1016/j.crpv.2009.06.006

Pieters, C.M., Englert, P.A.J., 1993. Remote Geochemical Analysis: Elemental and Mineralogical Composition, 1st ed. Cambridge University Press.

Pieters, C.M., Hiroi, T., 2004. REALB (Reflectance Experiment Laboratory): A NASA multiuser spectroscopy facility, in: Lunar and Planetary Science Conference XXXV. LPI, Houston, USA, p. 1720.

Pirajno, F., van Kranendonk, M.J., 2005. Review of hydrothermal processes and systems on Earth and implications for Martian analogues. Aust. J. Earth Sci. 52, 3, 329–351. doi:10.1080/08120090500134571

Plaza, A., Martín, G., Plaza, J., Zortea, M., Sánchez, S., 2011. Recent developments in spectral unmixing and endmember extraction, in: Prasad, S., Bruce, L.M., Chanussot, J. (Eds.), Optical Remote Sensing - Advances in Signal Processing and Exploitation Techniques. Springer, New York, pp. 235–267. doi:10.1007/978-3-642-14212-3_12

Poulet, F., Bibring, J.-P., Gondet, B., Langevin, Y., Mustard, J.F., Mangold, N., Chevrier, V.F., Gendrin, A., 2007. Discovery, mapping and mineralogy of phyllosilicates on Mars by MEx-OMEGA: A reappraisal, in: Seventh International Conference on Mars. LPI, Houston, USA.

Poulet, F., Cuzzi, J.N., Cruikshank, D.P., Roush, T.L., Dalle Ore, C.M., 2002. Comparison between the Shkuratov and Hapke Scattering Theories for Solid Planetary Surfaces: Application to the Surface Composition of Two Centaurs. Icarus 160, 2, 313–324. doi:10.1006/icar.2002.6970

Poulet, F., Erard, S., 2004. Nonlinear spectral mixing: Quantitative analysis of laboratory mineral mixtures. J. Geophys. Res. 109, E2, E02009. doi:10.1029/2003JE002179

Preston, L.J., Grady, M., Barber, S., 2013. TN2: The Catalogue of Planetary Analogues. ESA, Milton Keynes, UK.

Pugh, S., Barnes, D.P., Tyler, L., Gunn, M., Schmitz, N., Paar, G., Bauer, A., Cousins, C.R., Pullan, D., Coates, A.J., Griffiths, A.D., 2012. AUPE - A PanCam Emulator for the ExoMars 2018 Mission, in: International Symposium on Artificial Intelligence, Robotics and Automation in Space. Turin.

Quintano, C., Fernández-Manso, A., Shimabukuro, Y.E., Pereira, G., 2012. Spectral unmixing. Int. J. Remote Sens. 33, 17, 5307–5340. doi:10.1080/01431161.2012.661095

Reid, R.J., Smith, P.H., Lemmon, M.T., Tanner, R., Burkland, M., Wegryn, E., Weinberg, J., Marcialis, R.L., Britt, D.T., Thomas, N., Kramm, R., Dummel, A., Crowe, D.G., Bos, B.J., Bell III, J.F., Rueffer, P., Gliem, F., Johnson, J.R., Maki, J.N., Herkenhoff, K.E., Singer, R.B., 1999. Imager for Mars Pathfinder (IMP) image calibration. J. Geophys. Res. 104, E4, 8907–8925. doi:10.1029/1998JE900011

Rice, M.S., Ayoub, F., Ehlmann, B.L., Leprince, S., Grotzinger, J.P., Horgan, B.H., Avouac, J.-P., 2013a. Co-registration of CRISM and HiRISE observations for interpreting mineral stratigrraphy at Gale Crater, Mars, in: LPSC XXXXIV. Houston, USA, p. 2323.

Rice, M.S., Bell III, J.F., Cloutis, E.A., Wang, A.E., Ruff, S.W., Craig, M.A., Bailey, D.T., Johnson, J.R., de Souza, P.A., Farrand, W.H., 2010. Silica-rich deposits and hydrated minerals at Gusev Crater, Mars: Vis-NIR spectral characterization and regional mapping. Icarus 205, 2, 375–395. doi:10.1016/j.icarus.2009.03.035

Rice, M.S., Cloutis, E.A., Bell III, J.F., Bish, D.L., Horgan, B.H., Mertzman, S.A., Craig, M.A., Renaut, R.W., Gautason, B., Mountain, B., 2013b. Reflectance spectra diversity of silica-rich materials: Sensitivity to environment and implications for detections on Mars. Icarus 223, 1, 499–533. doi:10.1016/j.icarus.2012.09.021

Richards, J.A., Jia, X., 1999. Remote Sensing Digital Image Analysis, 3rd ed. Springer, Berlin.

Ruff, S.W., Christensen, P.R., 2002. Bright and dark regions on Mars: Particle size and mineralogical characteristics based on Thermal Emission Spectrometer data. J. Geophys. Res. 107, E12, 5119. doi:10.1029/2001JE001580

Rummel, J.D., Beaty, D.W., Jones, M.A., Bakermans, C., Barlow, N.G., Boston, P.J., Chevrier, V.F., Clark, B.C., de Vera, J.-P.P., Gough, R. V., Hallsworth, J.E., Head III, J.W., Hipkin, V.J., Kieft, T.L., McEwen, A.S., Mellon, M.T., Mikucki, J.A., Nicholson, W.L., Omelon, C.R., Peterson, R., Roden, E.E., Sherwood Lollar, B., Tanaka, K.L., Viola, D., Wray, J.J., 2014. A New Analysis of Mars "Special Regions": Findings of the Second MEPAG Special Regions Science Analysis Group (SR-SAG2). Astrobiology 14, 11, 887–968. doi:10.1089/ast.2014.1227

Sabins, F.F., 1999. Remote sensing for mineral exploration. Ore Geol. Rev. 14, 3-4, 157–183. doi:10.1016/S0169-1368(99)00007-4

Scanlon, K.E., Head III, J.W., Marchant, D.R., 2015. Volcanism-induced, local wet-based glacial conditions recorded in the Late Amazonian Arsia Mons tropical mountain glacier deposits. Icarus 250, 18–31. doi:10.1016/j.icarus.2014.11.016

Scanlon, K.E., Head III, J.W., Wilson, L., Marchant, D.R., 2014. Volcano–ice interactions in the Arsia Mons tropical mountain glacier deposits. Icarus 237, 315–339. doi:10.1016/j.icarus.2014.04.024

Schenker, P.S., Baumgartner, E.T., Backes, P.G., Aghazarian, H., Dorsky, L.I., Norris, J.S., Huntsberger, T.L., Cheng, Y., Arvidson, R.E., Squyres, S.W., 2001. FIDO: Field Integrated Design and Operations Rover for Mars Surface Exploration.

Schmidt, F., Legendre, M., Le Mouélic, S., 2014. Minerals detection for hyperspectral images using adapted linear unmixing: LinMin. Icarus 237, 61–74. doi:10.1016/j.icarus.2014.03.044

Schmidt, F., Schmidt, A., Treguier, E., Guiheneuf, M., Moussaoui, S., Dobigeon, N., 2010. Implementation Strategies for Hyperspectral Unmixing Using Bayesian Source Separation. IEEE Trans. Geosci. Remote Sens. 48, 11, 4003–4013. doi:10.1109/TGRS.2010.2062190

Schmidt, M.E., Farrand, W.H., Johnson, J.R., Schröder, C., Hurowitz, J.A., McCoy, T.J., Ruff, S.W., Arvidson, R.E., Des Marais, D.J., Lewis, K.W., 2009. Spectral, mineralogical, and geochemical variations across Home Plate, Gusev Crater, Mars indicate high and low temperature alteration. Earth Planet. Sci. Lett. 281, 3-4, 258–266. doi:10.1016/j.epsl.2009.02.030

Schmitz, N., Griffiths, A.D., Barnes, D.P., Coates, A.J., Hauber, E., Jaumann, R., Michaelis, H., Trauthan, F., 2008. ExoMars PanCam Field Test Report from the Arctic Mars Analogue Svalbard Expedition (AMASE) 2008, in: ASTRA 2008. Noordwijk.

Schulte, M., Blake, D.F., Hoehler, T., McCollom, T., 2006. Serpentinization and its implications for life on the early Earth and Mars. Astrobiology 6, 2, 364–76. doi:10.1089/ast.2006.6.364

Schulze-Makuch, D., Dohm, J.M., Fan, C., Fairén, A.G., Rodríguez, J.A.P., Baker, V.R., Fink, W., 2007. Exploration of hydrothermal targets on Mars. Icarus 189, 2, 308–324. doi:10.1016/j.icarus.2007.02.007

Sgavetti, M., Pompilio, L., Roveri, M., Manzi, V., Valentino, G.M., Lugli, S., Carli, C., Amici, S., Marchese, F., Lacava, T., 2009. Two geologic systems providing terrestrial analogues for the exploration of sulfate deposits on Mars: Initial spectral characterization. Planet. Space Sci. 57, 5-6, 614–627. doi:10.1016/j.pss.2008.05.010

Shanks III, W.C.P., 2010. Hydrothermal Alteration: Volcanogenic massive sulfide occurrence model, in: USGS Scientific Investigations Report 2010-5070-C. USGS, p. 12.

Shkuratov, Y., Kaydash, V., Korokhin, V., Velikodsky, Y., Petrov, D., Zubko, E., Stankevich, D., Videen, G., 2012. A critical assessment of the Hapke photometric model. J. Quant. Spectrosc. Radiat. Transf. 113, 18, 2431–2456. doi:10.1016/j.jqsrt.2012.04.010

Shkuratov, Y., Starukhina, L., Hoffmann, H., Arnold, G., 1999. A Model of Spectral Albedo of Particulate Surfaces: Implications for Optical Properties of the Moon. Icarus 137, 2, 235–246. doi:10.1006/icar.1998.6035

Skok, J.R., Fawdon, P., Mustard, J.F., Karunatillake, S., Fassett, C.I., 2014. Pinpointing habitability in Nili Patera's hydrothermal field, in: Mars 2020 Landing Site Meeting.

Skok, J.R., Mustard, J.F., Ehlmann, B.L., Milliken, R.E., Murchie, S.L., 2010. Silica deposits in the Nili Patera caldera on the Syrtis Major volcanic complex on Mars. Nat. Geosci. 3, 12, 838–841. doi:10.1038/ngeo990

Smellie, J.L., Skilling, I.P., 1994. Products of subglacial volcanic eruptions under different ice thicknesses: two examples from Antarctica. Sediment. Geol. 91, 1-4, 115–129. doi:10.1016/0037-0738(94)90125-2

Smith, M.O., Johnson, P.E., Adams, J.B., 1985. Quantitative determination of mineral types and abundances from reflectance spectra using principal components analysis. J. Geophys. Res. 90, S02, C797. doi:10.1029/JB090iS02p0C797

Smith, M.R., Bandfield, J.L., 2012. Geology of quartz and hydrated silica-bearing deposits near Antoniadi Crater, Mars. J. Geophys. Res. 117, E6. doi:10.1029/2011JE004038

Smith, M.R., Bandfield, J.L., Cloutis, E.A., Rice, M.S., 2013. Hydrated silica on Mars: Combined analysis with near-infrared and thermal-infrared spectroscopy. Icarus 223, 2, 633–648. doi:10.1016/j.icarus.2013.01.024

Smith, P.H., Tomasko, M.G., Britt, D.T., Crowe, D.G., Reid, R.J., Keller, H.U., Thomas, N., Gliem, F., Rueffer, P., Sullivan, R.J., Greeley, R., Knudsen, J.M., Madsen, M.B., Gunnlaugsson, H.P., Hviid, S.F., Goetz, W., Soderblom, L.A., Gaddis, L., Kirk, R., 1997. The imager for Mars Pathfinder experiment. J. Geophys. Res. 102, E2, 4003–4025. doi:10.1029/96JE03568

Somers, B., Asner, G.P., Tits, L., Coppin, P., 2011. Endmember variability in Spectral Mixture Analysis: A review. Remote Sens. Environ. 115, 7, 1603–1616. doi:10.1016/j.rse.2011.03.003

Squyres, S.W., Arvidson, R.E., Bell III, J.F., Calef, F.J., Clark, B.C., Cohen, B.A., Crumpler, L.S., de Souza, P.A., Farrand, W.H., Gellert, R., Grant, J.A., Herkenhoff, K.E., Hurowitz, J.A., Johnson, J.R., Jolliff, B.L., Knoll, A.H., Li, R., McLennan, S.M., Ming, D.W., Mittlefehldt, D.W., Parker, T.J., Paulsen, G., Rice, M.S., Ruff, S.W., Schröder, C., Yen, A.S., Zacny, K., 2012. Ancient Impact and Aqueous Processes at Endeavour Crater, Mars. Science (80-.). 336, 6081, 570–576. doi:10.1126/science.1220476

Squyres, S.W., Arvidson, R.E., Ruff, S.W., Gellert, R., Morris, R. V., Ming, D.W., Crumpler, L.S., Farmer, J.D., Des Marais, D.J., Yen, A.S., McLennan, S.M., Calvin, W.M., Bell III, J.F., Clark, B.C., Wang, A.E., McCoy, T.J., Schmidt, M.E., de Souza, P.A., 2008. Detection of silica-rich deposits on Mars. Science 320, 5879, 1063–1067. doi:10.1126/science.1155429

Stack, K.M., Milliken, R.E., 2015. Modeling near-infrared reflectance spectra of clay and sulfate mixtures and implications for Mars. Icarus 250, 332–356. doi:10.1016/j.icarus.2014.12.009

Steele, A., Amundsen, H.E.F., Conrad, P.G., Benning, L., 2010. Arctic Mars Analogue Svalbard Expedition (AMASE) 2009, in: 41st Lunar and Planetary Science Conference. Houston, USA, p. 2398.

Stroncik, N.A., Schmincke, H.U., 2002. Palagonite - A review. Int. J. Earth Sci. 91, 4, 680–697. doi:10.1007/s00531-001-0238-7

Summons, R.E., Amend, J.P., Bish, D.L., Buick, R., Cody, G.D., Des Marais, D.J., Dromart, G., Eigenbrode, J.L., Knoll, A.H., Sumner, D.Y., 2011. Preservation of martian organic and environmental records: final report of the Mars biosignature working group. Astrobiology 11, 2, 157–181. doi:10.1089/ast.2010.0506

Sunshine, J.M., Pieters, C.M., 1998. Determining the composition of olivine from reflectance spectroscopy. J. Geophys. Res. 103, E6, 13675. doi:10.1029/98JE01217

Sunshine, J.M., Pieters, C.M., 1993. Estimating modal abundances from the spectra of natural and laboratory pyroxene mixtures using the modified Gaussian model. J. Geophys. Res. 98, E5, 9075. doi:10.1029/93JE00677

Sunshine, J.M., Pieters, C.M., Pratt, S.F., 1990. Deconvolution of mineral absorption bands - An improved approach. J. Geophys. Res. Solid Earth 95, B5, 6955–6966. doi:10.1029/JB095iB05p06955

Swayze, G.A., Clark, R.N., Goetz, A.F.H., Livo, E.K., Breit, G.N., Kruse, F.A., Stutley, S.J., Snee, L.W., Lowers, H.A., Post, J.L., Stoffregen, R.E., Ashley, R.P., 2014. Mappng advance argillic alteration at Cuprite, Nevada using imaging spectroscopy. Ecomonic Geol. 109, 5, 1179–1221. doi:10.2113/econgeo.109.5.1179

Szwast, M.A., Richardson, M.I., Vasavada, A.R., 2006. Surface dust redistribution on Mars as observed by the Mars Global Surveyor and Viking orbiters. J. Geophys. Res. 111, E11. doi:10.1029/2005JE002485

Tanaka, K.L., Skinner, J.A., Dohm, J.M., Irwin, R.P., Kolb, E.J., Fortezzo, C.M., Platz, T., Michael, G.G., Hare, T.M., 2014. Geologic Map of Mars. U.S. Geol. Surv. Geol. Investig. 3292. doi:10.3133/sim3292

Themelis, K.E., Schmidt, F., Sykioti, O., Rontogiannis, A.A., Koutroumbas, K.D., Daglis, I.A., 2012. On the unmixing of MEx/OMEGA hyperspectral data. Planet. Space Sci. 68, 1, 34–41. doi:10.1016/j.pss.2011.11.015

Thi, H.-L.N., Jutten, C., 1995. Blind source separation for convolutive mixtures. Signal Processing 45, 2, 209–229. doi:10.1016/0165-1684(95)00052-F

Thompson, D.R., Castaño, R., Gilmore, M.S., 2009. Sparse superpixel unmixing for exploratory analysis of CRISM hyperspectral images, in: 2009 First Workshop on Hyperspectral Image and Signal Processing: Evolution in Remote Sensing. IEEE, pp. 1–4. doi:10.1109/WHISPERS.2009.5289045

Thordarson, T., Hoskuldsson, A., 2002. Iceland, 1st ed. Dunedin Academic Press Ltd, Edinburgh.

Todesco, M., 2008. Hydrothermal fluid circulation and its effect on caldera unrest, in: Gottsmann, J., Marti, J. (Eds.), Caldera Volcanism. Elsevier.

Treiman, A.H., Amundsen, H.E.F., Blake, D.F., Bunch, T., 2002. Hydrothermal origin for carbonate globules in Martian meteorite ALH84001: a terrestrial analogue from Spitsbergen (Norway). Earth Planet. Sci. Lett. 204, 3-4, 323–332. doi:10.1016/S0012-821X(02)00998-6

Tunstel, E., Huntsberger, T.L., Aghazarian, H., Backes, P.G., Baumgartner, E.T., Cheng, Y., Garrett, M., Kennedy, B., Leger, C., Magnone, L., Norris, J.S., Powell, M., Trebi-Ollennu, A., Schenker, P.S., 2002. FIDO ROVER FIELD TRIALS AS REHEARSAL FOR THE NASA 2003 MARS EXPLORATION ROVERS MISSION, in: Automation Congress, 2002 Proceedings of the 5th Biannual World. p. 8.

Ulrich, M., Hauber, E., Herzschuh, U., Härtel, S., Schirrmeister, L., 2011. Polygon pattern geomorphometry on Svalbard (Norway) and western Utopia Planitia (Mars) using high-resolution stereo remote-sensing data. Geomorphology 134, 3-4, 197–216. doi:10.1016/j.geomorph.2011.07.002

Ulrich, M., Wagner, D., Hauber, E., de Vera, J.-P.P., Schirrmeister, L., 2012. Habitable periglacial landscapes in martian mid-latitudes. Icarus 219, 1, 345–357. doi:10.1016/j.icarus.2012.03.019

van Kranendonk, M.J., 2006. Volcanic degassing, hydrothermal circulation and the flourishing of early life on Earth: A review of the evidence from c. 3490-3240 Ma rocks of the Pilbara Supergroup, Pilbara Craton, Western Australia. Earth-Science Rev. 74, 3-4, 197–240. doi:10.1016/j.earscirev.2005.09.005

Vaniman, D.T., Bish, D.L., Ming, D.W., Bristow, T.F., Morris, R. V., Blake, D.F., Chipera, S.J., Morrison, S.M., Treiman, A.H., Rampe, E.B., Rice, M.S., Achilles, C.N., Grotzinger, J.P., McLennan, S.M., Williams, J., Bell III, J.F., Newsom, H.E., Downs, R.T., Maurice, S., Sarrazin, P., Yen, A.S., Morookian, J.M., Farmer, J.D., Stack, K.M., Milliken, R.E., Ehlmann, B.L., Sumner, D.Y., Berger, G., Crisp, J.A., Hurowitz, J.A., Anderson, R.B., Des Marais, D.J., Stolper, E.M., Edgett, K.S., Gupta, S., Spanovich, N., Team, M.S., 2014. Mineralogy of a Mudstone at Yellowknife Bay, Gale Crater, Mars. Science 343, 6169, 1243480. doi:10.1126/science.1243480

Vincendon, M., Forget, F., Mustard, J.F., 2010. Water ice at low to midlatitudes on Mars. J. Geophys. Res. 115, E10. doi:10.1029/2010JE003584

Vincendon, M., Pilorget, C., Gondet, B., Murchie, S.L., Bibring, J.-P., 2011. New near-IR observations of mesospheric CO2 and H2O clouds on Mars. J. Geophys. Res. 116, E11. doi:10.1029/2011JE003827

Viviano, C.E., Moersch, J.E., McSween Jr., H.Y., 2013. Implications for early hydrothermal environments on Mars through the spectral evidence for carbonation and chloritization reactions in the Nili Fossae region. J. Geophys. Res. Planets 118, 9, 1858–1872. doi:10.1002/jgre.20141

Viviano-Beck, C.E., 2015. Early hydrothermal environments on Mars: Tyrrhena Terra, in: LPSC XXXXVI. LPI, Houston, USA, p. 2756.

Viviano-Beck, C.E., Seelos, F.P., Murchie, S.L., Kahn, E.G., Seelos, K.D., Taylor, H.W., Taylor, K., Ehlmann, B.L., Wiseman, S.M., Mustard, J.F., Morgan, M.F., 2014. Revised CRISM spectral parameters and summary products based on the currently detected mineral diversity on Mars. J. Geophys. Res. Planets 119, 6, 1403–1431. doi:10.1002/2014JE004627

Warner, N.H., Farmer, J.D., 2010. Subglacial hydrothermal alteration minerals in Jökulhlaup deposits of Southern Iceland, with implications for detecting past or present habitable environments on Mars. Astrobiology 10, 5, 523–47. doi:10.1089/ast.2009.0425

Warner, N.H., Gupta, S., Calef, F.J., Grindrod, P.M., Boll, N., Goddard, K., 2015. Minimum effective area for high resolution crater counting of martian terrains. Icarus 245, 198–240. doi:10.1016/j.icarus.2014.09.024

Wendt, L., Combe, J.-P., McGuire, P.C., Bishop, J.L., Neukum, G., 2009. Linear spectral unmixing of near-infrared hyperspectral data from Juventae Chasma, Mars, in: Bruzzone, L., Notarnicola, C., Posa, F. (Eds.), Proc. SPIE 7477, Image and Signal Processing for Remote Sensing XV. IEEE, Berlin, Germany, p. 74770M–74770M–12. doi:10.1117/12.830095

West, M.D., Clarke, J.D.A., Thomas, M., Pain, C.F., Walter, M.R., 2010. The geology of Australian Mars analogue sites. Planet. Space Sci. 58, 4, 447–458. doi:10.1016/j.pss.2009.06.012

Westall, F., Loizeau, D., Foucher, F., Bost, N., Betrand, M., Vago, J., Kminek, G., 2013. Habitability on Mars from a microbial point of view. Astrobiology 13, 9, 887–97. doi:10.1089/ast.2013.1000

Wierzchos, J., Davila, A.F., Artieda, O., Cámara-Gallego, B., de los Ríos, A., Nealson, K.H., Valea, S., Teresa García-González, M., Ascaso, C., 2013. Ignimbrite as a substrate for endolithic life in the hyper-arid Atacama Desert: Implications for the search for life on Mars. Icarus 224, 2, 334–346. doi:10.1016/j.icarus.2012.06.009

Winter, M.E., 1999. N-FINDR: an algorithm for fast autonomous spectral end-member determination in hyperspectral data, in: Proceedings of SPIE. SPIE, pp. 266–275. doi:10.1117/12.366289

Wiseman, S.M., Arvidson, R.E., Wolff, M.J., Morris, R. V., Seelos, F.P., Smith, M.D., Humm, D.C., Murchie, S.L., Mustard, J.F., 2012. Retrieval of atmospherically corrected CRISM spectra using radiative transfer modeling, in: LPSC XXXXIII. Houston, USA, p. 2146.

Wiseman, S.M., Arvidson, R.E., Wolff, M.J., Smith, M.D., Seelos, F.P., Morgan, M.F., Murchie, S.L., Mustard, J.F., Morris, R. V., Humm, D.C., McGuire, P.C., 2014. Characterization of Artifacts Introduced by the Empirical Volcano-Scan Atmospheric Correction Commonly Applied to CRISM and OMEGA Near-Infrared Spectra. Icarus in press. doi:10.1016/j.icarus.2014.10.012

Wray, J.J., Hansen, S.T., Dufek, J., Swayze, G.A., Murchie, S.L., Seelos, F.P., Skok, J.R., Irwin, R.P., Ghiorso, M.S., 2013. Prolonged magmatic activity on Mars inferred from the detection of felsic rocks. Nat. Geosci. 6, 12, 1013–1017. doi:10.1038/ngeo1994

Yang, K., Huntington, J.F., Boardman, J.W., Mason, P., 1999. Mapping hydrothermal alteration in the Comstock mining district, Nevada, using simulated satellite-borne hyperspectral data. Aust. J. Earth Sci. 46, 6, 915–922. doi:10.1046/j.1440-0952.1999.00754.x

Yokoyama, E., Nédélec, A., Baratoux, D., Trindade, R.I.F., Fabre, S., Berger, G., 2015. Hydrothermal alteration in basalts from Vargeão impact structure, south Brazil, and implications for recognition of impact-induced hydrothermalism on Mars. Icarus 252, 347–365. doi:10.1016/j.icarus.2015.02.001

Zare, A., Gader, P., 2007. Sparsity Promoting Iterated Constrained Endmember Detection in Hyperspectral Imagery. IEEE Geosci. Remote Sens. Lett. 4, 3, 446–450. doi:10.1109/LGRS.2007.895727

Appendix I: AUPE-2 processing pipeline and associated IDL code

Final Full Processing Pipeline in ENVI

1. Load filters in for left/right eye ensuring only using the geology filters (L/R04, L/R05, L/R06, L/R07, L/R08, L/R09) then save these as a standard ENVI file format stacking them in the correct wavelength order (as written above).
    a. File Name A04_02_154108LWACGeol (Site_Exposure#_Run#EyeFilterSet)
2. Edit header to include wavelength and FWHM values in nanometres.
3. Extract the exposure values from each image
    a. This can be extracted from the raw image metadata where it is recorded as ShutterSpeed.
    b. Save as row of values not column
4. Save image and copy onto memory stick to transfer to personal laptop
5. Ensure laptop already has copies of flat field filter image
6. Start up the IDL console and run ENVI from within it
    a. E=ENVI()
    b. This will open up ENVI 5.0 and run code
    c. Use e.close to close ENVI and return to IDL
7. Open the IDL script '***normalising_bm.pro***'
    a. Resulting file will be named according to the following convention - *A04_02_154108LWACGeolFF*
8. Change the output file name and destination as appropriate
9. Recompile script
10. Run script using appropriate eye flat field cube and image cube
11. Manually input wavelength and FWHM info into the header (inputting from original file appears to turn the image into noise)
12. Apply equation $RC_\lambda = K(T) \times (DN_C \div e_\lambda)$ where DN_C is the corrected image DN values, e_λ is the image exposure value and K(T) is the camera response function.
    a. I do not know the camera response function as it hasn't been measured yet by Aberystwyth so for now I'm going to assume it is perfect (i.e. K(T)=1) and doesn't change with temperature)
    b. Use ***exposures.pro*** routine to build values into image then use ***radiocorr_bm.pro*** to convert image data by applying this equation.
    c. Final files will named according to the following conventions - *A04_02_154108LWACExpo, A04_02_154108LWACGeolRad*

13. Calibration with Caltag
    a. Take average reflectance values from the RC_λ image from the following squares in the caltag; white, light grey, medium grey, dark grey, yellow, red green and blue.
        i. This will result in spectra for each of these covering the full wavelength range (so a 6 point spectrum from each eye).
    b. Extract these values and then for each filter plot them against the appropriate values from the lab calibration caltag spectra.
        i. Extract in ENVI
            1. Define ROI's over each colour (in the above order)
            2. Calculate Stats on all ROI's
            3. Save stats on all ROI's as text file
            4. Import into Excel template
            5. Save final RSfactors as text file in row
    c. Read into IDL using ***mvalues.pro*** routine and convert to 1024x1024x6 image as for exposures
    d. A04_02_154108LWACRSmvalues
14. Using the file *mvalues* file generated in step 13 convert RC_λ images into R* values which should give spectral values between 0-100 (possibly with a few outliers that can be masked out if required).
    a. $R^*_\lambda = RC_\lambda \times m_\lambda$
    b. Where m_λ is the slope value and RC_λ is the image pixel value at the appropriate wavelength and e_λ is the image exposure value.
    c. Use IDL routine ***calibrat.pro*** to give final calibrated image
    d. A04_02_154108LWACGeolRStarCal
15. Manually input wavelength and FWHM info into the header (inputting from original file appears to turn the image into noise)
16. Create mask using ENVI build mask function, masking out all pixels with values above 100
    a. Open image into display
    b. Select display image
    c. Input data range mask min value 100, no max value, mask is ANY band matches range, selected areas OFF, logical OR
    d. Apply mask with masked values = 0

The AUPE data is now ready to be processed, i.e. spectral parameters calculated, ROI spectra extracted.

IDL codes

normalising_bm.pro

```
;routine to correct for the AUPE filter flatfield response by dividing the image
;data by the normalised flatfield data

pro normalising_bm
compile_opt idl2

; select, open and query the two input files
input_file1 = dialog_pickfile(title='select image file')
envi_open_file, input_file1, r_fid=b1_fid, /no_realize
envi_file_query, b1_fid, nb=num_bands, ns=ns, nl=nl

input_file2 = dialog_pickfile(title='select flatfield file')
envi_open_file, input_file2, r_fid=b2_fid, /no_realize

;set up the dims, pos and fid arrays
dims=[-1L,0,ns-1,0,nl-1]
pos1=n_elements(lindgen(num_bands))
pos=lindgen(pos1,pos1)/pos1
fid=[b1_fid,b2_fid]
out_name='math_test'

;create an output fid array to hold each band processed
out_fid=lonarr(num_bands)

;the band math expression
expression='float(b1)/float(b2)'

;loop through each band and apply the equation
for i=0,num_bands-1 do begin
  envi_doit, 'math_doit', dims=dims, exp=expression, pos=pos[*,i],$
    fid=fid, r_fid=r_fid, /in_memory
    out_fid[i]=r_fid
endfor

;stack the output bands into one file
out_pos=lonarr(num_bands)
envi_doit, 'cf_doit', dims=dims, fid=out_fid, pos=out_pos, $

out_name='C:\Users\Jenn\Documents\IDL_Iceland\A071_00_105341\A071_00_P00_
105341LWACRGBFF', r_fid=result_fid

end
```

exposures.pro

```
;create file to read in exposure values and turn them into 1024x1024x6 datacube
;where each plane is filled with the exposure value for the relevant filter

pro exposures
compile_opt idl2

;create empty (6,1) array to hold exposure values
E=fltarr(6,1)

;read in exposure values from 6 row text file and add to E
openr,1,'E:\ENVI\A051_01_122723\A051_01_P02_122723RWACGeolExposures.txt'
readf,1,E

;convert to 1024x1024x6 array
E3D=rebin(reform(E,1,1,6),1024,1024,6)

;write 3D array to ENVI image format as BSQ
envi_write_envi_file,E3D,out_name='C:\Users\Jenn\Documents\IDL_Iceland\A051_0
1_122723\A051_01_P02_122723RWACExpo.img'

end
```

radiocorr_bm.pro

```
;routine to radiometrically correct the normalised image by multiplying by
;camera response function (assumed = 1) and dividing by exposure time

pro radiocorr_bm
compile_opt idl2

; select, open and query the two input files
input_file1 = dialog_pickfile(title='select image file')
envi_open_file, input_file1, r_fid=b1_fid, /no_realize
envi_file_query, b1_fid, nb=num_bands, ns=ns, nl=nl

input_file2 = dialog_pickfile(title='select exposures file')
envi_open_file, input_file2, r_fid=b2_fid, /no_realize

;set up the dims, pos and fid arrays
dims=[-1L,0,ns-1,0,nl-1]
pos1=n_elements(lindgen(num_bands))
pos=lindgen(pos1,pos1)/pos1
fid=[b1_fid,b2_fid]
out_name='math_test'

;create an output fid array to hold each band processed
out_fid=lonarr(num_bands)

;the band math expression, RClambda/exposure value
expression='float(b1)/float(b2)'
```

```
;loop through each band and apply the equation
for i=0,num_bands-1 do begin
  envi_doit, 'math_doit', dims=dims, exp=expression, pos=pos[*,i],$
    fid=fid, r_fid=r_fid, /in_memory
    out_fid[i]=r_fid
endfor

;stack the output bands into one file
out_pos=lonarr(num_bands)
envi_doit, 'cf_doit', dims=dims, fid=out_fid, pos=out_pos, $

out_name='C:\Users\Jenn\Documents\IDL_Iceland\A071_00_105341\A071_00_P00_
105341LWACRGBRad', r_fid=result_fid

end
```

mvalues.pro

```
;create file to read in calibration slope values and turn them into 1024x1024x6
; datacube where each plane is filled with the RStar mvalue for the relevant filter

pro mvalues
compile_opt idl2

;create empty (6,1) array to hold slope mvalues
M=fltarr(6,1)

;read in slope mvalues from 6 row text file and add to M
openr,1,'E:\ENVI\A051_01_122723\A051_01_122723RWACGeol_Rstar_mvalues.txt'
readf,1,M

;convert to 1024x1024x6 array
M3D=rebin(reform(M,1,1,6),1024,1024,6)

;write 3D array to ENVI image format as BSQ
envi_write_envi_file,M3D,out_name='C:\Users\Jenn\Documents\IDL_Iceland\A051_
01_122723\A051_01_122723RWACRSmvalues.img'

end
```

calibrat_bm.pro

```
;routine to calibrate the radiometrically corrected image by multiplying by
;RSfactorMvalue

pro calibrat_bm
compile_opt idl2

; select, open and query the two input files
input_file1 = dialog_pickfile(title='select RadCor image file')
envi_open_file, input_file1, r_fid=b1_fid, /no_realize
```

```
envi_file_query, b1_fid, nb=num_bands, ns=ns, nl=nl

input_file2 = dialog_pickfile(title='select mvalues file')
envi_open_file, input_file2, r_fid=b2_fid, /no_realize

;set up the dims, pos and fid arrays
dims=[-1L,0,ns-1,0,nl-1]
pos1=n_elements(lindgen(num_bands))
pos=lindgen(pos1,pos1)/pos1
fid=[b1_fid,b2_fid]
out_name='math_test'

;create an output fid array to hold each band processed
out_fid=lonarr(num_bands)

;the band math expression, RadCorr image X mvalues
expression='float(b1)*float(b2)'

;loop through each band and apply the equation
for i=0,num_bands-1 do begin
  envi_doit, 'math_doit', dims=dims, exp=expression, pos=pos[*,i],$
    fid=fid, r_fid=r_fid, /in_memory
    out_fid[i]=r_fid
endfor

;stack the output bands into one file
out_pos=lonarr(num_bands)
envi_doit, 'cf_doit', dims=dims, fid=out_fid, pos=out_pos, $

out_name='C:\Users\Jenn\Documents\IDL_Iceland\A071_00_105341\A071_00_P00_
105341LWACRGBRStarCal', r_fid=result_fid

end
```

Appendix II: Synthetic image endmember plots from Chapter 5

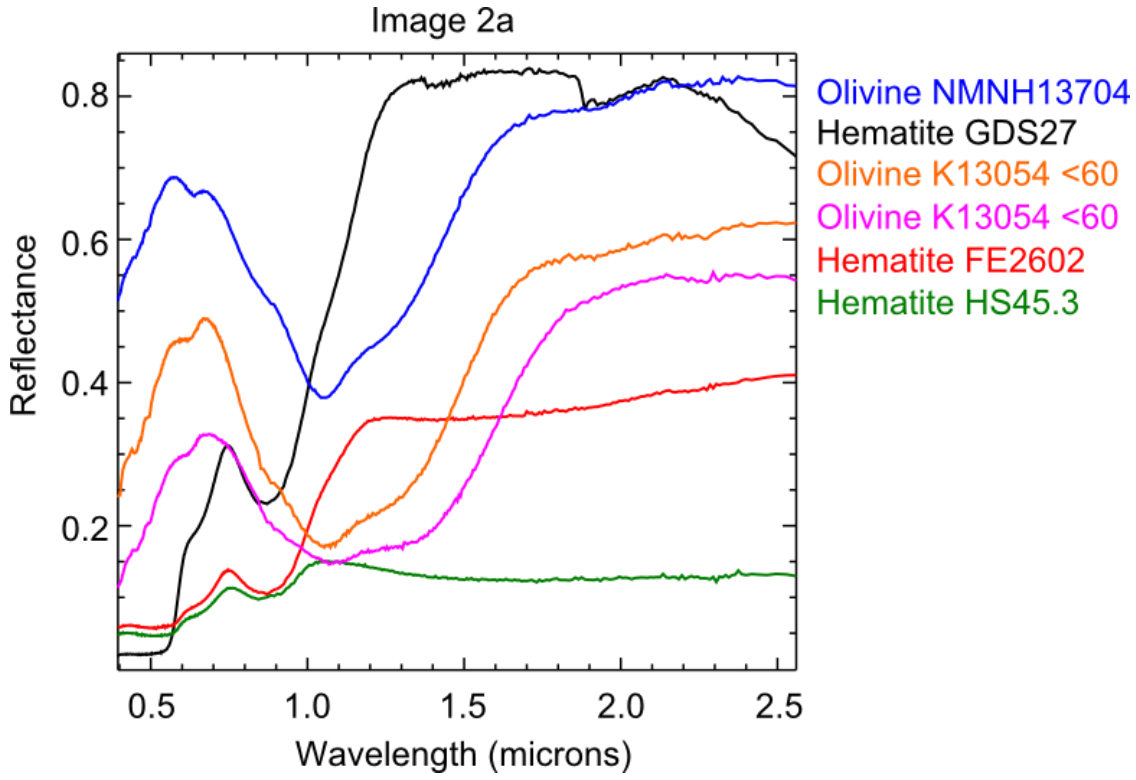

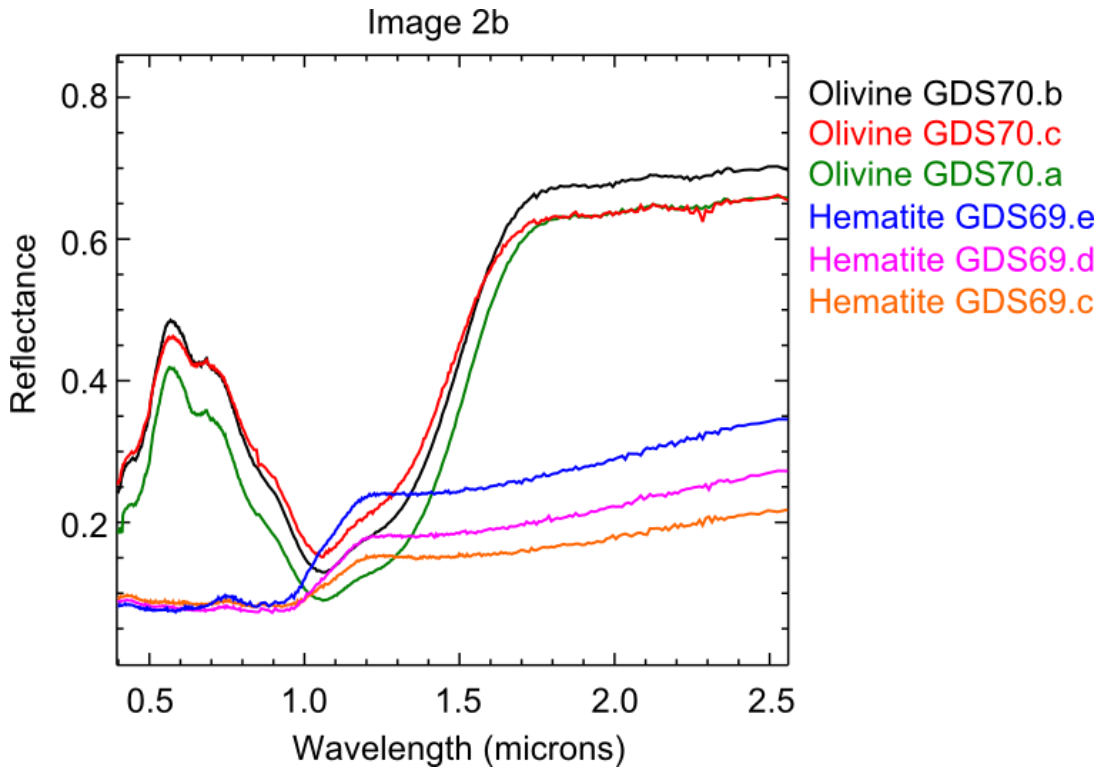

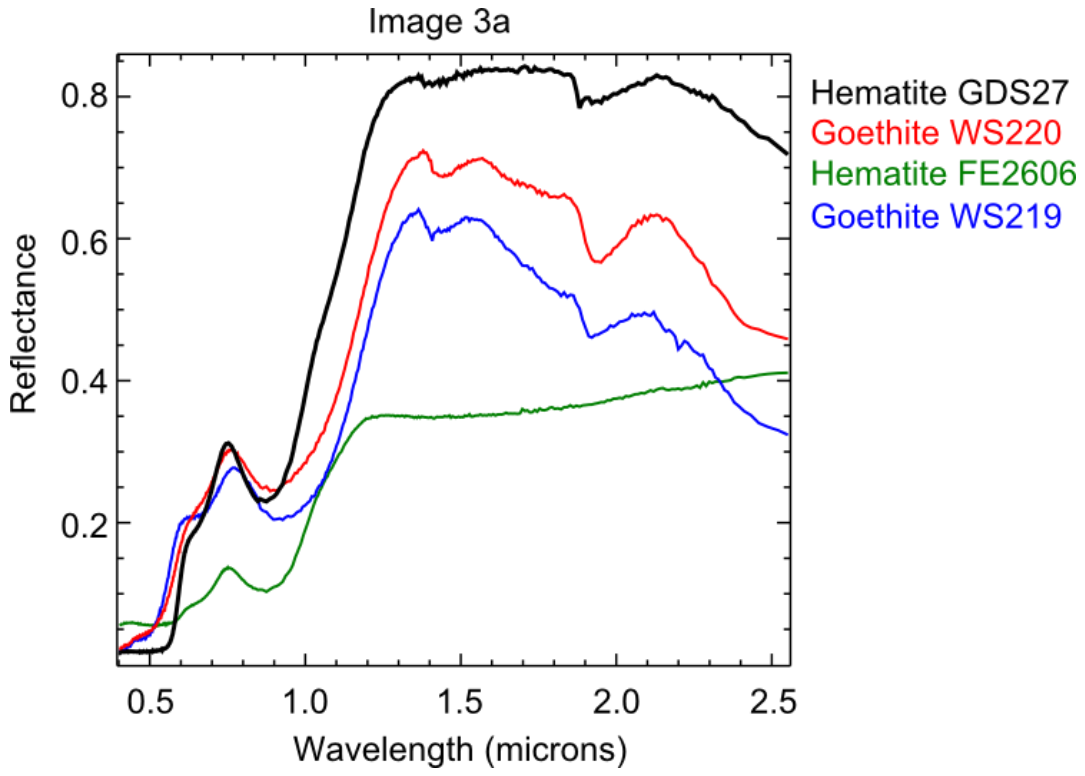
Image 3a
Reflectance
0.8
0.6
0.4
0.2
0.5
1.0
1.5
2.0
2.5
Wavelength (microns)
Hematite GDS27
Goethite WS220
Hematite FE2606
Goethite WS219

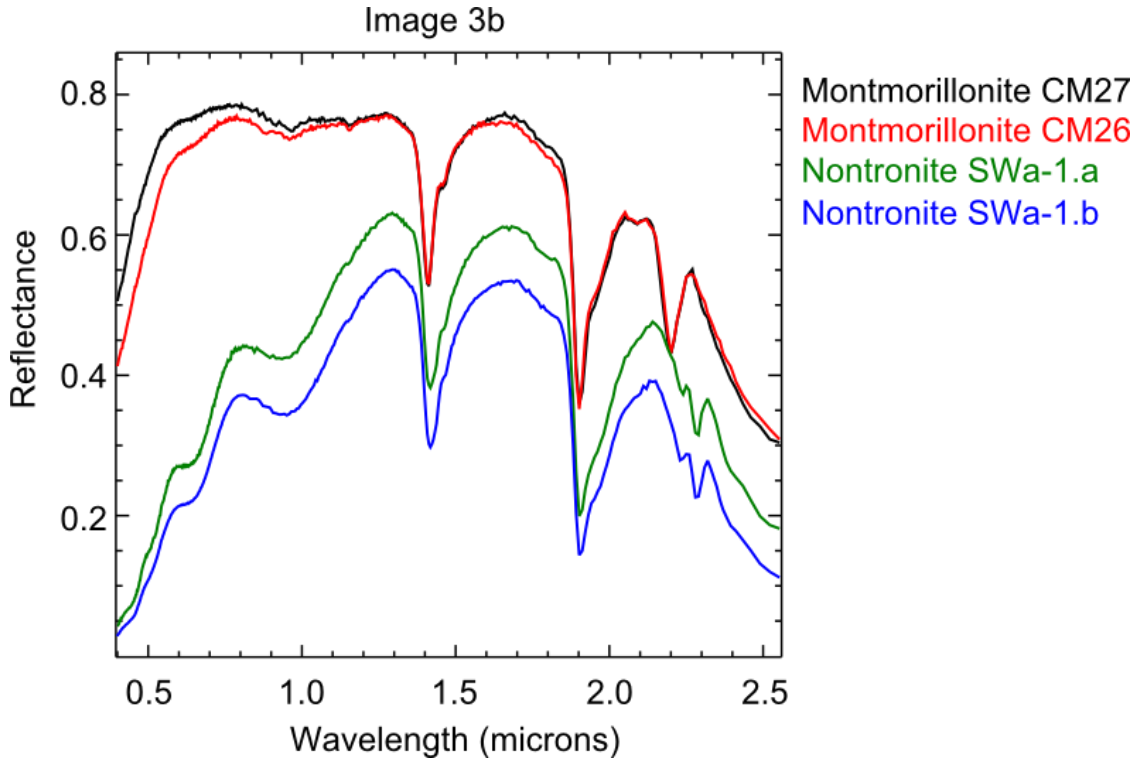
Image 3b
Reflectance
0.8
0.6
0.4
0.2
0.5
1.0
1.5
2.0
2.5
Wavelength (microns)
Montmorillonite CM27
Montmorillonite CM26
Nontronite SWa-1.a
Nontronite SWa-1.b

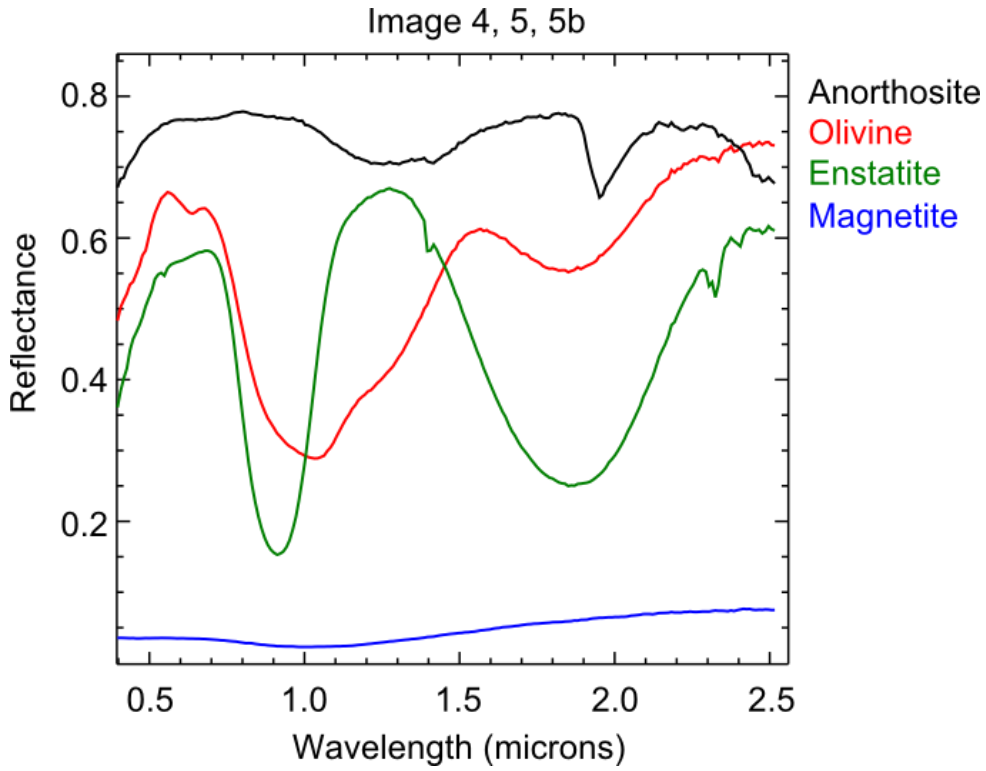
Image 4, 5, 5b
Reflectance
Wavelength (microns)
0.2
0.4
0.6
0.8
0.5
1.0
1.5
2.0
2.5
Anorthosite
Olivine
Enstatite
Magnetite

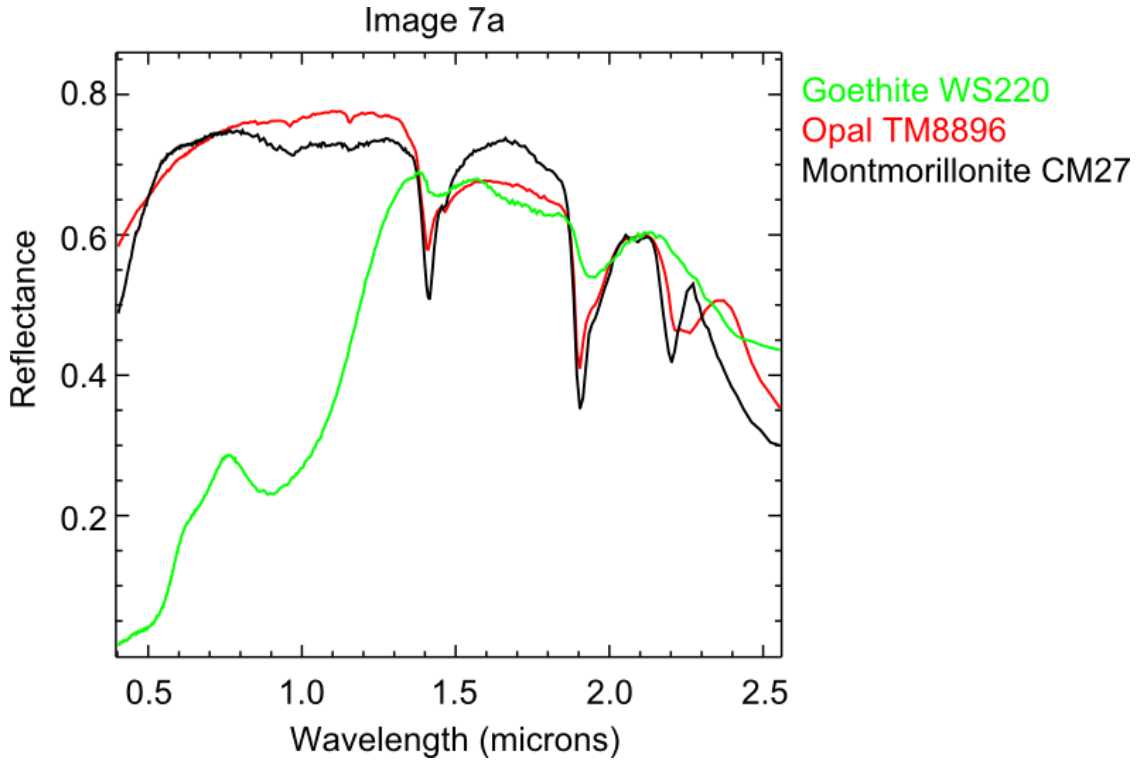
Image 7a
Reflectance
Wavelength (microns)
0.2
0.4
0.6
0.8
0.5
1.0
1.5
2.0
2.5
Goethite WS220
Opal TM8896
Montmorillonite CM27

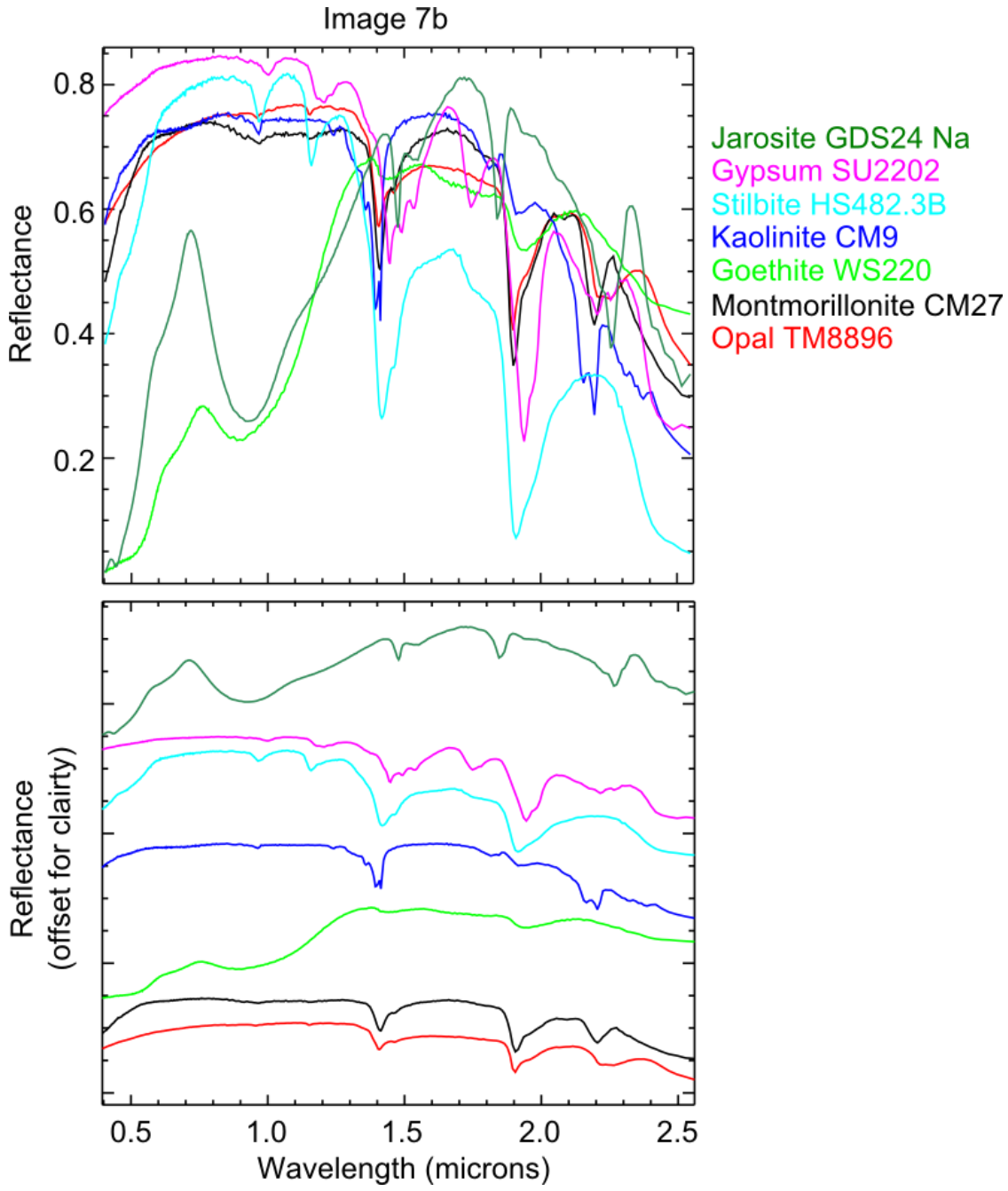
Image 7b
Reflectance
0.8
0.6
0.4
0.2
Jarosite GDS24 Na
Gypsum SU2202
Stilbite HS482.3B
Kaolinite CM9
Goethite WS220
Montmorillonite CM27
Opal TM8896
Reflectance
(offset for clairty)
0.5
1.0
1.5
2.0
2.5
Wavelength (microns)

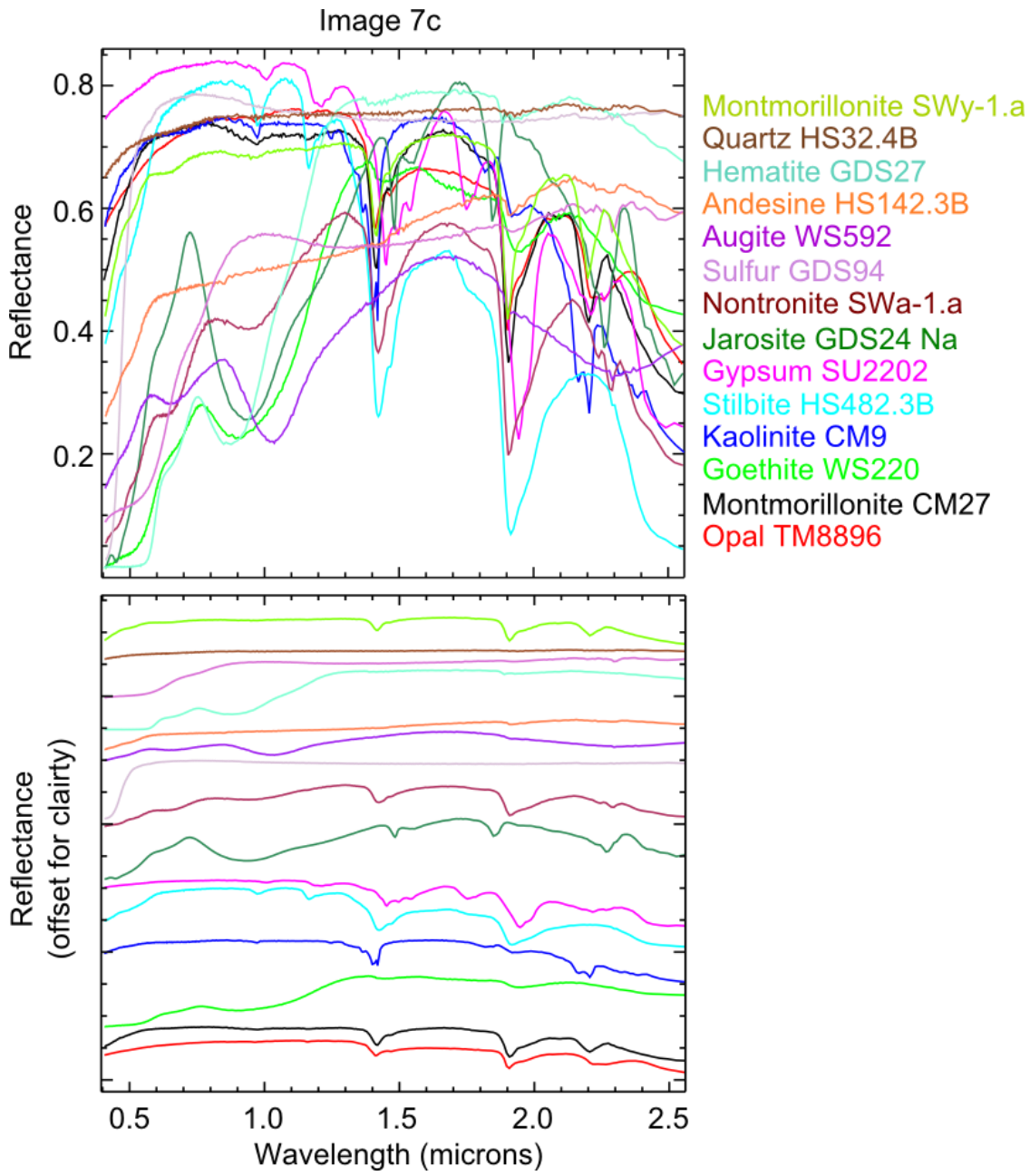
Image 7c
Reflectance
0.8
0.6
0.4
0.2
Reflectance
(offset for clairty)
0.5
1.0
1.5
2.0
2.5
Wavelength (microns)
Montmorillonite SWy-1.a
Quartz HS32.4B
Hematite GDS27
Andesine HS142.3B
Augite WS592
Sulfur GDS94
Nontronite SWa-1.a
Jarosite GDS24 Na
Gypsum SU2202
Stilbite HS482.3B
Kaolinite CM9
Goethite WS220
Montmorillonite CM27
Opal TM8896

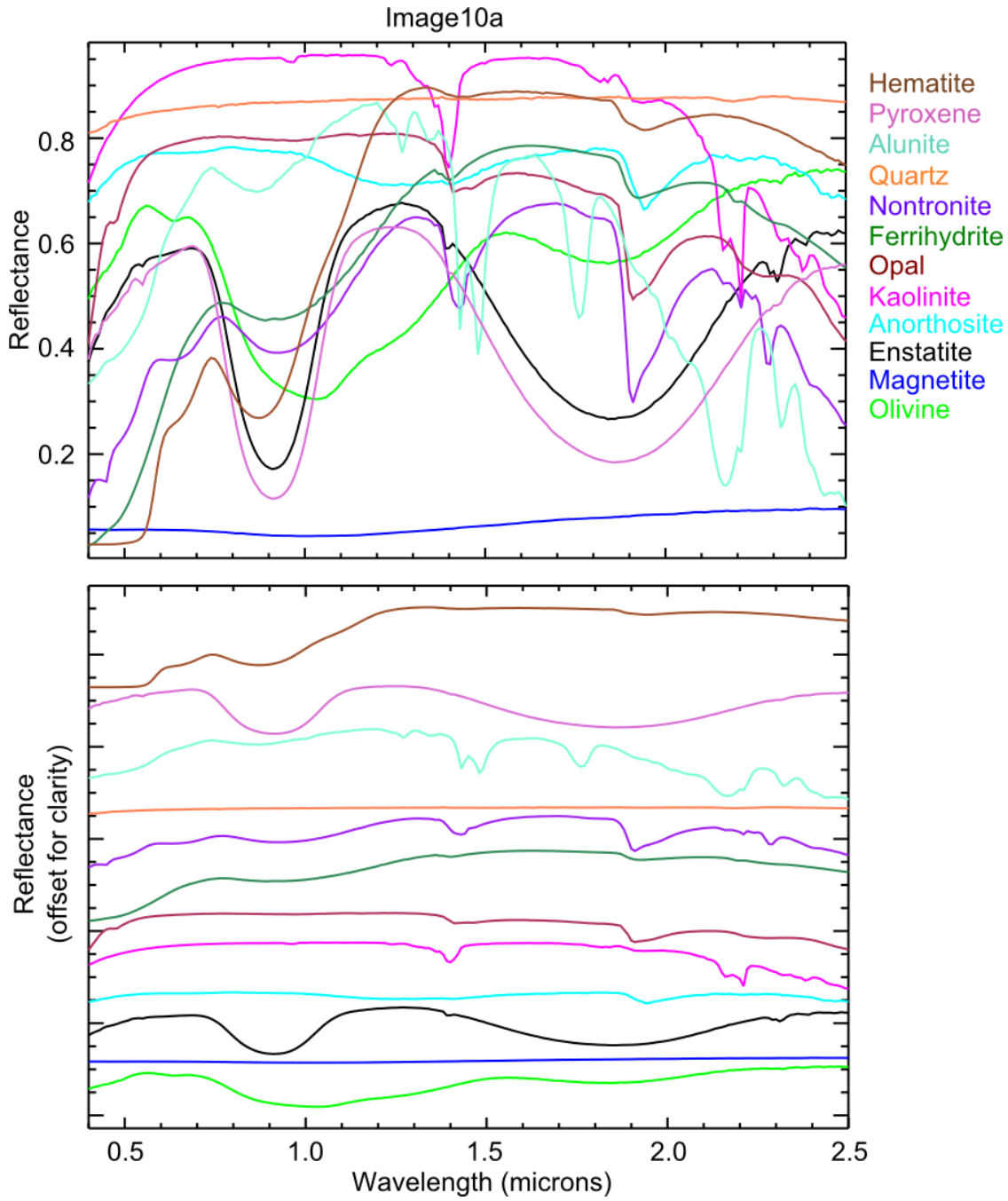
Image10a
Reflectance
0.8
0.6
0.4
0.2
Hematite
Pyroxene
Alunite
Quartz
Nontronite
Ferrihydrite
Opal
Kaolinite
Anorthosite
Enstatite
Magnetite
Olivine
Reflectance
(offset for clarity)
0.5
1.0
1.5
2.0
2.5
Wavelength (microns)

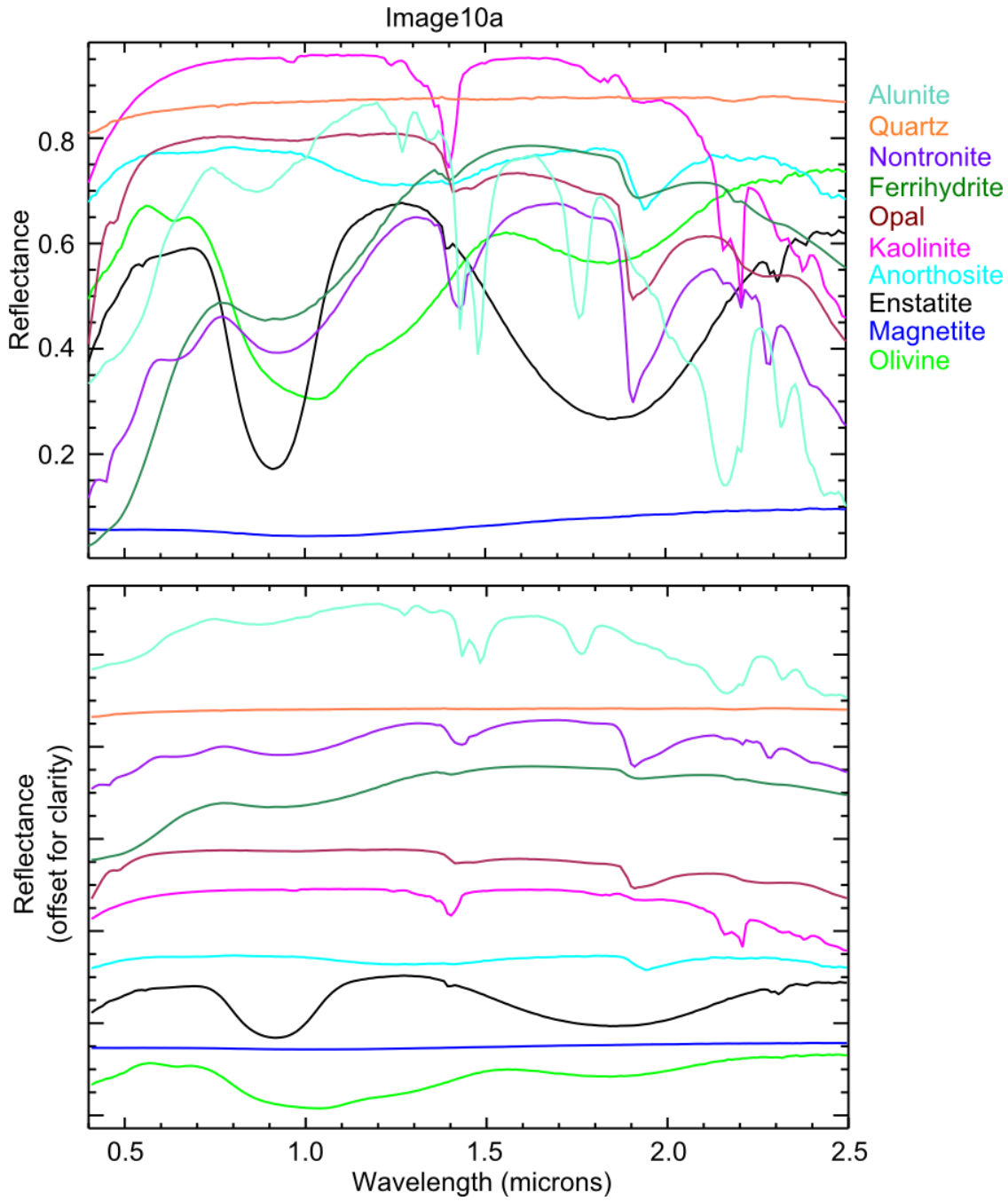
Image10a
Reflectance
0.8
0.6
0.4
0.2
Alunite
Quartz
Nontronite
Ferrihydrite
Opal
Kaolinite
Anorthosite
Enstatite
Magnetite
Olivine
Reflectance
(offset for clarity)
0.5
1.0
1.5
2.0
2.5
Wavelength (microns)

Appendix III: Matlab codes for EDA's from Chapter 5

ODM

1. Use estNoise.m from Bioucas-Dias HySIME code

2. white_transform.m

```
% code for step 2 of ODM, white noise data transformation, based on algorithm given
% in Andreou & Karathanassi 2014

% step 1 will use estNoise.m from HySIME

% Input:
%   Y is the sample matrix (LxN)
%   w is the noise estimates for every pixel (LxN) from estNoise
% Output:
%   T is the transformed whitened data (LxN)

function [T]=white_transform(Y,w,N)

% calculate the noise covariance matrix, can do this using hyperCov and the noise
% matrix w

Rn=hyperCov(w);

% now take orthogonal decomp of Rn to create Dn, an LxL matrix of the eigenvectors
% of Rn

[Dn,V]=eig(Rn);
F=Dn'*Y;   % equation (8)
W=F';  % W is now (NxL)

% now divide each row of W by the standard deviation of the noise for that band
% first create matrix of noise standard deviations along each band

sd=std(w,0,2);  % column vector of s.d. along each band (Lx1)

sd2=repmat(sd,1,N)';  % should create a (NxL) matrix with identical columns
Wn=W./sd2;    % equation (9)
Wnt=Wn';
Wntcov=hyperCov(Wnt);
[Dwnt,U]=eig(Wntcov);
T=Dwnt'*Wnt;   % equation (10)

return
```

3. ODM.m

```
% code for step 3 of ODM, Outlier Detection, based on algorithm given in
% Andreou & Karathanassi 2014

% Input
%     T = the transformed whitened data from step 2 (white_transform.m)
%     L = the number of bands used
% Output
%     p = number of endmembers
%     Er = standard deviations between transformed bands sorted in
%     descending order
%     ED2 = distances between standard deviations

function [p,Er,ED2]=ODM(T,L)

sd=std(T,0,2);
Er=sort(sd,'descend');

% calculate Euclidian distance between points in standard deviation vector

ED=zeros(1,(L-1));
for i=1:L-1
   ED(i)=Er(i,1)-Er((i+1),1);
end

ED2=sort(ED,'descend');

% calculate the quartiles and interquartile region for the distances
% between the standard deviations

Q=quantile(ED2,[0.25,0.5,0.75]);

 IQR=Q(3)-Q(1);

p=0;
for i=2:L
  if ED2(i-1)>(Q(3)+1.5*IQR)
     p=p+1;
   end
end

plot(ED2(1,1:30))

return
```

ELM

```
% My own ELM algorithm based on the paper "Empirical automatic estimation of the
% number of endmembers in hyperspectral images" by Luo, Chanussot, Doute and
% Zhang

function [H]=elm(y)

% algorithm needs to calculate both the covariance and correlation matrices of the
% input image matrix.  Both of these can be done using functions defined in the
% hyperspectral package 'hyperCov' and 'hyperCorr' respectively

% Input
%   y = signal matrix - a 2D matrix [L x n] where L is the number of bands and n the
% number of pixels.  So the spectral vectors are the columns.  % Output
%   H = estimate of number of endmembers

% General outline
% 1. input matrix x
% 2. calculate covariance matrix K
% 3. calculate correlation matrix R
% 4. calculate eigenvalues of K, called Ki
% 5. calculate eigenvalues of R, called Ri
% 6. calculate zi where zi = Ri - Ki
% 7. calculate si^2 where si^2 = (2/n)(Ri^2+Ki^2) and is the s.d. of the unknown mean
of the % zi distribution
% 8. A(i) = -sum[l=i to n]([zl^2]/2*sl^2)
% 9. B(i) = -sum[l=i to n](log[sl])
% 10. calculate H = A(i) + B(i)
% 11. calculate Nc = arg max[H]-1 but actually want the eigenvalue index position of
% the first local maximum which appears to be inputable as
% [row,col]=find(H==max(H(:))) and then it % is the col value that I want to use

[L,N]=size(y); % read in with spectra as columns and bands as rows
K=hyperCov(y);
R=hyperCorr(y);
[E,D]=svd(K); % calculating eigenvectors and values of covariance
Ki=diag(D);
[F,G]=svd(R); % calculating eigenvectors and values of correlation
Ri=diag(G);
zi=Ri-Ki;
si2=(2/L)*(Ri.^2+Ki.^2);
si=sqrt(si2);
zi=zi';
si=si';
si2=si2'; % necessary because Matlab performs these things as row-wise operations.

A=zeros(1,L); % place holder for output
 for i=1:L
    A(i)=-sum((zi(i)^2)/(2*si2(i)));
 end

B=zeros(1,L);
```

```
 for i=1:L
   B(i)=-sum(log(si(i)));
 end

H=A+B;

plot(H(1,1:30)) % plot the first 20 values of H to visualise first maxima

return
```

Appendix IV: Tables listing results of all SMA synthetic image tests

EDA

Tables giving results for each synthetic image and each set of initial criteria.

HFC was set to run with 3 different vectors of false alarm probability ($\alpha = 10^{-3}, 10^{-4}, 10^{-5}$) and hence are reported with 3 values each time.

ELM returns a plot that must be interpreted, in the majority of cases at least one spike was seen in the plot before the global maximum was reached, these spikes are the additional values, the global maximum is the final p estimate from this algorithm. These spikes are discussed in the algorithms description paper and are therefore not an error in the code presented in this work.

ODM returns both a plot and a final p value. The p value (as was discussed in Chapter 5) was consistently overestimating the correct p value whilst for simple datasets the plot was returning the correct values. In these tables it is only the plot value that is quoted, in some of the more complex images this value was ambiguous and so multiple potential p estimates are reported.

Where no value is recorded no value was returned by the algorithm in question.

Image 2a (6 endmembers, 2 minerals, different samples, N=8100)

ELM

SNR	Linear, RR, max a = 1.0	Linear, SSA, max a = 1.0	Linear, RR, max a = 0.8	Linear, SSA, max a = 0.8
15dB	2,6	1,5	2,5	4
25dB	2,4,6	1,6	2,4,6	3,5
35dB	2,4,6	1,6	2,4,6	3,7
45dB	2,4,6	1,6	2,4,6	6,8,11
55dB	2,4,6	1,6	2,4,6	6,11,15

HySIME

SNR	Linear, RR, max a = 1.0	Linear, SSA, max a = 1.0	Linear, RR, max a = 0.8	Linear, SSA, max a = 0.8
15dB	5	5	5	5
25dB	6	6	6	6
35dB	6	6	6	8
45dB	6	6	6	11
55dB	6	6	6	11

HFC

SNR	Linear, RR, max a = 1.0	Linear, SSA, max a = 1.0	Linear, RR, max a = 0.8	Linear, SSA, max a = 0.8
15dB	5,4,4	5,5,5	4,4,3	4,4,4
25dB	5,4,4	5,5,5	5,5,4	5,5,5
35dB	5,4,4	5,4,4	5,4,4	6,6,6
45dB	5,4,4	5,5,4	5,4,4	10,10,10
55dB	5,5,4	5,5,5	5,4,4	14,14,14

ODM

SNR	Linear, RR, max a = 1.0	Linear, SSA, max a = 1.0	Linear, RR, max a = 0.8	Linear, SSA, max a = 0.8
15dB	6	4	6	3
25dB	6	5	6	5
35dB	6	7	6	5
45dB	6	8	6	8
55dB	6	8	6	8

Image 2b (6 endmembers, 2 minerals, same samples different sizings, N=8100, max purity 100%)

ELM

SNR	Linear, RR, max a = 1.0	Linear, SSA, max a = 1.0	Linear, RR, max a = 0.8	Linear, SSA, max a = 0.8
15dB	2,4	2,4	3	2
25dB	2,4	2,4	2,4	2,4
35dB	2,4,6	2,4,6	2,4,6	2,4,6
45dB	2,4,6	2,4,6	2,4,6	2,4,6
55dB	2,4,6	2,4,6	2,4,6	2,4,6

HySIME

SNR	Linear, RR, max a = 1.0	Linear, SSA, max a = 1.0	Linear, RR, max a = 0.8	Linear, SSA, max a = 0.8
15dB	3	3	3	3
25dB	5	5	4	5
35dB	6	6	6	6
45dB	6	6	6	8
55dB	6	6	6	9

HFC

SNR	Linear, RR, max a = 1.0	Linear, SSA, max a = 1.0	Linear, RR, max a = 0.8	Linear, SSA, max a = 0.8
15dB	3,3,3	3,3,3	2,2,2	3,3,3
25dB	3,3,3	4,4,4	3,3,3	4,4,4
35dB	4,4,4	5,5,5	4,4,4	7,6,6
45dB	4,4,4	5,5,5	4,4,4	7,7,7
55dB	4,4,4	5,5,5	4,4,4	9,9,9

ODM

SNR	Linear, RR, max a = 1.0	Linear, SSA, max a = 1.0	Linear, RR, max a = 0.8	Linear, SSA, max a = 0.8
15dB	4	3	4	2
25dB	4	4	4	4
35dB	3	5	5	4
45dB	3	7	5	4
55dB	3	7	5	4

Image 3a (4 endmembers, 2 minerals, same samples different sizings, N=8100)

ELM

SNR	Linear, RR, max a = 1.0	Linear, SSA, max a = 1.0	Linear, RR, max a = 0.8	Linear, SSA, max a = 0.8
15dB	2,4	1,3	1,3	1,3
25dB	1,4	1,4	1,4	1,4
35dB	1,4	1,4	1,4	1,4
45dB	1,4	1,4	1,4	2,4,6
55dB	1,4	1,4	1,4	1,4,7

HySIME

SNR	Linear, RR, max a = 1.0	Linear, SSA, max a = 1.0	Linear, RR, max a = 0.8	Linear, SSA, max a = 0.8
15dB	4	3	3	3
25dB	4	4	4	4
35dB	4	4	4	5
45dB	4	4	4	6
55dB	4	4	4	7

HFC

SNR	Linear, RR, max a = 1.0	Linear, SSA, max a = 1.0	Linear, RR, max a = 0.8	Linear, SSA, max a = 0.8
15dB	3,3,3	3,3,3	2,2,2	5,3,3
25dB	3,3,3	3,3,3	3,3,3	3,3,3
35dB	3,3,3	3,3,3	3,3,3	4,4,4
45dB	3,3,3	3,3,3	3,3,3	8,6,5
55dB	3,3,3	3,3,3	3,3,3	11,9,7

ODM

SNR	Linear, RR, max a = 1.0	Linear, SSA, max a = 1.0	Linear, RR, max a = 0.8	Linear, SSA, max a = 0.8
15dB	3,4	3	3	5
25dB	4	3	4	3
35dB	4	4	4	4
45dB	4	5	4	4
55dB	4	7	4	4,7

Image 3b (4 endmembers, 2 minerals, same samples different sizings, N=8100)

ELM

SNR	Linear, RR, max a = 1.0	Linear, SSA, max a = 1.0	Linear, RR, max a = 0.8	Linear, SSA, max a = 0.8
15dB	3	2	2	2
25dB	2,4	2,4	4	3
35dB	2,4	2,4	2,4	2,4
45dB	2,4	2,4	2,4	2,5
55dB	2,4	2,4	2,4	2,7

HySIME

SNR	Linear, RR, max a = 1.0	Linear, SSA, max a = 1.0	Linear, RR, max a = 0.8	Linear, SSA, max a = 0.8
15dB	3	2	2	2
25dB	4	4	4	4
35dB	4	4	4	5
45dB	4	4	4	5
55dB	4	4	4	5

HFC

SNR	Linear, RR, max a = 1.0	Linear, SSA, max a = 1.0	Linear, RR, max a = 0.8	Linear, SSA, max a = 0.8
15dB	3,3,3	3,3,3	2,2,2	2,2,2
25dB	4,4,4	4,4,4	4,4,4	4,4,4
35dB	4,4,4	4,4,4	4,4,4	5,4,4
45dB	4,4,4	4,4,4	4,4,4	6,6,6
55dB	4,4,4	4,4,4	4,4,4	7,7,7

ODM

SNR	Linear, RR, max a = 1.0	Linear, SSA, max a = 1.0	Linear, RR, max a = 0.8	Linear, SSA, max a = 0.8
15dB	3	2	3	2
25dB	4	3	4	3
35dB	4	4	4	5
45dB	4	5	4	5
55dB	4	5	4	5

Image 4 (4 endmembers, 16 nonlinear mixtures, N=8096)

ELM

SNR	RR	SSA
15dB	1	1,3
25dB	1,6	1,4
35dB	1,7	1,5
45dB	1,7,16	1,5,7
55dB	1,7,16	1,5,7,11

HySIME

SNR	RR	SSA
15dB	3	4
25dB	5	4
35dB	7	5
45dB	11	9
55dB	15	14

HFC

SNR	RR	SSA
15dB	2,1,1	2,2,2
25dB	4,4,4	3,3,3
35dB	5,5,5	4,4,4
45dB	10,9,9	6,6,6
55dB	11,11,11	11,11,10

ODM

SNR	RR	SSA
15dB	4	4
25dB	4	4
35dB	4	4
45dB	4	4
55dB	4	4

Image 5 (4 endmembers, nonlinear then linear mixtures N=8096)

ELM

SNR	RR, max a = 0.8	SSA, max a = 0.8
15dB	1	1,3
25dB	1,5	1,4
35dB	1,7	1,4,6
45dB	1,7	1,7,9
55dB	1,7,16	1,7,9,11,16

HySIME

SNR	RR, max a = 0.8	SSA, max a = 0.8
15dB	3	3
25dB	5	5
35dB	6	7
45dB	9	8
55dB	13	9

HFC

SNR	RR, max a = 0.8	SSA, max a = 0.8
15dB	1,1,1	2,2,2
25dB	3,3,3	3,3,3
35dB	5,5,5	5,5,5
45dB	9,8,7	6,6,6
55dB	11,11,11	12,11,11

ODM

SNR	RR, max a = 0.8	SSA, max a = 0.8
15dB	4	4
25dB	4	4
35dB	4	4
45dB	4	4
55dB	4	4

Image 7a, b, c (N=8100, white noise, max a = 0.8, varying number of endmembers)

ELM

SNR	Linear 3	Linear 7	Linear 15
15dB	3	2,7	2,5,8,11 (all v. small after 1st)
25dB	3	2,5,7	2,5,11,14 (all v. small after 1st)
35dB	3	2,5,7	2,5,12,15
45dB	3	2,5,7	2,12,15
55dB	3	2,5,7	2,12,15

HySIME

SNR	Linear 3	Linear 7	Linear 15
15dB	3	7	10
25dB	3	7	13
35dB	3	7	15
45dB	3	7	15
55dB	3	7	15

HFC

SNR	Linear 3	Linear 7	Linear 15
15dB	3,3,3	7,7,7	9,7,7
25dB	3,3,3	7,7,7	12,12,11
35dB	3,3,3	7,7,7	13,13,13
45dB	3,3,3	7,7,7	13,13,13
55dB	3,3,3	7,7,7	13,13,13

ODM

SNR	Linear 3	Linear 7	Linear 15
15dB	3	7	8
25dB	3	7	7,14
35dB	3	7	8,15
45dB	3	7	8,15
55dB	3	7	7,15

Image 7a (p=3, white noise)

ELM

SNR	Linear 10000	Linear 5000	Linear 1000
15dB	3	3	3
25dB	3	3	3
35dB	3	3	3
45dB	3	3	3
55dB	3	3	3

HySIME

SNR	Linear 10000	Linear 5000	Linear 1000
15dB	3	3	130
25dB	3	3	132
35dB	3	3	115
45dB	3	3	51
55dB	3	3	3

HFC

SNR	Linear 10000	Linear 5000	Linear 1000
15dB	3,3,3	3,3,3	3,3,3
25dB	3,3,3	3,3,3	3,3,3
35dB	3,3,3	3,3,3	3,3,3
45dB	3,3,3	3,3,3	3,3,3
55dB	3,3,3	3,3,3	3,3,3

ODM

SNR	Linear 10000	Linear 5000	Linear 1000
15dB	3	3	3
25dB	3	3	3
35dB	3	3	3
45dB	3	3	3
55dB	3	3	3

Image 10a (p=12, white noise, 23 nonlinear RELAB spectra, L=211)

HySIME

SNR	RR, Non-linear only, N=290	RR, Linear mix, N=290	RR, Non-linear only, N=8700	RR, Linear mix, N=8700	SSA, Non-linear only, N=8700	SSA Linear mix, N=8700
15dB	124	132	6	6	6	6
25dB	127	128	9	8	8	9
35dB	121	117	13	11	9	14
45dB	70	71	16	14	12	17
55dB	20	17	19	16	13	18

ODM

SNR	RR, Non-linear only, N=290	RR, Linear mix, N=290	RR, Non-linear only, N=8700	RR, Linear mix, N=8700	SSA, Non-linear only, N=8700	SSA Linear mix, N=8700
15dB	7,12	5,9	10	9	5,9	5,7
25dB	10,12	8,12	11	10	7,9	7
35dB	12	10	13	12	10	12
45dB	11,15	10,12,15	13	13	11	16
55dB	10,15	12,16	14	14	11	15

HFC

SNR	RR, Non-linear only, N=290	RR, Linear mix, N=290	RR, Non-linear only, N=8700	RR, Linear mix, N=8700
15dB	-	1,1,1	-	3,3,3
25dB	-	1,1,1	-	3,3,3
35dB	-	1,1,1	-	3,3,3
45dB	-	1,1,1	-	6,5,5
55dB	-	1,1,1	-	8,6,6

ELM

SNR	RR, Non-linear only, N=290	RR, Linear mix, N=290	RR, Non-linear only, N=8700	RR, Linear mix, N=8700
15dB	-	3	-	4
25dB	-	6	-	6
35dB	-	9	-	8
45dB	-	10	-	13
55dB	-	14	-	16

EEA

The following tables give the SAM value results of the four Endmember Extraction Algorithm extracted spectra compared to the real endmember spectra. Where no value is noted the algorithm returned either no endmembers or they were so unlike the real endmembers that the SAM value was not calculated. The smallest SAM value for each set is highlighted in bold. Any misidentified extracted endmembers are noted where found.

Image 2a (6 endmembers, 2 minerals, diff samples, RR, p=6, max a = 1.0)

SNR	SISAL	VCA	RMVES	ICE
15db	N/A	**0.036717**	0.134117	N/A
25dB	0.330383	**0.012683**	0.090033	0.17965
35dB	0.058367	**0.003617**	0.1282	0.211783
45dB	0.017167	**0.002241**	0.084489	0.1466
55dB	0.004617	**0.000281**	0.005207	0.185633

Image 2a (6 endmembers, 2 minerals, diff samples, RR, p=6, max a = 0.8)

SNR	SISAL	VCA	RMVES	ICE
15db	0.2334[a]	**0.07573**	0.09617	N/A
25dB	0.18108	0.0664	**0.0468**	N/A
35dB	0.0455	0.06658	**0.02067**	N/A
45dB	0.01168	0.07432	**0.00695**	N/A
55dB	**0.00174**	0.08027	0.00707	0.21415
[a]3 mismatched endmembers				

Image 2b (6 endmembers, 2 minerals, diff particle sizings, RR, p=6, max a = 1.0)

SNR	SISAL	VCA	RMVES	ICE
15db	N/A	**0.057333**	0.1905	N/A
25dB	0.541317	**0.076017**[a]	0.221017	0.144967[b]
35dB	0.484917	**0.022733**	0.1064	0.1151
45dB	0.1459	**0.003754**	0.078428	0.045083[b]
55dB	0.028317	**0.000329**	0.082976	0.16325
[a]matches 4 hematite and 2 olivine [b]matches 2 hematite and 4 olivine				

Image 2b (6 endmembers, 2 minerals, diff particle sizings, RR, p=6, max a = 0.8)

SNR	SISAL	VCA	RMVES	ICE
15db	N/A	0.09197[a]	**0.09375**	N/A
25dB	0.1894[a]	**0.06898**	0.26805[b]	N/A
35dB	0.28328	0.09055[a]	**0.01908**	N/A
45dB	0.07942	0.04592	**0.0139**	N/A
55dB	0.01663	0.02727	**0.00943**	N/A
[a]1 misidentification [b]3 misidentifications				

Image 3a (4 endmembers, 2 minerals, diff particle sizings, RR, p=4, max a = 1.0)

SNR	SISAL	VCA	RMVES	ICE
15db	0.22655	**0.03395**	0.0439	N/A
25dB	0.11465	**0.00955**	0.02225	0.10195
35dB	0.02565	**0.002725**	0.048697	0.089975
45dB	0.005816	**0.000657**	0.048717	0.053825
55dB	0.001541	**0.000245**	0.003072	0.023875

Image 3a (4 endmembers, 2 minerals, diff particle sizings, RR, p=4, max a = 0.8)

SNR	SISAL	VCA	RMVES	ICE
15db	0.10633	**0.02393**	0.03545	N/A
25dB	0.04983	**0.02468**	0.07758	N/A
35dB	**0.01303**	0.03095	0.04475	0.07948
45dB	**0.00429**	0.02708	0.00642	0.06513
55dB	**0.00102**	0.03095	0.00268	0.06868

Image 3b (4 endmembers, 2 minerals, diff particle sizings, RR, p=4, max a = 1.0)

SNR	SISAL	VCA	RMVES	ICE
15db	0.251725	**0.0348**	0.1104	N/A
25dB	0.249925	0.08565	**0.064975**	0.078775
35dB	0.07865	**0.002825**	0.007	0.10595
45dB	0.0205	**0.002278**	0.0458	0.0853
55dB	0.005475	**0.000221**	0.006459	0.054825

Image 3b (4 endmembers, 2 minerals, diff particle sizings, RR, p=4, max a = 0.8)

SNR	SISAL	VCA	RMVES	ICE
15db	0.16595	**0.07415**	0.13838	N/A
25dB	0.1367	0.08163[a]	**0.03808**	0.12505
35dB	0.04928	**0.0228**	0.03365	0.13413
45dB	**0.01025**	0.03598	0.05835	0.1383
55dB	**0.00176**	0.04115	0.02383	0.10583
[a]2 misidentifications				

Image 5 (4 endmembers, 4 minerals, 16 nonlinear mixtures linearly mixed, RR, p=4, max a = 1.0)

SNR	SISAL	VCA	RMVES	ICE
15db	0.593075	**0.071975**	N/A	N/A
25dB	0.06145	0.086725	0.068575	0.1787
35dB	**0.059375**	0.074575	0.0961	0.130375
45dB	**0.060175**	0.104725	0.080325	0.157625
55dB	**0.060275**	0.06855	0.161825	N/A

Image 5 (4 endmembers, 4 minerals, 16 nonlinear mixtures linearly mixed, SSA, p=4, max a = 1.0)

SNR	SISAL	VCA	RMVES	ICE
15db	N/A	N/A	**0.19643**	N/A
25dB	N/A	0.12168	**0.05283**	0.16945
35dB	N/A	**0.08798**	0.10703	0.136
45dB	N/A	**0.06558**	0.08555	N/A
55dB	N/A	0.08288	**0.0545**	0.12358

Image 5 (4 endmembers, 4 minerals, 16 nonlinear mixtures linearly mixed, RR, p=4, max a = 0.8)

SNR	SISAL	VCA[a]	RMVES	ICE[a]
15db	**0.08368**	0.13388	N/A	N/A
25dB	**0.09603**	0.12305	0.09855	0.17618
35dB	**0.09565**	0.1352	0.09718	0.17873
45dB	**0.08895**	0.1151	0.09468	0.16378
55dB	0.09205	0.11728	**0.08778**	0.16635
[a]All endmembers poor visual matches – misidentifications				

Image 5 (4 endmembers, 4 minerals, 16 nonlinear mixtures linearly mixed, SSA, p=4, max a = 0.8)

SNR	SISAL	VCA	RMVES	ICE
15db	N/A	**0.14318**	0.15095	N/A
25dB	0.15323	0.1343	**0.11113**	N/A
35dB	**0.09523**	0.13348	0.09778	N/A
45dB	**0.09195**	0.12655	0.09248	N/A
55dB	0.0931	0.12883	**0.0855**	N/A

Image 7a, b, c (RR, linear mix) – ICE was not tested by this point as it had been consistently returning the worst results of the four algorithms

SISAL

SNR	p=3 (max a = 1.0)	p=3 (max a = 0.8)	p=7 (max a = 1.0)	p=7 (max a = 0.8)	p=15 (max a = 1.0)	p=15 (max a = 0.8)
15db	0.22393	0.1418	N/A	N/A	N/A	N/A
25dB	0.09793	0.04077	0.14946	0.09663[a]	N/A	0.33174[b]
35dB	0.02317	0.0304	0.05914	0.02873	N/A	**0.12724**
45dB	0.00508	**0.00494**	0.01566	**0.00851**	0.08921	0.04612
55dB	0.00126	**0.00198**	0.00471	**0.00211**	0.03235	**0.01723**

[a]1 misidentification
[b]6 misidentifications

VCA

SNR	p=3 (max a = 1.0)	p=3 (max a = 0.8)	p=7 (max a = 1.0)	p=7 (max a = 0.8)	p=15 (max a = 1.0)	p=15 (max a = 0.8)
15db	0.02673	0.07703	**0.03671**	**0.08194**	N/A	N/A
25dB	**0.00813**	0.08443	**0.0111**	0.05213	**0.02875[a]**	0.17448[b]
35dB	**0.00223**	0.0894	**0.00289**	0.0924[a]	**0.00904**	N/A
45dB	**0.00076**	0.08143	**0.00088**	0.05951	**0.00265**	0.15639
55dB	**0.000136**	0.08597	**0.00023**	0.07141	**0.000895**	0.13221

[a]1 misidentification
[b]5 misidentifications

RMVES

SNR	p=3 (max a = 1.0)	p=3 (max a = 0.8)	p=7 (max a = 1.0)	p=7 (max a = 0.8)	p=15 (max a = 1.0)	p=15 (max a = 0.8)
15db	**0.02057**	**0.02217**	N/A	0.143071	N/A	N/A
25dB	0.021	**0.02727**	0.03547	**0.0227**	N/A	**0.15989[a]**
35dB	0.02244	**0.0091**	0.01393	**0.022957**	N/A	0.16361[b]
45dB	0.0117	0.07873	0.00857	0.011814	N/A	**0.03595**
55dB	0.00956	0.01443	0.00613	0.004386	0.041587[c]	**0.01743**

[a]5 misidentifications
[b]3 misidentifications
[c]2 misidentifications

Image 8 (3 endmembers, 3 minerals, RR, varying N, max a = 0.8) – ICE was not tested by this point as it had been consistently returning the worst results of the four algorithms

SISAL

SNR	N=10000	N=5000	N=1000
15db	0.05713	0.05277	0.04377
25dB	0.03157	0.02333	0.0232
35dB	0.0144	0.0055	0.00333
45dB	**0.0007**	0.00594	0.00767
55dB	**0.00067**	0.00103	0.00377

VCA

SNR	N=10000	N=5000	N=1000
15db	0.06957	0.06297	0.0829
25dB	0.08023	0.08	0.10987
35dB	0.0887	0.0826	0.08133
45dB	0.0826	0.0839	0.11183
55dB	0.08403	0.0891	0.08187

RMVES

SNR	N=10000	N=5000	N=1000
15db	**0.025**	0.039267	0.0369
25dB	**0.0146**	0.0611	0.0084
35dB	0.016333	0.0194	0.011767
45dB	0.01283	0.020933	0.0074
55dB	0.004586	0.002105	0.003833

Image 10a (12 endmembers, 12 minerals, varying N, max a = 0.8) – ICE was not tested by this point as it had been consistently returning the worst results of the four algorithms

SISAL

SNR	N=8700	N=290
15db	N/A	N/A
25dB	N/A	N/A
35dB	0.1958[a]	**0.18048[a]**
45dB	**0.13743[b]**	**0.12408[a]**
55dB	**0.14503[a]**	**0.15991[a]**
[a]2 misidentifications [b]3 misidentifications		

VCA

SNR	N=8700	N=290
15db	-	-
25dB	-	-
35dB	-	-
45dB	-	-
55dB	-	-

RMVES

SNR	N=8700	N=290
15db	N/A	N/A
25dB	**0.183449[a]**	N/A
35dB	**0.184113[b]**	0.187685[c]
45dB	0.157573[b]	0.160202[a]
55dB	0.155374[a]	0.170186[c]
[a]3 misidentifications [b]2 misidentifications [c]7 misidentifications		

Image 10b (10 endmembers, 10 minerals, max a = 0.8) – ICE was not tested by this point as it had been consistently returning the worst results of the four algorithms and nor was VCA which had been shown by now to return poor results for non-linear mixtures

SNR	**SISAL**	**RMVES**
35	0.08494[a]	0.187102[b]
45	0.091044[a]	0.175820[c]
55	0.09389[a]	0.092345[a]
[a]1 misidentification [b]6 misidentifications [c]4 misidentifications		

AEA

The following tables contain the average maximum individual pixel percentage abundance error for each of the synthetic images tested against the FCLLS using both RR and SSA version (where appropriate) of the pure endmembers, the SISAL and the RMVES endmembers.

Image 2a (6 endmembers, 2 minerals, diff samples, RR, p=6, max a = 0.8)

SNR	Pure endmembers	SISAL	SISAL (normalised)
25	0.10791	0.20500	0.22088
35	0.03558	0.07187	0.16198
45	0.01180	0.02022	N/A
55	0.00360	0.00436	N/A

Image 2a (6 endmembers, 2 minerals, diff samples, SSA, p=6, max a = 0.8)

SNR	Pure endmembers	SISAL	SISAL (normalised)
25	0.12916	0.21941	0.23234
35	0.07874	0.10378	0.18518
45	0.07490	0.07892	N/A
55	0.07743	0.07739	N/A

Image 2b (6 endmembers, 2 minerals, same samples, diff particle sizes, RR, p=6, max a = 0.8)

SNR	Pure endmembers	SISAL	SISAL (normalised)
25	0.40213	0.54764	0.58461
35	0.17301	0.28690	0.49756
45	0.06116	0.12003	N/A
55	0.01953	0.03746	N/A

Image 2b (6 endmembers, 2 minerals, same samples, diff particle sizes, RR, p=6, max a = 0.8) this time combining same mineral abundances

SNR	Pure endmembers	SISAL	SISAL (normalised)
25	0.02078	0.08108	0.09507
35	0.00896	0.05858	0.08843
45	0.00327	0.03620	N/A
55	0.00102	0.01132	N/A

Image 3a (4 endmembers, 2 minerals, same samples, diff particle sizes, RR, p=4, max a = 0.8)

SNR	Pure endmembers	SISAL	SISAL (normalised)
25	0.21075	0.24276	N/A
35	0.06051	0.09692	N/A
45	0.02251	0.03096	N/A
55	0.00644	0.00806	N/A

Image 3a (4 endmembers, 2 minerals, same samples, diff particle sizes, RR, p=4, max a = 0.8) this time combining same mineral abundances

SNR	Pure endmembers	SISAL	SISAL (normalised)
25	0.05598	0.10456	N/A
35	0.01794	0.06398	N/A
45	0.00658	0.01883	N/A
55	0.00186	0.00402	N/A

Image 3a (4 endmembers, 2 minerals, same samples, diff particle sizes, SSA, p=4, max a = 0.8)

SNR	Pure endmembers	SISAL	SISAL (normalised)
25	0.20740	0.24923	N/A
35	0.07305	0.10643	N/A
45	0.03954	0.04476	N/A
55	0.03012	0.03019	N/A

Image 3a (4 endmembers, 2 minerals, same samples, diff particle sizes, SSA, p=4, max a = 0.8) this time combining same mineral abundances

SNR	Pure endmembers	SISAL	SISAL (normalised)
25	0.06603	0.11152	N/A
35	0.02526	0.05987	N/A
45	0.01322	0.02152	N/A
55	0.01135	0.01208	N/A

Image 3b (4 endmembers, 2 minerals, same samples, diff particle sizes, RR, p=4, max a = 0.8)

SNR	Pure endmembers	SISAL	SISAL (normalised)
25	0.26948	0.56806	0.47260
35	0.09544	0.14677	0.44516
45	0.02966	0.04677	N/A
55	0.00918	0.01202	N/A

Image 3b (4 endmembers, 2 minerals, same samples, diff particle sizes, RR, p=4, max a = 0.8) this time combining same mineral abundances

SNR	Pure endmembers	SISAL	SISAL (normalised)
25	0.03198	0.12168	0.16520
35	0.01077	0.05307	0.18009
45	0.00392	0.01476	N/A
55	0.00109	0.00339	N/A

Image 5a (4 endmembers, 4 minerals, linear mixture of nonlinear mixtures from Mustard and Pieters paper, max a = 0.8, RR)

SNR	Pure endmembers	SISAL	SISAL norm
25	0.11623	0.22890	N/A
35	0.10068	0.20819	N/A
45	0.10664	0.20215	N/A
55	0.10809	0.21764	N/A

Image 5a (4 endmembers, 4 minerals, linear mixture of nonlinear mixtures from Mustard and Pieters paper, max a = 0.8, SSA)

SNR	Pure endmembers	SISAL	SISAL norm
25	0.16662	0.26161	N/A
35	0.15989	0.24497	N/A
45	0.16538	0.25602	N/A
55	0.15989	0.26282	N/A

Image 5b (4 endmembers, 4 minerals, linear mixture of pure spectra from Mustard and Pieters paper, max a = 0.8, RR)

SNR	Pure endmembers	SISAL	SISAL norm
25	0.04397	0.26995	N/A
35	0.01433	0.27520	N/A
45	0.00465	0.25845	N/A
55	0.00138	0.28582	N/A

Image 5b (4 endmembers, 4 minerals, linear mixture of pure spectra from Mustard and Pieters paper, max a = 0.8, SSA)

SNR	Pure endmembers	SISAL	SISAL norm
25	0.31677	0.26995	N/A
35	0.31095	0.37254	N/A
45	0.30836	0.35069	N/A
55	0.31038	0.35326	N/A

Image 7c (15 hydrothermal endmembers, taken from USGS library, 80% pure, p=15, RR)

SNR	Pure endmembers	SISAL	SISAL norm
25	0.20425	0.30510	0.27981
35	0.09007	0.19376	0.15394
45	0.03250	0.08241	0.14145
55	0.01165	0.02727	0.12348

Image 10b (10 endmembers, 10 minerals, p=10, RR, max a = 0.8)

SNR	Pure endmembers	SISAL	SISAL norm	RMVES
25	0.14742	0.25758	0.30316	0.65842
35	0.09452	0.13582	0.11623	0.53754
45	0.08245	0.14152	-	-
55	0.02791	0.15462	-	0.17117

Image 10b (10 endmembers, 10 minerals, p=10, SSA, max a = 0.8)

SNR	Pure endmembers	SISAL	RMVES
25	0.24230	0.31820	0.57492
35	0.19985	0.20487	0.44843
45	0.16392	-	-